THÈSE POUR OBTENIR LE GRADE DE DOCTEUR DE L'UNIVERSITÉ DE MONTPELLIER

En Chimie et Physico-Chimie des Matériaux

École doctorale Sciences Chimiques Balard

Unité de recherche UMR 5253 – Institut Charles Gerhardt Montpellier

Valorising Wadsley-Roth $FeNb_{11}O_{29}$ as Li-ion battery high-rate negative electrode material

Présentée par Dat LE THANH
Le 12 Decembre 2025

Sous la direction de Romain BERTHELOT
et co-directrice : Emmanuelle SUARD

Devant le jury composé de

Valérie PRALONG, Directrice de recherche, CRISMAT	Rapporteuse
Thibaut GUTEL, Directeur de recherche, CEA	Rapporteur
Thierry BROUSSE, Professeur, Université de Nantes	Examinateur
Laure MONCONDUIT, Directrice de recherche, ICGM	Examinatrice
Romain BERTHELOT, Chargé de recherche, ICGM	Directeur de thèse
Emmanuelle SUARD, Senior scientist, ILL	Co-directrice

UNIVERSITÉ DE MONTPELLIER

Résumé de la thèse

La transition énergétique, portée par le déploiement massif des énergies renouvelables et l'électrification de la mobilité, impose des exigences accrues aux technologies de stockage électrochimique. Les batteries lithium-ion, qui constituent aujourd'hui la technologie dominante, doivent conjuguer densité énergétique élevée, capacité de puissance, sécurité d'utilisation et longévité. Cependant, aucun matériau d'électrode ne satisfait pleinement l'ensemble de ces critères, en particulier du côté de l'électrode négative.

Les électrodes négatives conventionnelles illustrent clairement les compromis inhérents à ces matériaux. Le graphite, qui demeure la référence industrielle, présente une capacité spécifique élevée et un coût relativement faible. Toutefois, il présente des limitations majeures : lors de charges rapides, le risque de dépôt de lithium métallique est important, compromettant la sécurité et accélérant le vieillissement. À l'inverse, $Li_4Ti_5O_{12}$, qui offre une stabilité structurale remarquable et une excellente tolérance aux régimes de cyclage élevés, possède un potentiel de fonctionnement trop élevé, ce qui limite fortement la densité énergétique atteignable, et donc son attractivité pour les applications où l'autonomie et la compacité sont prioritaires. Ce constat justifie l'exploration de matériaux alternatifs susceptibles de concilier densité énergétique compétitive, cinétique rapide et sécurité opérationnelle.

Dans ce cadre, les oxydes de niobium adoptant la structure Wadsley–Roth apparaissent comme des candidats particulièrement intéressants. Issus de structures à cisaillement dérivées du type ReO_3, ils se distinguent par une charpente cristallographique robuste et par des réseaux de tunnels interconnectés qui favorisent la diffusion rapide des ions lithium. Leur potentiel d'insertion élevé, comparable à celui du $Li_4Ti_5O_{12}$, représente un compromis intéressant permettant de limiter les risques de dépôt de lithium tout en conservant une densité énergétique satisfaisante. Parmi ceux-ci, $FeNb_{11}O_{29}$ se singularise par la combinaison de la stabilité du squelette Nb–O et de la réactivité redox du fer, offrant un équilibre prometteur entre robustesse structurale et activité électrochimique. Ces caractéristiques en font un matériau particulièrement pertinent pour combler l'écart entre graphite et $Li_4Ti_5O_{12}$ et répondre ainsi aux besoins émergents des batteries de nouvelle génération.

Cette thèse s'est attachée à évaluer le potentiel de $FeNb_{11}O_{29}$ en tant qu'électrode négative, selon plusieurs approches complémentaires. Le travail s'est structuré autour de quatre volets : l'optimisation de la morphologie à travers des synthèses par chauffage micro-ondes afin de contrôler la taille des particules et d'améliorer la diffusion ionique; l'étude *operando* par diffraction neutronique pour élucider le mécanisme de lithiation et comparer différentes configurations expérimentales; la mise en œuvre pratique en cellules complètes, depuis des formats bouton jusqu'aux prototypes industriels 18650, accompagnée d'analyses de vieillissement systématiques; et enfin l'intégration du matériau dans des batteries tout solide, avec une attention particulière portée à la composition des électrodes et aux phénomènes interfaciaux.

Le premier volet a démontré les avantages du chauffage micro-ondes par rapport au chauffage conventionnel en four. Cette méthode permet de réduire considérablement les temps de réaction et limite la croissance cristalline, aboutissant à des poudres submicrométriques mieux adaptées au transport ionique. Les caractérisations électrochimiques (GITT, courbes de capacité différentielle, XRPD *operando*) ont confirmé que ces poudres favorisent une diffusion plus aisée du lithium et réduisent la polarisation. Le polymorphe monoclinique issu de ce procédé a atteint 179 mAh g^{-1} avec une rétention de 90% après 500 cycles à 2 A g^{-1}, soulignant l'efficacité de cette approche. La comparaison avec le polymorphe orthorhombique a mis en évidence l'importance de la microstructure : les échantillons à grains fins surpassent systématiquement les échantillons plus grossiers. Il convient de souligner que même les poudres micrométriques obtenues par chauffage conventionnel ont présenté d'excellentes performances (~150 mAh g^{-1} à 10 C), illustrant les cinétiques intrinsèquement rapides des phases de Wadsley–Roth. Ces résultats sont particulièrement encourageants d'un point de vue industriel, car ils montrent qu'il est possible d'obtenir de bonnes performances sans recourir à des nanostructurations complexes et coûteuses.

Le deuxième volet a porté sur la compréhension du mécanisme de fonctionnement par diffraction neutronique *operando*. Cette technique, adaptée à l'étude des matériaux de batterie, permet de suivre en temps réel les évolutions structurales et de détecter les éléments légers tels que le lithium. Deux types de cellules et deux diffractomètres (D2B à haute résolution et D20 à haut flux) ont été évalués. La première configuration de cellule, optimisée pour la diffraction, s'est avérée facile à assembler et a permis d'obtenir des données d'excellente qualité grâce à l'utilisation de composants non hydrogénés. Cependant, elle a montré des performances électrochimiques limitées,

caractérisées par une forte polarisation et une cinétique ralentie, liées notamment à l'épaisseur des électrodes. À l'inverse, la deuxième configuration, proche d'une cellule cylindrique, bien que générant davantage de bruit de fond, a permis une électrochimie plus réaliste, avec des cinétiques rapides et une compatibilité avec les électrolytes conventionnels.

Les deux diffractomètres se sont avérés complémentaires : D2B, grâce à sa haute résolution, a permis des affinements structuraux précis, tandis que D20, grâce à son flux élevé, s'est révélé adapté au suivi de processus rapides en temps réel. Les expériences menées ont confirmé que $FeNb_{11}O_{29}$ se lithie selon un mécanisme de solution solide, comme en attestent les décalages continus et réversibles des pics de diffraction. Ces résultats indiquent que les réactions électrochimiques se produisent de manière homogène dans l'électrode, même à haute vitesse de cyclage, traduisant les cinétiques rapides propres au matériau. Outre ces résultats spécifiques, ce travail fournit des repères méthodologiques pour un usage plus systématique de la diffraction neutronique *operando*, en soulignant les compromis entre réalisme électrochimique, qualité des données et contraintes instrumentales.

Le troisième volet a concerné la mise en œuvre pratique de $FeNb_{11}O_{29}$ en cellule complète. L'objectif était de dépasser le cadre des demi-cellules, qui fournissent des informations fondamentales mais limitées en termes de pertinence technologique. Les électrodes négatives de $FeNb_{11}O_{29}$ ont été testées contre des électrodes positives NMC, d'abord en cellules bouton puis dans des prototypes cylindriques 18650. La mise à l'échelle de la synthèse et du traitement des électrodes a été réalisée avec succès, confirmant la faisabilité de ce passage au format industriel. Les résultats ont montré que l'utilisation de $FeNb_{11}O_{29}$ permet de délivrer des densités énergétiques intermédiaires à celles obtenues avec des électrodes de graphite et de $Li_4Ti_5O_{12}$. Néanmoins, une polarisation marquée et une dégradation progressive ont été observées, attribuées à des limitations cinétiques et à la présence d'impuretés.

Les études de vieillissement ont révélé que les conditions de fonctionnement avaient une influence déterminante : des températures élevées, des régimes de cyclage rapides et un stockage à haut état de charge accélèrent la perte de capacité et la croissance de la résistance. Ces phénomènes sont associés à des dégradations interfaciales et à l'instabilité de l'électrolyte. Ces résultats mettent en évidence la nécessité de stratégies

d’ingénierie des électrodes et de stabilisation des interfaces, ainsi que d’analyses post-mortem approfondies pour identifier et comprendre les mécanismes de dégradation.

Enfin, un quatrième volet a exploré l’intégration de $FeNb_{11}O_{29}$ dans des batteries tout solide, technologie prometteuse en matière de sécurité et de densité énergétique. Les électrodes négatives ont été formulées avec différentes teneurs en carbone conducteur (VGCF), afin d’optimiser l’équilibre entre conduction électronique et conduction ionique. La composition intermédiaire a donné les meilleures performances, avec une capacité réversible élevée, une polarisation réduite et de bonnes performances en puissance. Une teneur trop faible en carbone limite la conduction électronique, tandis qu’une teneur excessive perturbe le réseau de conduction ionique et augmente la résistance.

Les essais électrochimiques ont révélé certaines limitations cinétiques, notamment à haute vitesse de cyclage, mais ont montré qu'il était possible d'atténuer ces contraintes en appliquant un palier à tension constante lors de la décharge. Les analyses structurales et chimiques ont confirmé la stabilité globale de $FeNb_{11}O_{29}$ et de l’électrolyte Li_6PS_5Cl en volume, avec une légère expansion de la maille indiquant une rétention partielle de lithium. Toutefois, les analyses XPS ont révélé une dégradation chimique à l’interface, marquée par la formation d’espèces soufrées (Li_2S, SO_x^{n-}). Ces résultats soulignent l’importance cruciale des interfaces et la nécessité de développer des stratégies d’ingénierie adaptées pour améliorer la durabilité des batteries tout solide.

Dans son ensemble, cette thèse met en évidence le potentiel de $FeNb_{11}O_{29}$ en tant qu’électrode négative capable d’offrir un compromis original entre densité énergétique et sécurité. Sa stabilité structurale, ses cinétiques rapides et sa compatibilité avec des électrolytes liquides comme solides constituent des atouts majeurs. Néanmoins, des défis subsistent, parmi lesquels la polarisation, la dégradation des interfaces et la sensibilité aux conditions de fonctionnement. Au-delà de ce matériau particulier, cette thèse apporte des contributions méthodologiques notables : mise au point de protocoles de synthèse assistés par micro-ondes, comparaison de cellules et d’instruments pour la diffraction neutronique *operando*, prototypage au format industriel et analyse du vieillissement. Ces avancées offrent un cadre solide pour le développement de matériaux d’électrodes de nouvelle génération et ouvrent des perspectives concrètes pour la conception de batteries plus performantes, plus sûres et mieux adaptées aux enjeux de la transition énergétique.

Funding

As one of the projects of the DESTINY PhD programme, this PhD thesis was co-funded by the Institut Laue-Langevin (ILL) and the European Union's Horizon2020 Research and Innovation programme under the Marie Skłodowska-Curie Actions COFUND (Grant Agreement #945357).

This project has received funding from the European Union's Horizon 2020 research and innovation programme under Grant Agreement N° 945357

Acknowledgement

First and foremost, I would like to express my deepest gratitude to my supervisors, Romain Berthelot and Emmanuelle Suard, who have been extremely supportive, open-minded, as well as dedicated project leaders. Together, they have given me invaluable advice, helpful guidance with certain degrees of freedom so that I could navigate through the research myself relatively autonomously, which is important to develop my independent and critical thinking skills. In particular, while I was struggling through my lost sense of direction in the second year, Romain and Emma were very open to let me work with two side projects. One of them was on the mix-alkali indium chloride solid-state electrolytes, leading to a communication article, while the other on mixed phosphate pyrophosphate compounds has given me a postdoc position. Besides, they gave me the opportunity to collaborate with other laboratories and institutes, contributing to the diversity of my work. In addition, I am also wholeheartedly indebted to Long Nguyen, my mentor in the third year for the works on full-cell ageing and solid-state batteries. Working with him was an immense pleasure and unlimited mental support during my last year.

Second, I am also grateful to the DESTINY program, including Prof. Christian Masquelier and the administrative board, not only for the funding but also for the invaluable networking opportunities during the scientific trainings, annual meetings. It was actually Prof. Masquelier and the MESC+ program that enabled me to step out of my country, to join the European academic community and then to continue on my doctoral studies with DESTINY framework, also coordinated by him. Thirdly, my gratitude is also for the jury members: Valérie Pralong, Thibaut Gutel, Thierry Brousse, and Laure Monconduit, who have dedicated their time and energy to evaluate my thesis manual and presentation. I really appreciate their interesting and thought-provoking questions during the discussion, giving me more perspectives on my research subject. Importantly, my gratitude also goes for my CSI members, Frédéric Favier, Andrea Piarristegy, Marine Reynaud, Maria Teresa Fernandez-Diaz, who have followed and helped keep my project in check, as well as ensured that I was mentally healthy.

Fourthly, I couldn’t thank enough my colleagues and collaborators, without whom I could have completed some parts of my investigation. My works have been greatly complemented by the SEM images by Amandine Guiet (IMMM, Le Mans) and XPS data by Dominique Foix (IPREM, Pau). Besides, I have grown a lot during the time working at LEPMI and ILL (Grenoble) for cylindrical cell assembling and neutron diffraction benchmarking, LRCS (Amiens) for 18650 cell prototyping, Elettra synchrotron facility (Trieste, Italy) for the operando experiments. At LEPMI, I was grateful to have worked with Claire Villevieille (LEPMI) under her invaluable

guidance, as well as other friendly and helpful colleagues: Corentin, Benjamin. At the ILL, help was always around, including Thomas Hansen, Clemens Ritter, Oscar, Ludo, Alain, Sreelakshmi, Ove, … For LRCS in Amiens, it has been a pleasure to discuss with Prof. Masquelier and Mathieu Morcrette and work directly with François Rabuel at the prototyping platform who was extremely hard working and supportive. Thank you, Lorenzo Stievano, Thomas Devic, Pablo and Long for having given me to chance to join your experiments at Elettra and have some beam time for myself, as well as for the great time, food, beer and discussion in Italy.

As I spent most of my time at ICGM Montpellier, I was surrounded by a lot of assistance and technical support. My big thanks are for Bernard Fraisse and Dominique Granier, who were always there to help me for the routine XRD measurement or *in situ* experiments during electrochemical cycling or temperature variation. I am also grateful to Julien Fullenwarth, who was always in the lab to fix everything, provide experimental perspectives and also to collaborate in the joint project. Thank you, Moulay Sougrati, Lorenzo Stievano, Laure Monconduit, Steven Le Vot, …, for providing more insights and advice to my work. I also cherish the time that I shared with my lab mates: Eunice, Jean, Armando, Daniella, Théo, Andrea C, Loïc, Léo, Cédric, Patricia, Antoine, Gerhard, Nicholas V, Andrea G, Gabriele. My working environment would not be as memorable and fun without you. Thank you for the photo album and the gifts that you prepared for me.

Last but not least, I am forever and immensely grateful to my family, teachers and friends in Viet Nam, who have been supporting me unconditionally ever since. I am so lucky to have received so much love from everyone.

Table of Contents

Chapter I

Wadsley-Roth $FeNb_{11}O_{29}$ phases for fast charging batteries

I.1. Batteries as energy storage systems

Batteries are electrochemical devices that store chemical energy and convert it into electrical energy on demand. By enabling efficient storage and delivery of electricity, batteries play a critical role in reducing reliance on fossil fuels and accelerating the transition to low-carbon, sustainable energy systems.

Generally, batteries can be classified into primary (non-rechargeable) and secondary (rechargeable) systems. While primary batteries are used in single-use applications, secondary batteries dominate sectors where frequent recharging is essential. Among the various rechargeable technologies, lithium-ion batteries (LIBs) have emerged as the most widespread due to their combination of performance, scalability, and economic viability.

Battery performance is evaluated using several key metrics. Energy density (Wh kg^{-1} or Wh L^{-1}) measures how much energy can be stored for a given mass or volume, directly influencing device runtime or EV driving range. Power density (W kg^{-1} or W L^{-1}) reflects the rate at which energy can be delivered or recharged, an important factor for applications requiring high bursts of power or rapid charging. Cycle life measures how many charge–discharge cycles a battery can sustain before significant capacity loss occurs. Other critical considerations include cost, safety, and sustainability, encompassing both raw material sourcing and end-of-life recycling.

I.1.1. Lithium-ion batteries

Since their commercialization in the early 1990s, lithium-ion batteries have transformed energy storage. Their success stems from their high energy density, relatively long cycle life, and good efficiency compared to other rechargeable technologies such as nickel–metal hydride or lead–acid batteries. From powering portable electronics and electric vehicles (EVs) to facilitating the large-scale integration of intermittent renewable energy, batteries are the heart of modern society towards the net-zero emission target [1–6].

A typical LIB consists of a positive electrode (commonly layered lithium transition-metal oxides, spinels, or olivine-type compounds), a negative electrode (graphite being the most prevalent), a liquid electrolyte (a lithium salt dissolved in an organic solvent), and a separator that prevents direct contact between electrodes while allowing lithium-ion transport [1–8]. During charging and discharging, lithium ions shuttle between the two electrodes through the electrolyte, accompanied by electron flow through the external circuit.

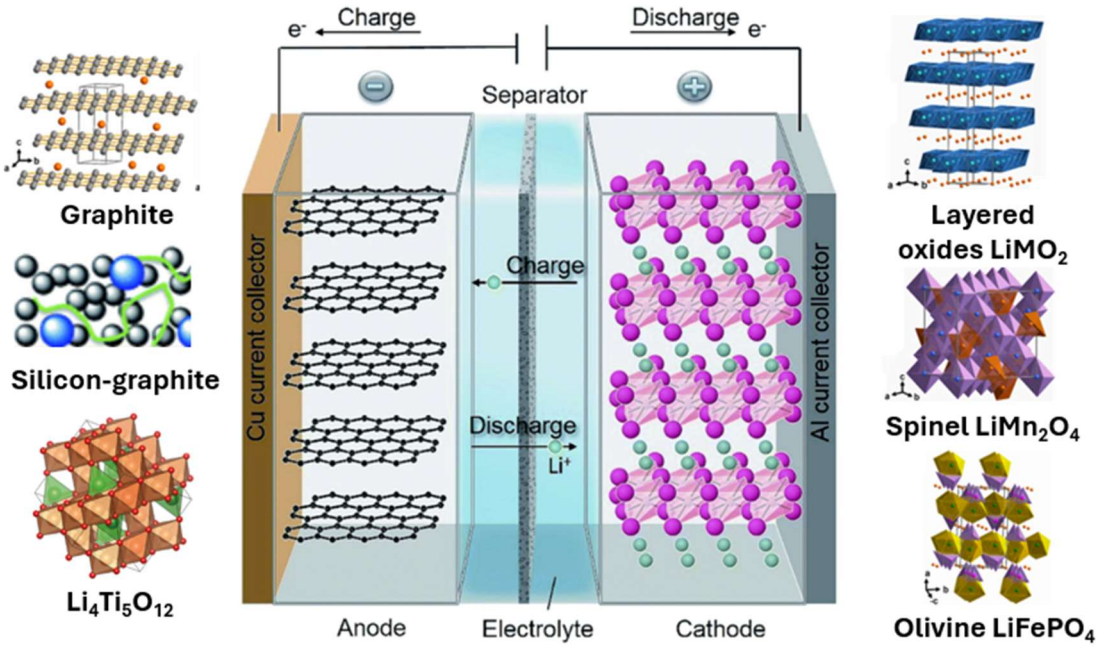

Figure I.1. Lithium-ion battery structure with common negative and positive electrode materials. Modified from [1].

Despite their advantages, LIBs face notable limitations. High charging currents can cause lithium plating on the negative electrode, leading to capacity fade and safety risks. Elevated temperatures during fast charging increase the likelihood of thermal runaway, while low temperatures exacerbate internal resistance and hinder ion transport. In addition, reliance on critical raw materials such as cobalt raises concerns about cost, supply stability, and environmental impact. These challenges have motivated extensive research into alternative materials, new architectures, and safer electrolyte systems [7–11].

I.1.2. Diverse research directions on batteries

The pursuit of improved LIBs spans a wide spectrum of strategies, targeting different components and performance parameters [1–21].

- Positive electrode development focuses on enhancing capacity, stability, and resource sustainability. High-nickel layered oxides offer increased energy density, while cobalt-free cathodes aim to reduce cost and supply risk. Sulfur-based and polyanionic compounds are also under active investigation for their high theoretical capacities and elemental abundance.
- Negative electrode innovations explore alternatives to graphite, including silicon-based materials, and titanium-based oxides such as $Li_4Ti_5O_{12}$ and Wadsley–Roth phases, which offer high rate capability and structural stability.

- Electrolyte research aims to improve safety and broaden the operational temperature range. Solid-state electrolytes—including sulfides, oxides, and halides—show promise for enabling lithium metal, while ionic liquids and flame-retardant additives enhance the safety of liquid systems.
- Sustainability and recycling efforts address the environmental footprint of battery production and disposal, seeking closed-loop manufacturing cycles and second-life applications for used batteries.

Beyond general performance improvements, there is increasing focus on application-specific optimization. High energy density is crucial for EV range, long cycle life is indispensable for stationary grid storage, and low-temperature resilience is vital for cold-climate operation. Among these goals, fast charging stands out as one of the most urgent and challenging targets, especially for widespread EV adoption.

I.2. Fast charging batteries

I.2.1. State of the art and challenges of fast-charging batteries

In the global transition to electric vehicles (EVs), it is important to have an optimal balance between energy density and power density of batteries. This is required to achieve a good compromise between the driving range and the charging time. Currently, LIBs take more time to charge compared with the quick refuelling of internal combustion engines vehicles. In fact, long charging time of batteries is one of the main obstacles for the widespread applications of EVs. This emphasizes the need for fast charging or even extremely fast charging (XFC), which aims to deliver 80% state of charge within just 15 minutes, as targeted by US Advanced Battery Consortium (USABC) [22]. Achieving such charging performance would bring EV user experience closer to that of conventional gasoline cars, giving more satisfaction for customers.

While research has made significant progress toward faster charging, the best-performing commercial EVs still fall short of the XFC target. The driving range of Tesla Model 3, for example, is about 500 km, enabled by $LiNi_xCo_yAl_{1-x-y}O_2$ (NCA) paired with graphite. Using a high-power direct-current charger, the battery can charge from 10% to 80% SoC in 20–30 minutes [23–25]. This is the highest charging rate among all EVs in the market, yet it remains below XFC target.

Fast charging requires high power density, but this comes at the cost of reduced energy density. Additionally, these fast-charging conditions can adversely affect the performance, safety and lifespan of the battery, and may accelerate degradation of cells, for example lithium

dendrites, electrolyte decomposition, and low active material utilization. Therefore, robust high-rate materials and stable cell designs are required to meet these needs.

I.2.2. Kinetic limitations in the negative electrode

To improve the rate capability and enhance fast charging performance of batteries, it is crucial to gain a deeper understanding of the fundamental mechanisms that govern battery behaviour at different scales. Fast-charging of lithium-ion batteries is inherently limited by processes occurring at material, electrode and cell levels [22,25–30].

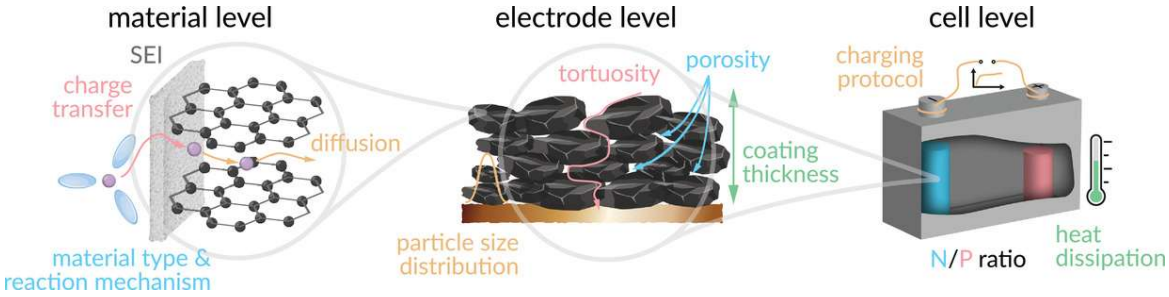

Figure I.2. Parameters relevant for fast-charging batteries from material to cell level. Adapted from [26].

I.2.2.1. Kinetic limitations on the material level

At the material level, three key processes govern the fast-charging performance: (i) Li^+ charge transfer, (ii) Li^+ solid-state diffusion, and (iii) electronic conductivity.

Firstly, charge-transfer is associated with Li^+ migration from the electrolyte into the active material particles. In case of lithium insertion, this migration involves Li^+ desolvation, its transport across the solid electrolyte interface (SEI) if present, and finally, and subsequent electron acceptance from the external circuit (Figure I.3) [26,31]. Each of these phenomena is associated with an energy barrier that contributes to the charge-transfer resistance and overpotential, both of which affect the electrochemical reaction kinetics. SEI layer, though essential for interface stabilisation and suppression of electrolyte decomposition, can still hinder Li^+ transport if it is poorly conductive or energetically unfavourable for Li^+ desolvation. For example, the energy barrier of Li^+ transfer into lithium titanate ($Li_4Ti_5O_{12}$) is only around 0.33 eV, lower than 0.54 eV required for graphite [32]. This difference could be explained by the absence of an SEI layer on the $Li_4Ti_5O_{12}$ surface, which partially accounts for its enhanced fast-charging performance.

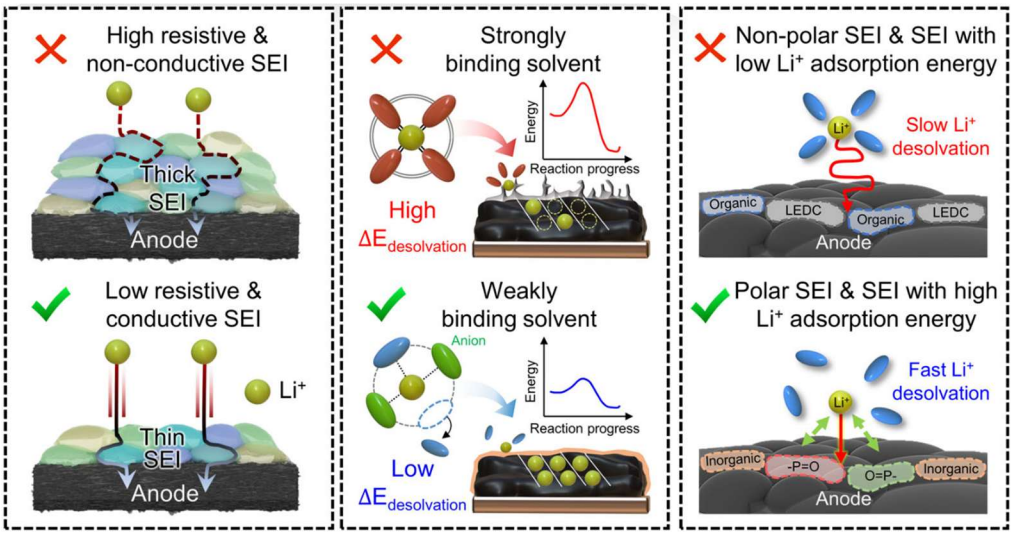

Figure I.3. Factor affecting charge-transfer process in fast-charging LIBs. Adapted from [33].

Inside the bulk of active material, Li^+ solid-state diffusion is the dominant rate-limiting step. This process is governed by the intrinsic solid-state Li^+ diffusivity in the active material and the effective diffusion lengths, which are strongly influenced by the particle size. Larger particles exhibit longer diffusion pathways, which hinder Li^+ transport across the entire solid bulk and result in lower capacity at high C-rates. Nanostructuring and porous morphologies are widely used to shorten diffusion distances and enhance Li^+ transport. However, these strategies increase the surface area of active materials in contact with the electrolyte, inducing more electrolyte degradation except protected by coating layers.

Finally, electron transport is also critically important for electrochemical reaction kinetics. For example, highly conductive materials such as graphite and lithium metal are less limited by electronic transport, whereas silicon and $Li_4Ti_5O_{12}$, with inherently low electronic conductivity, require modifications to enhance their performance. These strategies include carbon coating, nanosizing, or incorporating conductive additives.

I.2.2.2. Kinetic limitations on the electrode level

On the electrode level, the electrochemical kinetics of batteries mainly depends on three interconnected factors: porosity, tortuosity, and coating thickness, which are influenced by the active material microstructure and the electrode coating process. The electrode fabrication starts with the preparation of a slurry, typically composed of well-mixed active material, conductive carbon and polymeric binder in a solvent. This mixture then goes through the casting, drying and calendaring steps. The obtained electrode would contain the pores between the components, tortuous paths connecting the pores and a certain thickness.

Firstly, porosity—the fraction of void volume in the electrode—is a crucial parameter for cell performance, as it governs electrolyte infiltration and the ease of ion transport through the

composite electrode. Optimizing electrode porosity is essential during electrode manufacturing to have a good compromise between electronic and ionic conductivity, as well as a balance between energy and power density. Higher porosity is favorable for ionic conduction but can disrupt the electronic percolation network and reduce both gravimetric and volumetric energy density. By contrast, low porosity improves energy but restricts ionic pathways, limiting high-rate performance. During cycling, pores can be clogged due to ongoing SEI formation, reducing effective porosity and impairing ion transport.

Secondly, tortuosity quantifies the efficiency of the ion transport through the zigzag, convoluted pathways formed by electrolyte-filled pores within a porous composite electrode microstructure. It arises from the locally heterogeneous distribution of active material, conductive additives and binder, which forms irregular and extended pore networks that increase the effective ion transport distance [26]. While porosity quantifies the volume fraction of voids, it does not indicate whether these voids are well-connected. For example, an electrode may have high porosity yet still exhibit high tortuosity if many pores are disconnected or form dead-end routes. An ideal, straight ion pathway would have a tortuosity value of $\tau = 1$, whereas real electrode microstructures often exhibit complex, tortuous paths. Tortuosity can be experimentally quantified by impedance spectroscopy and tomography, often combined with simulations to optimize electrode architecture [34]. Higher tortuosity impedes ion transport, especially under high-rate conditions, leading to significant ohmic and concentration polarization. These effects are worsened in thick, highly loaded electrodes, where long and obstructed ion pathways can cause large overpotential and reduced material utilization.

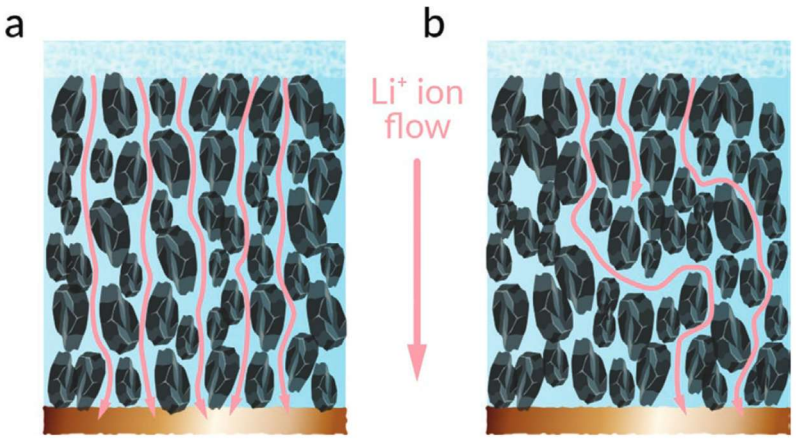

Figure I.4. (a) straight and efficient ionic pathways, and (b) blocked pores with high tortuosity [26]

The third factor in electrode engineering that affects battery performance is the electrode coating thickness. Reducing coating thickness is an effective strategy for better fast-charging capabilities, as thinner electrodes facilitate shorter ion and electron transport paths. However, this comes at the expense of lower energy densities and higher manufacturing costs. In current

commercial cells, single-sided coatings can reach thickness of up to 100 µm. While thicker electrodes theoretically offer higher energy density, they are often impractical due to high internal cell polarization and ineffective utilization of active material.

Fast-charging performance can be improved through various electrode engineering strategies, such as adjusting active material loading, thickness, and porosity, reducing tortuosity, and minimizing non-active additives. Among these, calendaring is particularly important. Calendaring compresses the electrode, improving adhesion to the current collector, essential for mechanical integrity during cycling, and increasing both gravimetric and volumetric energy density. It also reduces pore volume and enhances electronic contact between active particles, thereby optimizing both electronic conductivity and ionic transport. However, excessive calendaring can collapse pores, restrict ionic pathways, induce particle cracking, or damage the current collector. Therefore, calendaring parameters must be carefully optimized to balance efficient ion/electron transport.

I.2.2.3. Key requirements for fast charging batteries: from material design to cell architecture

Fast-charging materials should ideally possess the following characteristics:

- low energy barriers for lithium-ion insertion into the material,
- low barriers for lithium-ion diffusion within the solid phase, and
- small, uniformly distributed particle sizes, e.g. nanoparticles, to enhance kinetics, while maintaining good processability and minimizing irreversible capacity losses.

Besides, additional factors at the electrode level must be optimized:

- low tortuosity, which is challenging for small particle size;
- balanced porosity to ensure effective electronic and ionic conductivity; and
- minimized volume change of electrode during cycling for mechanical integrity.

At the cell level, fast charging must address thermal management and minimize lithium plating [26].

- At low ambient temperatures, controlled internal heating can enhance lithium-ion mobility and diffusion while suppressing lithium plating.
- At high ambient temperatures, heat buildup should be minimized through effective thermal dissipation in cell design.
- Charging protocols should be carefully managed to avoid low negative electrode potentials, which can lead to lithium deposition.

I.2.3. Degradation of materials and interfaces induced by fast charging

Degradation mechanisms in Li-ion cells have been extensively investigated in previous studies, notably by Howey et al. [35]. These mechanisms arise from a complicated interplay of multiple parameters, leading to lithium inventory loss or active material degradation. Under fast charging, the most critical pathways are: (i) lithium plating on the negative electrode; (ii) accelerated side reactions caused by overpotentials and internal heating; and (iii) mechanical damage such as particle cracking [22,26,27].

Firstly, lithium plating and dendrite formation can occur in low-potential electrodes such as lithium metal and graphite, and are especially pronounced at high currents. This issue poses serious safety risks of short circuits, which can trigger exothermic reactions. A well-known example was Moli Energy's commercial cells using metallic lithium, which suffered severe safety failures and were ultimately withdrawn from the market in 1989 [36]. Since then, carbonaceous materials, including graphite, were proposed by Akira Yoshino as negative electrode materials, laying the foundation for commercially viable LIBs [37]. However, lithium plating cannot be completely avoided even in carbon-based electrodes due to their low lithiation potential (e.g. < 0.2 V vs. Li^+/Li for graphite).

Thermodynamically, metallic lithium deposition occurs when the negative electrode potential is below 0 V vs. Li^+/Li, but in practice, kinetic limitations also play a critical role. If Li^+ flux from the electrolyte to the electrode surface exceeds the intercalation rate—due to slow charge transfer, sluggish solid-state diffusion, local overpotentials or electrode inhomogeneities—surface plating can occur [38–40]. Lithium plating is particularly accelerated under harsh charging conditions such as (1) low temperatures, (2) high C-rates, (3) high states of charge (SOC), or their combinations (Figure I.5) [38,39,41–43]. At low temperatures, slower Li^+ diffusion in graphite and electrolyte slows down intercalation kinetics, leading to Li^+ build-up at particle surfaces. Likewise, during fast charging, the rate of Li^+ charge-transfer and Li^+ solid-state diffusion cannot catch up with fast incoming Li^+ flux, which causes increased polarization and can drive the potential below 0 V vs. Li^+/Li – favorable for lithium deposition. Even at low charge rate of C/6 at 20 °C, lithium plating can still occur [43]. At high SOC, the combined effects of low potential, restricted diffusion pathways and limited residual capacity can further promote Li^+ accumulation and plating at the electrode-electrolyte interface. Deposited lithium may not be fully stripped during subsequent delithiation, even under slow discharge, leading to "dead lithium" that reduces capacity and heightens safety risks [44]. These effects can be mitigated by minimizing electrode overpotentials, through optimized charging protocols or thermal management strategies such as internal heating during charging.

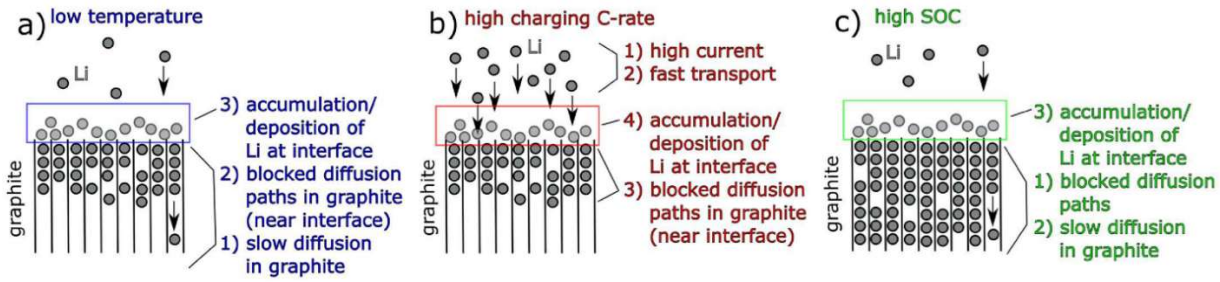

Figure I.5. Schematic of factors influencing lithium deposition on graphite electrodes: (a) low temperatures, (b) high charging C-rates, and (c) high states of charge (SOC). Numbering indicates their relative importance, with highlighted boxes showing the solid–liquid interface where lithium deposition occurs. Adapted from [45].

Secondly, under fast charging conditions, increased overpotentials could lead to higher risks of electrolyte degradation and gas evolution due to parasitic processes. Even under normal charging protocols, conventional carbonate-based electrolytes can still be decomposed when the electrode potential is outside the electrochemical stability window, resulting in electrolyte oxidation or reduction. For negative electrode, potentials below ≈ 1.0 V vs. Li trigger electrolyte reduction and SEI formation. Besides, fast charging can also exacerbate degradation through heat generation. When battery pack is not optimally designed for good heat dissipation, high current densities may lead to a substantial rise in internal cell temperatures, causing different aging mechanisms. While high temperatures tend to suppress lithium plating, they simultaneously worsen the electrolyte decomposition, promote SEI growth, which accelerates long-term degradation. At ~60 °C, SEI decomposition can occur via reactions between LiC_6 and the electrolyte, posing a risk of thermal runaway [46].

Thirdly, fast charging can cause mechanical degradation. High currents applied on large active particles may cause large lithiation gradients between surface and core, resulting in non-uniform stress and particle cracking. These cracks not only disrupt the electronic and ionic networks but also expose fresh surface for further side reactions with the electrolyte. In graphite, high currents may induce co-intercalation between graphite sheets, leading to exfoliation, large volume change, and structural degradation [47]. In silicon, significant lithiation-induced expansion similarly causes cracking, exposing new interfaces and triggering continuous SEI formation [33]. Particle size of active materials strongly influences mechanical stability: large particles suffer from diffusion-induced stress due to lithiation gradients, while smaller particles allow faster Li^+ transport but have higher surface areas, accelerating side reactions and SEI growth. Therefore, optimizing particle size distribution is essential to strike a balance between fast charging capability, capacity retention, and structural integrity.

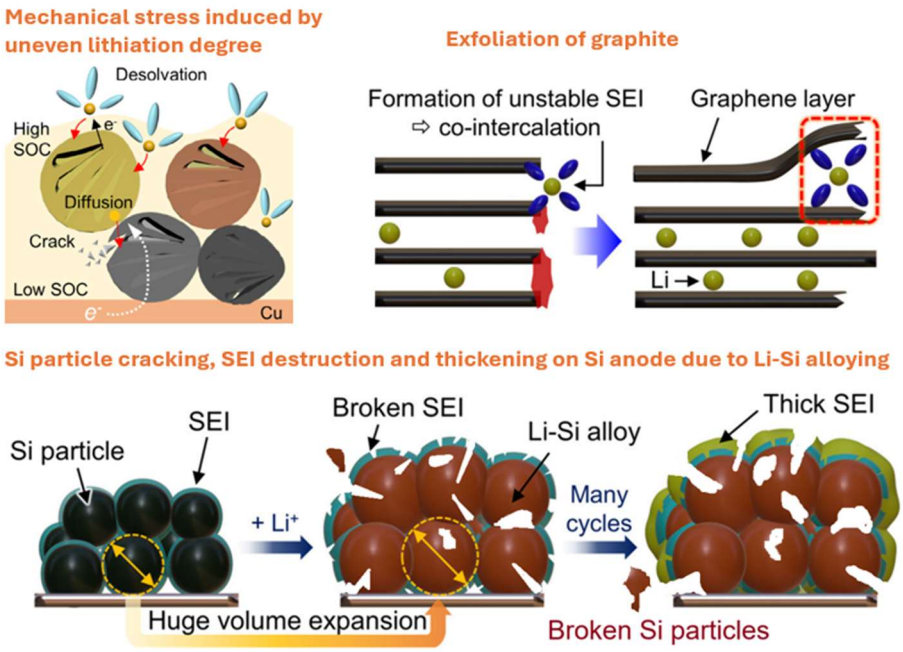

Figure I.6. Mechanical degradation of graphite and silicon are exacerbated under fast charging [33].

I.2.4. Typical negative electrode materials for LIBs

I.2.4.1. Graphite

In commercial LIBs, graphite is the dominant negative electrode material thanks to its high energy density and low cost. This high energy density arises from a high theoretical capacity (372 mAh g^{-1}) and low lithiation potential enabling high cell voltage. The lithium intercalation into graphite is a well-understood, stepwise process occurring through several stages, characterized by the progressive filling of the interlayer spaces between graphene sheets. This staging behavior involves the formation of specific lithium–graphite intercalation compounds (Li-GICs), such as LiC_{36} (stage 4), LiC_{18} (stage 3), LiC_{12} (stage 2), and ultimately the fully lithiated LiC_6 (stage 1) [47,48].

However, graphite's working potential is outside the electrochemical stability window of conventional carbonate-based electrolytes, leading to formation of SEI layer, which is electronically insulating and ionically conducting. This passivating layer plays an integral role as it provides an extended window (≈5.0 V) through kinetic protection, allowing stable lithium insertion/deinsertion in graphite and suppressing further electrolyte's degradation. However, it increases cell impedance, consumes Li^+ during formation and lowers the initial coulombic efficiency [49]. Moreover, as discussed in section I.2.3., sluggish Li^+ transport across the SEI layer and low operational potential of graphite limits its rate capability due to particle fracture and the risk of Li dendrites, the latter causing short-circuit and posing serious safety hazards. Therefore, graphite does not satisfy the requirements for fast charging applications.

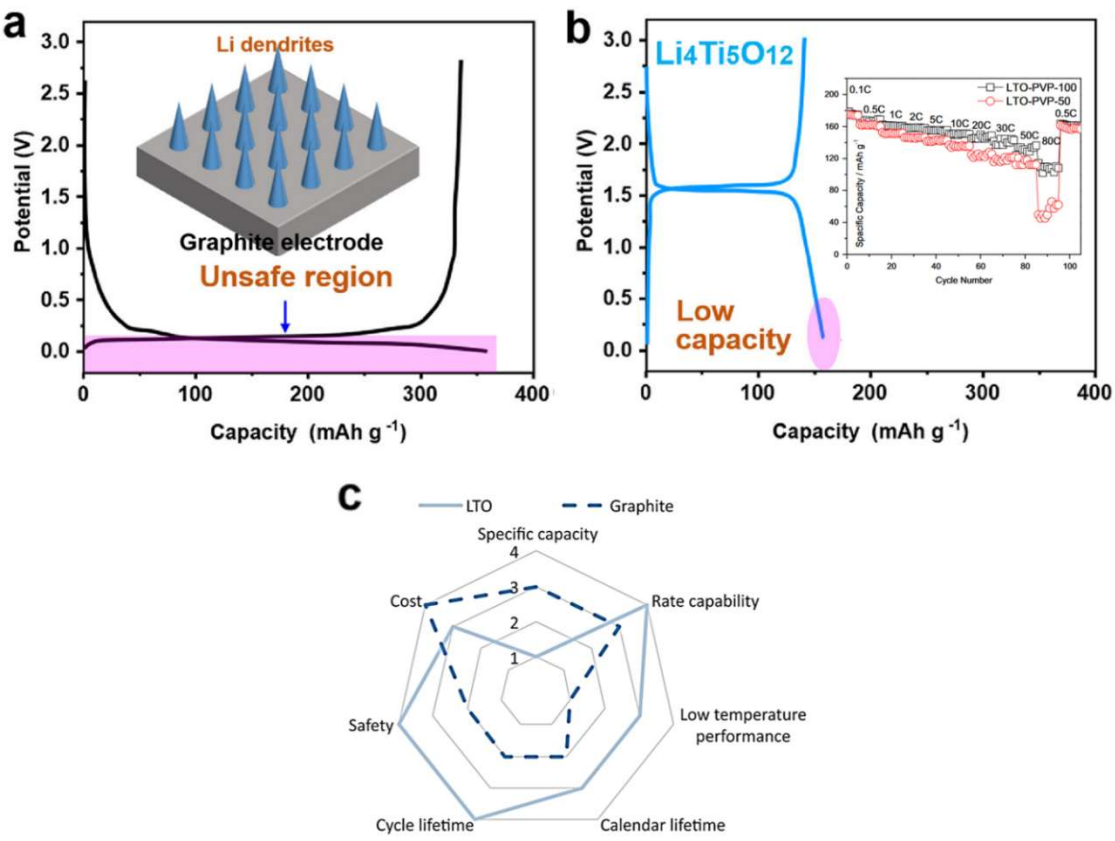

Figure I.7. Comparison between graphite and lithium titanate. Modified from [50–52]

I.2.4.2. Lithium titanate ($Li_4Ti_5O_{12}$)

On the other hand, $Li_4Ti_5O_{12}$, with a higher working potential of 1.55 V vs. Li^+/Li, is a promising candidate for high power applications because it allows for high-rate Li^+ insertion/extraction without the risks of dendrite growth or significant SEI formation. Moreover, it is a "zero-strain" material with negligible volume change during the phase transformation between spinel-type $Li_4Ti_5O_{12}$ and a rock salt-type structure $Li_7Ti_5O_{12}$, giving it long-term cycling stability [53]. However, its moderate specific capacity of 175 mAh/g and low full-cell voltage gives lower energy density. Additionally, $Li_4Ti_5O_{12}$ has poor electronic ($< 10^{-13}$ S cm^{-1}) and ionic conductivity ($< 10^{-11}$ S cm^{-1}) at room temperatures [54,55]. Different strategies have been adopted to address this drawback and access high-rate capability: particle morphology control and nanosizing to reduce the transport distances of Li^+ ions and electrons, and incorporation of conductive coating. For example, $Li_4Ti_5O_{12}$ electrodes with active material loading 4.4 mg/cm^2, composed of 1 um particles synthesized via solid-state method, deliver only ~60 mAh/g at 10C rate [56]. By contrast, a novel solution-based synthesis yields much smaller particles of ~120 um, enabling electrodes with a loading of 2.0 mg/cm^2 to achieve an outstanding capacity of 150 mAh/g at the same rate [50]. Nevertheless, nanometric and porous materials inherently suffer from low tap density, which is a severe penalty in terms of volumetric energy

density. Additionally, their high surface area in contact with electrolytes make them more susceptible to degradation during electrochemical cycling. Moreover, the synthesis, characterization and large-scale manufacturing of these materials are also often time-consuming and costly. Additionally, $Li_4Ti_5O_{12}$ also suffers from the problems of gassing (mostly H_2, CO, and CO_2) during cycling due to reactions between standard carbonate solvents and $Li_4Ti_5O_{12}$ interface [57], which lead to swelling and further safety issues.

These challenges highlight the need for alternative electrode materials better suited for fast-charging applications.

I.3. Wadsley-Roth phases as promising high-rate negative electrode materials for LIBs

I.3.1. Introduction and promising aspects

Wadsley–Roth compounds, also known as block phases, are a family of metal oxides derived from the ReO_3-type perovskite structure. They are characterized by corner-sharing MO_6 octahedral blocks, which are connected via edge-sharing along crystallographic shear planes. These structures exhibit several desirable electrochemical properties, including:

- "Zero-strain" frameworks that ensure robust structural integrity during cycling
- Wide diffusion channels enabling high-rate lithium transport
- High lithiation potentials that limit electrolyte decomposition and suppress SEI formation
- Multi-electron redox activity and multiple Li^+ insertion sites that offer decent specific capacities

Initial investigations into these compositions started in the 1950s-1960s [58–63] by Wadsley and Roth, whose work laid the foundation for the structural classification now bearing their names. In the 1980s, Cava et al. demonstrated that many compositions in this family could undergo chemical lithiation via the reactions with n-butyllithium [64–66], giving the prospects of using them as battery electrodes. Later in 1999, Kumagai conducted an extensive study on the thermodynamics and kinetics of electrochemical lithium intercalation into Nb_2O_5 [67], which is the first time it was used in batteries. Research into this class of materials slowed down until the pioneering works of Goodenough's group in 2011 on $TiNb_2O_7$ phase, with excellent electrochemical properties in terms of capacity and rate capability in both half- and full-cells [68,69]. Since then, the renewed interests have led to considerable advances, e.g. $TiNb_2O_7$ [70,71], Nb_2O_5 [72–74], and $Ti_2Nb_{10}O_{29}$ [75]. Later, the concept of intercalation

pseudocapacitance was introduced to explain the excellent rate properties of this material family [74]. Recent studies have shown that even large micron-sized particles of these shear structured phases, for example, $WNb_{12}O_{33}$ [76], H-Nb_2O_5 [74,77], $TiNb_{24}O_{62}$ [78], $Nb_{16}W_5O_{55}$ [79], $TiNb_2O_7$ [68,69], and PNb_2O_{25} [80–82] can deliver impressive lithium storage capacity at high current rates.

Academic research of Wadsley-Roth niobium-based materials have been strongly active for around 15 years since early 2010s. These efforts have led to proof-of-concept demonstrations and successful laboratory validation. Motivated by these advances, several companies began developing and producing such materials, including Battery Streak, which provides nano-structured niobium oxides ("niobia") [83], and NEI Corp, which supplies $TiNb_2O_7$ and Nb_2O_5 powder [84]. This progress has paved the way for development beyond materials R&D, reaching the stage of sample cell fabrication and prototype testing. For example, Toshiba is currently developing SCiB^{TM} Nb cells (Super Charge Ion Batteries) based on next-generation $TiNb_2O_7$ material [85] and is testing electric buses in Brazil in collaboration with Brazilian company of metallurgy and mineral (Companhia Brasileira de Metalurgia e Mineração, CBMM) [86]. More recently, two UK-based start-ups, Echion [87] and Nyobolt [88], have been launched from the pioneering works at Grey's research group at Cambridge University, targeting at commercializing niobium-based materials and cells for high-power applications.

In comparison with the mature, well-established and commercialized $Li_4Ti_5O_{12}$ material, Wadsley-Roth phases show promising advantages, including comparable production costs, higher gravimetric capacity, and enhanced volumetric energy densities. In terms of energy and power performance, they represent a balanced compromise between graphite's high energy density and lithium titanate's excellent rate capability and safety. However, for large-scale production, it is crucial to consider the cost and supply chain of niobium, a key element in Wadsley–Roth compounds, to ensure long-term scalability and economic viability.

Niobium (Nb) is ranked 33rd in elemental abundance, with a concentration of approximately 10-26 ppm in the Earth's crust, comparable to some critical elements in battery industry, such as Co (10−18 ppm), Ni (19−60 ppm), Li (20−41 ppm), and Cu (14−32 ppm), but much lower than Mn (600−735 ppm), Ti (0.45%), and Fe (4.1−4.7%) [89–91]. A comparison of niobium's abundance with other elements is represented in Figure I.8 [92,93]. Outside the field of energy storage, niobium has a wide range of applications, such as dopant in high-strength, corrosion-resistant steels, in superconducting magnets in MRI scanners, NMR equipment, as well as aerospace, atomic energy, medical and electronics industries. However, according to the US Geological Survey, "the estimated global reserves and resources of niobium and tantalum are

large and appear more than sufficient to meet global demand for the foreseeable future, possibly the next 500 years." [94] Therefore, niobium resources are still sufficient to meet the demand for producing Wadsley-Roth Nb-based oxides. However, niobium has been designated as "critical" element by the US government because of its many uses in technology and its limited supply chains. Remarkably, about 88% of the world's niobium production comes from Brazil, where CBMM company dominates the global supply of niobium compounds [95].

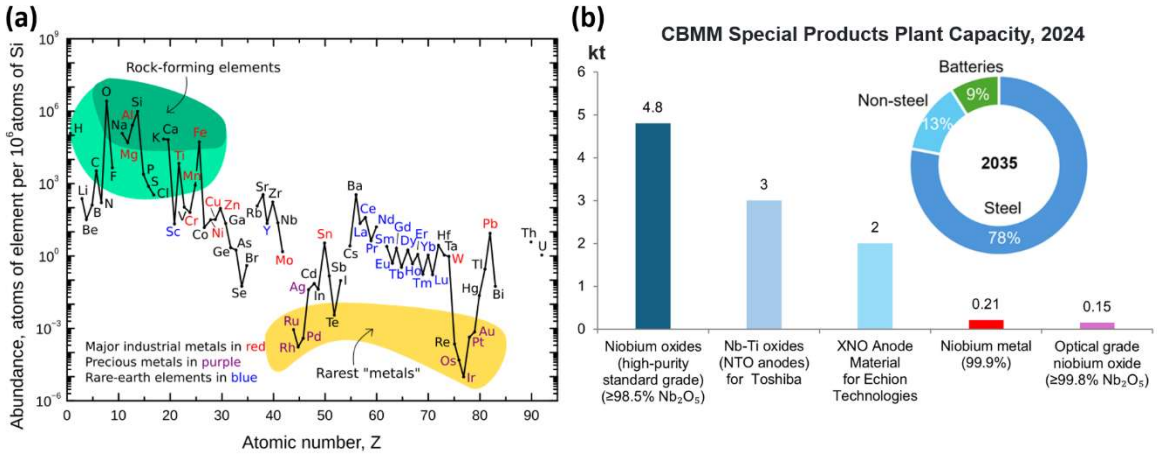

Figure I.8. Relative elemental abundance of niobium compared with others in the Earth's crust [92], and some niobium-based products for battery industry by CBMM [96]

Regarding the precursors for material manufacturing, the price of Nb_2O_5 (56–73 €/kg, 99.99%, Ganzhou Qian Yi Advanced Materials Co., Ltd.) is higher than TiO_2 (33–43 €/kg, 99%, Luoyang Tongrun Nano Technology Co., Ltd.). However, taking into account lithium compounds for $Li_4Ti_5O_{12}$ synthesis, e.g., Li_2CO_3 (10–13 €/kg, 99.9%, Ganzhou Qian Yi Advanced Materials Co., Ltd.), the cost of raw materials for producing Nb-oxides and $Li_4Ti_5O_{12}$ are not so different. Besides, the development of materials for LIBs requires compromises and a diverse choice of material suitable for each application as there's no perfect materials with all desirable properties. Wadsley-Roth phases typically exhibit high tap density which provides significantly higher volumetric energy densities than $Li_4Ti_5O_{12}$, which is an important factor in the cell and package level. Moreover, niobium-based oxides are non-toxic, chemically stable, and air-stable, which makes it safer and easier to handle during synthesis, processing, and electrode fabrication.

I.3.2. Crystallographic shear structure

Wadsley-Roth structure is derived from ReO_3-type perovskite structure. The parent ReO_3 compound belongs to a group of MO_3 oxides (e.g., β-MoO_3, WO_3, and ReO_3) with a three-dimensional network of conner-sharing MO_6 octahedra [78], forming continuous perovskite channels for lithium diffusion. However, its lithium storage ability is limited due to the correlated

tilting and rotations of the octahedra upon lithiation, which distorts and disrupts these lithium diffusion pathways [97]. In addition, the material becomes electronically insulating a high level of lithiation, further hindering its electrochemical activity [97,98].

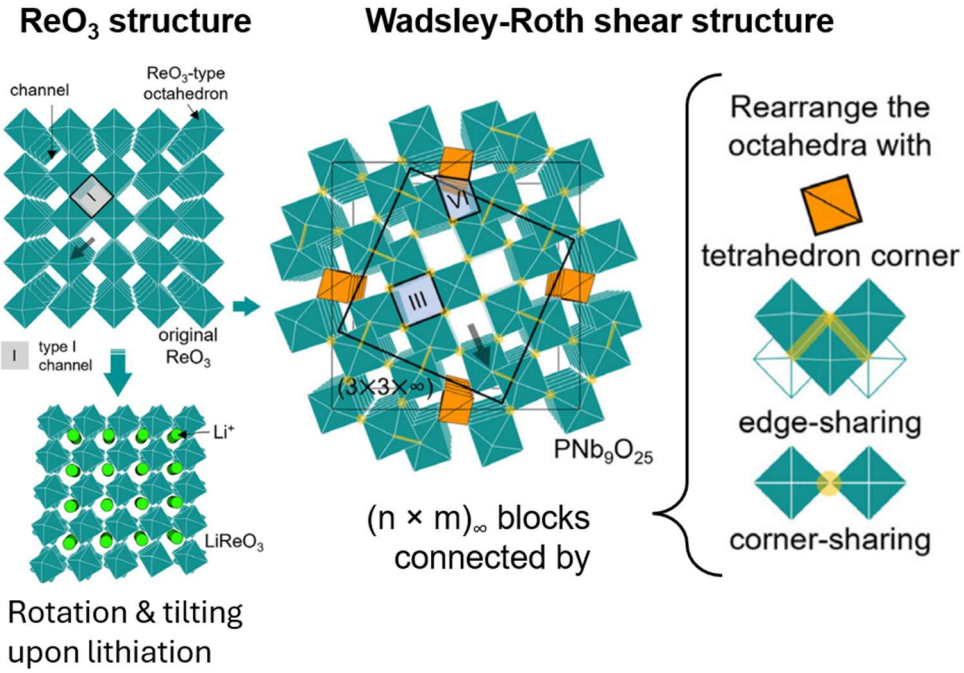

Figure I.9. Structural evolution from parent ReO_3 to Wadsley-Roth phases, with their connectivities [81]

When the valence states of the transition metals are below M^{VI}, the oxides become oxygen-deficient, such as V_6O_{13}, MoO_{3-x}, WO_{3-x}, and $NbO_{2.5-x}$ [78]. In the case of Wadsley-Roth niobium-based oxides, their structure cannot adopt the perfect corner-connected octahedral ReO_3-type network. Instead, a defect structure is formed to accommodate such oxygen deficiency by creating crystallographic shear planes consisting of edge-sharing octahedra at the periphery between corner-connected blocks. The interplay between corner- and edge-sharing connectivity, along with the specific chemical composition, significantly impacts their structural stability and electrochemical behavior. These shear planes not only promote electron delocalization but also reinforce structural integrity, as they protect the structure against the tilting and rotation typically observed in pristine ReO_3-type structures [99]. With only negligible rotation and titling of the octahedra, the wide lithium diffusion pathways are kept open to facilitate ion insertion and transport, especially at high cycling rates. Additionally, this edge-sharing feature also minimizes the volume change of the structure, giving the materials zero-strain property and exceptional robustness.

The notation $(m \times n)_\infty$ of the corner-sharing blocks indicates the finite dimensions m x n in one plane and the octahedra units connect infinitely to form one-dimensional diffusion channels in the perpendicular direction. Each block has multiple parallel tunnels that facilitate ion movements. In one particular Wadsley-Roth composition, $Nb_{16}W_5O_{55}$, bond valence sum (BVS)

mapping was used to investigate possible Li pathways. This study revealed that Li^+ can migrate not only along each parallel channel within the blocks but also through window sites, allowing the ions to switch between the adjacent "lanes" within the same block [79]. As an analogy, these 3D interconnected tunnels are similar to multi-lane highways which enable facile Li^+ diffusion and mitigate the channel-blocking problems at high rate conditions [100].

The block size of these phases is partially governed by the oxygen-to-metal ratio of the compound. A higher number of oxygens per metal indicates less oxygen deficiencies and a composition that more closely approaches that of the parent MO_3. This means more corner-sharing connections between octahedra, and therefore larger blocks [99]. Locally, within these blocks, the octahedra are strongly distorted due to the combined effects of electrostatic repulsion between neighboring cations and the second-order Jahn-Teller (SOJT) distortion [79,101]. SOJT effect occurs in transition metals with d^0 or d^{10} electronic configurations, where slight interaction between the metal's empty or fully filled d-orbitals and surrounding ligand orbitals leads to local asymmetry.

I.3.3. Diverse chemistries

This family of materials exhibits rich chemical versatility, mainly composed of niobium oxide, including Nb_2O_5, oxygen-deficient phases such as $Nb_2O_{5-\delta}$, as well as other compounds within the phase diagrams of MO – Nb_2O_5 (M=Mg, Ni, Zn), M_2O_3 – Nb_2O_5 (M=Al, Ga, Cr, Fe), MO_2 – Nb_2O_5 (M=Ti, Nb), and MO_3 – Nb_2O_5 (M=W, Mo) systems. In most cases, they are typically based on early transition metals (e.g. Nb, W, Ti) capable of multielectron redox reactions, allowing the exchange of more than one lithium per transition metal [100,102]. This contributes to their high theoretical specific capacity in the range of 350 – 400 mAh g^{-1}. Some of the most investigated compounds belong to $TiNb_xO_{2+2.5x}$, Nb-W-O and $XNb_{11}O_{29}$ systems.

The research on this Wadsley-Roth family started with the parent compound Nb_2O_5 in the 1980s. This composition exists in several polymorphs, depending on the heat treatment conditions, including pseudohexagonal (TT-Nb_2O_5), orthorhombic (T-Nb_2O_5) tetragonal (M-Nb_2O_5), and monoclinic (H-Nb_2O_5) phases. These distinct crystal structures significantly influence the electrochemical performance of Nb_2O_5. Among the various polymorphs, T-Nb_2O_5 exhibits significantly superior electrochemical performance. T-Nb_2O_5 has similar structure with tungsten bronzes but consists of highly distorted octahedral and pentagonal bipyramidal niobium environments, rather than regular octahedra. The TT-phase is a metastable structure which shares similarities with T-Nb_2O_5. Monoclinic B-Nb_2O_5 adopts a TiO_2(B)-like structure, while H-Nb_2O_5, another monoclinic polymorph, belongs to the Wadsley–Roth family of crystallographic shear structures, characterized by $(3\times4)_1$ and $(3\times5)_\infty$ octahedral blocks [100,103].

The development of Wadsley–Roth phases from monoclinic H-Nb_2O_5 to other compositions is driven by the need to improve electrochemical performance, structural stability, and versatility for use as negative electrode materials in LIBs. By incorporating other metals, we can tailor block sizes, introduce cation disorder, and modulate electronic properties to enhance lithium storage and diffusion. Block size plays a crucial role in this family of materials. While the crystallographic shear planes, formed by edge-sharing between adjacent blocks, help stabilize the host structure against severe distortion during Li^+ insertion, they can also hinder Li^+ migration across blocks. Therefore, designing shear structures with larger block dimensions and minimized tetrahedral sites is one approach commonly used for this family [102].

I.3.4. Current progress, challenges and outlooks

Future research and development of Wadsley-Roth niobium-based oxides need to follow several strategies as outlined below to meet the requirements for high-rate negative electrode materials in the market.

Regarding commercial viability, electrodes must deliver areal capacity of at least 3.0 mAh cm^{-2}, requiring Wadsley–Roth materials to be loaded above 10 mg cm^{-2}. Most improvement strategies, however, are based on low loadings (~1–2 mg cm^{-2}), and their effectiveness at higher loadings remains uncertain. In addition, a high initial Coulombic efficiency ($\geq$ 90%) is crucial for full-cell lithium-ion batteries to ensure high energy density. However, this modification strategy often triggers severe interfacial side reactions, lowering the initial efficiency. Besides, large-scale synthesis and processing of Wadsley–Roth phase compounds require strict control over key material characteristics such as microstructure, particle size distribution, crystallinity, and uniformity of carbon coating to maintain consistent electrochemical performance. Achieving this at large scale requires scalable, cost-effective methods, such as sol–gel processing, or solid-state reactions, optimized for industrial throughput. Furthermore, process parameters must ensure batch-to-batch reproducibility, compatibility with electrode fabrication techniques (e.g., slurry casting), and low environmental impact. Therefore, to meet commercial requirements, Wadsley–Roth materials must be optimized to deliver high power and balanced gravimetric/volumetric energy densities under high loading conditions.

Wadsley–Roth phases are less susceptible to side reactions with electrolytes due to their moderate operating potentials. However, such reactions can still occur under more demanding conditions, such as high cycling rates or elevated temperatures. The ageing mechanisms of Wadsley–Roth phases, along with their potential interfacial reactions with electrolytes, still require thorough investigation. This is important to fully understand long-term stability, identify degradation pathways, and develop strategies to enhance cycle life and safety in practical battery

systems. Moreover, the safety performance of LIB full cells based on Wadsley–Roth phases must be thoroughly assessed through standardized tests such as accelerating rate calorimetry, nail penetration, and overcharge evaluations.

To assess the feasibility and commercial potential of Wadsley–Roth materials, it is important to evaluate their electrochemical performance in full-cell configurations under practical operating conditions. This includes assembling full cells using industry-available positive electrodes and testing them across a wide range of operating parameters. Specifically, several key factors must be considered to ensure realistic and scalable performance assessments. These include (1) electrode architecture—such as thickness, porosity, and density—which directly affect electron, ion transport and mechanical stability; (2) capacity balancing between negative and positive electrodes; and (3) cell format, whether prismatic, cylindrical, or pouch-type, which influences thermal management and packing efficiency. Additionally, metrics such as total cell capacity, rate capability, and abuse tolerance—including stability under high or low temperature cycling, overcharge, or mechanical stress—must be systematically investigated. These parameters are crucial for moving from laboratory-scale research into commercially viable lithium-ion batteries.

I.4. Target composition: $FeNb_{11}O_{29}$

I.4.1. Strengths and weaknesses

Regarding the development history, this material was first reported in the 1970s [104] but for a long time, it did not inspire any interests in the field of energy storage. In 2005, Tabero synthesized the two stable polymorphs of this iron niobate [105], but it was not until 2014 that its potential use as an negative electrode material in LIBs was proposed [106]. Since then, $FeNb_{11}O_{29}$ has gained attention as a promising new intercalation-type negative electrode material for LIBs. Up to now, there are a few articles published on this particular composition [100,104–120].

Thanks to multiple redox couples Fe^{3+}/Fe^{2+}, Nb^{5+}/Nb^{4+}, and Nb^{4+}/Nb^{3+}, $FeNb_{11}O_{29}$ can theoretically support the exchange of up to 23 electrons per formula unit (f.u.), giving it an impressive theoretical capacity of 400 mAh g^{-1}. This is a slight improvement compared with 22 electron transfer per f.u. of the parent compound $Nb_{12}O_{29}$ ($Nb^{4+}{}_2Nb^{5+}{}_{10}O_{29}$). The theoretical capacity of $FeNb_{11}O_{29}$ about 1.3 times higher than the well-known $Li_4Ti_5O_{12}$ (175 mAh g^{-1}) and even exceeds the capacity of graphite (372 mAh g^{-1}). Moreover, $FeNb_{11}O_{29}$ operates at a relatively high voltage of around 1.6 V, similar to $Li_4Ti_5O_{12}$, which avoids the reduction of

electrolytes and the formation of lithium dendrites, enhancing the cell safety. In practice, the real capacity obtained in the voltage range between 1 V and 3 V versus Li^+/Li is around 260 mAh g^{-1}, corresponding to around 16 Li^+ exchanged per f.u. Further lithium insertion down to low potentials leads to electrolyte degradation but with little capacity enhancement.

$FeNb_{11}O_{29}$ has a double shear structure constituted by blocks of corner- and edge-sharing octahedra that offer an excellent structural robustness and impressive cycling performance. This material also demonstrates intrinsic pseudocapacitive behavior, which can enhance the specific capacity, rate capability, and the long-term cycling stability [112,113].

However, the diffusion of Li^+ ions in $FeNb_{11}O_{29}$ still needs further improvement. Moreover, the material also has poor electronic conductivity, which stems from the oxidation states of the iron (Fe^{3+}) and niobium (Nb^{5+}) ions. Nb^{5+} has empty 4d orbitals, meaning it does not have any free electrons to participate in electronic conduction. As for Fe^{3+}, its 3d orbitals are half-filled, making it relatively stable and unlikely to give up electrons, according to Hund's rule. Together, these factors, insufficient ion diffusion and low electronic conductivity, pose a great challenge on the material's ability to perform well at high charge/discharge rates.

I.4.2. Structures of two $FeNb_{11}O_{29}$ polymorphs

$FeNb_{11}O_{29}$ is isostructural with $Nb_{12}O_{29}$ ($Nb^{4+}{}_2Nb^{5+}{}_{10}O_{29}$), which exists in two polymorphs: an orthorhombic phase (space group *Cmcm*) and a monoclinic phase (space group *A*2/*m*). In both forms, Nb^{4+} and Nb^{5+} cations are randomly distributed within the crystallographic blocks. This structural flexibility allows for partial substitution of Nb^{4+} with other transition metals, enabling the formation of $Nb_{12}O_{29}$ analogues with similar frameworks but improved electrochemical properties, particularly enhanced cycling capacity. Similar to its parent compound, $FeNb_{11}O_{29}$ material also exists in two polymorphs, which are different in their formation temperatures. According to previous studies, the monoclinic phase of $FeNb_{11}O_{29}$ is synthesized at temperature of 900-1100 °C, while the orthorhombic polymorph is obtained above 1250 °C through an irreversible phase transition [105,111,112,114]. Both phases are constructed from blocks of 4×3 $Nb(Fe)O_6$ octahedra which are corner-connected within one individual block. The interblock connection is made by edge-sharing of octahedra, typical of Wadsley-Roth phases, creating crystallographic shear planes to accommodate the oxygen deficiencies.

The subtle structural change between the two polymorphs lies on the linkage of blocks at the same level, sharing *cis* or *trans* corners in orthorhombic and monoclinic forms, respectively [105,111,112,114]. A comparative analysis between their X-ray diffractograms shows very close resemblance because of the close structural similarity of the two phases, with some overlapping peaks. In addition to some characteristic reflections of the monoclinic phase, the formation of orthorhombic polymorph is accompanied by the presence of the reflections (104), (111), (106) and (711), allowing for the distinguishment of the two phases.

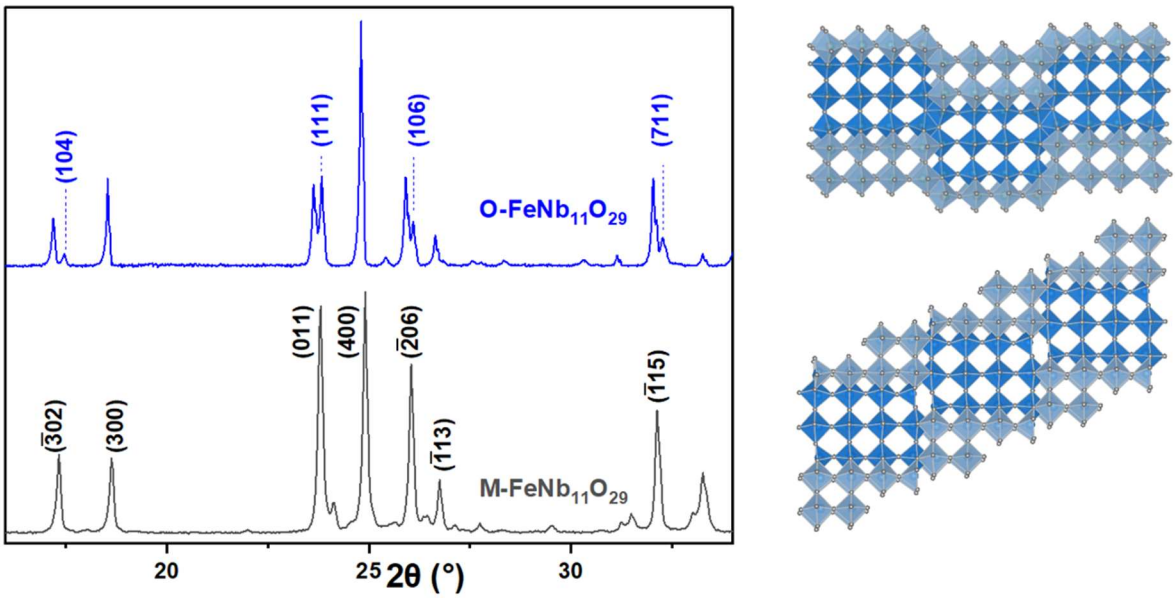

Figure I.10. XRD patterns of monoclinic (M) and orthorhombic (O) $FeNb_{11}O_{29}$, highlighting subtle differences in reflection peaks, such as (104), (111), (106), and (711) in the orthorhombic phase, and corresponding block linkage (cis vs. trans) shown on the right

In both structures, niobium atoms occupy six distinct crystallographic sites, each having varying degrees of octahedral distortion (Figure I.11). Nb6, positioned at the center of the structural block, is the only site that forms corner-sharing connections and is therefore the most regular. Nb1 and Nb3 connect adjacent blocks at the same level through edge-sharing and are highly distorted. Nb2, Nb4, and Nb5 also participate in edge-sharing but connect blocks that are offset by half an octahedron along the *b*-axis; among them, Nb2 is significantly distorted, whereas Nb4 and Nb5 are relatively regular. In the orthorhombic phase, this arrangement suggests electrostatic repulsion between edge-sharing cations. In contrast, in the monoclinic phase, structural comparisons with an idealized model of regular octahedra indicate a possible tilting of the entire block to accommodate these interactions [114].

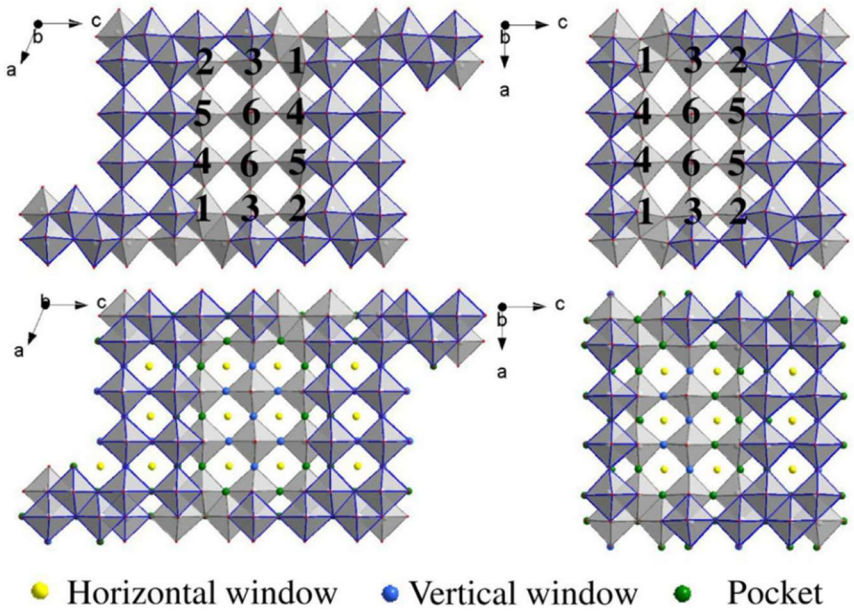

Figure I.11. Coordination environment of Nb^{5+} in $FeNb_{11}O_{29}$ (top) and Li^{+} ions in $Li_{23}FeNb_{11}O_{29}$ (bottom), shown for both monoclinic (left) and orthorhombic (right) structures. Different Li sites are marked in various colors (more details in section I.4.5), and the numbers correspond to the six distinct niobium sites [112].

I.4.3. Effect of Fe^{3+} ion on structure, electrochemical and conducting properties

The effect of Fe^{3+} ions within the $FeNb_{11}O_{29}$ crystal structure was also investigated, as it can significantly influence the material's electrochemical behavior. To clarify this, a combination of complementary techniques was used, including X-ray diffraction (XRD), neutron diffraction (ND), X-ray absorption near edge structure (XANES), and Mössbauer spectroscopy. Pinus et al. used Rietveld refinement of ND data for the orthorhombic polymorph and tested two models for Fe distribution: (i) a fully disordered model with Fe and Nb randomly distributed (1/12 Fe, 11/12 Nb) across all six Nb sites, and (ii) six ordered models with Fe localized on one site (1/2 Fe, 1/2 Nb) and full Nb occupancy elsewhere. The disordered model gave better agreement factors, suggesting Fe is fully disordered [106]. Later, a synchrotron X-ray study confirmed these findings, showing that models with localized Fe did not align with the experimental data, whereas only the model with a uniform Fe distribution across all sites provided a satisfactory match [107].

Between two phases, very similar local structures for both Nb and Fe were observed by X-ray absorption (XAS) and Mössbauer spectroscopy (Figure I.12) [109], which is logical since they are constructed from the same block type. Interesting observations on Fe^{3+} local structure were made. Specifically, a single Fe^{3+} environment cannot explain the observed XAS spectra, suggesting occupation of Fe^{3+} in multiple sites. Furthermore, Mossbauer spectra were deconvoluted into five contributions associated with distinct local environment of Fe^{3+} with

different degrees of octahedral distortion. This could be due to the favorable energetic environment for Fe^{3+} in two cases: (1) reduced cation-cation repulsion at the edge-sharing sites due to its smaller charge, and (2) the energetic stabilization of the less distorted, corner-sharing octahedra at the block center, where Fe^{3+}, a non-Jahn-Teller ion, is preferentially accommodated.

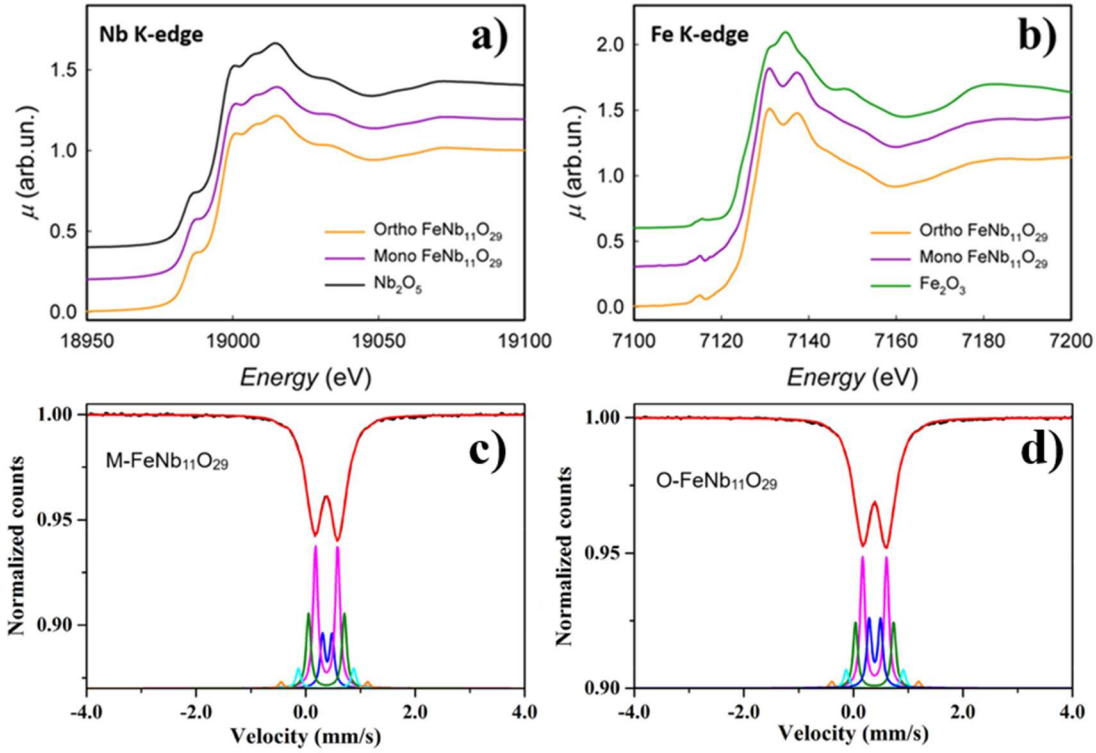

Figure I.12. (a) Nb K-edge and (b) Fe K-edge XANES spectra of orthorhombic and monoclinic $FeNb_{11}O_{29}$, with Nb_2O_5 and α-Fe_2O_3 references. Mössbauer spectra (black) of (c) monoclinic and (d) orthorhombic $FeNb_{11}O_{29}$ at 293 K, with fits (red) and five deconvoluted components (coloured). Adapted from [109].

This phenomenon brings about several effects on $FeNb_{11}O_{29}$ material. First, cationic disorder introduces variability in the Li site energies, which can prevent lithium ordering, thereby increasing the number of accessible intercalation sites for lithium during electrochemical reactions. This disordered distribution of Fe and Nb was also supposed to modify the band structure and improve electronic conductivity of the compound but only to some extent [109].

I.4.4. Electrochemical behavior

I.4.4.1. Redox reactions during cycling

Cyclic voltammograms of both $FeNb_{11}O_{29}$ polymorphs reveal multiple redox peaks attributed to different oxidation states of Nb and Fe: Nb^{3+}/Nb^{4+} (~1.0–1.4 V), Nb^{4+}/Nb^{5+} (~1.5–2.0 V), and Fe^{2+}/Fe^{3+} (~2.4 V). the splitting of the Nb^{4+}/Nb^{5+} peak may originate from the different local environments of Nb atoms occupying six crystallographic sites.

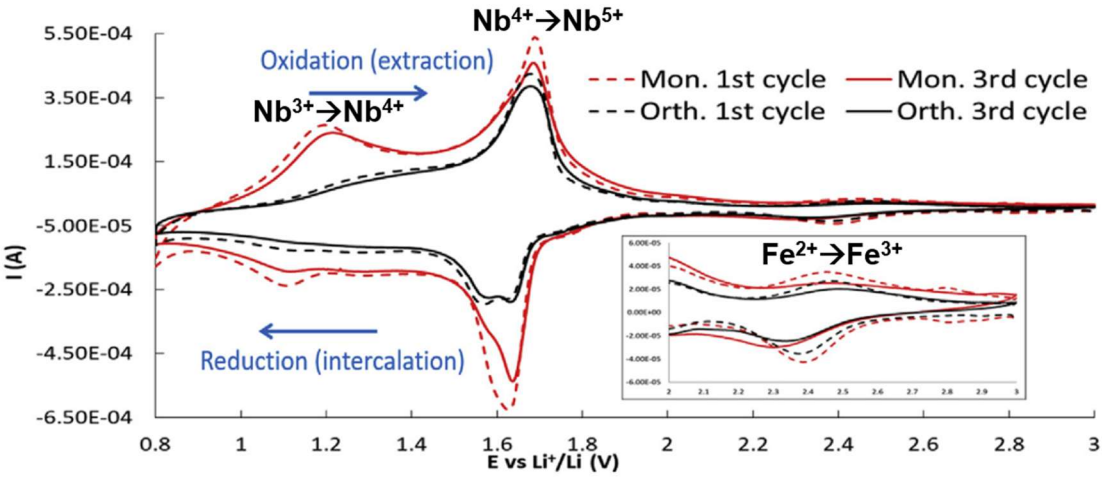

Figure I.13. Cyclic voltammograms of the 1st and 3rd cycles for monoclinic and orthorhombic $FeNb_{11}O_{29}$ [111].

However, their practical capacity significantly differs in literature. For example, the orthorhombic polymorph obtained by conventional furnace treatment was reported to deliver up to 400 mAh g^{-1} at 0.1 A g^{-1} [108], whereas all other research showed lower capacity in the range of 250-300 mAh g^{-1}, depending on the synthesis protocol [108]. The electrochemical difference between the two polymorph was investigated only by Spada et al., where monoclinic one mainly has the charge storage on the surface with higher pseudocapacitive contribution determined by cyclic voltammetry, leading to its lower specific capacity than orthorhombic one [108].

I.4.4.2. A synergy between faradaic and pseudocapacitive behavior

Electrochemical properties of $FeNb_{11}O_{29}$ are an interplay between pseudocapacitive and diffusion-controlled lithium storage mechanisms. Both phases predominantly stores charge via intercalation pseudocapacitance, in which Li^+ ions insert into the structure via fast, faradaic charge-transfer processes without a phase transformation [111,115]. This behavior is enabled by the large, interconnected perovskite-like cavities, which are too large for proper Li^+ coordination, thereby facilitating rapid ion transport and minimizing kinetic limitations [111,121]. As a result, the electrochemical reactions are not constrained by solid-state diffusion, leading to excellent rate capability. Key structural factors influencing this mechanism include crystallinity, surface orientation, crystal structure, and particle size. Generally, high crystallinity and small crystallite sizes are essential for achieving pseudocapacitive behavior [72].

Quantitative analysis of CV profiles at varying scan rates allows for the separation of capacitive and diffusion-controlled charge storage mechanisms. The current at a given potential can be expressed as $i(V) = k_1\nu + k_2\nu^{1/2}$, where ν is the scan rate, and k_1 and k_2 are coefficients corresponding to the capacitive and diffusion-controlled contributions, respectively. In this model, purely capacitive current is linearly dependent on v, whereas diffusion-controlled current follows a $v^{1/2}$ dependence. To extract these contributions, the equation is often rearranged as:

$i(V)/v^{1/2} = k_1 v^{1/2} + k_2$. For each potential value within the electrochemical window, a linear regression of $i(V)/v^{1/2}$ versus $v^{1/2}$ is performed, from which k_1 and k_2 values are obtained, allowing for the separation of these contributions at each potential [111,115,121,122].

This approach was applied for two $FeNb_{11}O_{29}$ polymorphs (Figure I.14). Qualitatively, a signature of capacitive behavior in CV profiles is only slight peak shift at increasing scan rates. Quantitative analysis further reveals distinct trends between the redox couples. During the cathodic scan (from 3.0 V to 1.0 V), Nb^{4+}/Nb^{5+} redox process shows stronger diffusion-controlled behavior, as indicated by more pronounced peak shifts, whereas the Nb^{3+}/Nb^{4+} couple exhibits a predominantly capacitive response. In contrast, the anodic scan shows the opposite behavior: Nb^{3+}/Nb^{4+} becomes more diffusion-limited, while Nb^{4+}/Nb^{5+} demonstrates greater capacitive character.

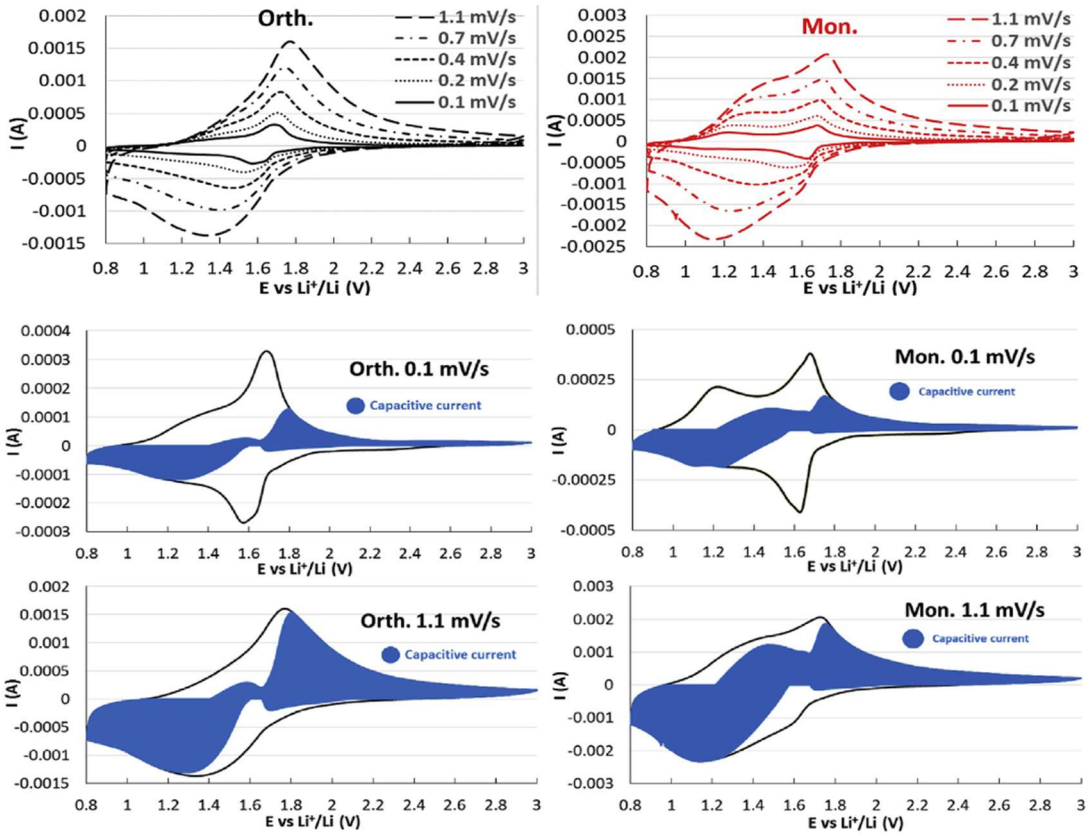

Figure I.14. Cyclic voltammetry curves at different sweep rates for monoclinic and orthorhombic samples, showing pseudocapacitive current contributions at 0.1 and 1.1 mV/s.

I.4.4.3. Structural evolution via *operando* X-ray diffraction studies

Several *operando* X-ray diffraction studies have investigated structural evolution of $FeNb_{11}O_{29}$ during electrochemical cycling with consistent conclusions. One representative study, as shown in Figure I.15, focused on monoclinic $FeNb_{11}O_{29}$ coated with a nitridation layer.

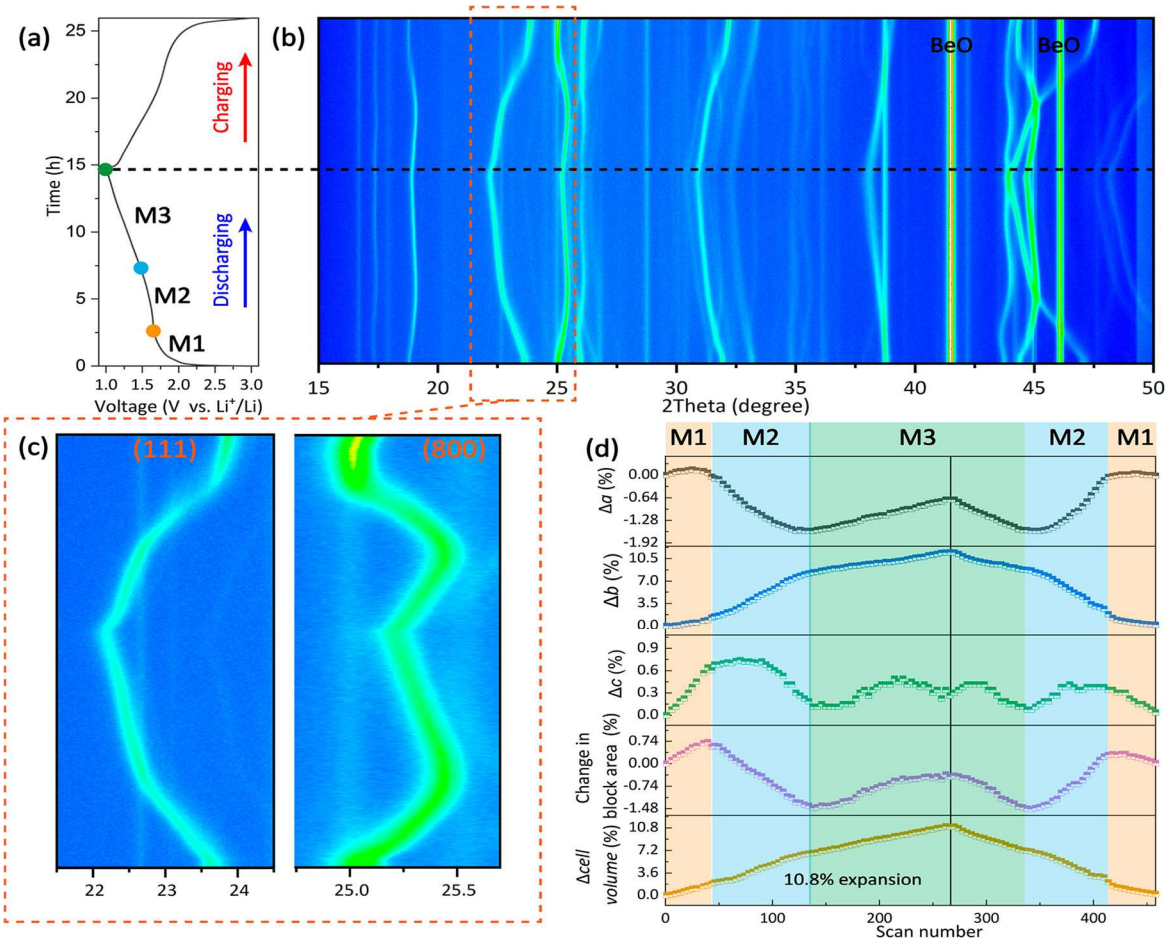

Figure I.15. (a) Charge–discharge profile and (b) *operando* X-ray diffraction contour plot of $FeNb_{11}O_{29}$, with (c) enlarged view in 2θ = 21.5°–25.75°. (d) Evolution of lattice parameters and unit cell volume.

During discharge and charge, the diffraction peaks shifted continuously but returned to their original positions after a full cycle, with no new peaks emerging. This indicates a reversible lattice change without any phase transformation, suggesting a single-phase reaction mechanism.

The evolution of lattice parameters during discharge could be divided into three stages, each correlated with characteristic electrochemical regions of the shear structure:

- High-voltage region (~2.5–1.7 V): expansion of the blocks within the ac-plane, along with slight expansion perpendicular to the block plane (b direction).
- Intermediate region (~1.7–1.4 V): anisotropic behavior with block contraction in the ac-plane, together with significant expansion along the b-axis.
- Low-voltage region (~1.4–1.0 V): multi-redox activity (beyond 1 Li^+ exchanged per transition metal), lattice expansion occurred in all directions, attributed to the reduction of Nb^{4+} (ionic radius: 68pm) to Nb^{3+} (72 pm).

Throughout the entire discharge process, the b-axis expanded continuously, implying that Li^+ diffusion predominantly occurs along this direction. Overall, the total volume increase upon full lithiation was ~10.8%.

I.4.5. Lithium sites and Li^+ insertion/extraction mechanism

I.4.5.1. Lithium crystallographic sites in monoclinic $FeNb_{11}O_{29}$

In Wadsley–Roth phases with block-type structures, lithium sites are typically classified into three groups: (i) fivefold-coordinated 'pocket' sites located at the edges of the blocks, (ii) fourfold-coordinated horizontal 'window' sites, and (iii) fourfold-coordinated vertical 'window' sites [73,123]. The horizontal window sites feature a relatively symmetric oxygen coordination environment, whereas the vertical window sites and some of the pocket sites exhibit lower symmetry. Density Function Theory (DFT) calculations reveal that Li^+ insertion into fivefold-coordinated pocket sites is the most energetically favorable partly due to high coordination number, while vertical window sites are the least favorable due to their large size and lower symmetry [99]. Such lithium coordination environments were observed in orthorhombic $Li_{11}FeNb_{11}O_{29}$, where each formula unit contains 5 Li(V) atoms and 6 Li(IV) atoms [106].

Similarly, monoclinic $FeNb_{11}O_{29}$ exhibits three types of lithium sites (Figure I.16):

- 5 pocket sites (P) at edge-sharing positions, characterized by five-fold coordination.
- Window sites, which are four-fold coordinated, can be further divided into:
  - 3 horizontal window (HW) sites, coordinated by four oxygen atoms in the block plane (ac-plane).
  - 4 vertical window (VW) sites, coordinated by four oxygen atoms in the planes perpendicular to the block.

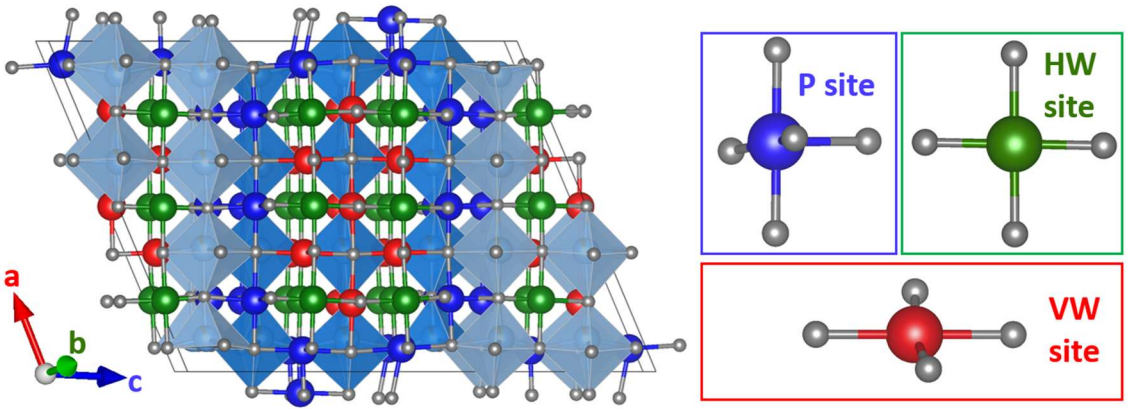

Figure I.16. Monoclinic $FeNb_{11}O_{29}$ structure with three types of lithium sites: pocket sites (P, blue), horizontal window (HW, green) and vertical window (VW, red) sites.

Table I.1. Three types of lithium sites in monoclinic $FeNb_{11}O_{29}$ with their Wykoff position and atomic coordinates

Li site	Wyckoff position	x/a	y/b	z/c	Site
Li1	4i	0.0640	0	0.2646	P
Li2	4i	0.0700	0	0.4773	P
Li3	4i	0.2150	0	0.2074	P
Li4	4i	0.2210	0	0.6261	P
Li5	4i	1/2	0	0.2941	P
Li6	2a	1/2	1/2	0	VW
Li7	4i	0.2075	0	0.4128	VW
Li8	4i	0.3600	1/2	0.0541	VW
Li9	4i	0.3585	0	0.3556	VW
Li10	4i	0.4975	0	0.0947	HW
Li11	4i	0.2180	0	0.8188	HW
Li12	4i	0.2160	0	0.0162	HW

This unit cell contains (4 × 5) + (4 × 3 + 2) + (4 × 3) = 46 Li sites. With two formula units (f.u.) of $FeNb_{11}O_{29}$ per unit cell, this corresponds to 46 / 2 = 23 Li sites per f.u.

I.4.5.2. Suggestive lithiation mechanism of monoclinic $FeNb_{11}O_{29}$

A semi-qualitative approach combining cyclic voltammetry and DFT calculations was used to propose the sequence of lithium site occupation in monoclinic $FeNb_{11}O_{29}$. First, the dominant electrochemical behavior (pseudocapacitive or diffusive) of three redox regions was identified from cyclic voltammetry data [111,112], as discussed in I.4.4.2. These experimental observations were then compared with the site energy predicted by DFT, allowing correlations to be suggested between each redox process and the corresponding lithium insertion site.

Specifically, pseudocapacitive behavior is associated with lithium insertion into window sites located at perovskite-like cavities, where weaker Li–O coordination allows for fast ion transport kinetics and minimal diffusion limitations. By contrast, the diffusion-controlled behavior corresponds to lithium insertion into the more stable fivefold-coordinated pocket sites at the block edges, with limited Li^+ mobility. In terms of bonding energy, as mentioned earlier from DFT results, pocket sites are energetically the most favorable, while vertical window sites are the least [99].

For monoclinic $FeNb_{11}O_{29}$, the suggested sequence of Li^+ insertion/deinsertion is shown in Figure I.17 [112]. During lithiation, the broad feature around 2.4 V, assigned to Fe^{3+}/Fe^{2+} redox couple, exhibits pseudocapacitive behavior [110,111,113,115] and is attributed to lithium intercalation into horizontal window positions. By contrast, the main Nb^{5+}/Nb^{4+} redox peak is diffusion-controlled and therefore corresponds to Li^+ occupation of pocket sites. At lower

potentials, Nb^{4+} to Nb^{3+} reduction again exhibits pseudocapacitive characteristics, suggesting Li^+ insertion into window positions, including both remaining horizontal and newly accessible vertical sites.

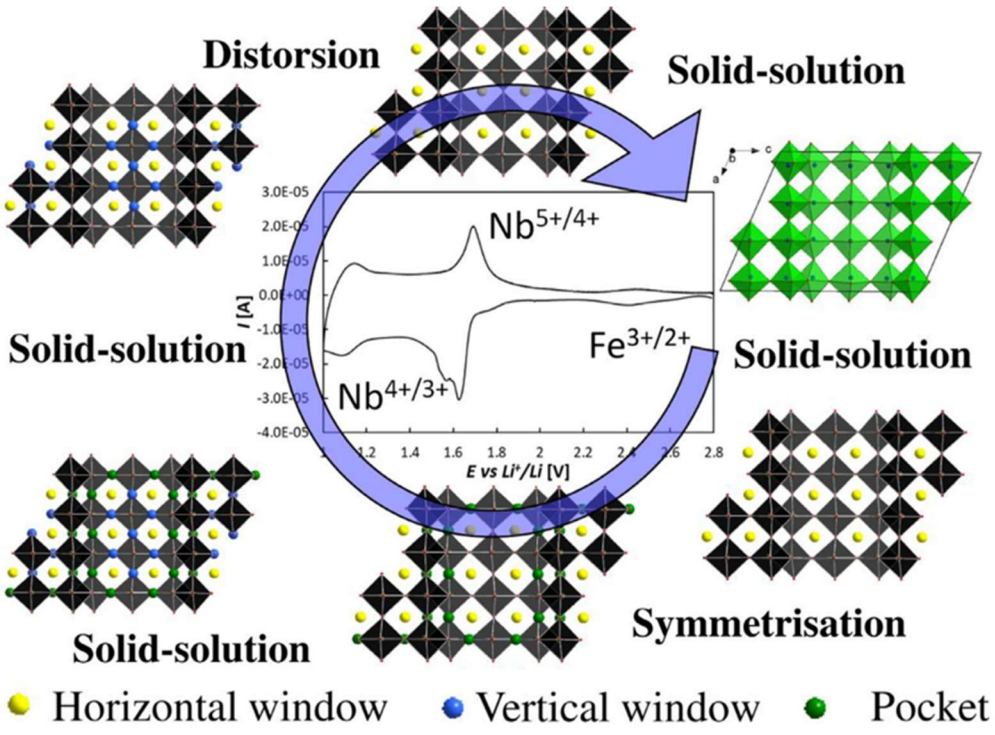

Figure I.17. First-cycle voltammetry of monoclinic $FeNb_{11}O_{29}$ with associated structural changes; the pristine phase is shown in green, and lithiated phases in black. Adapted from [112].

However, delithiation proceeds through a different sequence due to the different behavior of each redox process, as discussed in section I.4.4.2 [111]. The initial oxidation of Nb^{3+} to Nb^{4+} is diffusion-controlled, suggesting that Li^+ ions are first extracted from the pocket sites. This is followed by Nb^{4+}/Nb^{5+} and Fe^{2+}/Fe^{3+} oxidation processes with pseudocapacitive behavior, where Li^+ ions are removed from vertical and horizontal window sites.

I.5. Conclusions and objectives of the thesis

The growing demand for advanced energy storage requires negative electrode materials that have a balance of energy density, power capability, safety, and applicability. Conventional negative electrode materials have inherent trade-offs: graphite provides high capacity but suffers from safety risks such as lithium plating during fast charging, while $Li_4Ti_5O_{12}$ offers excellent safety and rate performance but at the expense of lower energy density. This motivates the exploration of high-rate materials such as Wadsley–Roth phases, and in particular $FeNb_{11}O_{29}$, which combines structural stability, fast ion transport, and a favourable operating potential.

Despite these promising features, several challenges remain for $FeNb_{11}O_{29}$. Therefore, this thesis is structured around the following objectives:

- **Impact of synthesis methods on microstructure and electrochemical behavior:** We seek to study the effect of synthesis routes (microwave-assisted vs. conventional furnace heating) on particle size and morphology, and in turn on Li^+ transport, rate capability, and long-term cycling stability. The ultimate goal is to develop rapid, energy-efficient synthesis methods.
- ***Operando* neutron diffraction and benchmarking of experimental setups:** By investigating structural evolution of $FeNb_{11}O_{29}$ during (de)lithiation using *operando* neutron diffraction, we aim to benchmark cell configurations (coin-type vs. cylindrical) and diffractometers (D2B vs. D20) in terms of practicality, electrochemical performance, data quality, and suitability for different experimental strategies. The objective is to make *operando* neutron diffraction a more accessible and routine tool in battery research.
- **Full-cell evaluation and ageing behavior investigation:** This chapter sets out to assess $FeNb_{11}O_{29}$ in full-cell configurations by (i) evaluating the feasibility of synthesis scale-up, prototyping in 18650-format cells, and benchmarking its competitiveness against graphite and $Li_4Ti_5O_{12}$, and (ii) performing ageing studies in coin cells to identify degradation mechanisms under different temperatures, cycling rates, and storage states of charge.
- **Implementation and optimization in solid-state batteries:** The viability of $FeNb_{11}O_{29}$ in lithium solid-state batteries will be evaluated to identify both its opportunities and interfacial/transport limitations. The work is directed towards optimizing composite electrode formulations for balanced ionic/electronic transport and interfacial stability.

Through these objectives, this thesis aims to valorise $FeNb_{11}O_{29}$ as a promising high-rate negative electrode material for Li-ion and solid-state batteries. Besides, it also seeks to contribute methodological advances in synthesis, *operando* neutron characterization, and electrode optimization relevant to next-generation battery technologies.

Chapter II

Particle downsizing of $FeNb_{11}O_{29}$ by microwave-assisted solid-state synthesis for enhanced electrochemical behavior

II.1. Introduction

II.1.1. Reported modification approaches of $FeNb_{11}O_{29}$

Despite promising properties of Wadsley–Roth $FeNb_{11}O_{29}$ material for high-rate Li^+ storage, its rate capability and cycling stability remain insufficient due to inherently low electronic conductivity. Moreover, further optimization is required for practical applications, which include synthesis methods and scalability, microstructure control, surface modifications or coating, and electrode designs. Addressing these challenges requires a fundamental understanding of the electrochemical processes involved. As shown in Figure II.1, Li^+ insertion into negative electrode materials occurs in three key steps.

i) Li^+ crosses the electrical double layer and removes its solvation shell at the electrode-electrolyte interface.

ii) De-solvated Li^+ ions migrate across the interface and electron transfer occurs.

iii) Li^+ ions diffuse through the bulk of negative electrode materials.

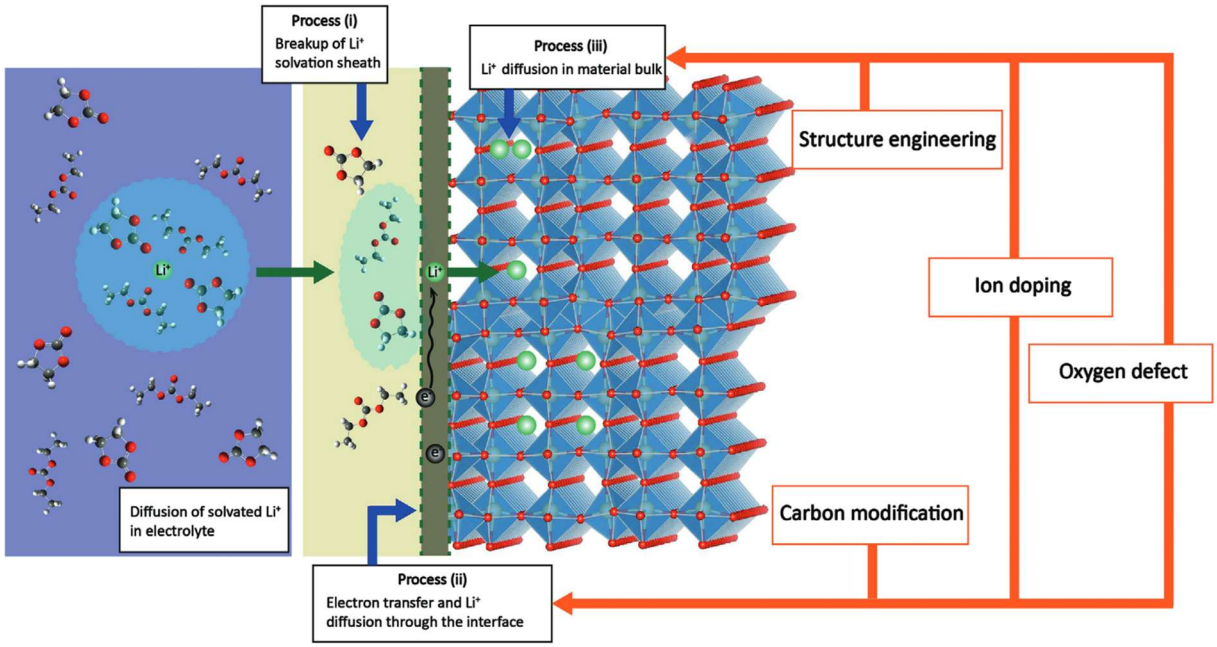

Figure II.1. Schematic of Li^+ insertion into negative electrode and the roles of modification strategies [100]

By aiming to optimize one or several of these processes, a range of modification approaches have been developed to enhance the electrochemical performance of $FeNb_{11}O_{29}$. These include partial substitution of iron with other transition metals such as Ti, V or Mn [110,114,117], creation of oxygen defects by annealing under vacuum or inert atmosphere [115], nitridation surface formation by treatment in Ar/NH_3 atmosphere [108], or nanostructuration by electrospinning [113]. Each of these strategies addresses specific aspects of Li^+ insertion and has been explored in previous studies, as detailed below.

II.1.1.1. Isovalent substitution of iron

A simple and effective method to improve the electronic conductivity of $FeNb_{11}O_{29}$ is partial substitution of iron with other transition metals. Lou et al. demonstrated this approach by doping $FeNb_{11}O_{29}$ with chromium, producing $Fe_{0.8}Cr_{0.2}Nb_{11}O_{29}$ via solid-state reaction, with the oxidation states of Cr^{3+}, Fe^{3+}, and Nb^{5+} confirmed by XPS [124]. The free 3d electrons in Cr^{3+} significantly improved electronic conductivity by nearly three orders of magnitude. As a result, the doped sample exhibited superior electrochemistry: delivering 123 mAh g^{-1} at 10C with 86.9% retention after 500 cycles, compared to 57 mAh g^{-1} (41.6% retention) for pristine sample. Nyquist plots further demonstrated reduced impedance in the Cr-doped material (Figure II.2).

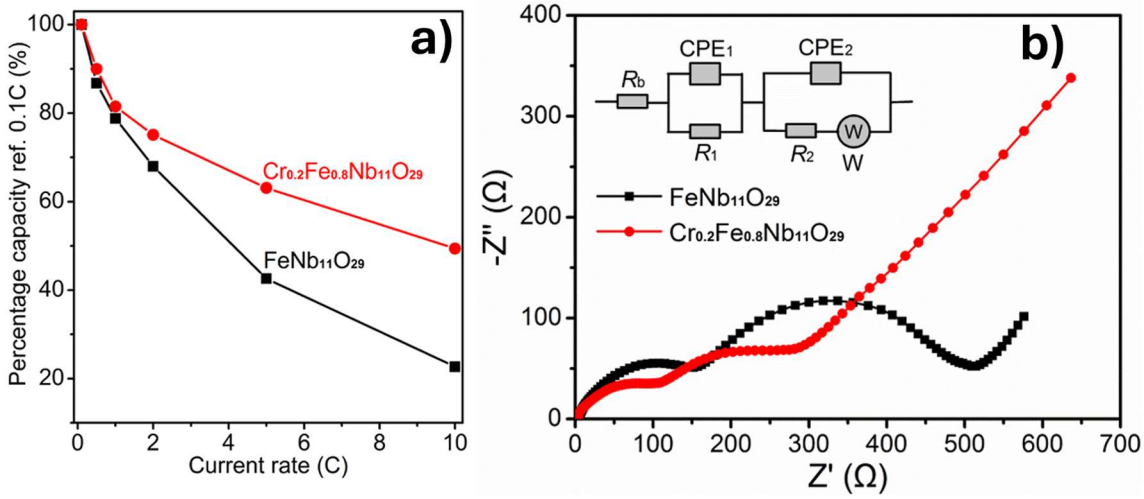

Figure II.2. Effect of Cr substitution on $FeNb_{11}O_{29}$: (a) superior rate capability and (b) reduced impedance of of $Fe_{0.8}Cr_{0.2}Nb_{11}O_{29}$ [124].

Further studies extended this approach to Mn- and V-doped $FeNb_{11}O_{29}$, with compositions such as $Fe_{0.8}Mn_{0.2}Nb_{11}O_{29}$ and $Fe_{0.8}V_{0.2}Nb_{11}O_{29}$ prepared by solid-state synthesis in both orthorhombic and monoclinic forms [110,114]. Electron Paramagnetic Resonance (EPR) and magnetic measurements revealed the presence of Mn^{3+} and V^{3+}. Electrochemical testing demonstrated high capacities of all doped samples (100–150 mAh g^{-1} at 10C). V-doping mainly improved cycling stability, whereas Mn-doping enhanced both capacity and rate capability.

By contrast, Al^{3+} doping on $FeNb_{11}O_{29}$ was aimed at improving structural stability through strong Al–O bonds rather than electronic conductivity. XRD confirmed structure integrity after doping. $Al_{0.2}Fe_{0.8}Nb_{11}O_{29}$ sample showed superior electrochemical properties: its capacity decreased from 318 to 134 mAh g^{-1} as current density rose from 0.1C to 10C, compared to 262 to 104 mAh g^{-1} for pristine $FeNb_{11}O_{29}$. Cycling stability was also excellent for the doped sample, with 92.9% capacity retention after 1000 cycles at 10C [118].

II.1.1.2. Formation of oxygen vacancies

To address the insufficient rate capability of $FeNb_{11}O_{29}$, an oxygen-deficient composition $FeNb_{11}O_{27.9}$ was prepared via a solid-state reaction under N_2 atmosphere [115]. The obtained material preserved the orthorhombic structure of the pristine sample but exhibits a larger unit-cell volume, ~3.8% oxygen vacancies, and Nb^{4+} ions with free 4d electrons as confirmed by XPS (Figure II.3). These modifications significantly enhanced transport properties: Li^+ diffusivity increased by 88.3%, and electronic conductivity improved by three orders of magnitude owing to the presence of Nb^{4+}. Consequently, pseudocapacitive behavior and electrochemical performance were markedly improved. $FeNb_{11}O_{27.9}$ delivered an initial reversible capacity of 270 mAh g^{-1} at 0.1C. Even at 10C, it retained 145 mAh g^{-1} and 93.1% capacity after 200 cycles, far surpassing pristine sample (99 mAh g^{-1} and 88.9% under the same conditions).

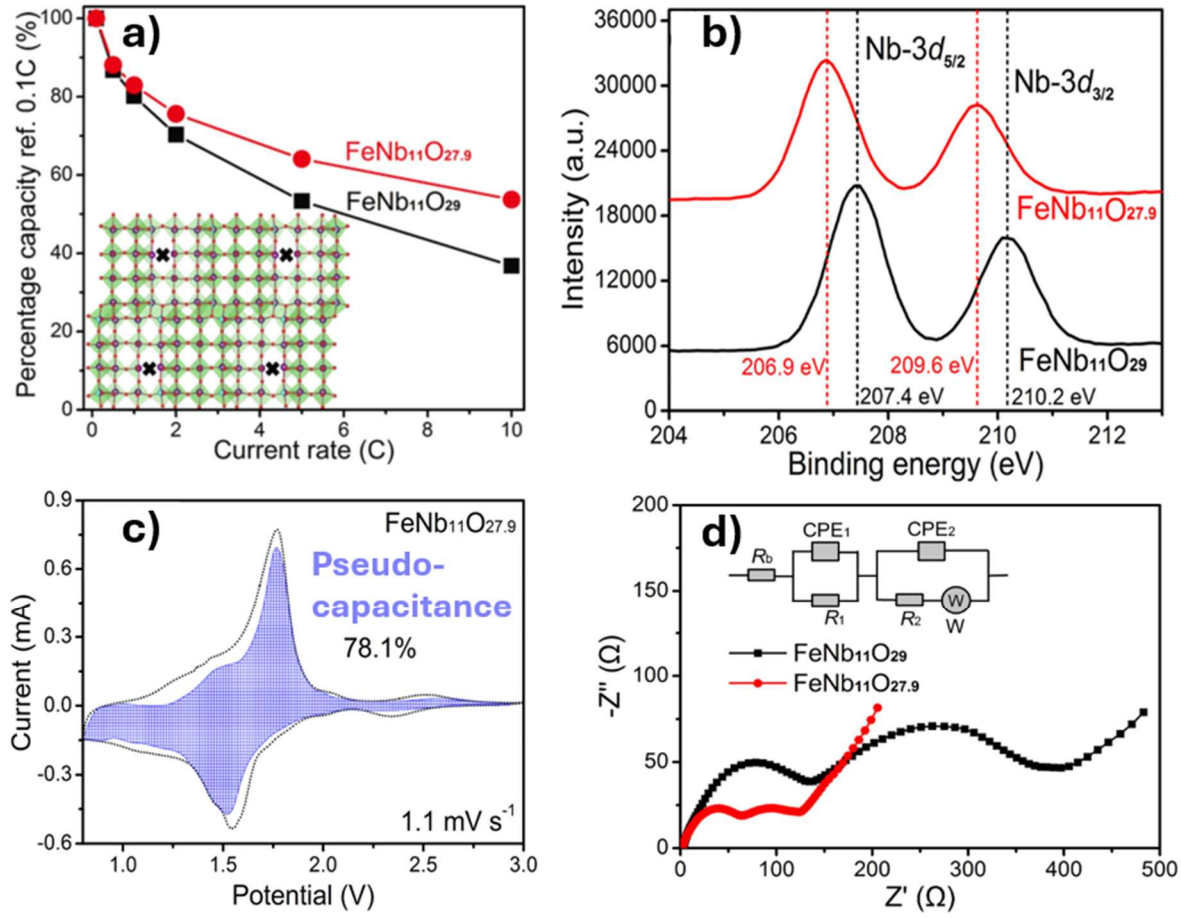

Figure II.3. Enhanced properties of oxygen-deficient $FeNb_{11}O_{27.9}$. (a) Superior rate capability (b) XPS Nb 3d confirming Nb^{4+} due to oxygen vacancies. (c) CV curve showing dominant pseudocapacitive behavior. (d) Nyquist plots with reduced charge-transfer resistance [115].

II.1.1.3. Nano-architecturing

A straightforward and commonly used approach for enhancing rate performance is to form nanometric materials or porous structures which minimize Li^+ solid-state diffusion distances for faster Li^+ transport. For example, $FeNb_{11}O_{29}$ nanotubes fabricated by electrospinning, delivered excellent performance, achieving ~142 mAh g^{-1} at 10 C and retaining ~100 mAh g^{-1} over 2000 cycles [113]. Full cells assembled with commercial positive electrodes confirmed their practicality, with $LiFePO_4$// $FeNb_{11}O_{29}$ system performing best, maintaining 87.4 mAh g^{-1} after 100 cycles with 74.3% retention at 1C.

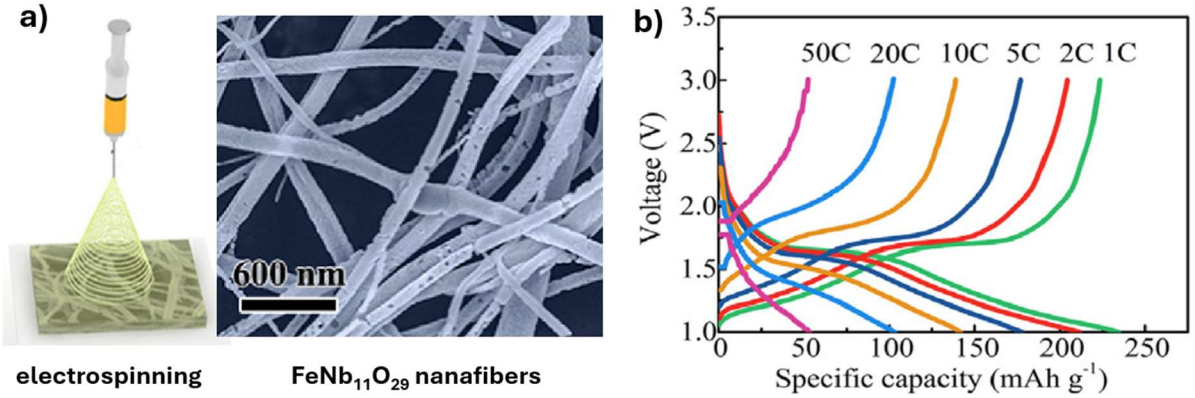

Figure II.4. (a) Electrospinning schematic and SEM image of $FeNb_{11}O_{29}$ nanofibers. (b) Voltage–capacity profiles at various C-rates showing high-rate performance.

Morphology engineering has also proven effective. A porous, biscuit-like nanoplate structure with carbon coating and oxygen vacancies ($FeNb_{11}O_{29}$@C) was developed for LIBs and oxygen evolution reactions (OER) [116]. This design offered several advantages: the 2D porous structure provided increased surface area and active sites, oxygen vacancies and lattice defects improved Li^+ storage, and the carbon layer enhanced electronic conductivity while suppressing side reactions with the electrolyte. As a result, $FeNb_{11}O_{29}$@C delivered 240.8 mAh g^{-1} at 0.25C and 117.6 mAh g^{-1} at 10C, with only 0.98% capacity loss after 500 cycles, significantly better than the 74.7% loss for pristine material under the same conditions.

II.1.1.4. Formation of desolvation promoting layer

Fast energy storage requires overcoming kinetic limitations, particularly charge transfer at the electrode–electrolyte interface. While strategies such as elemental substitution, nanostructuring, oxygen vacancies, and carbon coatings mainly enhance electronic conductivity and bulk Li^+ diffusion, Li^+ desolvation behavior at the interface has been less explored. To address this rate-limiting step, a multifunctional nitridation layer were coated on $FeNb_{11}O_{29}$ particles via heat treatment in Ar/NH_3 atmosphere [108]. The nitridated surface acts as a desolvation promoter, facilitating more efficient interfacial Li^+ transfer. DFT calculations

showed stronger adsorption of solvated Li^+ ions, with a higher binding energy for Li^+–EC complexes on modified sample (−3.92 eV) compared to pristine one (−3.84 eV). XPS confirmed nitrogen incorporation, increased oxygen vacancies, and more Nb^{4+} species, while TEM images revealed a ~10 nm amorphous layer surrounding a crystalline core. Electrochemical analyses further supported these findings: impedance spectroscopy showed a reduced charge-transfer resistance (57.4 vs. 180.8 Ω) and lower desolvation activation energy (55.8 vs. 69.7 kJ mol^{-1}), and Galvanostatic Intermittent Titration Technique indicated a higher Li^+ diffusion coefficient. As a result, outstanding electrochemical performance was achieved: reversible capacity of ~147 mAh g^{-1} at 10 C and 43.6 mAh g^{-1} at 100 C, along with superior cycling stability, retaining 129.7 mAh g^{-1} at 10 C after 10 000 cycles.

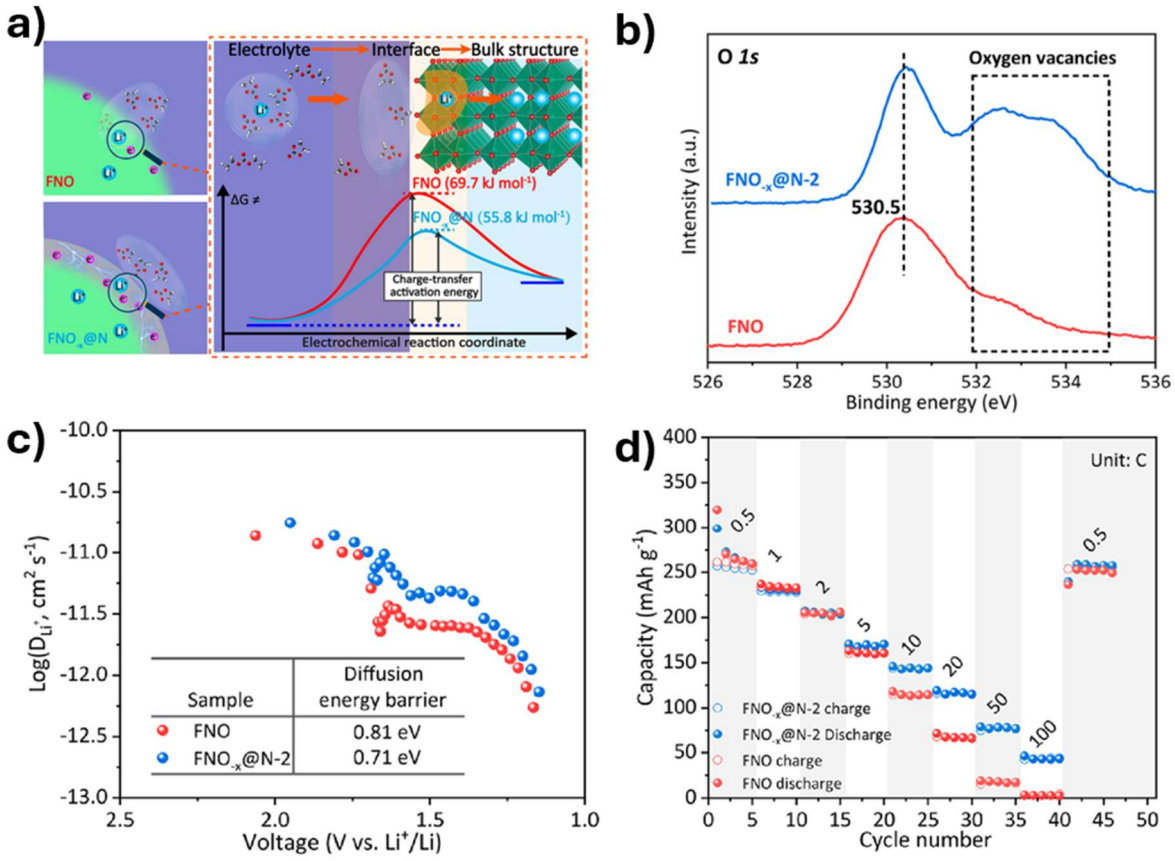

Figure II.5. Enhanced interfacial kinetics in nitridated $FeNb_{11}O_{29}$: (a) schematic of reduced Li^+ desolvation energy, (b) O 1s XPS showing increased oxygen vacancies, (c) GITT-derived Li^+ diffusivity with lower energy barrier, (d) rate performance vs. pristine sample [108].

Overall, these strategies have provided high-performance materials through composition tuning, structural modification or microstructure control, thereby mitigating one or more of the rate-limiting processes described above. Nevertheless, they require either long annealing time, inert or reducing atmospheres (N_2 or Ar/NH_3), or sophisticated fabrication techniques. Therefore, it is necessary to develop alternative approaches that are efficient, fast and simple, and capable of delivering superior performance.

II.1.2. Microstructural modification strategy in this study

II.1.2.1. Optimizing particle size: balancing advantages and trade-offs

The power capability of LIBs is governed by both electronic and ionic transport. At the material level, one of the most critical factors influencing fast-charging is Li^+ solid-state diffusion within the electrode bulk. This process is dictated not only by the intrinsic diffusion energy barrier of the host lattice but also by the diffusion distance, the latter strongly affecting the overall kinetics. Their relationship is given by $\tau = L^2 / D_{Li+}$, where τ is the characteristic diffusion time, D_{Li+} is the Li^+ diffusion coefficient, and L is the diffusion length.

Because diffusion length is strongly dependent on the particle size, particle engineering is a key aspect in electrode design. Optimizing size distribution is essential to balance fast-charging performance, capacity retention, and structural stability. Two limiting cases are considered: “small” or “large” particles, each offers distinct advantages and drawbacks (Figure II.6).

At one end of the spectrum, reducing particle size or creating porous structures has been reported to effectively shorten Li^+ diffusion pathways and improve transport kinetics, as demonstrated in numerous studies and commercial $Li_4Ti_5O_{12}$ materials. However, small particles suffer from lower volumetric density, costly and complicated fabrication processes, and increased instability with electrolytes.

Conversely, large particles, typically produced by high-temperature annealing, exhibit longer diffusion that generally hinder ion and electron transport, thereby limiting rate performance. Nevertheless, they offer several advantages, including higher tap density, improved volumetric energy density, and greater industrial scalability. Breaking from the traditional view that only small particles or porous structures can enable high-rate performance, pioneering work by Grey’s group at Cambridge demonstrated that micrometer-sized niobium tungsten oxides particles can also deliver exceptional rate capabilities [79]. Their findings highlight that, with a suitably structured host lattice, conventional design principles are not absolute requirements for achieving practical high-rate behavior.

Motivated by these opposite perspectives, our study aims to investigate both cases of particle size to evaluate their impact on the electrochemical behavior of Wadsley-Roth $FeNb_{11}O_{29}$ materials. By comparing small and large particles, we seek to understand how microstructural feactures influence Li^+ diffusion, charge-transfer kinetics, and overall rate capability. These approaches are illustrated in Figure II.6.

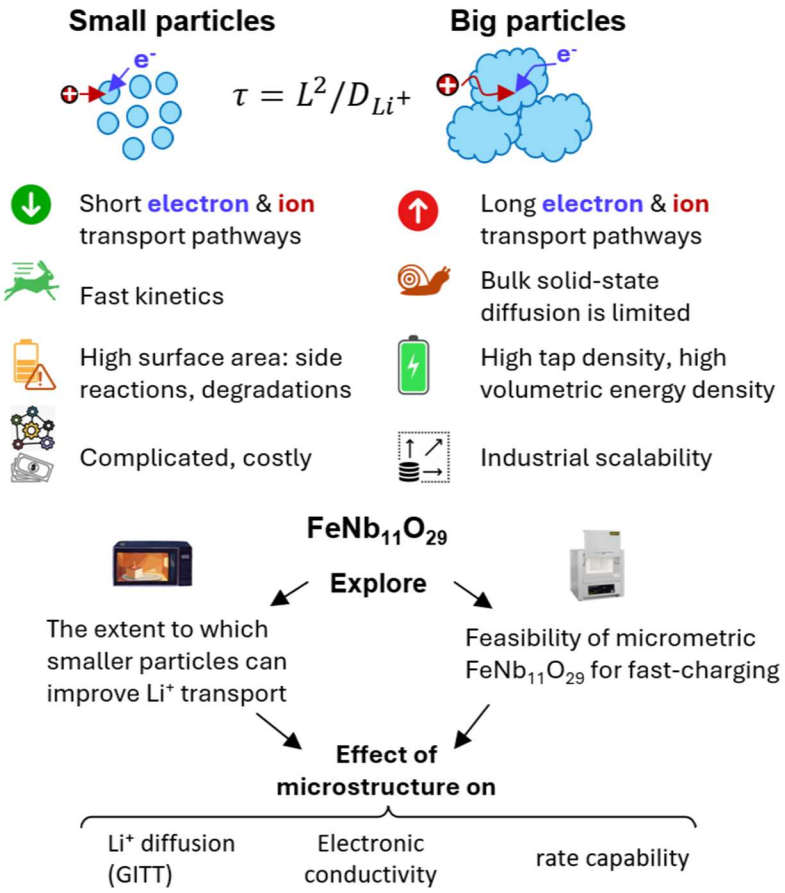

Figure II.6. Two opposite approaches for particle size modifications with respective benefits and trade-offs in Li^+ transport, cell performance and scalability; and the research motivations in this study

II.1.2.2. Motivation of using microwave-assisted synthesis

In this work, large-particle samples were prepared via conventional furnace annealing, which often results in significant particle growth, therefore limiting high-rate performance. These samples serve as a reference to evaluate the high-rate behavior of micrometric particles in fast-charging applications. On the other end, we employed a combination of rapid microwave heating and submicron-sized precursors to suppress particle growth and produce downsized particles. This approach allows us to explore the extent to which this microstructural modification can enhance Li^+ transport and improve high-rate performance.

The ultrafast microwave heating is known to offer the possibility of decreasing the particle size and has been adapted for a wide range of inorganic compounds [125], including battery electrode and electrolyte materials such as Chevrel phase $Cu_2Mo_6S_8$, disordered rocksalt $Li_{1.3}Mn_{0.4}Nb_{0.3}O_{1.9}F_{0.1}$ and thiophosphate solid electrolyte Na_3PS_4, with comparable performance as those obtained by conventional method [126–129]. Concerning Wadsley-Roth phases, microwave-assisted solvothermal method was used to prepare $TiNb_2O_7$ [26], whereas very recent works reported microwave-assisted solid-state synthesis for $AlNb_{11}O_{29}$ and $Ti_2Nb_{10}O_{29}$ [130].

II.1.2.3. Microwave heating mechanisms

Compared with conventional heating, which relies on external heat transfer and thermal conduction within the sample, microwave heating converts electromagnetic energy directly into thermal energy through interaction with the microwave field. This leads to rapid and uniform heating that is independent of thermal conductivity. Because energy is absorbed primarily by the sample rather than the environment, microwave-assisted processes are more energy-efficient, require shorter reaction times, and typically yield powders with smaller particle sizes and more uniform morphologies. Microwave heating occurs mainly through three mechanisms, depending on the material type [125,131]:

(i) Dielectric heating (polar liquids and insulators): caused by frictional losses from the oscillation and reorientation of electric dipoles under the alternating electric field.

(ii) Magnetic heating (magnetic and conductive solids): arises from (1) relaxation of magnetic dipoles aligning with oscillating magnetic field and (2) resistive heating from eddy currents.

(iii) Conduction loss heating (conductors or semiconductors): results from resistive motion of free charge carriers under the oscillating electric field, producing Joule heating.

The efficiency of these processes is quantified by the loss tangent, defined as $\tan\delta = \varepsilon''/\varepsilon'$, where ε' is the real part of permittivity (energy storage) and ε'' the imaginary part (energy dissipation as heat [125,131]. This parameter is critical for designing microwave-assisted experiments. In many cases, reactants do not couple strongly to microwaves at room temperature; heating is therefore initiated using a susceptor material (typically conductive carbon). The susceptor rapidly absorbs microwave energy, heats up, and transfers thermal energy to nearby reactants. Once a critical temperature is reached, the reactants themselves begin to interact efficiently with the microwave field and heat rapidly to the target temperature.

II.1.2.4. Practical aspects of microwave synthesis

As the microwave energy is transferred to both the susceptor and sample, their mass ratio should be carefully optimized. Excessive susceptor takes longer time to heat up and reduces the energy available for the target reaction, while insufficient susceptor may fail to generate the required temperature. In addition, limiting the heating duration is crucial, as prolonged exposure can cause rapid temperature rise, overheating, and poor product quality. To prevent thermal runaway, stepwise or intermittent heating protocols are often employed. Overall, the amount of susceptor, microwave power, power cycle settings, and reaction time must be tailored to the material, its quantity, and its coupling efficiency with microwaves [125]. A schematic illustration of microwave synthesis setup is shown in Figure II.7 [126].

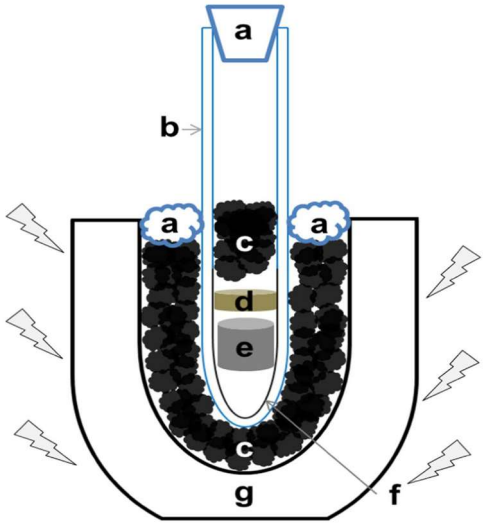

Figure II.7. Schematic illustrations of microwave-assisted synthesis. a) mineral wool; b) quartz tube; c) carbon; d) alumina disk; e) sample ingot; f) graphitized inner layer; g) alumina crucible. Adapted from [126].

II.2. Experimental conditions

II.2.1. Synthesis protocols

Stoichiometric amounts of oxide precursors Fe_2O_3 (≥ 99 %, < 5 µm, Honeywell) and Nb_2O_5 (obtained by heating Nb powder (99.8 %, ~ 325 mesh, Alfa Aesar) at 900 °C for 24 h), weighed around 2 g, were mixed in SPEX 8000M high-energy ball mill for 20 minutes. The mixture was recovered and then pelletized under 2 t in a hydraulic press.

In conventional solid-state synthesis, the pellets were heated in air in Nabertherm muffle furnace for 4 h at 1100 or 1300 °C (with a heating rate of 2 °C min^{-1}) to obtain either monoclinic or orthorhombic polymorphs, respectively. A second series of synthesis has been carried out similarly with submicrometric oxide precursors Fe_2O_3 (99.9 %, 80 nm, Nanoshel) and Nb_2O_5 (99.9 %, 80-100 nm, Nanoshel). In a typical microwave-assisted solid-state synthesis, the pellet of mixed oxide precursors, weighed around 0.5 g, was put inside a graphitized quartz tube placed in a porcelain crucible filled with thermally conductive carbon powder (C-NERGY Super C45) and covered by mineral wool (5-30 µm, Sodipro). The heat treatment was conducted in a classic kitchen microwave oven at 1200 W during one or subsequent steps of 5 minutes, with intermediate resting time to avoid overheating and possible irreversible damage of the quartz tube. At the end, the tube was kept inside the oven to cool down gradually. The as-obtained pellets were manually ground in an agate mortar into fine powder for further characterization and electrochemical evaluation. Overall, three parameters were used as illustrated in Figure II.8, producing eight powder samples which were labelled according to (i) the series of oxide precursors (micrometric -*µ*- or submicrometric -*sµ*-), (ii) the thermal treatment (furnace -*f*- or microwave -*w*-), and finally (iii) the polymorph (monoclinic -M- or orthorhombic -O-).

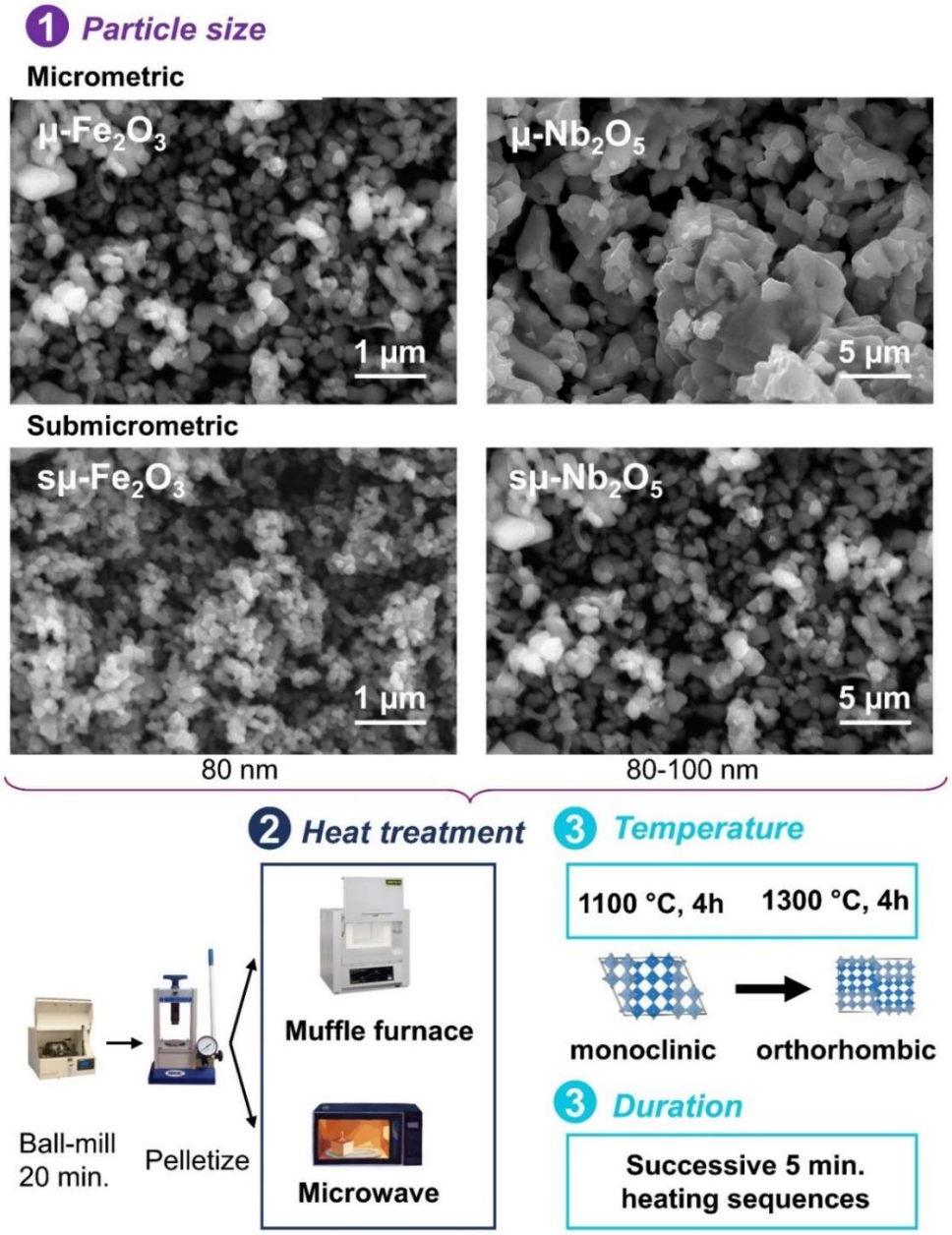

Figure II.8. Synthesis strategy of monoclinic or orthorhombic $FeNb_{11}O_{29}$ with three parameters: (1) particle size (micrometric vs. submicrometric oxide precursors), (2) heat treatment (furnace vs. microwave), and (3) temperature/duration (1100–1300 °C for 4 h or successive 5 min microwave heating).

II.2.2. Characterizations

II.2.2.1. X-ray diffraction

In this study, X-ray powder diffraction (XRD) patterns were collected by using PANAlytical Empyrean diffractometer (equipped with Co $K\alpha_{1,2}$ X-ray source) in Bragg-Brentano θ-θ geometry, within the angular range of 10-70° and with a step size of 0.033°. Lattice parameters were obtained from profile matching method using Fullprof package.

For high-temperature X-ray diffraction (HT-XRD), a stoichiometric mixture of Fe_2O_3 and Nb_2O_5 powders was finely ground, and ethanol was added to form a uniform suspension. Several droplets of this suspension were deposited onto a platinum plate to achieve a homogeneous distribution. The experiment was conducted using a PANalytical X'Pert Spinner diffractometer with Cu $K\alpha_{1,2}$ radiation. Measurements were performed from room temperature up to 1300 °C in 50 °C increments, with a heating rate of 1 K/min. Each scan was acquired over a 2θ range of 5° to 40°, with a step size of 0.0394° and a total acquisition time of 1 hour. XRD data collection was also carried out during cooling from 1300 °C to 1000 °C to examine the reversibility of the phase transition.

Operando XRD experiments were carried out for two microwave-heated samples: sμ-w-M and sμ-w-O, using a PANAlytical Empyrean diffractometer equipped with Co $K\alpha_{1,2}$ X-ray source. Data were recorded during the first discharge and first charge at the rate of 0.5 Li^+/hour, under similar acquisition conditions as described earlier, using LeRiche version 1 electrochemical cell [132]. Self-standing electrode was prepared by mixing $FeNb_{11}O_{29}$ powder with Super P carbon (Alfa Aesar) and poly(tetrafluoroethylene) (PTFE) binder in 70:20:10 weight ratio. Each electrode contained approximately 30 mg of active material. The cell assembling was conducted inside an Ar-filled glovebox, where the self-standing electrode was first placed onto the beryllium window, followed by two electrolyte-soaked separators (Whatman grade D), and finally with a lithium foil pressed against a stainless-steel plunger.

II.2.2.2. Scanning electron microscopy

Scanning Electron Microscopy (SEM) were carried out using a JEOL microscope (JSM 6510 LV) at 20 kV. Analyses were performed by Dr. Amandine Guiet at IMMM (Le Mans). All samples were coated with gold before analysis. Energy Dispersive X-ray Spectroscopy (EDX) was performed on selected areas of the particles to obtain semi-quantitative elemental abundance, as well as in mapping mode to assess the special distribution of elements. The mean particle size was deduced by statistical evaluation of about 100 particles using ImageJ software.

II.2.2.3. X-ray photoelectron spectroscopy

X-ray photoelectron spectroscopy (XPS) analyses were conducted by Valerie Flaud (ICGM) using a Thermo Electron ESCALAB 250 instrument equipped with a monochromatic Al Kα excitation source (1486.6 eV). The analysed area had a diameter of 500 μm. Photoelectron spectra were calibrated in binding energy relative to the C–C component at 284.8 eV. Charge compensation was provided using a low-energy electron beam (−2 eV).

II.2.2.4. Electronic conductivity

Electronic conductivity measurements of pristine samples were conducted inside a PEEK-lined, airtight press cell equipped with stainless steel stamps (Φ = 7 mm) as current collectors. About 30 mg of powder was pressed into a pellet under 260 MPa using a hydraulic press. Conductivity was evaluated at room temperature by direct current (DC) polarization, where a constant voltage step (ΔV) was applied and the resulting current decay was recorded until stabilization. Stainless-steel plungers acted as ion-blocking electrodes, ensuring that the measured current arose predominantly from electronic transport. The electronic conductivity (σ) was calculated as: $\sigma = L/(R \times S)$, where $R = \Delta V/I$ is the steady-state resistance, L and S represent the thickness and area of the pellet, respectively.

II.2.2.5. Electrode casting and coin cell assembly

This procedure of electrode casting and coin cell assembly is shown in Figure II.9.

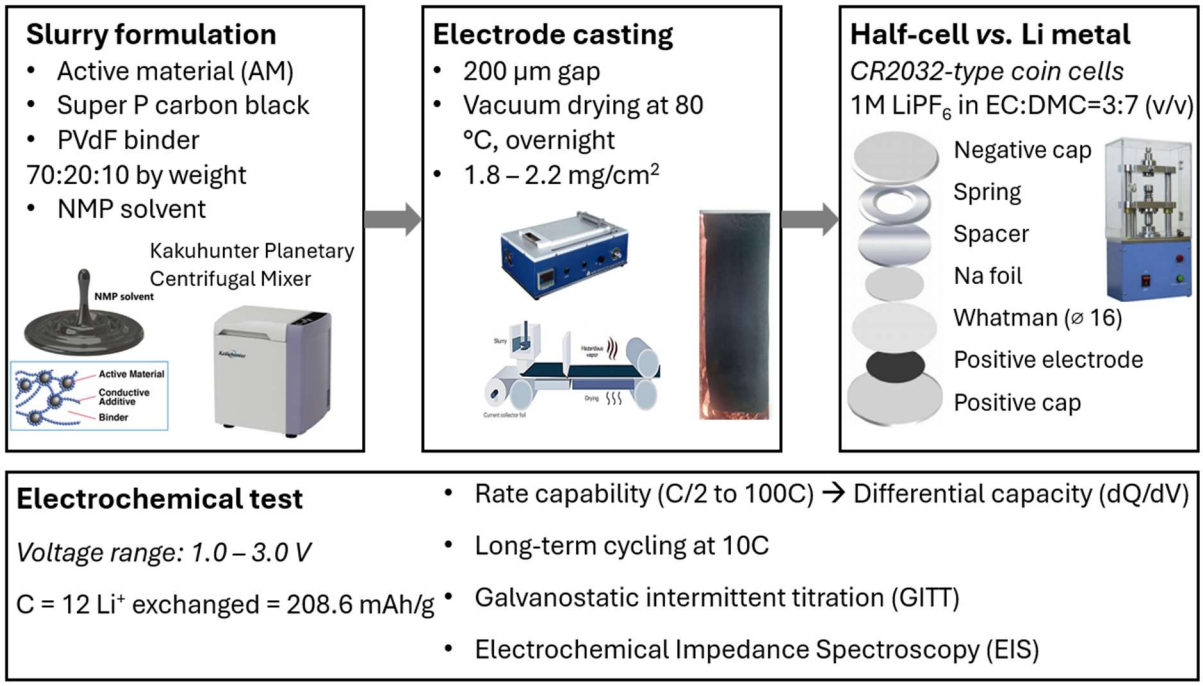

Figure II.9. Process flow for Li-metal half-cell assembly and testing, including slurry preparation, electrode casting, coin cell fabrication, and electrochemical characterization.

Regarding electrode casting, $FeNb_{11}O_{29}$ powder was manually ground with carbon (Super P, Alfa Aesar) and polymeric binder (polyvinylidene fluoride, PVdF, Solef® 5130) in 70:20:10 weight ratio. The mixture was then dispersed in N-methyl-pyrrolidone (NMP, 99.5 %, Sigma-Aldrich) solvent and homogenized using a planetary centrifugal mixer (SK-300SII, Kakuhunter). The obtained slurry was casted onto Cu foil (Goodfellow, thickness of 0.02 mm) and dried under vacuum at 80 °C for 12 h. Disc electrodes (12.7 mm diameter) were then punched, with an average coating thickness of ~50 µm (excluding Cu foil), corresponding to a mass loading of

1.8–2.2 mg cm^{-2}. Coin cells were assembled inside an Ar-filled glovebox with metallic lithium as counter and reference electrode, glass fiber separator (Whatman grade D) and 1M $LiPF_6$ in EC:DMC (3:7 vol.%) (Solvionic) as electrolyte.

II.2.2.6. Galvanostatic cycling

Electrochemical measurements have been performed at room temperature using potentiostats (MPG-2 and VMP, Bio-Logic). The nominal capacity C was set at 208.6 mAh g^{-1}, corresponding to the insertion of one Li^+ per transition metal or 12 Li^+ ions per formula unit. Galvanostatic cycling with potential limitation (GCPL) was carried out by applying a constant current to the cell, positive for the charge and negative for discharge, and the voltage response over time is recorded. In GCPL, the cycling is constrained by upper and lower potential limits, within a voltage window of 1.0–3.0 V vs. Li^+/Li, without any voltage hold at the end of charge or discharge. Rate capability tests were performed by cycling the cell at various C-rates, from C/2 (104 mA g^{-1}) up to 100 C (21 A g^{-1}) with five cycles at each rate before returning to C/2.

II.2.2.7. Galvanostatic Intermittent Titration Technique (GITT)

Galvanostatic Intermittent Titration Technique (GITT) was carried out on monoclinic $FeNb_{11}O_{29}$ synthesized from submicrometric precursors using either conventional or microwave heat treatment, with C/20 current pulses of 10 minutes followed by relaxation of 20 minutes.

GITT is widely used to extract kinetic and thermodynamic information from battery electrodes. By applying a series of small constant-current pulses followed by a relaxation period, the method records transient voltage response and equilibrium open-circuit voltage (OCV).

- During positive current pulse, the cell voltage first rises sharply due to ohmic contribution (iR), then gradually increases as Li^+ diffusion establishes a concentration gradient.
- During relaxation, the voltage drops instantly (iR drop) and then relaxes slowly toward OCV as the electrode composition homogenizes.
- During discharging, the voltage response is similar but inverted.

Based on Fick's law for derivation of the equation, the apparent Li^+ diffusion coefficient can be determined as a function of state of charge (SOC):

$$D = \frac{4}{\pi\tau}\left(\frac{m_B V_M}{M_B S}\right)^2 \left(\frac{\Delta E_s}{\Delta E_t}\right)^2 \quad \left(\tau \ll \frac{L^2}{D}\right)$$

where τ is the pulse duration, V_M the molar volume, S the electrode/electrolyte contact area, and mB and MB the mass and molar mass of the active material [133].

Key assumptions and experimental conditions for GITT

- Electrode structure: homogeneous and dense, with negligible volume change during cycling. Porosity, cracks, inhomogeneity, or large volume change lead to variable diffusion pathways and unreliable diffusivity values.
- Current and pulse duration: small currents and short pulses are required to ensure linear behavior of transient potential vs. $(\text{time})^{1/2}$ and satisfy the semi-infinite diffusion ($\tau \ll L^2/D$).
- Relaxation time: sufficiently long to reach thermodynamic equilibrium ($dE/dt \approx 0$).
- Phase stability: the active material should not undergo phase transitions during measurement, ensuring a single, well-defined diffusivity value.

Although GITT is valuable for studying Li-ion kinetics, it is time-consuming, unsuitable for materials with phase transitions, and yields only apparent diffusion coefficients that reflect the whole heterogeneous electrode rather than the intrinsic active material.

II.2.2.8. Electrochemical Impedance Spectroscopy (EIS)

Electrochemical Impedance Spectroscopy (EIS) were conducted on two monoclinic $FeNb_{11}O_{29}$ samples synthesized from submicrometric precursors by conventional or microwave heat treatment. Measurements were carried out at room temperature, in the frequency range between 10^4 Hz and 10^{-2} Hz, with a 10 mV sinusoidal voltage pertubation, during open circuit voltage, at the end of discharge and end of charge.

II.3. Results and discussion

II.3.1. X-ray diffraction

II.3.1.1. XRD of furnace-heated samples

At first, conventional solid-state synthesis in muffle furnace was used to prepare $FeNb_{11}O_{29}$ reference samples. Whatever the particle size of Fe_2O_3 and Nb_2O_5 precursors (micrometric or submicrometric), the heat treatments performed at 1100 °C lead to the monoclinic form of $FeNb_{11}O_{29}$, with XRD pattern indexed in the space group *A*2/*m*, while going up to 1300 °C induces the formation of the orthorhombic polymorph (space group *Amma*), as shown in Figure II.10. In both cases, cell parameters obtained from profile matching refinement of XRD data (Table II.1) are in good agreement with the literature [108,111,114].

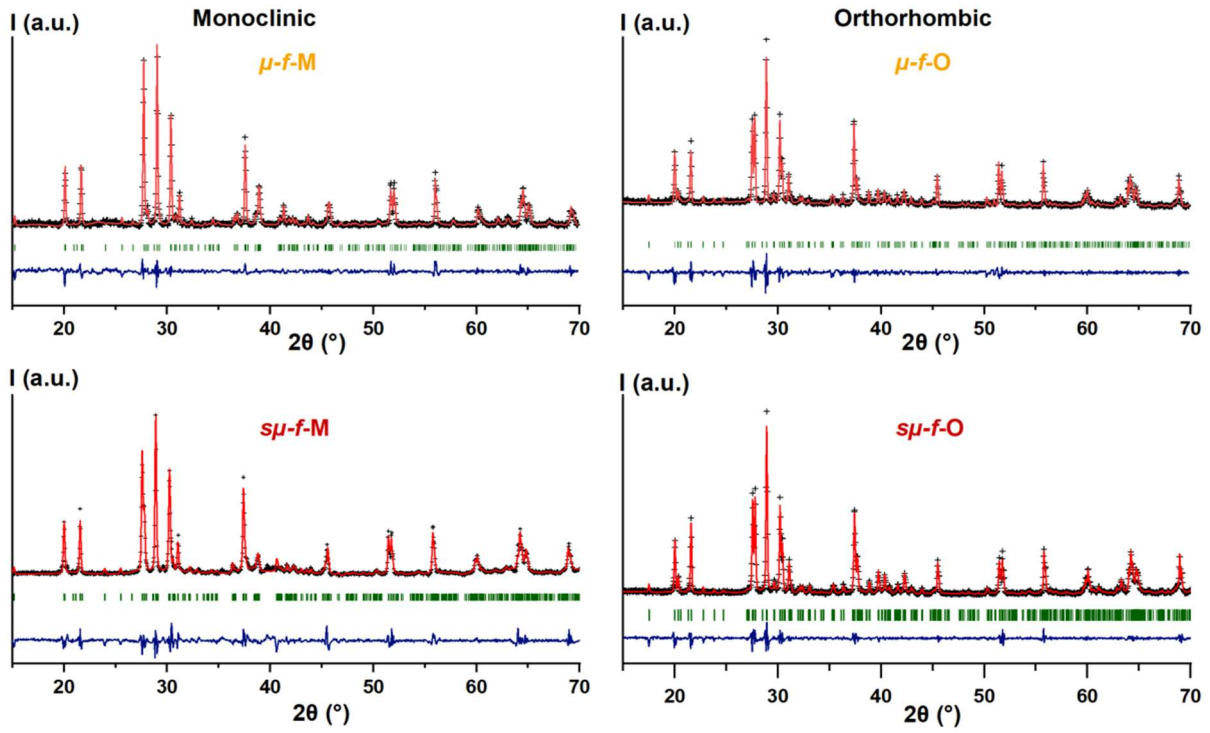

Figure II.10. XRD pattern of four $FeNb_{11}O_{29}$ samples obtained by furnace heating which confirm the phase formation (observed, Le Bail fitted, and difference profile are represented respectively on black crosses, red and blue lines, Bragg position on green vertical bars)

II.3.1.2. Temperature-dependent XRD following the synthesis

The temperature-dependent X-ray diffraction plot (Figure II.11) shows the sequential phase evolution during the heating process of Fe_2O_3 and Nb_2O_5 precursors mixed in stoichiometric ratio. At 700–800 °C, an intermediate $FeNbO_4$ phase appears, as indicated by a distinct diffraction peak near $2\theta \approx 21.5°$. With further heating to 850–900 °C, new reflections emerge, corresponding to the formation of monoclinic phase (M-$FeNb_{11}O_{29}$). The intensity and sharpness of these peaks grow with temperature, confirming the progressive crystallization of the monoclinic phase. Beyond 1250 °C up to 1300 °C, additional reflections appear, indicating the transformation to the orthorhombic phase (O-$FeNb_{11}O_{29}$). This monoclinic-to-orthorhombic transition is clearly seen in the magnified patterns on the right, where the (011) peak of the monoclinic phase splits into (011) and (111) reflections at 1300 °C. In summary, the XRD analysis identifies $FeNbO_4$ as an intermediate phase at around 700–800 °C, formation of monoclinic $FeNb_{11}O_{29}$ at ~850–1200 °C, and a transition to the orthorhombic phase occurring above 1250 °C.

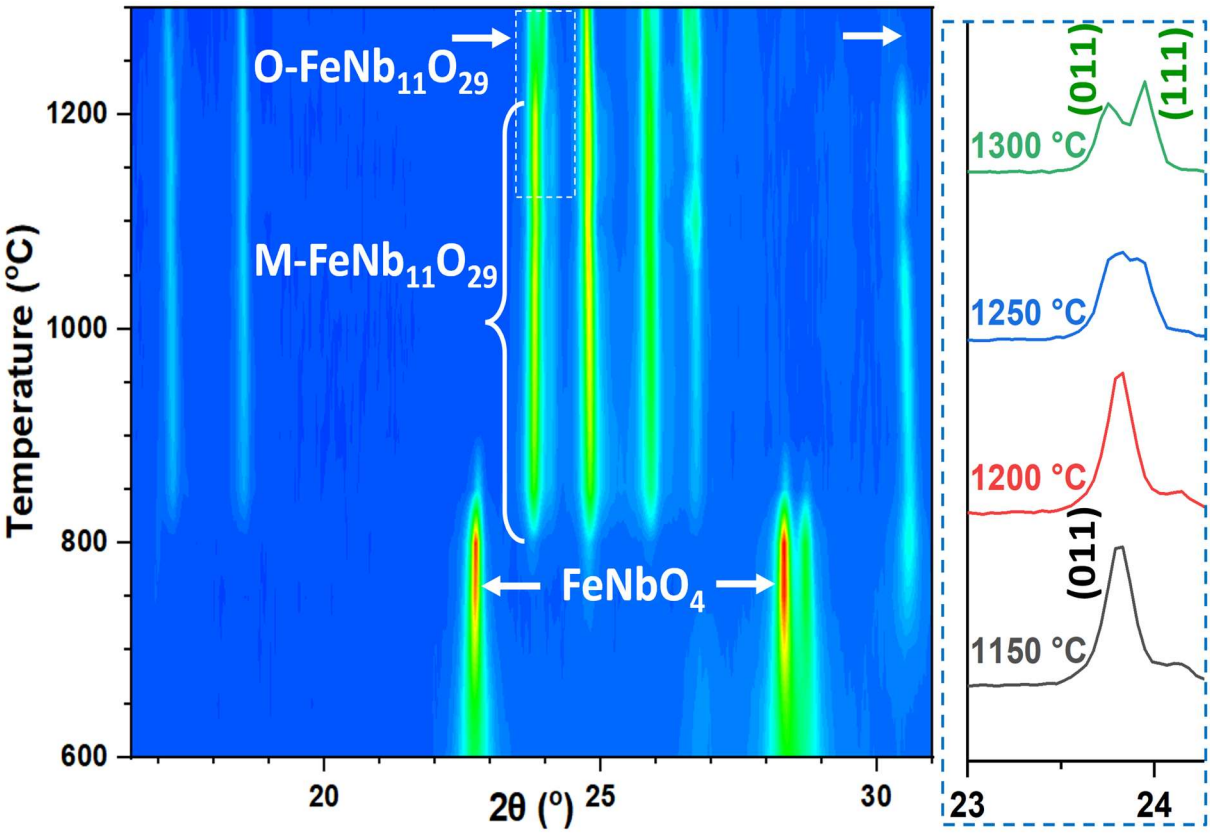

Figure II.11. *In situ* high temperature XRPD patterns during the synthesis of $FeNb_{11}O_{29}$ from micrometric Fe_2O_3 and Nb_2O_5 oxide precursors, obtained by Empyrean diffractometer with Cu Kα X-ray source

II.3.1.3. XRPD patterns of microwave-heated samples

Microwave-assisted thermal treatment has been applied on both micrometric and submicrometric oxide precursors. The mixture was heated during four steps of five minutes each, at 1200 W, and XRD was performed after each step to monitor the chemical reaction . With the micrometric precursors, after only 5 minutes the main peak of monoclinic $FeNb_{11}O_{29}$ at 28° is observed (Figure II.12). However, another peak at 36° is present and assigned to $FeNbO_4$ [105]. After a third heating step, $FeNbO_4$ and Nb_2O_5 precursor are no longer present and pure monoclinic form of $FeNb_{11}O_{29}$ is observed. An additional step is necessary to obtain the orthorhombic polymorph.

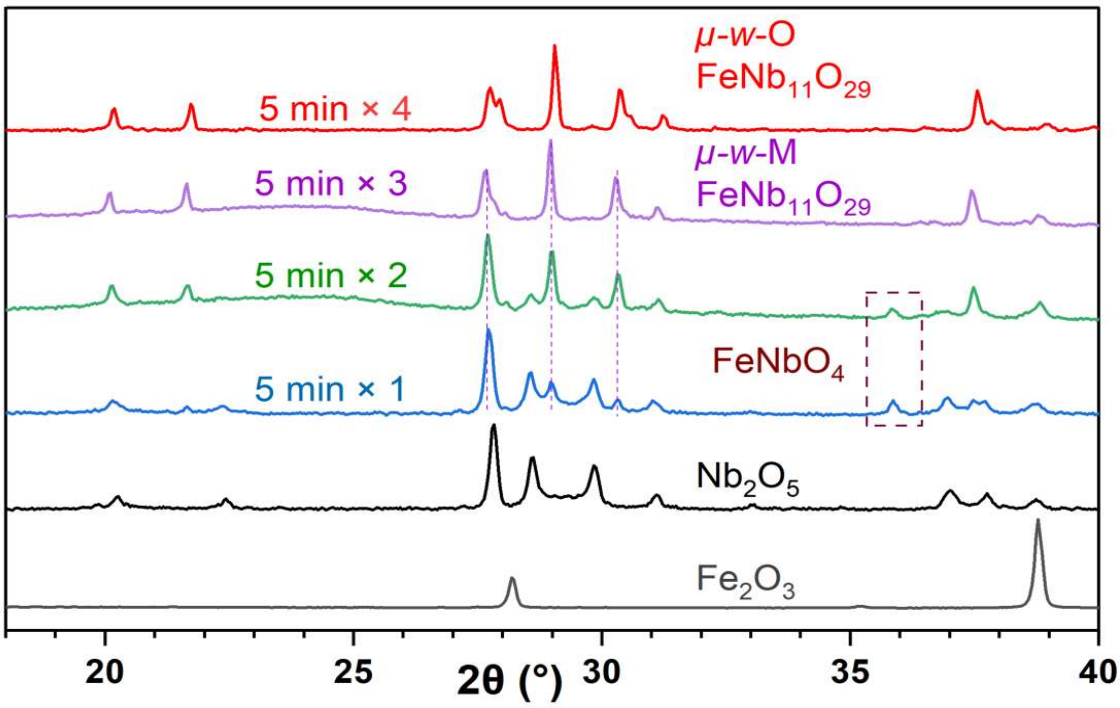

Figure II.12. Successive XRD patterns of 5-minute microwave-heating steps to follow the progress of $FeNb_{11}O_{29}$ synthesis from micrometric precursors.

The use of submicrometric oxide precursors Fe_2O_3 and Nb_2O_5 significantly shortened the synthesis duration. Indeed, pure and highly crystalline monoclinic form of $FeNb_{11}O_{29}$ is obtained after one heating step of 5 minutes, and the orthorhombic polymorph only needs an additional step to be observed. The Le Bail-fitted XRD patterns of four microwave-heated $FeNb_{11}O_{29}$ samples are presented in Figure II.13, with the fitting details in Table II.1, showing comparable cell parameters.

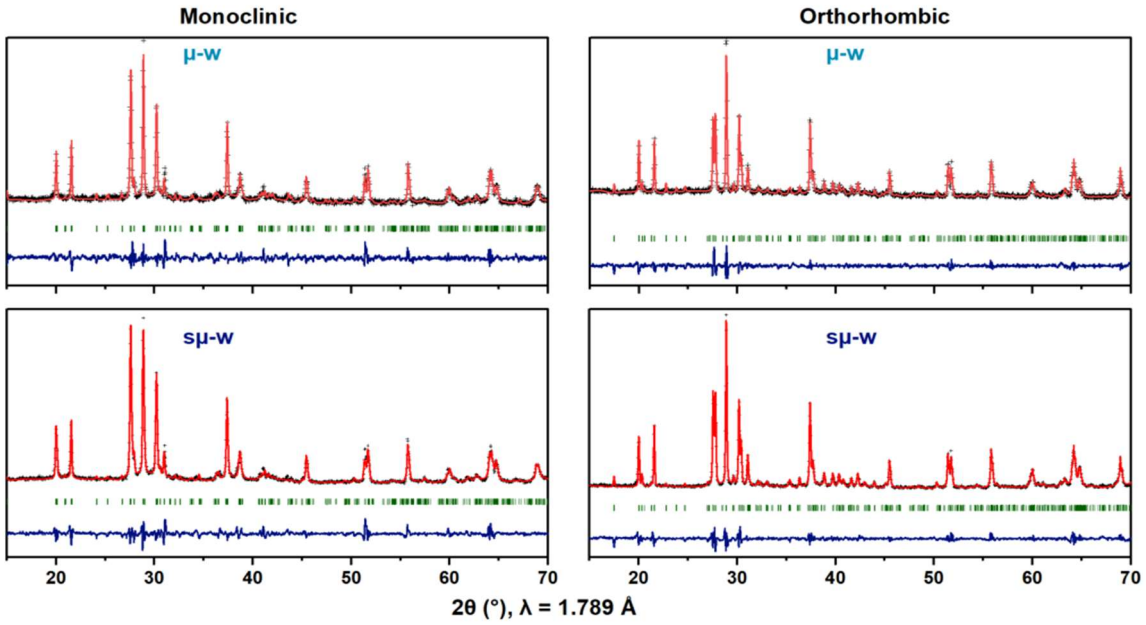

Figure II.13. Le Bail-fitted XRD patterns of four microwave-heated $FeMn_{11}O_{29}$ samples

Table II.1. Le Bail-refine cell parameters of eight $FeNb_{11}O_{29}$ samples and the agreement parameters.

Samples	a (Å)	b (Å)	c (Å)	β (°)	χ^2	R_p	R_{wp}	R_{exp}
***sμ-w*-M**	15.507(1)	3.8377(4)	20.656(1)	112.095(4)	4.30	5.52	7.90	3.81
***sμ-f*-M**	15.5944(6)	3.8337(2)	20.616(1)	112.925(5)	5.23	5.96	8.62	3.77
***μ-w*-M**	15.512(1)	3.8417(4)	20.657(1)	112.183(5)	8.19	2.75	4.10	1.43
***μ-f*-M**	15.529(1)	3.8113(1)	20.533(1)	113.042(5)	6.89	2.22	3.24	1.24
***sμ-w*-O**	28.706(1)	3.8236(1)	20.625(1)	90.0	4.30	5.35	7.76	3.74
***sμ-f*-O**	28.698(1)	3.8242(1)	20.6149(8)	90.0	4.71	5.61	8.24	3.79
***μ-w*-O**	28.706(1)	3.8245(1)	20.623(1)	90.0	6.13	1.67	2.57	1.04
***μ-f*-O**	28.7285(6)	3.8292(1)	20.6321(5)	90.0	7.39	2.03	3.04	1.12

II.3.2. Scanning Electron Microscopy

Firstly, Energy Dispersive X-ray spectroscopy (EDX) confirms the Nb/Fe ratio and the homogeneous elemental distribution in the samples (Figure II.14). SEM is used to study the influence of three synthesis parameters on the particle size of $FeNb_{11}O_{29}$ powder, as shown in Figure II.15 and II.16. Comparing between the two polymorphs of $FeNb_{11}O_{29}$, it is reasonable to observe that the four orthorhombic samples – synthesized either at higher temperature or during a longer treatment time under microwave – have significant particle growth with respect to the monoclinic ones. Regarding heating process, the four samples obtained from microwave method show the aggregation of small primary particles (≈ 0.5 μm) into larger secondary assembly, while powder samples heated hours in furnace are characterized by larger particles (≈ 2 μm) and smooth surface. Finally, for a similar heating process, using submicrometric oxide precursors allows to limit the grain growth. Logically, the combination of these precursors with the rapid microwave-assisted synthesis remarkably limits particle growth and yields the product with a limited particle size. This is particularly evidenced with the monoclinic form of $FeNb_{11}O_{29}$ obtained in only 5 minutes and exhibiting particle size of 0.3-0.5 μm, slightly larger than its oxide precursors.

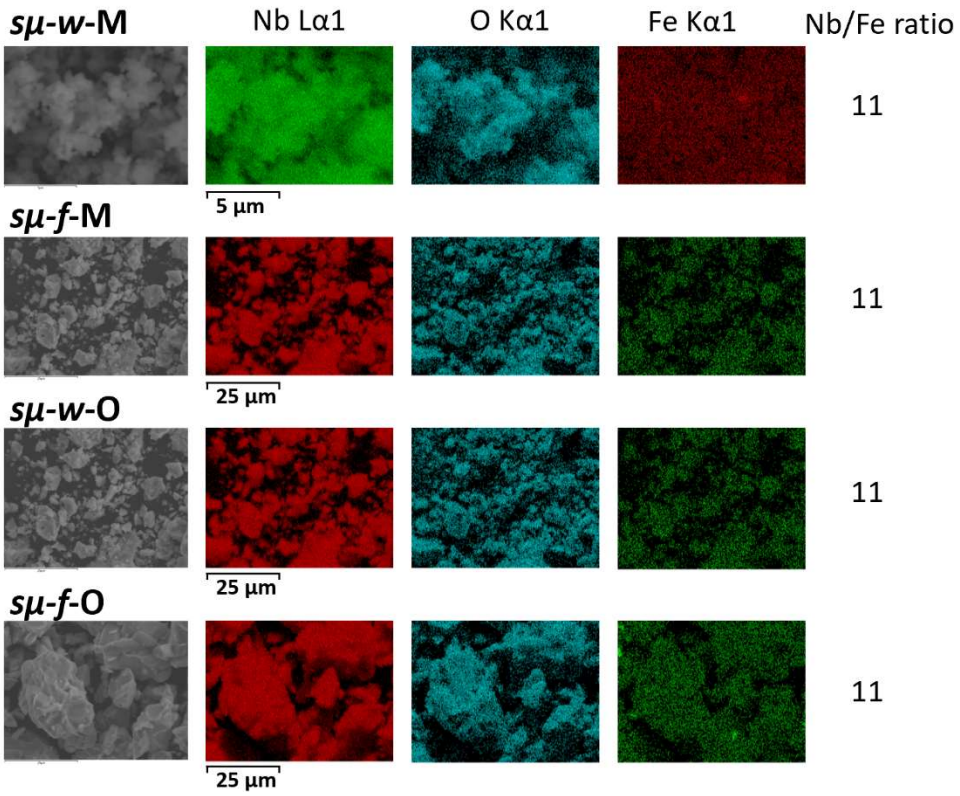

Figure II.14. Energy Dispersive X-ray spectroscopy (EDX) mapping of four $FeNb_{11}O_{29}$ samples from submicrometric precursors shows uniform elemental distribution and Nb/Fe ratio consistent with stoichiometry.

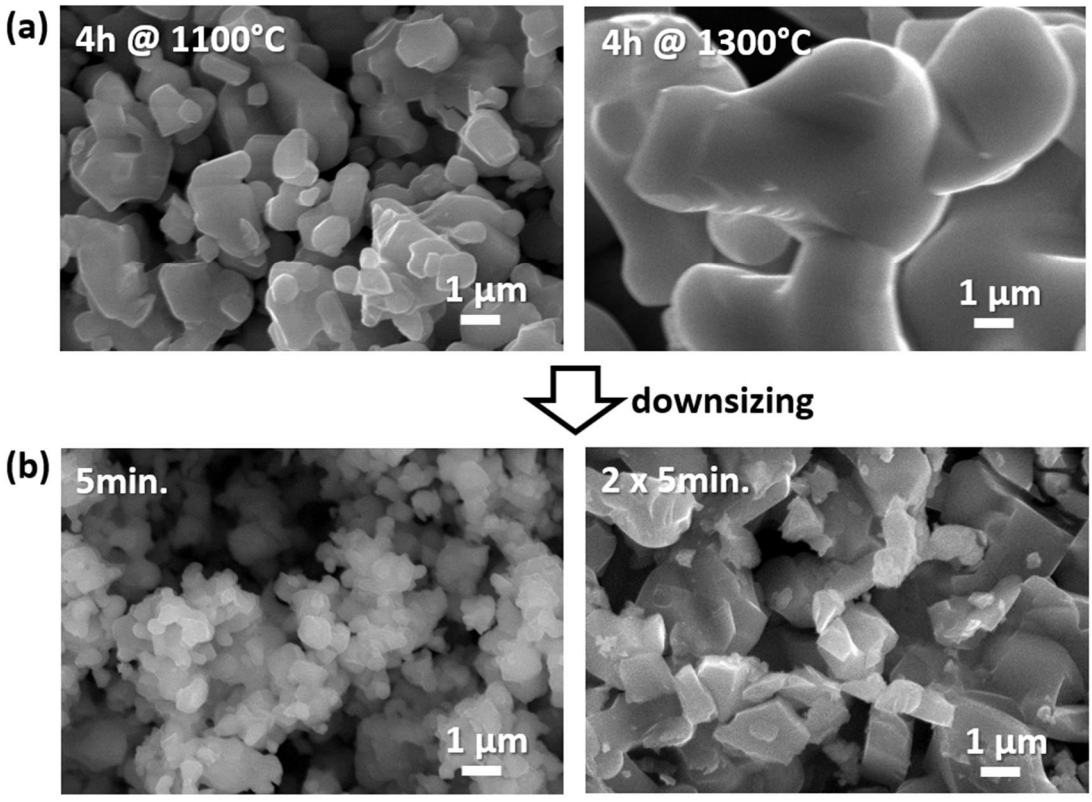

Figure II.15. SEM images showing how $FeNb_{11}O_{29}$ particles could be downsized from (a) a conventional heat treatment with micrometric Fe_2O_3 and Nb_2O_5 precursors to (b) an ultrafast microwave heating with submicrometric precursors . In both cases, the left and right images show monoclinic and orthorhombic polymorphs, respectively.

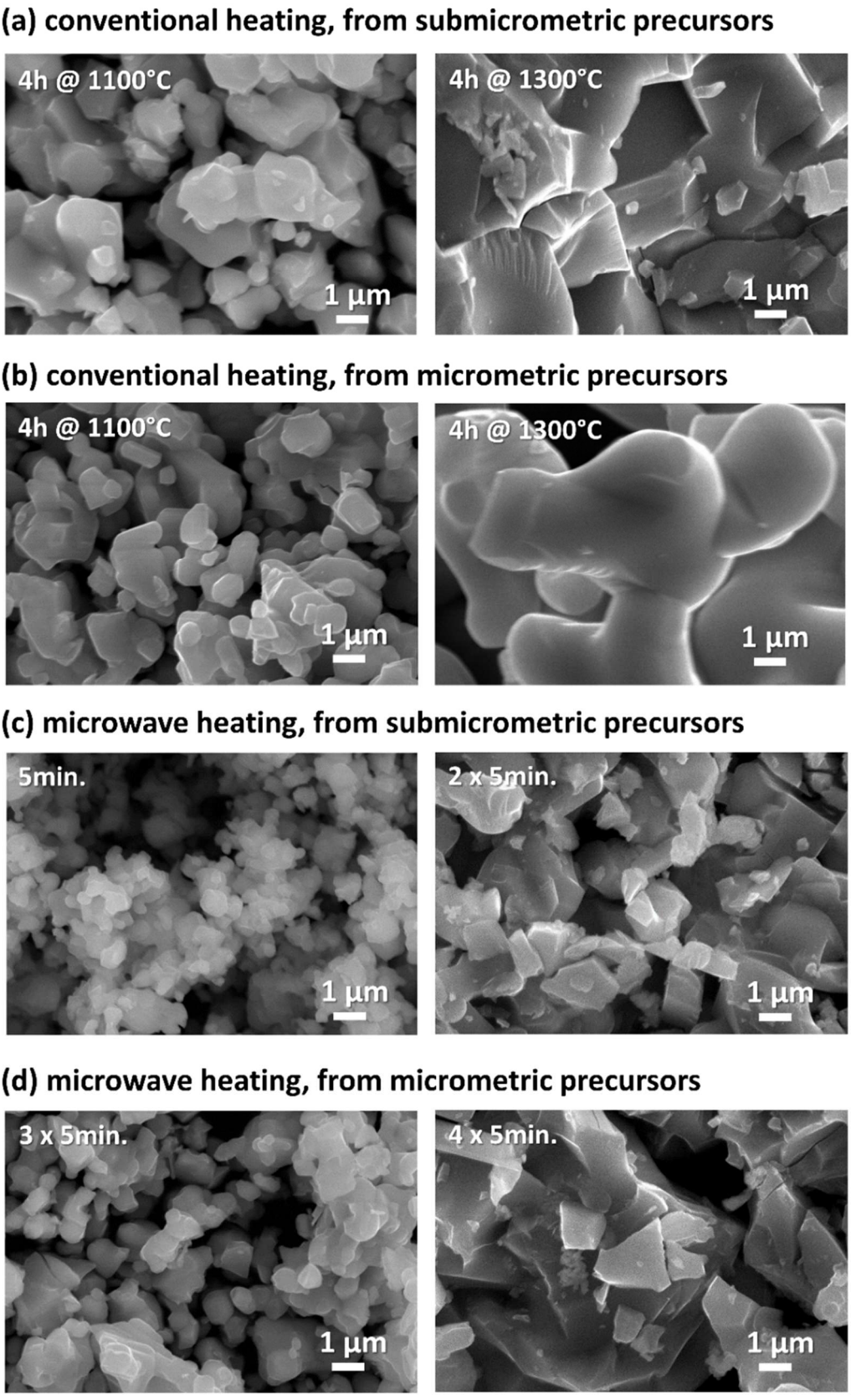

Figure II.16. SEM images of eight $FeNb_{11}O_{29}$ samples at 10000x magnification showing the influence of three factors on particle size: precursors (micrometric or submicrometric), type of heat treatment (furnace or microwave), and temperature (1100 °C or 1300 °C) or microwave-heating duration. The left and right images show monoclinic and orthorhombic polymorphs, respectively.

II.3.3. Electronic conductivity

The influence of synthesis method on the electronic conductivity of $FeNb_{11}O_{29}$ samples synthesized by microwave heating or furnace from submicrometric precursors. was assessed for two representative samples prepared from submicrometric precursors, either by conventional furnace annealing (*sμ-f*-M) or by microwave heating (*sμ-w*-M). Figure II.17 shows the applied potential steps and the corresponding current decay, from which steady-state currents were extracted. The linear current–voltage relationship in the 5–30 mV range confirms reliable measurements and well-stabilized conductivity values. The electronic conductivities were determined to be 2.66×10^{-8} S cm^{-1} for *sμ-f*-M and 4.26×10^{-8} S cm^{-1} for *sμ-w*-M. These values are slightly higher than 4.89×10^{-9} S cm^{-1} reported for pristine $FeNb_{11}O_{29}$ [115], possibly due to differences in applied pressure and pellet thickness. These results suggest that the smaller particle size induced by microwave heating does not lead to a significant improvement in electronic conductivity of the obtained sample.

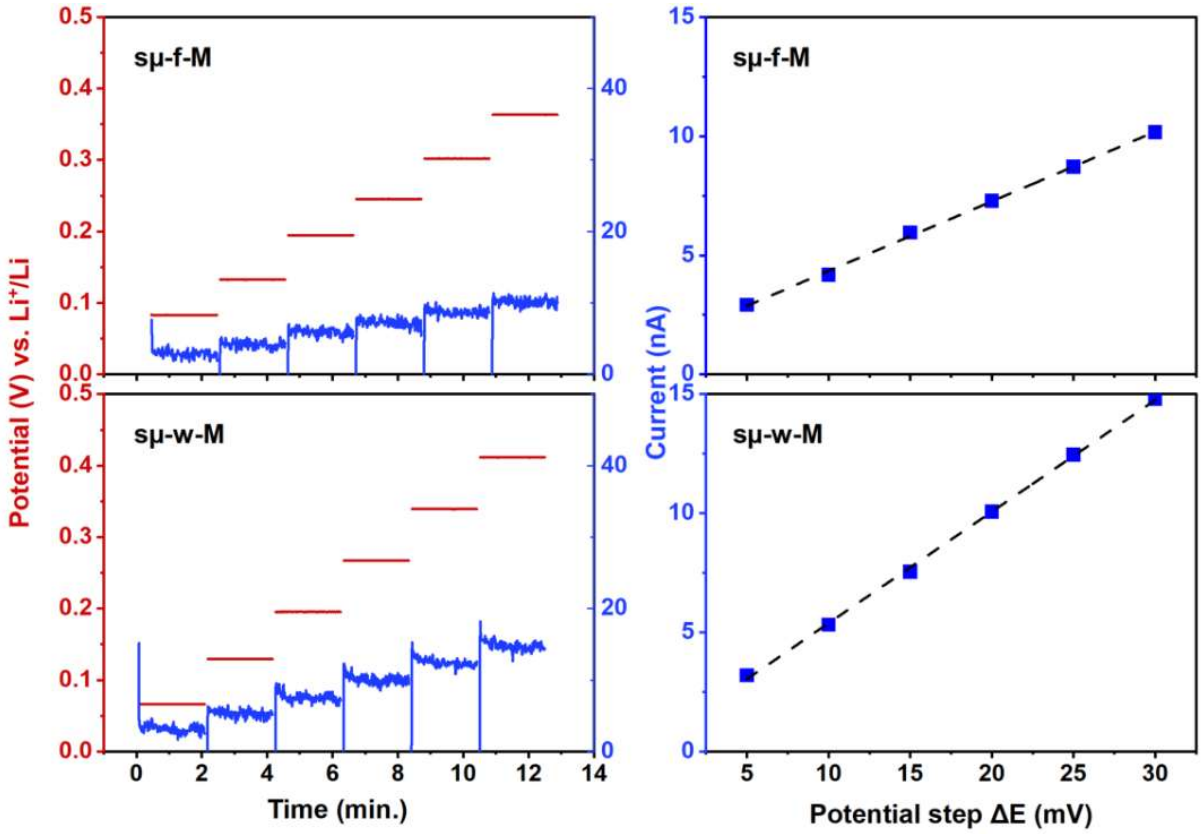

Figure II.17. DC polarization tests of *sμ-f*-M and *sμ-w*-M $FeNb_{11}O_{29}$ samples. Left: Applied voltage steps (red) and current response (blue). Right: Linear current-voltage plots confirming stable electronic conductivity and method reliability.

II.3.4. X-ray photoelectron spectroscopy

To probe the valence states in $FeNb_{11}O_{29}$, XPS was performed on four representative samples prepared from micrometric precursors. The XPS spectra are shown in Figure II.18, with the corresponding binding energies and atomic percentages summarized in Table II.2.

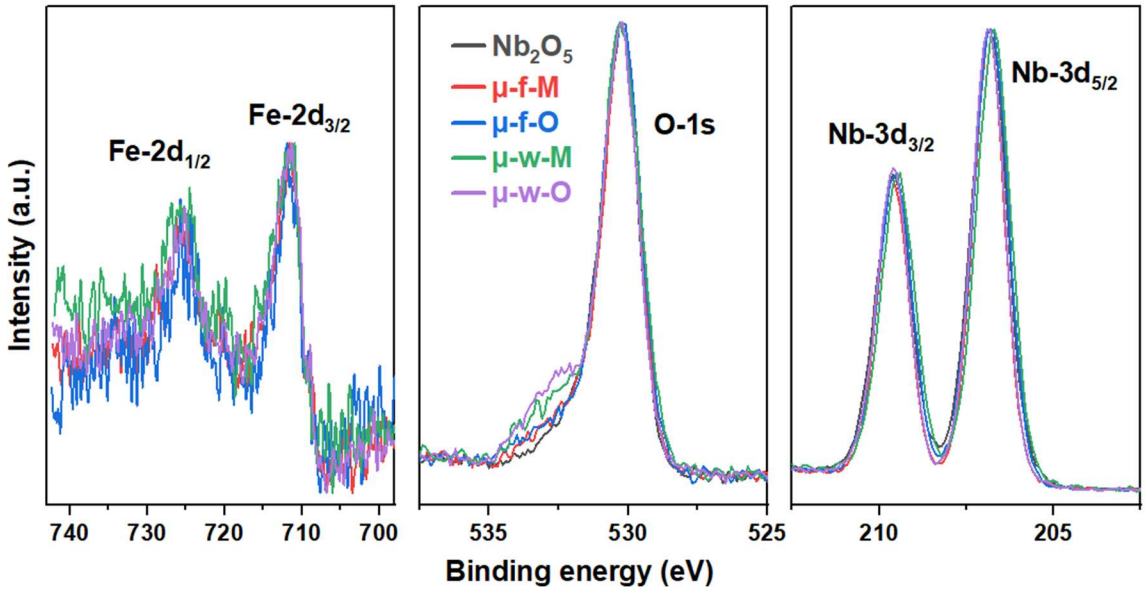

Figure II.18. XPS spectra of four representative $FeNb_{11}O_{29}$ samples and Nb_2O_5 precursor showing Fe 2p, O 1s, and Nb 3d regions, confirming consistent Fe and Nb valence states of different synthesis and samples.

Table II.2. XPS binding energies and atomic percentages of key elements (Nb, Fe, O, C) in $FeNb_{11}O_{29}$ samples synthesized under different conditions, compared with Nb_2O_5 precursor. The consistent binding energies confirm stable Nb^{5+} and Fe^{3+} oxidation states, while the O/Nb ratio reflects slight changes in surface oxygen.

	Element	**Nb_2O_5**	***μ-f*-M**	***μ-f*-O**	***μ-w*-M**	***μ-w*-O**
Peak binding energy (eV)	Nb $3d_{5/2}$	207.01	206.83	206.79	206.71	206.86
	Nd $3d_{3/2}$	209.76	209.59	209.56	209.48	209.62
	Fe $2p_{3/2}$	-	711.51	711.51	711.45	711.47
	Fe $2p_{1/2}$	-	725.21	725.22	725.19	725.20
	C 1s	284.82	284.77	284.84	284.76	284.84
	O 1s	530.28	530.22	530.23	530.27	530.28
Atomic %	Nb	17.58	15.23	15.63	12.87	13.89
	Fe	-	0.97	0.6	0.68	0.95
	C	40.22	44.51	42.49	51.88	45
	O	42.2	39.3	41.29	34.57	40.16
	O/Nb	2.40	2.58	2.64	2.68	2.89

The Nd 3d peaks of all four samples appear at closely similar binding energies (differences < 0.2 eV), consistent with those of Nb_2O_5 precursor. The same observation can be made for Fe 2p peaks, which also show negligible variation between the samples. These results indicate that Nb and Fe remain in +5 and +3 valance state after the synthesis.

Regarding O 1s signal, the main peak matches well with Nb_2O_5 precursor, but the tail at higher binding energy is more pronounced for two microwave-heated samples. This feature likely originates from oxygen species bonded to carbon (O-C, O=C bonds), suggesting surface contamination. Such contamination is possible, as carbon was used as a susceptor during the microwave heating. This result is consistent with the higher O/Nb ratio in these two samples (μ-*w*-M and μ-*w*-O), 2.68 and 2.89, compared to the expected stoichiometry values of 2.64. Such surface contamination is a common artifact in XPS measurements.

II.3.5. Electrochemistry

II.3.5.1. Charge-discharge and differential capacity curves

The electrochemical behavior of the eight $FeNb_{11}O_{29}$ samples has been evaluated under similar conditions, from the electrode formulation to the cycling conditions. Notably, these electrodes have relatively low loading of active materials (∼1.8–2.2 mg cm^{-2}), similar to the values eported in other studies, allowing for a justified comparison. Their capacity is discussed in different ways, in terms of gravimetric charge delivered mAh g^{-1}, amount of Li^+ ions exchanged per formula unit (Li^+/f.u.), or number of Li^+ ions exchanged per transition metals (Li^+/TM).

The first galvanostatic cycles at C/2 are compared in Figure II.19. For the monoclinic polymorphs, the discharge/charge curves are very similar and start by short pseudoplateau at 2.4 V, followed by a more apparent yet sloping plateau around 1.6 V. A total of 14 Li^+ ions per formula unit (1.17 Li^+/TM) could be inserted, corresponding to a capacity of 243 mAh g^{-1}, and with an excellent reversibility observed during the subsequent charge. The corresponding differential capacity plots distinguish three redox reactions. Following previous works [108,111,113,114], the first faint broad cathodic/anodic peak around 2.4 V is assigned to Fe^{3+}/Fe^{2+} redox couple. The important peaks around 1.6-1.7 V correspond to Nb^{5+}/Nb^{4+} redox couple, whereas the broad features below 1.5 V are attributed to further redox activity of Nb^{4+}/Nb^{3+}. Interestingly, a significant extra capacity is observed with the sample prepared by microwave heating from the submicrometric oxide precursors (*s*μ-*w*-M) and this gain is occurring below 1.25 V. This extra capacity is attributed to the multi-redox activity of niobium, specifically involving Nb^{4+}/Nb^{3+} redox couple. This behavior is supported by the more

pronounced dQ/dV peak observed in this region for *sμ-w*-M sample. These observations slightly differ for the orthorhombic samples of $FeNb_{11}O_{29}$. Stronger polarization is observed below 1.5 V and induces a lower discharge capacity as only 12 Li^+ (1.0 Li^+/TM) could be inserted. This decrease of capacity is however not noticed for the sample prepared by microwave heating from the submicrometric oxide precursors (*sμ-w*-O), and here as well this extra capacity seems to be explained by a stronger activity at low voltage.

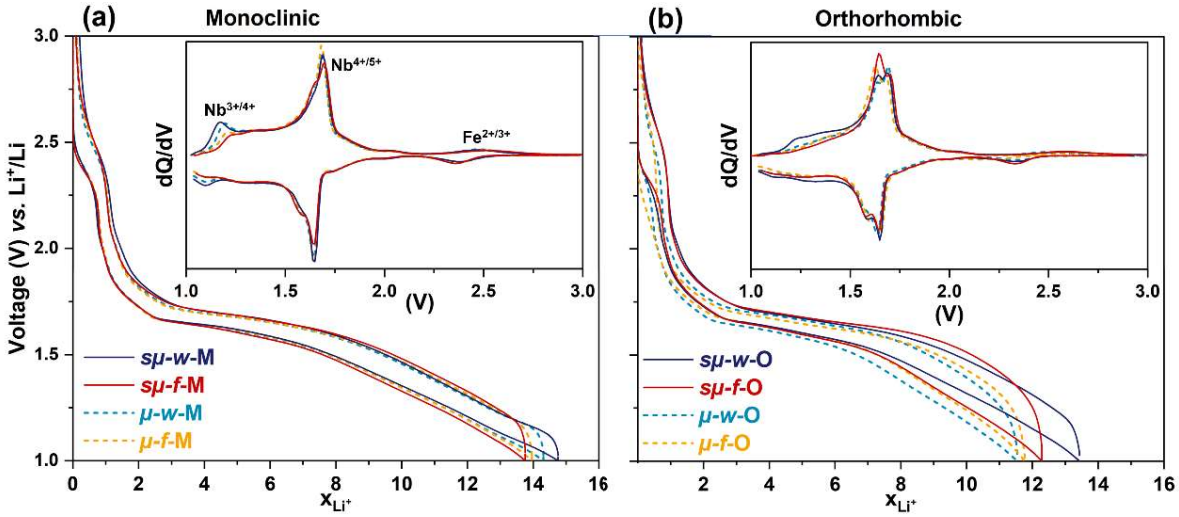

Figure II.19. First C/2 galvanostatic cycles and dQ/dV plots for monoclinic (a) and orthorhombic (b) $FeNb_{11}O_{29}$ samples, highlighting the impact of synthesis conditions on electrochemical performance.

II.3.5.2. Rate capability test

As stated in the introduction, Wadsley-Roth phases recently attracted the attention thanks to their good electrochemical activity, especially at high current rates. Consequently, rate-capability tests have been applied to the $FeNb_{11}O_{29}$ electrodes (Figure II.20). First, the four monoclinic samples with smaller-sized particles generally exhibit better rate capabilities than orthorhombic ones. This was evidenced by lower polarization, less dQ/dV peak shifts, smaller distortion of peak shapes at high current rates, as observed in a representative monoclinic sample (*sμ-w*-M) compared to the orthorhombic one (Figure II.19). Second, even for micrometric samples obtained by conventional furnace heating (e.g., *μ-f*-M), impressive rate behaviors were observed, attaining 150 mAh g^{-1} at 10 C. This is a striking example of the outstanding fast kinetics of Wadsley-Roth phases, emphasizing that excellent rate performance can still be achieved with larger particle sizes and standard solid-state synthesis. Such samples offer practical advantages for scale-up, as they simplify manufacturing and processing without the need for additional nano- or porous structuring. As a result, these furnace-treated materials are suitable for further investigation in the following chapters.

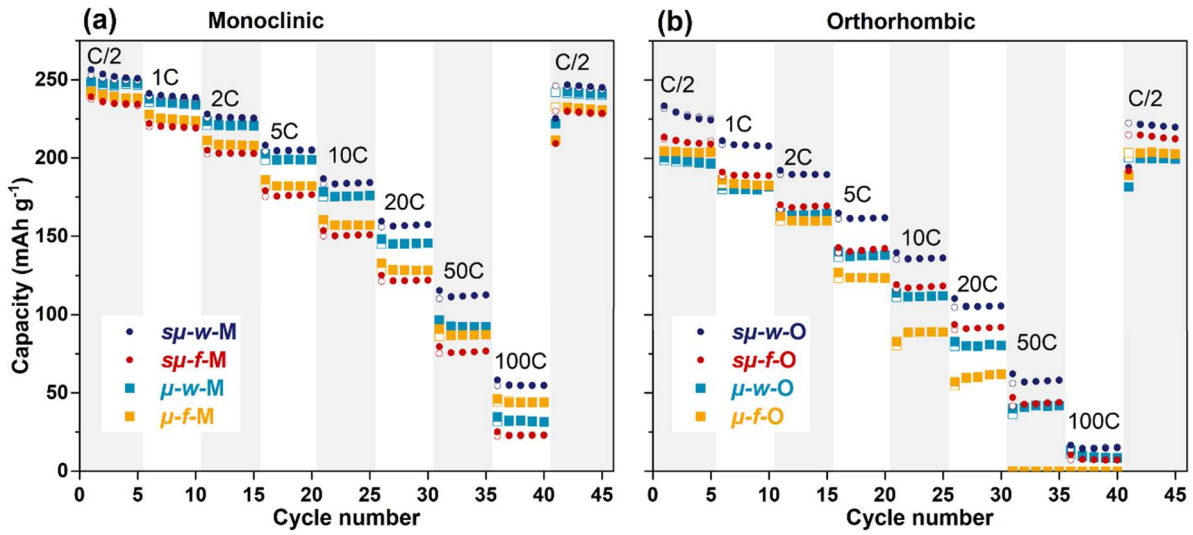

Figure II.20. Rate capability tests of monoclinic (a) and orthorhombic (b) $FeNb_{11}O_{29}$ samples

Third, we demonstrated that using microwave heating for micrometric precursors gives a clear improvement of rate behavior, with sample μ-w-M delivering a better capacity of around 170 mAh g^{-1} at 10 C. Finally, with even further downsized particles, obtained from submicrometric oxide precursors by microwave heating (*sμ-w*-M and *sμ-w*-O), their rate capability was further significantly enhanced. The extra capacity gained at C/2 for these two samples is still observed and interestingly even more pronounced at higher current rates. A closer analysis of these two representative samples is shown in Figure II.21, with the charge-discharge and differential capacity (dQ/dV) curves at progressively increasing currents. Over the range of currents from C/2 to 100 C, *sμ-w*-M sample showed superior rate performance. At C/2, around 1.2 Li^+/TM can be reversibly exchanged for a gravimetric capacity of about 250 mAh g^{-1}. When the rate is increased by a factor of 20 from C/2 to 10 C, which corresponds to a six-minute discharge, the sample can still deliver a capacity of 0.9 Li^+/TM (185 mAh g^{-1}). Differential capacity curves showed little peak shifts at 10 C compared with slow currents, indicating very fast kinetics. The orthorhombic phase exhibited slightly lower performance, likely due to larger particle size.

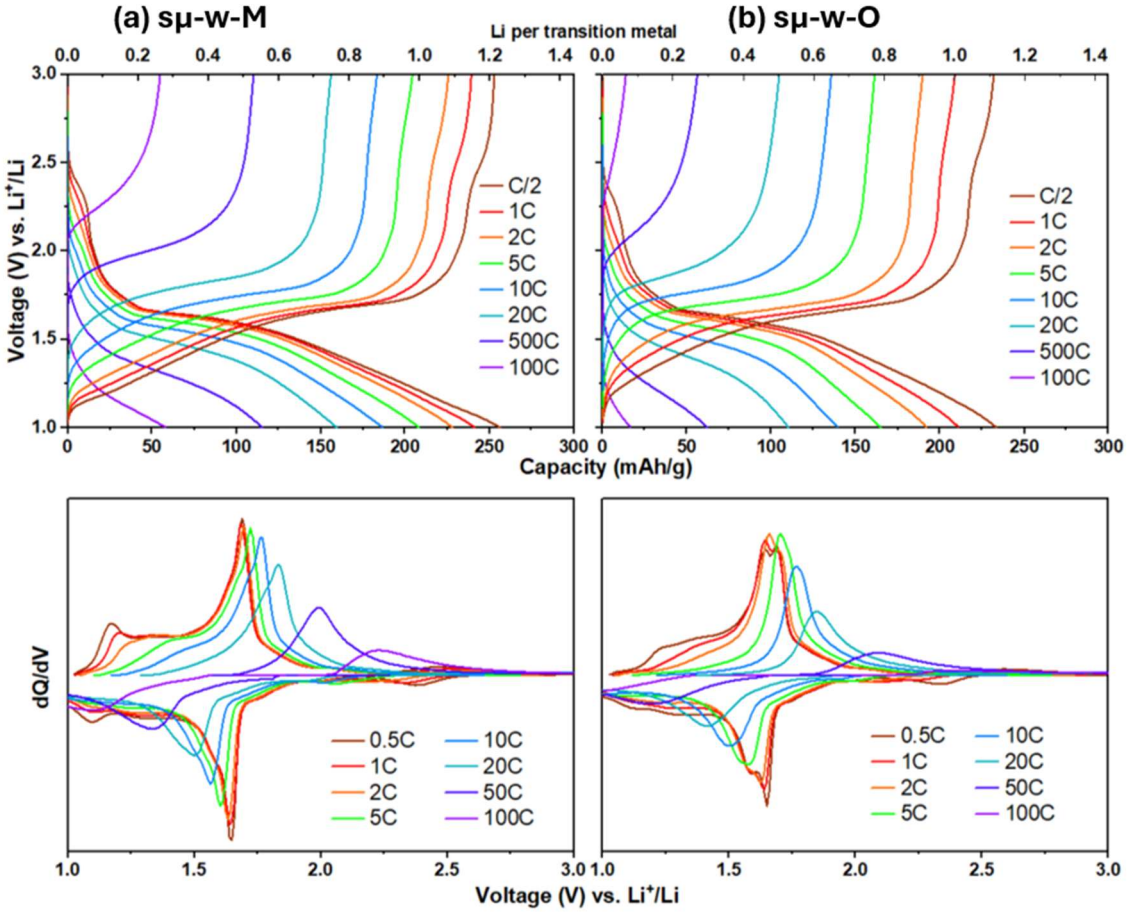

Figure II.21. Charge–discharge and dQ/dV curves of sμ-w-M and sμ-w-O samples at increasing current rates

These results demonstrate significantly beneficial impact of microwave-assisted synthesis and downsized particles on the enhancement of $FeNb_{11}O_{29}$ fast-charging capabilities, giving further improvements compared with the reference micrometric furnace-heated samples, which already exhibit excellent rate behavior.

II.3.5.3. Long-term cycling

Long-term cycling tests have been carried out at 10 C (Figure II.22). The better electrochemical behavior of the two microwave-heated samples with submicrometric oxide precursors is unambiguously highlighted. The monoclinic form of $FeNb_{11}O_{29}$ exhibits the best cycling performance, delivering 198 mAh g^{-1} initially and retaining a capacity of 90.4 % after 500 cycles (179 mAh g^{-1}) and 77 % after 1300 cycles (153 mAh g^{-1}). These rate capability and long-term cycling tests show good repeatability, as shown in Figure II.23 for four samples made from submicrometric precursors. This highest initial capacity at 10 C in the present work surpasses previously reported values for the best $FeNb_{11}O_{29}$-based materials enhanced by different strategies. For example, at the same rate of 10 C, monoclinic $Fe_{0.67}Ti_{0.67}Nb_{10.67}O_{29}$ initially delivered 170.4 mAh g^{-1} and retained 133.1 mAh g^{-1} after 10 000 cycles [117], while monoclinic $FeNb_{11}O_{29}$ nanotubes achieved 142.3 mAh g^{-1} and still sustained 101.4 mAh g^{-1} after

2000 cycles [113] (Table II.3). However, more effort is still needed to improve the long-term cycling and capacity retention of our materials. Comparing between two polymorphs in this work, monoclinic samples with smaller particle size show higher long-term capacity and better rate capability with respect to orthorhombic ones. This result, however, is contrary to the study by Spada et al. [108], as mentioned in the introduction part, with 200 mAh g^{-1} and 130 mAh g^{-1} delivered at 10 C by the orthorhombic and monoclinic sample, respectively.

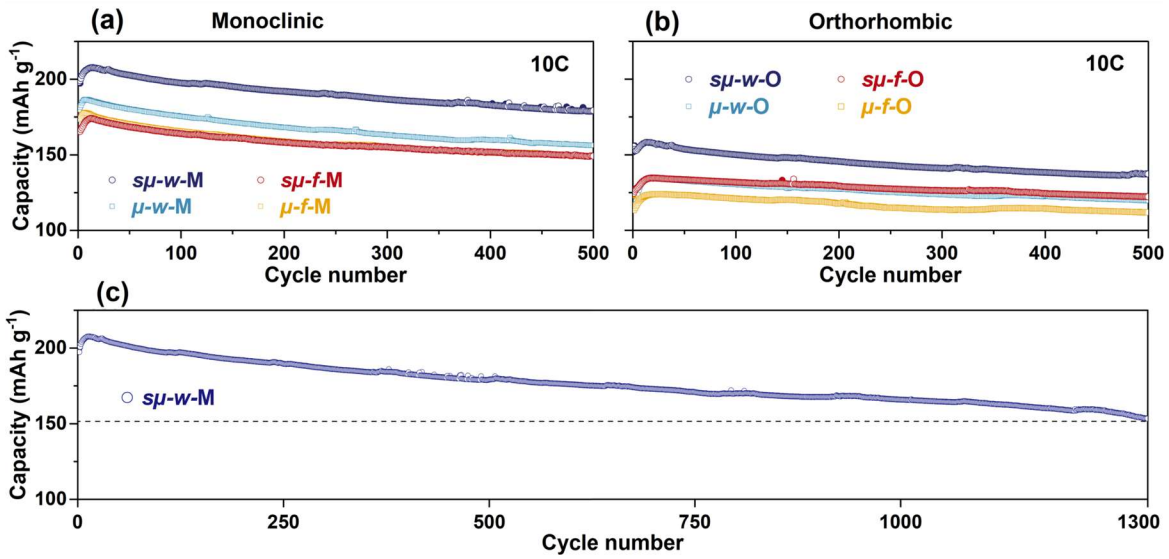

Figure II.22. Comparison of 500 galvanostatic cycles at 10 C for eight $FeNb_{11}O_{29}$ samples (a–b), and long-term cycling of the sμ-w-M sample over 1300 cycles at 10 C (c).

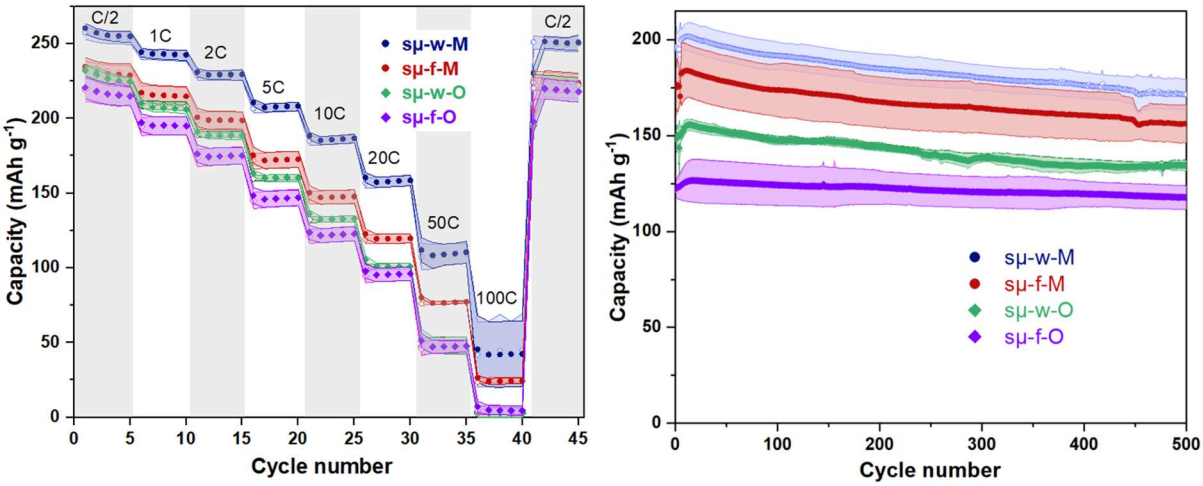

Figure II.23. Reproducibility of four samples made from submicrometric precursors, in terms of rate performance and long-term cycling at 10 C

The overall superior performance of microwave-heated samples can be suggested to result from smaller particle size, allowing effective electrolyte impregnation, faster Li^+ diffusion and better material utilization during electrochemical cycling. This hypothesis will be investigated in the following sections.

Table II.3. Long-term cycling performance of $FeNb_{11}O_{29}$ from various studies. Monoclinic and orthorhombic phases are indicated as M and O. Capacity values are reported as **initial** (in bold) followed by final value after prolonged cycling.

Materials	Phase	Synthesis method	Loading (mg cm^{-2})	Rate	Capacity (mAh g^{-1})	Cycle number	Capacity retention	Ref
sμ-w-M $FeNb_{11}O_{29}$	M	Microwave heating, 5 minutes	1.8−2.2	10 C	**~198**−179	500 cycles (1.0−3.0 V)	90%	This work
sμ-f-M $FeNb_{11}O_{29}$	M	Furnace heating, 1100 °C, 4 h, air		10 C	**~165**−149		90%	
$FeNb_{11}O_{29}$ nanotubes	M	electrospinning	N/A	10 C	**142**−101.4	2000 cycles (1.0−3.0 V)	71%	[113]
$FeNb_{11}O_{29}$ bulks	M	Solid state		1 C	151.8	100 cycles (1.0−3.0 V)	N/A	
$FeNb_{11}O_{29}$	O	1250 °C, 4 h, air	~1.4	10 C	**99**−88	200 cycle (0.8−3.0 V)	89%	[115]
$FeNb_{11}O_{27.9}$	O	1250 °C, 4 h, N_2			**145**−135		93%	
$FeNb_{11}O_{29}$ bulks	O	1300 °C, 4 h, air	1.0−2.5	2 C	~**350**−275	100 cycles (0.8−3.0 V)	78 %	[111]
$FeNb_{11}O_{29}$ bulks	M	1100 °C, 4 h, air			~**250**−180		72 %	
$FeNb_{11}O_{29}$	O	1300 °C, 4 h, air	N/A	2 C	~**300**−235	100 cycles (0.8−3.0 V)	78%	[110]
$Fe_{0.8}Mn_{0.2}Nb_{11}O_{29}$	O	1400 °C, 4 h, air			~**238**−240		100.9 %	
$Fe_{0.8}V_{0.2}Nb_{11}O_{29}$	O	1300 °C, 4 h, air			~**222**−220		99%	
$Fe_{0.67}Ti_{0.67}Nb_{10.67}O_{29}$	M	Solution combustion: 800 °C, 3 h, then 1200 °C, 3 h	~1	10 C	**170**−133.1	10 000 cycles (1.0−3.0 V)	72%	[117]
$FeNb_{11}O_{29}$	M				**183**−122.4		60%	
$FeNb_{11}O_{29}$ @N (nitridation layer)	O	1.hydrothermal: 200 °C, 4 h 2. 1000 °C, 5 h, air 3. 700 °C, 0.5 h, Ar/NH_3	1.5−2.0	10 C	~**147**−130	10 000 cycles (1.0−3.0 V)	88%	[108]
$FeNb_{11}O_{29}$	O	Only steps 1 & 2 above			~**150**−70		46%	

II.3.5.4. Electrochemical Impedance Spectroscopy (EIS)

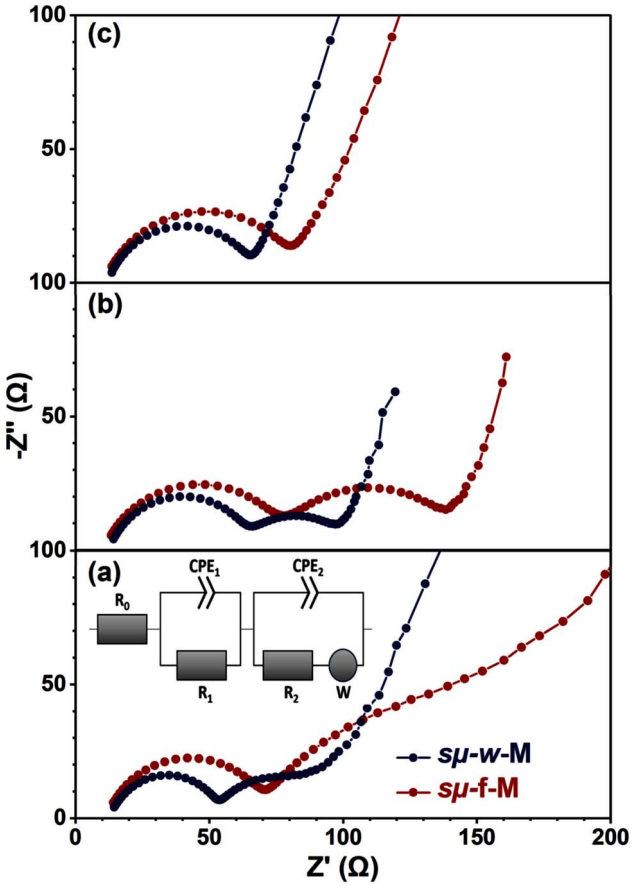

Figure II.24. Nyquist plots of two $FeNb_{11}O_{29}$ samples: sμ-f-M and sμ-w-M, (a) at open circuit voltage (OCV), (b) at the end of discharge (EoD) and (c) at the end of charge (EoC). The inset shows the equivalent circuit to fit the plots, where R, CPE and W represent resistance, constant phase element and Warburg resistance.

Electrochemical impedance spectroscopy (EIS) tests were carried out for two submicrometric $FeNb_{11}O_{29}$ samples prepared by conventional or microwave heating. Each Nyquist plot contains two depressed semicircles regions and one slope, which are fitted using the equivalent circuit in the inset. The single semicircle in plot (c) can be modelled by the overlap of two semicircles in a close frequency range. The first element, R_0, represents the Ohmic resistance of the cell. From the literature [113,115], the depressed semicircle in the high-frequency range corresponds to the electron transfer and Li^+-ion adsorption/desolvation processes, which are ascribed as R_1 and CPE_1. In the medium-frequency region, the other depressed semicircle can be assigned to Li^+-ion insertion at particle surfaces, denoted as R_2 and CPE_2. The low-frequency slope represents the Warburg resistance (W), describing Li^+-ion diffusion in the bulk of the particles. From size of semicircles and the fitted resistance values in Table II.4, it is evident that the microwave-heated sample has lower resistance than the furnace-heated one, presumably due to its smaller particles, which enhances electrochemical processes described above. This further confirms the better rate capability and better Li^+-ion diffusion of microwave-heated sample as evidenced in GCPL and GITT.

Table II.4. Resistance values of sμ-f-M and sμ-w-M samples by fitting EIS data with the equivalent circuit.

Sample	State	R_0 (Ω)	R_1 (Ω)	R_2 (Ω)
***sμ-w*-M**	OCV	13.09	40.05	45.23
	EoD	12.59	33.43	52.76
	EoC	12.67	54.14	2.823
***sμ-f*-M**	OCV	11.89	57.56	141.1
	EoD	10.71	67.45	65.25
	EoC	10.90	72.77	0.05

II.3.5.5. Galvanostatic Intermittent Titration Techniques (GITT)

To investigate further the electrochemical lithiation/delithiation of the material and confirm the assumption of better Li^+ solid-state diffusion in small particles, GITT technique was implemented (Figure II.25 and 26). This technique only focuses on two monoclinic samples obtained from submicrometric precursors by either furnace or microwave heating, *i.e.* sμ-w-M and *sμ-f*-M samples, as they offer the best electrochemical performance. This method gives two types of information: (i) thermodynamic equilibrium potential of the material as a function of lithiation degree and (ii) dynamic information on apparent Li^+ diffusion coefficient. As Li-ion diffusivity calculated from GITT is inversely proportional to the active mass, two electrodes of similar mass loading were chosen for a better comparison.

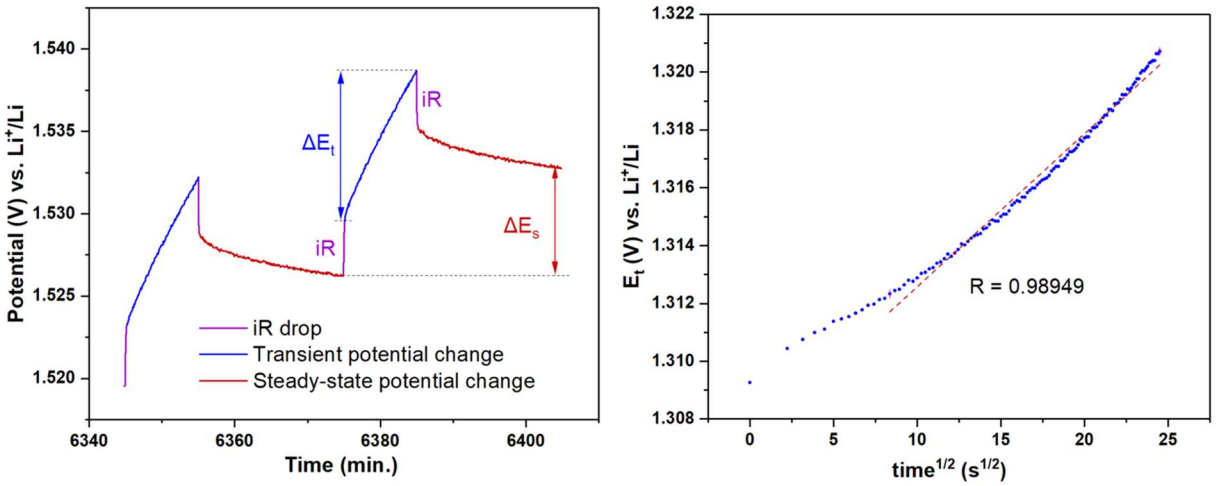

Figure II.25. (a) Representative GITT voltage profile showing the iR drop, transient (ΔE_t), and steady-state (ΔE_s) potential changes over two current pulses. (b) Linear relationship between potential (E_t) and time$^{1/2}$, confirming the validity of the GITT analysis.

The validity of the method was verified by checking the linear relationship between potential (E_t) and time$^{1/2}$ (Figure II.25), and the results were shown in Figure II.26. At first glance, similar GITT potential profiles were observed for both samples, indicating no significant change in thermodynamics of the material. Moreover, the apparent diffusion coefficients of Li+ ions are also close, remaining steadily high during the early stage of the discharge, followed by a sharp decrease from 1.8 to 1.5 V and then an increase till 1.2 V. However, the enhancement of the diffusion coefficient during the end of discharge (below 1.5 V) is evidently more pronounced for the electrode with active material prepared by microwave-assisted heating (*sμ-w*-M) and the situation remains in the subsequent charge until the voltage reaches 1.6 V. After that both electrodes exhibit a similar evolution. The higher lithium-ion diffusivity of the microwave-heated sample at low voltage echoes with its more intense differential capacity (dQ/dV) peak observed in Figure II.19 in the same voltage range.

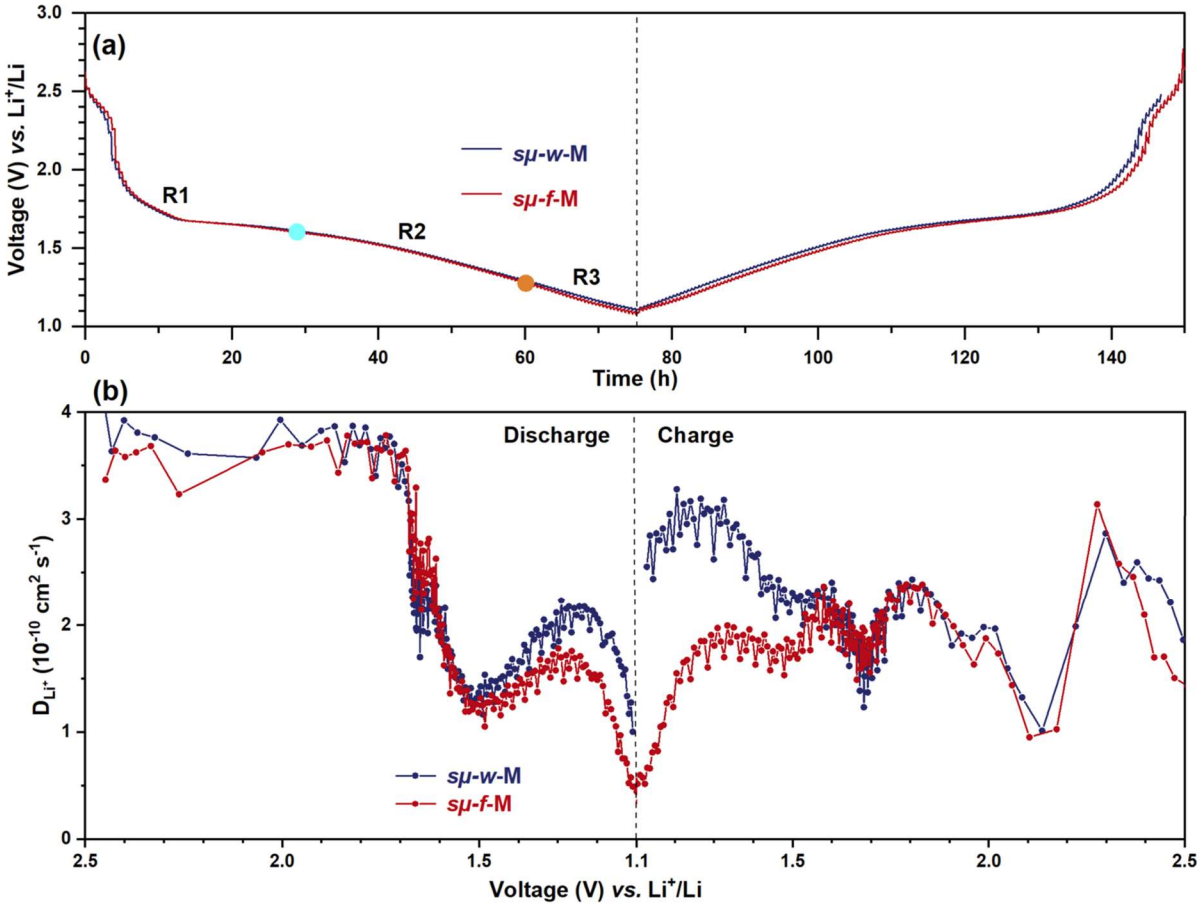

Figure II.26. GITT profiles of two samples prepared from submicrometric precursors: sμ-w-M and sμ-f-M, with (a) three ranges of lithiation degree corresponding to the three-stage evolution of (a,c) plane (*operando* XRD), and (b) the evolution of GITT-extracted Li^+ diffusion coefficient vs. voltage during discharge and charge.

II.3.6. *Operando* X-ray diffraction

Operando X-ray diffraction experiments were carried out for submicrometric microwave-heated sample of monoclinic $FeNb_{11}O_{29}$ phase, as shown in Figure II.27.

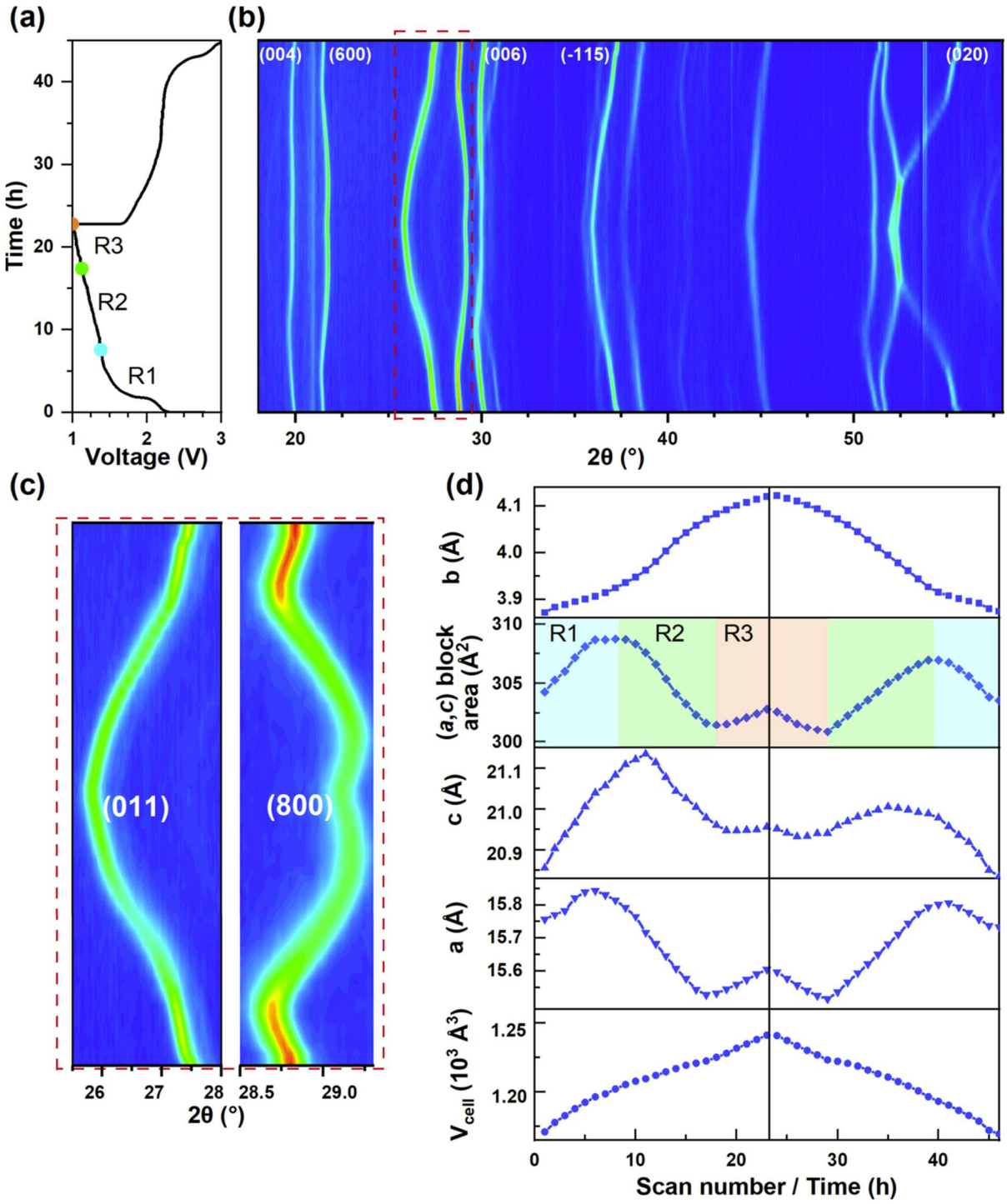

Figure II.27. The charge-discharge curve (a) and corresponding 2-dimensional contour plot of operando XRPD patterns for monoclinic FeNb11O29 (b), magnified view of (800) and (011) reflections (c), and the evolution of lattice parameters, (a,c) block area and unit cell volume during cycling (d).

Firstly, from the 2-dimensional contour plot of the XRD patterns, all the diffraction peaks evolve continuously and return to their initial positions without any newly appeared features during the whole discharge-charge process (Figure II.27b). The overall electrochemical process follows reversible lattice changes without any phase transformation or biphasic reaction as previously reported [108,113]. Secondly, the evolution of the cell parameter is scrutinized. Along the lithium insertion, the *b* parameter increases steadily and significantly, indicating that lithium ions diffuse along the channels perpendicularly to the block planes. Meanwhile, *a* and *c* parameters evolve in a more complex way, with an initial expansion of the (*a,c*) plane until around 1.4 V *vs.* Li^+/Li (region R1), which can be explained by Li^+-ion insertion in the structure. Afterwards, the (*a*,*c*) plane contracts until 1.2 V (region R2) due to the enhanced electrostatic attraction between intercalated Li^+ and O^{2-} ions [108]. At the third stage of discharge, both parameters increase again (region R3), probably because of the reduction of niobium, from Nb^{4+} (68 pm) to Nb^{3+} (72 pm) [108]. This three-stage feature somehow mimics the evolution of lithium-ion diffusivity in similar ranges of lithiation degree as shown in Figure II.26. This indicates the close relationship between the size of the diffusion channels and the diffusive behavior, where the expanded (*a*,*c*) plane results in faster diffusion of lithium-ions and *vice versa*.

Over the charge process, these lattice parameters undergo reverse evolutions and return to their original values, which further confirms the reversibility of the reactions. Overall, unit-cell volume expansion after full lithiation is 5.4 %. This low value appears in line with the literature [113] and also contributes to the long-term cycling stability.

II.4. Conclusions and perspectives

Two Wadsley-Roth polymorphs of $FeNb_{11}O_{29}$ were successfully and rapidly synthesized by microwave-assisted solid-state synthesis. This method presents significant benefits, including remarkably shorter time and limited particle growth, which turns to facilitate lithium-ion diffusion as evidenced by GITT coupled with differential capacity curves and *operando* XRD. This easier ionic diffusion in turn induces enhanced rate capability and long-term cycling, with a high capacity of 179 mAh g^{-1} (90% retention) after 500 cycles at 2 A g^{-1} delivered by microwave-heated monoclinic sample obtained from submicrometric precursors. The effect of smaller particle size is also seen when comparing between the two polymorphs, where the monoclinic samples exhibit higher capacity than the larger-sized orthorhombic ones. These results open the possibility for more efficient and upscalable protocols for other Wadsley-Roth phases as well as other battery materials.

Interestingly, even micrometric powders obtained by conventional furnace heating demonstrated remarkable rate performance, e.g. ~150 mAh g^{-1} at 10 C for µ-f-M sample. This striking result highlights the intrinsic fast kinetics of Wadsley–Roth phases, showing that excellent rate capability can still be achieved with larger particle sizes and standard solid-state synthesis. In addition to their electrochemical performance, such furnace-heated samples offer practical advantages: no need for complex nano- or porous structuring, simplified processing, and inherent compatibility with large-scale manufacturing. These characteristics make them attractive candidates for further study in practical implementations.

From a broader perspective, the promising results obtained here raise important opportunities and challenges. On the one hand, the effectiveness of microwave-assisted synthesis suggests a strong potential for upscaling this rapid and energy-efficient method, provided that uniform heating and reproducibility can be ensured at larger batch sizes. On the other hand, further optimization is still required to understand and mitigate long-term degradation mechanisms, particularly under the conditions of highly loaded electrodes relevant for practical devices. Addressing these aspects will be essential to fully unlock the potential of $FeNb_{11}O_{29}$ and related Wadsley–Roth phases for high-power, scalable energy storage applications.

Chapter III

Operando neutron diffraction studies of $FeNb_{11}O_{29}$: benchmarking cell designs and neutron diffractometers

III.1. Insights from neutrons for Li-ion batteries

III.1.1. Introduction to neutrons and neutron diffraction

Neutrons are electrically neutral subatomic particles found in atomic nuclei. They were discovered in 1932 by James Chadwick through his experiment involving the bombardment of alpha particles with beryllium. Neutrons have a mass of approximately 1.675×10^{-27} kg, slightly heavier than protons, and a mean lifetime of about 880 seconds in free space. With a spin of ½ and a magnetic moment of –1.91 nuclear magnetons, neutrons can interact with magnetic fields, allowing for magnetic structure determination of magnetic phases.

Neutrons can be produced through controlled nuclear fission in reactors or by spallation. In fission reactors, heavy nuclei like uranium-235 absorb neutrons and split into lighter fragments, releasing energy and more neutrons to sustain the chain reaction. For example, the Institut Laue-Langevin uses this principle to produce neutrons for experimental purposes. Alternatively, spallation sources generate neutrons by bombarding a heavy metal target with high-energy protons, causing the emission of neutrons among other particles.

Neutrons interact with matter in several ways, and these interactions are largely isotope dependent. First, coherent elastic scattering occurs when neutrons are scattered in a correlated manner by different nuclei, producing diffraction patterns and revealing structural information. Second, incoherent elastic scattering arises from isotopic or nuclear spin disorder, which causes random variations in neutron–nucleus interaction strengths and results in a diffuse, featureless background. The third phenomenon is neutron absorption, which is strong for certain isotopes (e.g., ^{6}Li, ^{10}B, ^{113}Cd). A key parameter in neutron scattering experiments is the scattering length (b), which characterizes the strength and nature of the neutron–nucleus interaction. This value depends on the isotope and can be either positive or negative, reflecting repulsive or attractive interactions, respectively.

III.1.2. Advantages and challenges of neutron-based techniques for batteries

The first significant advantage of neutron diffraction (ND) lies in its sensitivity to light elements, even when they are surrounded by heavier elements. Such light elements, including lithium and oxygen, are commonly found in battery materials but are nearly transparent to X-rays. Lithium is of central interest in battery research, as its crystallographic position, quantity, and dynamics are closely related to the structural and electrochemical properties of the host material. Additionally, neutrons can distinguish between neighboring transition metals—such as Mn, Fe, Co, and Ni—which are commonly present in electrode materials. Differentiating these

elements using X-ray diffraction is difficult because X-rays interact predominantly with the electrons of the sample, and the resulting X-ray scattering factors vary linearly with atomic number. However, neutron scattering is governed by complex interactions with the atomic nuclei, resulting in neutron scattering lengths that vary irregularly across the periodic table (Figure III.1). This non-monotonic trend provides enhanced contrast between light and heavy elements, as well as between neighboring elements, making neutron powder diffraction particularly effective for their identification and structural analysis. For example, the coherent neutron scattering lengths of Mn, Co, and Ni are -3.73 fm, 2.49 fm and 10.3 fm, respectively, highlighting their strong contrast [134,135].

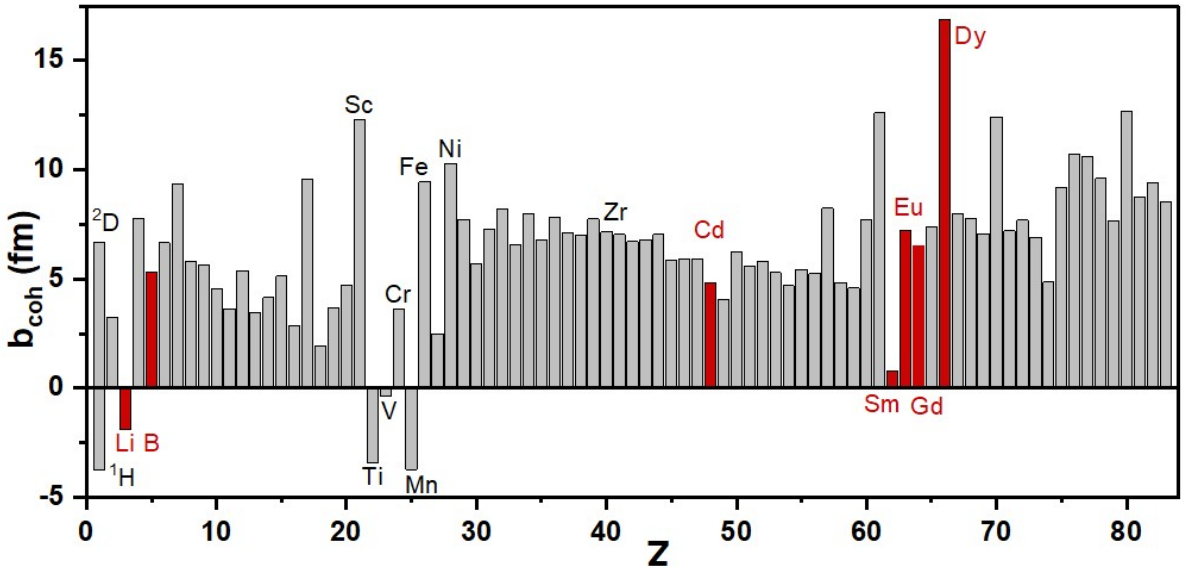

Figure III.1. Neutron scattering lengths for most elements (at natural abundance) across the periodic table. Elements highlighted in red are strong absorbers of neutrons. Plotted from data in [134].

Regarding lithium, despite its small neutron scattering length (-1.90 fm), its negative value creates strong contrast compared with most other elements, which generally possess positive scattering lengths. In all experiments presented in this chapter, natural lithium was used, which consists of approximately 92.5% ^{7}Li and 7.5% ^{6}Li. The dominant abundance of ^{7}Li is a strong advantage because this isotope not only has a negative scattering length but also has a relatively low neutron absorption cross-section. The relevant scattering properties of lithium are summarized in Table III.1.

Moreover, neutrons are non-destructive and exhibit far greater penetration depths than X-rays or most other characterization probes, due to their weak interaction with matter. This allows for the bulk analysis of entire electrodes—or even full battery assemblies—depending on the experimental geometry. Additionally, the underlying physical phenomenon of neutron scattering offers a distinct advantage: whereas X-rays interact with electron clouds and produce a form factor that decays with increasing scattering vector Q ($Q = 4\pi\sin\theta/\lambda$), neutrons interact directly

with atomic nuclei. This point-like interaction leads to scattering lengths that are effectively independent of Q. As a result, ND patterns still exhibit significant intensity at high-Q regions, enabling more precise determination of structural parameters such as site occupancies and Debye–Waller factors.

Table III.1. Neutron scattering properties of ^{6}Li, ^{7}Li, and natural lithium ($^{6.94}$Li), adapted from [134]. Columns are the nuclide, relative abundance (%), nuclear spin I; bound coherent (b_{coh}), incoherent (b_{inc}) scattering lengths in fm; and coherent (σ_{coh}), incoherent (σ_{inc}), total scattering (σ_{scatt}), and absorption (σ_{abs}) cross sections in barns.

Isotope	**%**	**I**	**b_{coh}**	**b_{inc}**	**σ_{coh}**	**σ_{inc}**	**σ_{scatt}**	**σ_{abs}**
$^{6.94}$Li	---		-1.90	---	0.454	0.92	1.37	70.5
^{6}Li	7.5	1	2.00-0.261*i*	-1.89+0.26*i*	0.51	0.46	0.97	940.4
^{7}Li	92.5	3/2	-2.22	-2.49	0.619	0.78	1.4	0.0454

These benefits have been motivations for using *in situ* ND as a powerful tool for battery research. However, several limitations must be acknowledged. First, the flux at neutron facilities is several orders of magnitude lower than that of X-ray sources, and neutron scattering lengths are an order of magnitude lower than that of X-rays, which demands large sample size and long acquisition time for sufficient counting statistics and good signal-to-noise ratio. Second, the large amount of sample (typically > 200 mg) required for neutron experiments further complicates sample preparation and in the case of *operando* experiments, it usually necessitates the use of thick electrodes. As a result, achieving homogeneous electrochemical reactions is more difficult and the maximum charge/discharge rate is limited. Thirdly, lithium-ion batteries contain components that pose challenges for neutron-based analysis: hydrogen-rich components (e.g. electrolytes, separators) produce strong continuous backgrounds; natural lithium exhibits neutron absorption; and metallic parts like aluminum/copper current collectors and steel casings contribute intense Bragg peaks. In fact, hydrogen's strong incoherent scattering (σ_{coh} = 1.75 barns vs. σ_{inc} = 80.27 barns) from the electrolyte results in strong featureless background in the whole angular range, with little influence on the Bragg peaks, which significantly reduces signal-to-noise ratio. This can be overcome by using deuterated electrolyte and low-hydrogen materials for other components, but the deuteration is highly expensive.

III.1.3. Neutron diffractometers at the Institute Laue-Langevin

The neutron powder diffractometers used in this work are D2B and D20 at the Institute Laue-Langevin (ILL, Grenoble), with complementary characteristics (Figure III.2). Regardless of the type and characteristics of the diffractometer, the basic components along the beam path are similar. The beam transmission begins with neutron emitted from the source and guided through H11 thermal beam tube and then beam divergence can be reduced using removable collimators. A monochromator then selects a single neutron wavelength according to Bragg's law, and monochromator slits control the beam's size and shape. For all setups, a compromise between incident neutron flux and instrumental resolution needs to be considered.

III.1.3.1. High resolution D2B diffractometer

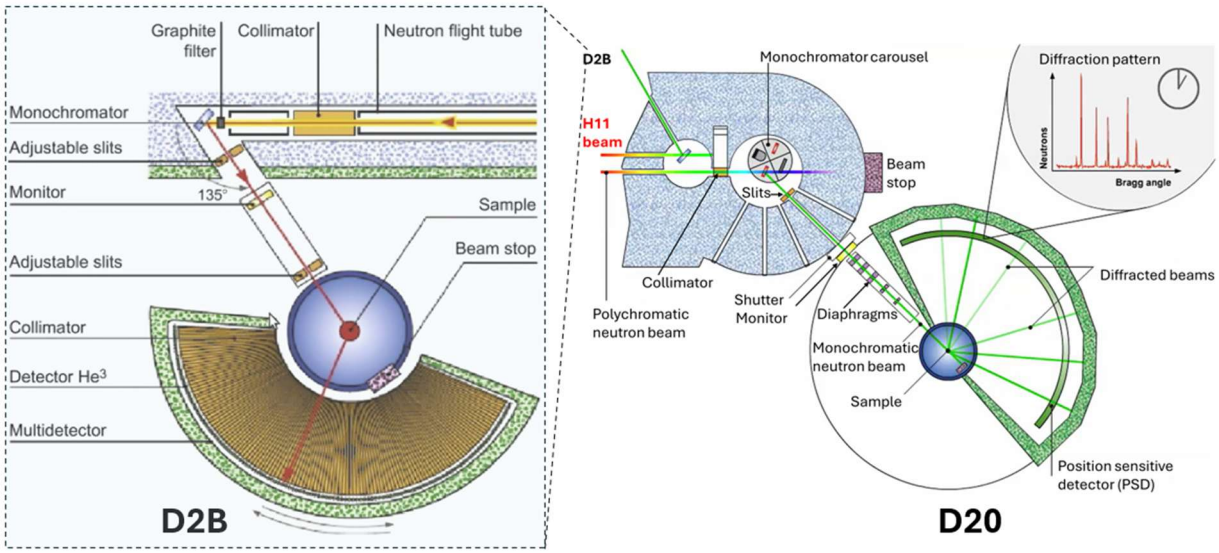

Figure III.2. D2B and D20 neutron powder diffractometers at the ILL

The D2B diffractometer is a very high-resolution powder diffractometer designed to achieve the ultimate resolution, limited only by powder particle size ($\Delta d/d$ $5x10^{-4}$). Its operation begins with neutron collimation and diffraction by a Ge monochromator, which is set at a very high take-off angle of 135°, *i.e.* the angle between the incident and diffracted beam after the monochromator. This high take-off angle helps in narrowing the incident neutron wavelength dispersion ($\Delta\lambda/\lambda=\cot\theta\cdot\Delta\theta$ is small at high θ). Enabling high resolution in neutron diffraction experiments. However, this configuration naturally reduces neutron intensity. To counteract this, the monochromator wafer is made with a relatively large mosaic spread (20 arcminutes), allowing it to reflect a broader range of neutron angles, thereby compensating for the intensity loss due to the high take-off angle. The outgoing neutron beam from the monochromator is a narrow distribution of wavelength, $\lambda \pm \Delta\lambda$.

The monochromatic neutron beam interacts with the sample and is scattered with an angle of 2θ, which are finally detected. The diffraction patterns were recorded by a bank of 128 vertically sensitive detectors (30 cm high) spaced at 1.25° intervals. During each scan, the detectors are moved to cover the angular range from 0° to 160°. Such scans are typically 30 minutes long and repeated to improve the statistics. Depending on the wavelength and desired resolution, as well as the amount and crystallinity of the samples, the typical acquisition time for a diffractogram may vary between 1h and 8h. Since the detectors are vertically sensitive, they produce a 2-dimesional scattering pattern that must be corrected for geometry and sample-to-detector distance before being integrated into the final intensity vs 2θ diffractogram.

Its high resolution makes D2B diffractometer versatile and suitable for a wide range of studies, including (i) the structural chemistry of non-rigid molecules; (ii) ab-initio structure solution from powders; (iii) crystal and magnetic structure determination of powder compounds (even small samples); and (iv) effect of temperature/pressure/magnetic field on crystal/magnetic structures. However, its lower neutron flux and the low active material mass in conventional *in situ* cells limits its use for *in situ* or *operando* electrochemical experiments. Up to date, no such *operando* electrochemical experiment has been done at D2B.

In our work, D2B was used for standard neutron powder diffraction measurements of pristine $FeNb_{11}O_{29}$ powder, as well as *in situ* studies of the cylindrical cell. A neutron wavelength of $\lambda = 1.594$ Å was chosen. This configuration gives a neutron flux of around 10^6 $cm^{-1}s^{-1}$. A typical sample preparation for room-temperature measurements at D2B is done by filling the sample in a cylindrical vanadium can (diameter 6.5 mm or larger). Air-sensitive samples were prepared inside an Ar-filled glovebox and sealed with indium wire to ensure airtightness. Vanadium is used to make sample containers because it has very low neutron absorption and weak neutron scattering, giving no Bragg peaks and minimized background noise. It is also chemically stable, machinable and suitable for a wide temperature range.

III.1.3.2. High flux D20 diffractometer

D20 is a very high intensity 2-axis diffractometer equipped with a large microstrip detector. Its extremely high neutron flux, ranging from 10^7 to 10^8 $cm^{-1}s^{-1}$, opens new possibilities for real-time experiments in short times or on very small samples. Therefore, it is particularly suitable for *in situ* or *operando* experiments.

The thermal neutron beam H11 from the reactor is split into two parallel paths, one directed to D2B, the other to D20. In the D20 path, the beam first reaches one of four available monochromators. The monochromatic beam exits through one of five take-off ports, each offering a different instrumental resolution, providing flexibility for various experimental

requirements. The beam then arrives at the sample and is scattered in various directions, which are then simultaneously detected by the large microstrip multidetector. The counts are collected over a certain duration for sufficient statistics and good signal-to-noise for the powder diffractograms. Typical acquisition times can be about 5 minutes for small samples but can decrease to one minute or even a few seconds for larger or highly crystalline samples.

The detector used at D20 is a position-sensitive detector (PSD), which is enclosed in aluminum housing and provides a detection area of 4 meters in length and 15 centimeters in height. It is filled with a gas mixture of 3.1 bar helium-3 (^{3}He) and 0.8 bar CF_4, and uses micro-strip gas chamber (MSGC) technology. Each of the 48 detection plates contains 32 cells, each 2.568 mm wide (equivalent to 0.1°), allowing the PSD to cover a total angular range of 153.6°.

In our work, a take-off angle of 90° with a Germanium monochromator at reflection (335) (λ = 1.54 Å) to have a compromise between good flux and resolution. In some cases, radial oscillating collimator (ROC) was used to average out artefacts in the diffractograms due to the cell or air, thus enhancing signal-to-noise ratio.

III.2. *In situ* electrochemical cells for neutron diffraction studies

III.2.1. *Ex situ, in situ* and *operando* characterizations

Development of battery materials strongly depends on the characterization techniques to obtain information on their structures, physicochemical and electrochemical properties both for newly discovered compounds and existing ones. The latter point is of central importance for further improvement and maximized exploitation of material capabilities. The materials need to be investigated not only in the pristine, as-synthesized state but also for intermediate compositions during electrochemical cycling. This allows for more insights into their structural evolution, working and degradation mechanisms. They can be characterized under different conditions: *ex situ*, *in situ* or *operando.*

Ex situ measurements are done out of the electrochemical cell, where a certain composition is obtained by lithium insertion or extraction in the cell and the sample is subsequently recovered and washed by disassembling the cell in an Ar-filled glovebox. This approach is commonly used since it is relatively easy to perform and when the equipment, cell or measurement conditions are not suitable for *in situ*/*operando* experiments. However, the compositions under study may be metastable and transform when the sample is recovered from the cell. Samples can be exposed to contamination or side reactions with atmospheric agents or tools in the recovery process.

Several drawbacks of *ex situ* studies can be overcome by *in situ* or *operando* investigations. In both cases, the electrochemically prepared compound is investigated directly inside the cell, which offers the advantage of avoiding exposure to contaminants in outside environments. However, a clear difference is made between these two terms. While *in situ* means "in place", i.e. in the battery, *operando* refers to "during operation". In the first case, *in situ* studies are carried out when the battery is stopped at the desired compositions, put in relaxation and mounted at the equipment stage for the measurement. Meanwhile, in an *operando* experiment, the cell is always mounted at experimental setup and the measurement is conducted in real time when the battery is being cycled. This approach enables real-time monitoring of structural evolution and possible metastable phases that exist only out of the equilibrium. Besides, kinetics-related reactions can be observed when varying the cycling rates of the cell.

III.2.2. Development history of *in situ* electrochemical cells for ND

During *in situ* or *operando* experiments, obtaining high-quality neutron diffraction data is challenging due to strict requirements of achieving good electrochemistry while cycling large amounts of materials for sufficient counting statistics and optimal signal-to-noise ratio. These conditions are important for the development of *in situ* electrochemical cells for neutron studies.

The first electrochemical cell design for *in situ* neutron diffraction studies was reported in 1998, featuring a cylindrical geometry with 5 g of powder contained in a Pyrex tube designed by Edström's group at Uppsala University [136,137]. The cell enabled effective charge-discharge cycling of $LiMn_2O_4$ and allowed refinement of its structure and lithium occupancies at selected potentials. However, the use of a thick, loosely packed cathode layer restricted the current rate to below C/50. Since then, several cell designs have been developed to meet the requirements of *in situ* ND experiments. They can be grouped into three categories: coin-type cells, pouch-type cells (Figure III.3), and cylindrical roll-over cells.

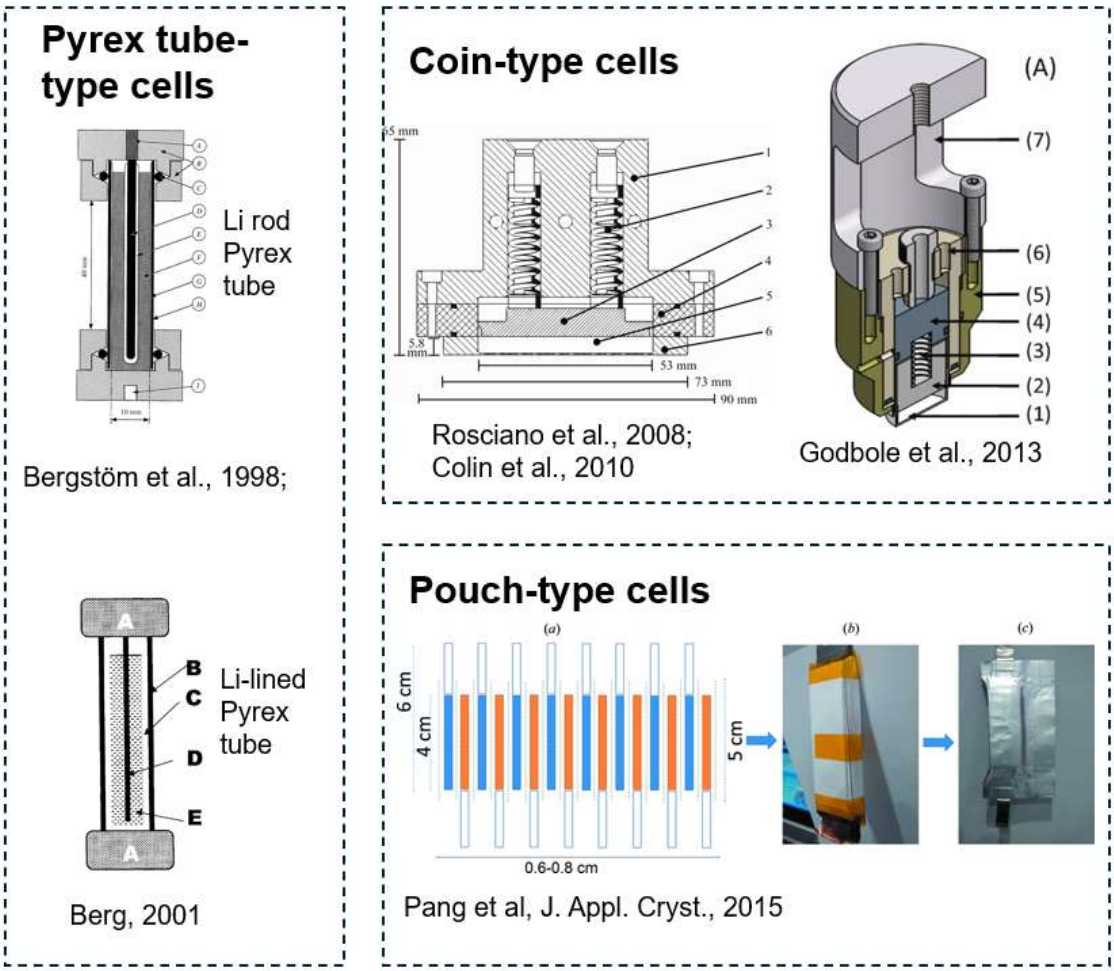

Figure III.3. Schematics of the earliest Pyrex tube-type electrochemical cell design used for *in situ* neutron diffraction, with subsequent developments including coin-type and pouch-type cell configurations [136–141].

III.2.2.1. Coin-type cell configuration

In coin-type configuration, a large amount of loose active material or self-standing composite electrodes (often using poly(tetrafluoroethylene), PTFE, as binder) is compacted into a pellet and housed in a separate compartment, which is usually the only part exposed to the neutron beam. Different designs, geometries and materials were used for the cell body, including PEEK, aluminum or titanium [138–140]. The cell components can contribute significantly to the diffraction background and produce overlapping peaks with the active material. This issue was overcome by using neutron-transparent $Ti_{2.1}Zr$ alloys [142] for cell housing and carefully selecting the cell components to minimize incoherent scattering, most notably through the use of deuterated electrolytes and glass fiber separator [143]. Such improvements have enabled high-quality structural refinement from *operando* ND patterns. However, thick electrodes may be detrimental to electrochemical performance as it resulted in considerable polarization, inhomogeneous reactions and limited current rates. This cell is used in our work and will be described in more details in section III.2.3.

III.2.2.2. Pouch cell configuration

The second neutron cell design is pouch-cell, and its use is growing due to its relatively simple assembly and the flexibility it offers in selecting components such as separators and electrodes. Similar to commercial pouch cells, the positive, negative electrodes and separators are stacked and enclosed in a propylene-coated aluminium pouch, which is then heat-sealed after electrolyte injection. While this design supports relatively high cycling rates and delivers decent electrochemical performance, the polymer coating on the pouch contributes significantly to background noise in the diffraction data [141].

III.2.2.3. Cylindrical roll-over configuration

Finally, another cell design is cylindrical cell resembling the cylindrical 18650-type cell. Three research groups have developed variations of this cell design: (1) Sharma's group in Australia, (2) Edström's group at Uppsala University, Sweden in collaboration with ISIS Neutron and Muon Source, and (3) Villevieille's group at Paul Scherrer Institute (PSI), as shown in Figure III.4. The cell assembly involves rolling the electrode, separator, and Li foil into a cylindrical form, followed by electrolyte filling, current collector connections and cell sealing. In all reported studies, deuterated electrolytes were used, effectively reducing background signals. Despite having similar configuration, these studies differ in their optimization approaches, particularly in the following aspects: the mass loading and formulation of active material electrode, the choice of materials for the cell body, the designs of gasket and connections, and the type of separator used.

The first roll-over design was reported by Sharma et al. since 2011 in which around 0.4 – 0.6 g active material was coated on Cu/Al current collector. The combination of deuterated electrolytes and vanadium casing provided good-quality ND data, but only lattice parameters and phase fractions were refined. These results offered insights into the structural evolution of positive ($Li(Co_{0.16}Mn_{1.84})O_4$) and negative ($MoS_2$, $Li_4Ti_5O_{12}$) electrode materials under *operando* conditions [144–147]. This first version of roll-over design offered the possibility to cycle the cell at faster current rates, up to 15 mA (corresponding to around C/2) [147], this high current was applied only for some short portions of charge-discharge cycle.

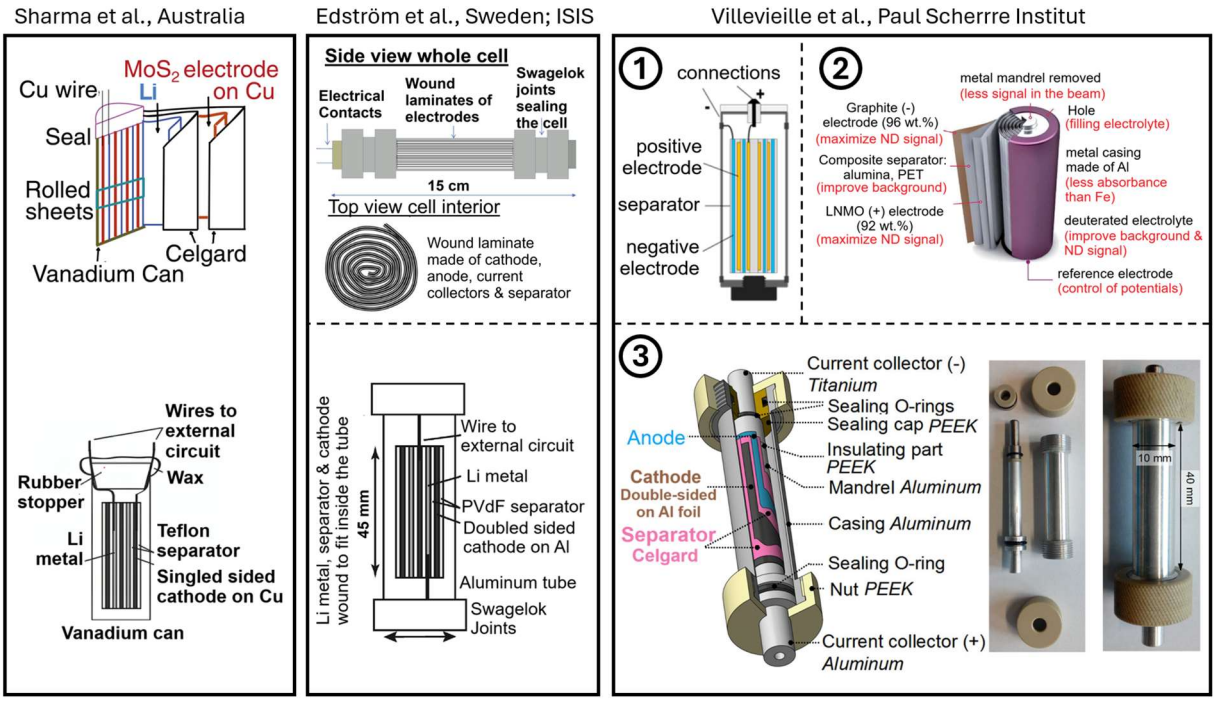

Figure III.4. Illustrations of cylindrical roll-over cell designs used for *in situ* neutron diffraction, developed by three research groups. Adapted from [144,148–152]

The second group, a collaboration between Upsala University and ISIS, has been working on cylindrical neutron cell development since 2013, focusing on half-cells using $LiFePO_4$ [148] or $Li_{0.18}Sr_{0.66}Ti_{0.5}Nb_{0.5}O_3$ [149] versus lithium. They adapted and modified the earlier designs by using quartz or aluminum casing and Swagelok-type metallic joints as current collectors and cell sealing components. To increase data quality, they used higher active material loadings—typically around 1–2 g, and selected either quartz glass fiber [148] or PVdF membranes [149] as separators. These modifications allow for the detailed refinement of some structural parameters (e.g., atomic coordinates, lithium occupancy), but long measurement time was required, ranging from 1-3 hours [148] to even 15 hours per pattern [149]. These limited cycling conditions may be better described as *in situ* rather than *operando*.

The third group based at PSI continued the work on cylindrical cell development since 2016. Their first version in 2016 was a full cell of $LiNi_{0.5}Mn_{1.5}O_4$ vs. graphite mimicking 18650-type cell, adapted with a screw for electrolyte filling, while the inner core (mandrel) was removed, and high mass loading of 2 g was used for the electrodes [150]. However, its metallic body and current collectors contribute many reflections of Fe, Al, Cu, and Ni to the diffraction patterns, and significant background was caused by polyethylene/polypropylene (PE/PP) polyolefin (20 µm thick) separator. Further improvement in 2017, using full cell of the same active materials, includes the replacement of iron casing by aluminum case to remove one Bragg contribution to the patterns, and the use of a composite separator composed of alumina (10–15 µm, described as quasi-transparent to neutrons) and PET (ca. 10 µm) [151]. The electrode

was highly loaded with 4 g of active material and reliable electrochemical cycling was achieved at high rates up to C/7. This second design by PSI enables successful Rietveld refinement of 40-minute patterns, allowing for the quantification of Li consumed by surface reactions after 100 cycles. The research group continue on the third version for half-cell of $LiNi_{0.6}Co_{0.2}Mn_{0.2}O_2$ (NMC622) vs. Li [152]. In this set-up, the cell was assembled from Al foil doubly coated with 0.7 g of NMC622, Celgard 2500 separator and lithium foil, which was then contained in an aluminum body. The cell exhibits good electrochemical performance at C/20, even after long-term cycling. High quality neutron diffraction patterns could be obtained after 1 hour of acquisition. Despite Celgard's considerable contribution to the background, an appropriate background subtraction could allow for reliable Rietveld refinement of three phases: NMC622, Al and Li. The results provided insight into important parameters such as Li occupancy and oxygen atomic positions.

III.2.3. Coin-type ILLBAT#1 cell

III.2.3.1. Designs of ILLBAT#1 cell

Designing *in situ* electrochemical cells for neutron diffraction raises the challenge of balancing good electrochemistry with sufficient neutron diffraction statistics—two requirements that often conflict. For instance, neutron diffraction typically requires a large quantity of active material, whereas such high loadings can hinder homogeneous electrochemical reactions.

These issues were addressed by Bianchini et al. [143] with a custom-designed cell for *in situ* and *operando* neutron diffraction (Figure III.5), developed with the following specific criteria:

- Electrochemical compatibility: The cell is capable of stable cycling for tens of cycles at a C/5 rate, with electrode material loadings ranging from 10 mg up to 200 mg.
- User-friendly design: The cell is easy to assemble, clean, and reuse, which is practical at large-scale neutron scattering facilities.
- High-quality diffraction data: The cell is able to produce neutron powder diffraction patterns of sufficient quality within 30 minutes for a 200 mg loading, with minimal contributions from components other than the electrode material of interest.

The central component of the cell is the powder container, shown in blue, which houses the electrode material. It is strictly required for this component to be electrochemically stable (i.e., resistant to oxidation or reduction during cycling) and transparent to neutron radiation. To meet these criteria, a titanium-zirconium (Ti-Zr) alloy of composition close to $Ti_{2.08}Zr$ was chosen. This alloy is well-known as "null matrix material" due to the complementary neutron scattering properties of its constituents. This unique transparency to neutrons is brought about by the

contrasting neutron scattering lengths of titanium and Zirconium, which are opposite in sign and differ in magnitude by roughly a factor of two ($b_{Ti} = -3.37\times10^{-12}$ cm and $b_{Zr} = 7.16\times10^{-12}$ cm). When combined in the appropriate stoichiometric ratio, the alloy exhibits near-zero overall coherent scattering intensity, making it an ideal container material for neutron diffraction studies. Beyond its electrochemical inertness and neutron transparency, the alloy also offers good mechanical strength, resistance to corrosion and excellent electrical conductivity, making it an ideal container material for ND. With dimensions of 3 cm in height and 1 cm in diameter, this cell can accommodate 200 mg of composite electrode in a thin layer of approximately 1 mm thickness, which is exposed to the neutron beam.

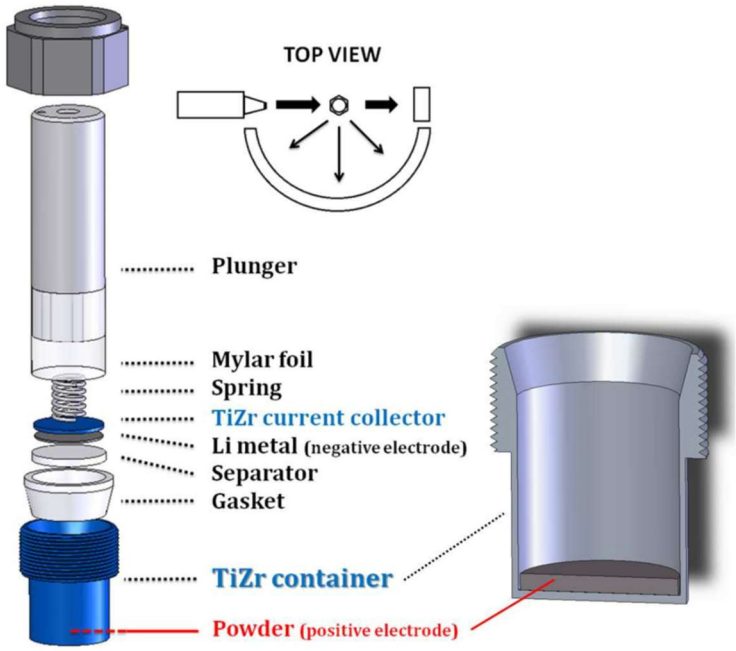

Figure III.5. Coin-type ILLBAT#1 *in situ* cell for neutron diffraction

III.2.3.2. Considerations for cell components

In neutron diffraction experiments, neutron beam is ideally focused on the active material under study, through optimization of cell geometry and the use of cadmium mask to block neutron exposure to other components. However, some scattering from surrounding materials is often unavoidable, as other cell components may still be partially exposed to the beam and contribute to the diffraction pattern. Therefore, it is important to wisely select cell components during such experiments for minimized background and reliable data.

The first component is the electrode containing the material of interest, usually fabricated in the form of self-standing films instead of loose powder, allowing better electronic and ionic transport and mechanical integrity between particles. Self-standing electrodes for *in situ*

electrochemical experiments are usually composed of active materials, conductive carbon, and polymeric binder. In this work, amorphous Carbon Super P was used, which only contributed a slowly incoherent background to the diffractograms. Regarding binder, polytetrafluoroethylene C_2F_4 (PTFE or Teflon®) was chosen due to no presence of hydrogen to avoid incoherent scattering, as well as its electrochemical inertness, good mechanical and binding properties.

The second component in close contact with the electrode, which can be exposed to neutron, is separator. Common separator materials include glass fiber, PVDF ($[C_2H_2F_2]_n$), and Celgard ($[C_3H_6]_n$), which are hydrogen-rich and therefore unsuitable for neutron diffraction. Glass-fiber separators, composed mainly of amorphous SiO_2 and ~3% B_2O_3 is a viable choice. Although natural boron (^{10}B:^{8}B = 20:80) is a strong neutron absorber (σ_{abs} = 767 barns), the low boron content in glass-fiber results in only minor signal attenuation.

Regarding organic electrolytes, the conventional choice is hydrogen-rich systems, typically consisting of $LiPF_6$ dissolved in organic solvents such as carbonate-based compounds. The presence of hydrogen generates a strong incoherent background in neutron diffractograms, which can submerge the Bragg peaks especially in the case of low active material loading. To address this, deuterated solvents can be a good approach, where deuterium's much lower incoherent cross section (2.05 barns) significantly reduces background noise. However, this solution greatly increases experimental costs (e.g., d-DMC: ~€2000/10 mL vs. H-DMC: €43/100 mL; d-EC: ~€2500/5 g vs. H-EC: €22/100 g). For ILLBAT#1 cell, a small amount of deuterated LP30 electrolyte (1M $LiPF_6$ in d-EC:d-DMC=1:1, v/v) was used.

III.2.3.3. Assembling of ILLBAT#1 cell

Regarding cell assembling, firstly the self-standing electrode is prepared and placed onto the bottom compartment of the cell. To ensure electrical insulation, a Mylar film lines the cell interior. The half-cell is assembled by stacking several components over the electrode: (i) A glass fiber separator is placed directly on top. (ii) ~0.4 mL of electrolyte is then uniformly distributed onto the separator. (iii) The negative side of the cell is assembled in this order: a lithium metal counter electrode, a 1 mm thick $Ti_{2.08}Zr$ disc serving as the negative current collector, a spring to apply constant pressure, and a plunger that seals the cell from above, and a plastic gasket for airtight sealing. The assembly is completed by tightening a screw that maintains pressure and secures the components in place. Once sealed, the cell is installed vertically in the diffractometer, with an insulating plastic screw at the top of the plunger allowing for easy mounting. The design ensures that only the bottom section, where the electrode is placed, is exposed to the neutron beam via precise alignment using slits and cadmium mask.

III.2.4. Cylindrical ILL-LEPMI cell

III.2.4.1. Design of cylindrical ILL-LEPMI cell

The design of the cylindrical electrochemical cell for *in situ* or *operando* neutron diffraction is illustrated by a schematic and photograph in Figure III.6. This cell was developed from the expertise of Claire Villevieille, building on her experience at PSI, and in collaboration with the well-established neutron community at the ILL. Therefore, its design closely resembles that of the cell reported previously at PSI, while the materials and cell dimensions were optimized by the ILL for maximized data quality.

The central component of the setup is the cell body – a hollow tube, shown in gray, which houses the "jelly-roll" configuration of the rolled electrodes. Strict requirements are considered for choosing the body materials: it must exhibit high chemical and electrochemical stability against both reduction and oxidation, maintain mechanical integrity under operating conditions, be compatible with practical cell manufacturing, and crucially, possess low neutron absorption and scattering to ensure data quality. As described in the cell development history, different materials have been tested for cell casing, including aluminum, iron or quartz, all of which contribute Bragg reflections or broad background to the neutron diffraction patterns.

In our case, the cylindrical cell body was fabricated from $Ti_{2.08}Zr$ neutron-transparent alloy, previously used in ILLBAT#1 cell, which produces no Bragg peaks and negligible background noise. Additionally, it is a good electrical conductor and is chemically and mechanically robust, making it suitable for the current collector, i.e. the central rod of the cell. This hollow rod is composed of two parts: the long rod is the positive current collector around which the positive electrode foil is directly rolled for electrical contact, while the shorter part is the negative current collector, which is connected via a tab. These two parts are electrically insulated from each other by insulating polyetheretherketone (PEEK) material. Besides, as PEEK is chemically stable and mechanically strong, it is also used to design the sealing caps.

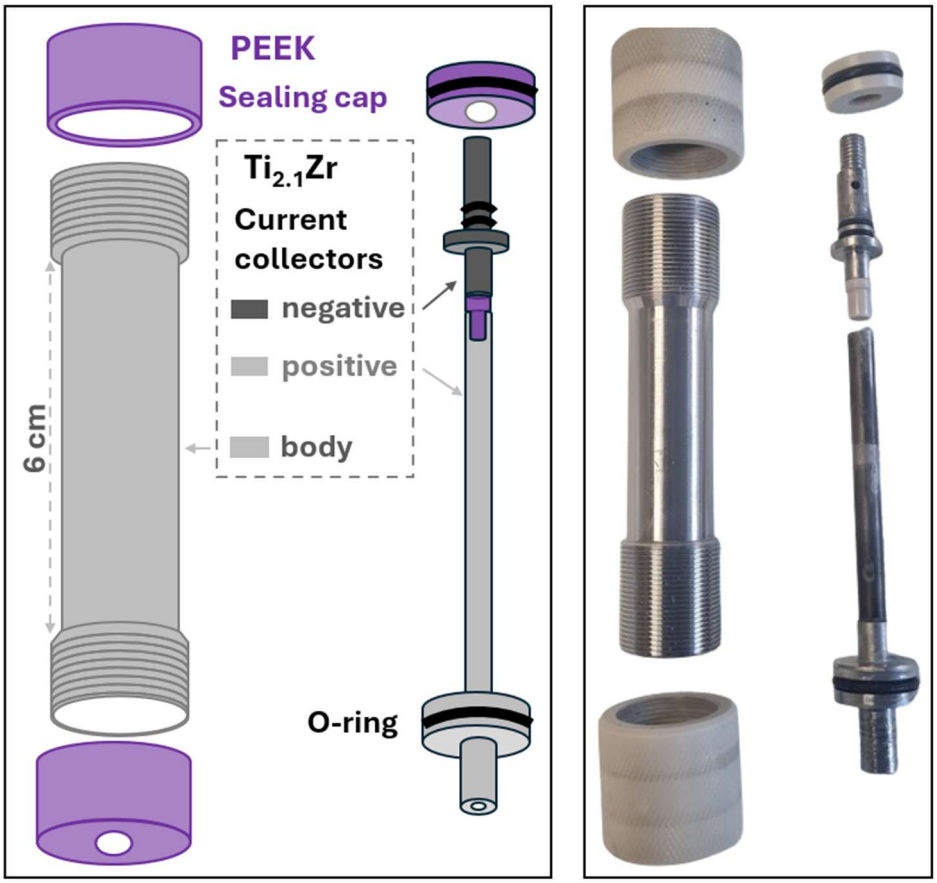

Figure III.6. Illustration of cylindrical roll-over cell designed by the ILL and LEPMI, and its photograph

III.2.4.2. Considerations for cell components

Celgard is usually chosen as separator for *in situ* ND experiments because of its high tensile strength, good resistance to tear and puncture, decent flexibility, and excellent ion transport properties. Despite containing a large quantity of hydrogen, which causes incoherent scattering contributes greatly to the high and irregular background, Celgard is still the most suitable separator. In fact, a comparative study was conducted on the normalized neutron scattering intensities of several separators (Celgard 2400 & 2500, polyethylene, PVdF), revealing that Celgard 2500 is the best choice [152]. Another possibility that has been used in previous work was composite separator made of PET (polyethylene terephthalate) and alumina layer [151]. This material was described as quasi-transparent to neutrons, mechanically strong and good for ion transport. However, challenges remain regarding the stiffness and brittleness of the alumina layer, which can crack or delaminate if mishandled. After considering all the compromises from the previous arguments, Celgard 2500 is used as separator in this work.

The second component that can significantly affect the data quality is the current collector. As copper does not alloy with lithium at low potentials (unlike aluminum), copper grid is used as the mesh on which lithium foil is placed. Therefore, it is more preferable to also use copper

foil as current collector for casting electrode films of active material. Although some copper reflections overlap with those of the active material ($FeNb_{11}O_{29}$), the extent of overlap is less significant compared to that observed with aluminum.

The third component is metallic lithium foil. Lithium can contribute some peaks to the diffractograms, but also absorbs considerable amounts of neutron, which means less neutrons are available for coherent scattering with the active material. This lowers the signal-to-noise ratio of the obtained data. Therefore, lithium foil was made as thin as possible. Besides, thin lithium foil also facilitates the cell rolling process and ensures better contact with the electrode foil, giving lower ohmic resistance to the cell.

Fourthly, electrolytes are an important contributor to data quality. Its ability to produce incoherent scattering not only arises from the hydrogen atoms but also from the liquid content. Therefore, it is essential to have balanced amount of electrolyte: sufficient to ensure good electrochemical performance, but not excessive to avoid background noise. While many studies conventionally use deuterated electrolytes to minimize such noise, we chose to use a standard hydrogen-containing carbonate-based electrolyte to reduce experimental costs and make such measurements more accessible. Given the relatively large amount of active material in our cells, we aimed to evaluate whether using a standard electrolyte would still yield high-quality data, with the expectation that the diffraction signal would be dominated by the electrode rather than the electrolyte.

III.2.4.3. Assembling of cylindrical cell

The procedure of cylindrical cell assembly is illustrated in Figure III.7. First, the double-coated electrode was cut to the dimensions of 5.5 cm × 20 cm. Two Celgard separator strips (6 cm × 30 cm) were prepared and joined along their two parallel edges by Kapton tape to ensure reliable electrical insulation. A copper grid of the same size as the electrode (5.5 × 20 cm) was cut, and its sharp edges were carefully covered with narrow strips of Kapton tape to avoid accidental tearing or puncturing of the separator, which could cause short circuits. This grid was then attached to a small Cu grid tab, which served as an electrical lead to the negative terminal. All these cell components and materials were dried overnight at 60 °C before being transferred into an Ar-filled glovebox.

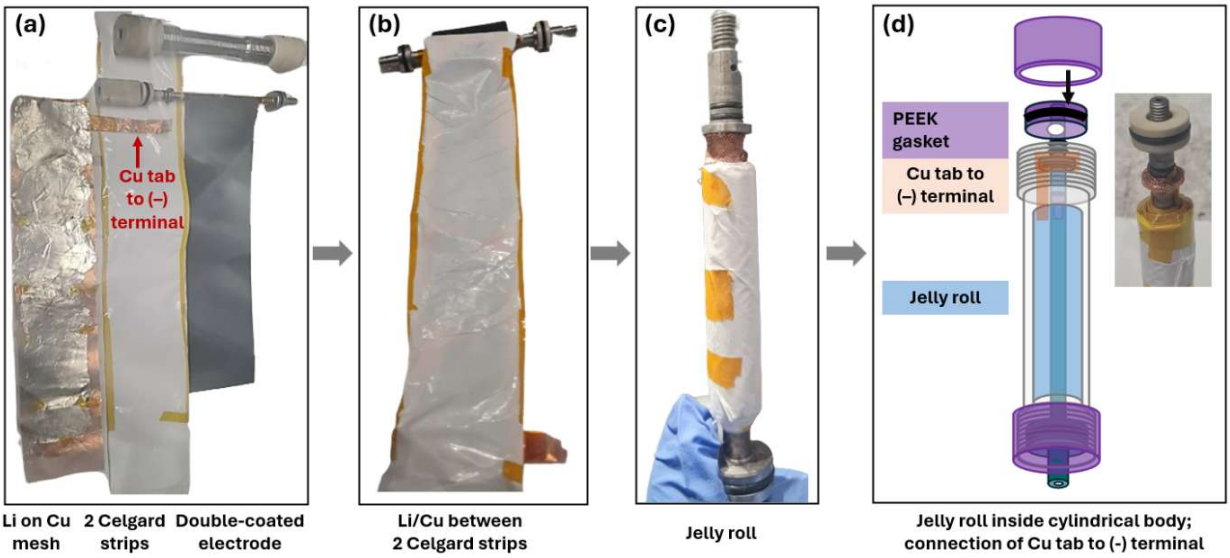

Figure III.7. Assembling procedure of cylindrical cell.

Lithium foil was manually flattened by rolling a glass vial over it to decrease its thickness, yielding foils approximately 200-250 um thick. These foils were then firmly pressed onto the prepared Cu grid to ensure strong adhesion, then the grid is inserted between the two Celgard separator strips. Cell assembly started by connecting the electrode to central rod with Kapton tape for good electrical contact. The remaining components were then attached to the rod in the order: electrode/ separator/ Li on Cu mesh/ separator, and then tightly rolled around it. Careful attention was given to maintain proper alignment of the four-layer stack and ensure sufficient tightness, while avoiding any possible tearing or damage. After verifying the absence of short circuits and fixing the jelly roll in place, the negative tab is connected to the negative terminal as shown in Figure III.7d. Finally, around 2 mL of 1 M $LiPF_6$ in EC:DMC (3:7 by volume) was gradually and uniformly filled in the cell to achieve sufficient electrolyte wetting.

III.2.5. Objectives of this neutron diffraction study

The overall goal of this work is to benchmark complementary instruments and cell configurations for *in situ* and *operando* neutron diffraction of battery materials. Specifically, we aim to (i) compare the performance of two diffractometers at the ILL (D2B and D20), (ii) evaluate two *in situ* cell designs (the coin-type ILLBAT#1 and a cylindrical cell). Our objective is to evaluate these designs in terms of practicality, electrochemical performance, and suitability for different experimental strategies (e.g., slow or fast cycling). This work is intended to identify the opportunities and challenges for making *in situ*/ *operando* neutron diffraction experiments more accessible, cost-effective, and ultimately closer to routine use.

- **Benchmarking of neutron diffractometers**

D2B diffractometer offers high resolution that enables reliable structural refinements, while D20 provides higher intensity and faster data acquisition, making it suitable for following electrochemical reactions in real time. As a proof of concept, we aim to perform the first operando battery experiment on D2B, thereby highlighting how optimized cell designs and instrument capabilities can be combined to improve neutron diffraction studies.

- **Benchmarking of *in situ* cell designs**

The coin-type ILLBAT#1 cell is user-friendly, easy to assemble, wash and reuse. Its design minimizes background contributions and can yield high signal-to-noise data, but this comes at the cost of expensive deuterated electrolytes and slow achievable cycling rates caused by the thick electrode. By contrast, the cylindrical cell accommodates larger electrode loadings with thin coating, which may provide better counting statistics and allow faster cycling, though this remains to be verified. The drawback, however, is additional peaks and background from current collectors, lithium metal, separator, and electrolyte. In this work, we aim to explore whether the larger active-material content in the cylindrical cell can outweigh these drawbacks by providing more dominant diffraction signals and sufficient data quality for structural refinement.

These objectives were realized by using $FeNb_{11}O_{29}$ as a high-rate negative electrode material, tested in half-cell configuration versus Li metal. Both *in situ* cell designs were assembled in this configuration and measured on D2B and D20 at different current rates, which enables the comparison of data quality, electrochemical performance, and suitability for various experimental conditions.

III.3. Reference cell parameters of $FeNb_{11}O_{29}$ from *operando* synchrotron XRD

III.3.1. Experimental

Operando synchrotron X-ray diffraction (SXRD) experiments were carried out on the MCX beamline at the synchrotron Elettra (Trieste, Italy), using the LeRiChe v2 electrochemical cell [153]. Self-supported electrodes were made by mixing dried $FeNb_{11}O_{29}$ powder with carbon additive (Super P, Alfa Aesar) in the 70:20 wt% ratio, followed by the addition of 10 wt% of polytetrafluoroethylene (PTFE, Sigma-Aldrich), and the mixture was pressed into electrode films. The cell was assembled inside Ar-filled glovebox with metallic lithium as counter electrode, glass fiber separator (Whatman grade D) and 1M $LiPF_6$ in EC:DMC (3:7 vol.%, Solvionic) as electrolyte. Two cells were assembled: the first, containing 23.8 mg of $FeNb_{11}O_{29}$, was cycled at a slow rate of C/3, while the second used a lower active mass of 5.95 mg to enable cycling at higher rates of 2.5 C and 5 C. Data were collected in transmission mode at $\lambda = 0.6889$ Å over $2\theta = 2.0 - 29.2°$. *Operando* measurements were performed during the first discharge and charge at the three current rates, with a 10-min voltage hold at the end of each step to promote complete reaction. Backgrounds of the obtained SXRD patterns were subtracted using the same background function to clearly monitor peak shifts, intensity changes, broadening, and the appearance or disappearance of reflections during cycling.

III.3.2. Results and discussion

Figure III.8 illustrates *operando* SXRD patterns of $Li_xFeNb_{11}O_{29}$ during the first cycle at three C-rates: C/3, 2.5 C, and 5 C, along with corresponding voltage profiles and lithium content.

In all three current rates, the smooth and continuous peak shifts confirm the solid-solution behavior of $FeNb_{11}O_{29}$, with no evidence of phase separation or abrupt structural transitions. While this solid-solution mechanism has been reported under slow-rate conditions, this study demonstrates, for the first time, its persistence at significantly higher C-rates for this particular composition. Additionally, the consistent and symmetric evolution of peaks during three discharge/charge cycles indicates that the reversible structural evolution of $FeNb_{11}O_{29}$ is well preserved even under fast cycling. This reversibility is further supported by reversible expansion/contraction of the unit cell: qualitatively by the symmetric shifts of some reflections such as (011), ($\bar{1}$15), and (020), and quantitatively by the reversible evolution of Rietveld-refined lattice parameters (Figure III.9).

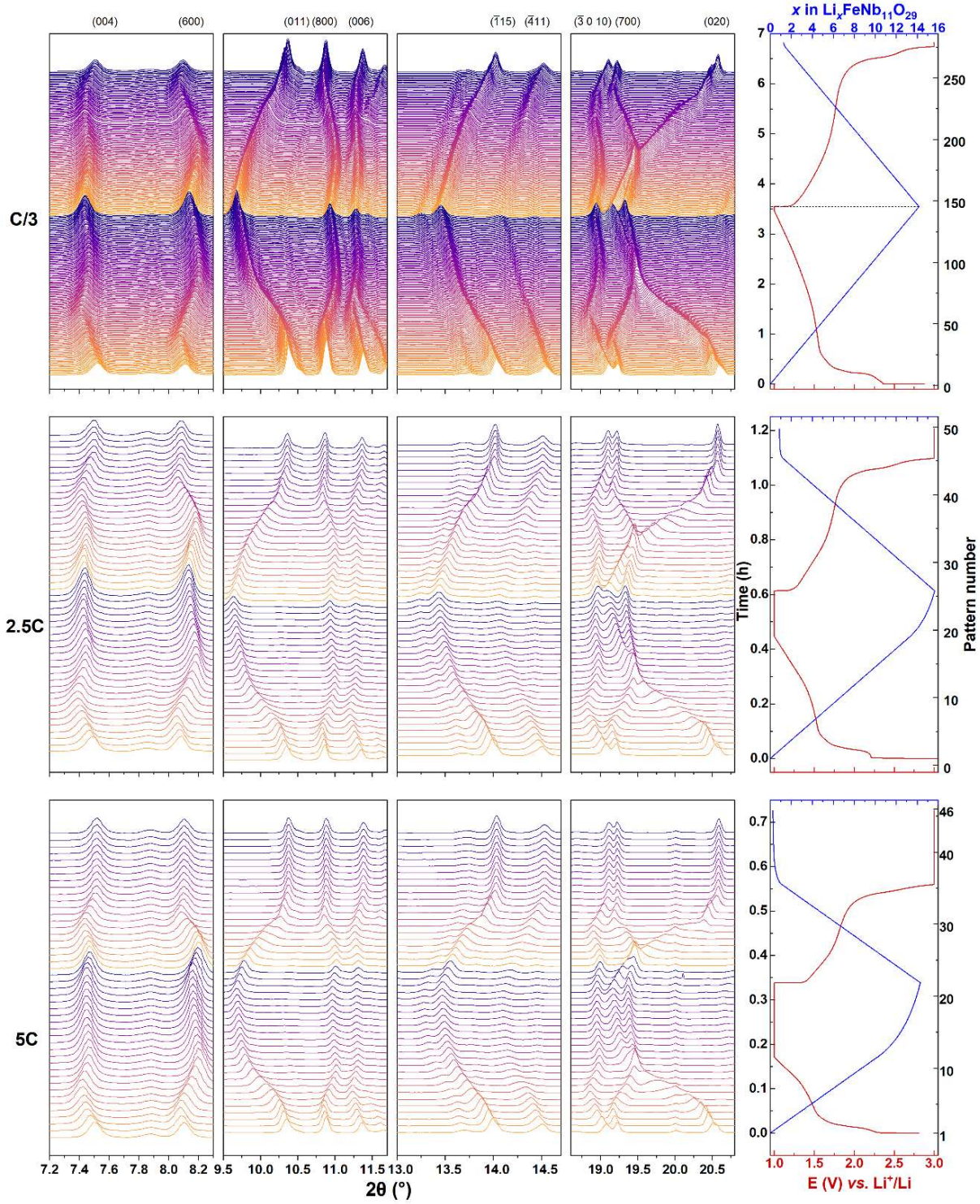

Figure III.8. *Operando* SXRD patterns of $Li_xFeNb_{11}O_{29}$ measured at synchrotron Elettra during the first cycle at C/3, 2.5 C, and 5 C, showing similar peak position evolutions and indicating reversible structural changes even at high rates. Right: voltage profile (red) and Li content x (blue) during cycling.

Overall, these results confirmed the structural robustness and impressive Li^+ transport kinetics of $FeNb_{11}O_{29}$, validating its prospects as a fast-charging negative electrode material.

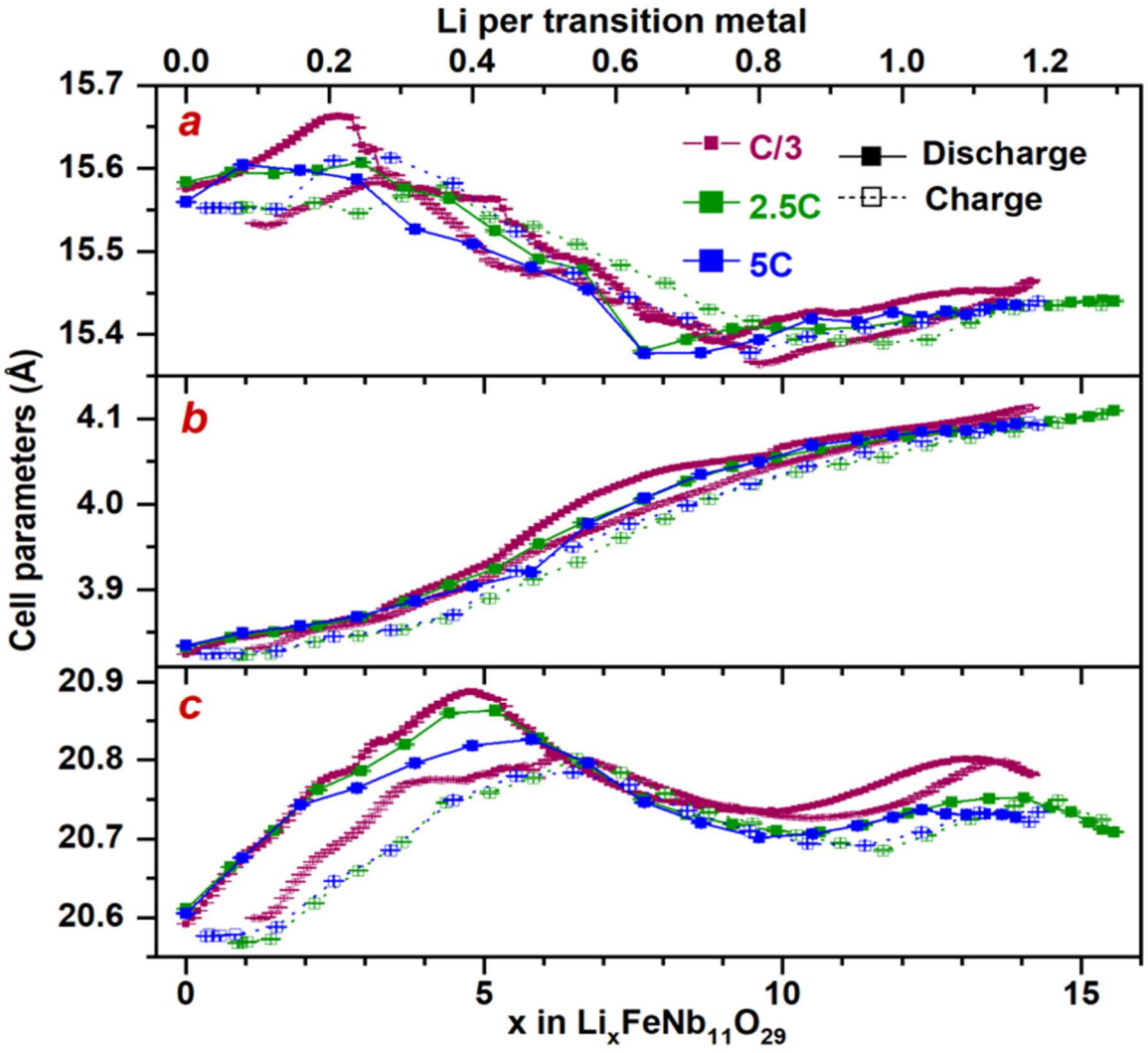

Figure III.9. Cell parameter evolution of $Li_xFeNb_{11}O_{29}$ during the first cycle at C/3, 2.5 C, and 5 C, showing similar and reversible structural changes at different rates.

III.4. *Operando* analysis of $FeNb_{11}O_{29}$ in coin-type and cylindrical cell

III.4.1. Experimental and data analysis

III.4.1.1. Coin-type cell

A self-standing electrode was prepared by grinding 400 mg of $FeNb_{11}O_{29}$, carbon super P and PTFE in 80:10:10 ratio, followed by pressing the mixture into a pellet of around 1 mm thick. The half-cell was assembled using metallic lithium as the counter electrode and 0.4 mL of deuterated electrolyte (1 M $LiPF_6$ in d-EC:d-DMC=1:1 by volume) absorbed in one Whatman glass fiber separator. Neutron diffraction data were collected at D20, with one pattern acquired every 15 minutes while the cell was cycled at C/36 between 0.9 and 3.0 V vs. Li^+/Li.

III.4.1.2. Cylindrical cell

Double-coated electrodes on Cu foil with a high mass loading (~20 mg cm^{-2}) were prepared following similar procedures described in Section II.2.2.5, with a modified formulation of active material: carbon: binder ratio to be 90:5:5 by weight. A total of 3 g of dry mixture ($FeNb_{11}O_{29}$; carbon Super P, Alfa Aesar; PVdF, Solef® 5130) was hand-mixed for 10 minutes, transferred to a polypropylene cup, and dispersed in ~3.5 mL NMP, corresponding to 45% dry mass. The slurry was homogenized in a Kakuhunter planetary centrifugal mixer (SK-300SII) for 12 minutes and then coated onto 0.02 mm Cu foil (Goodfellow) using a 0.4 mm doctor blade gap. The coated foil was air-dried for 2 hours to prevent cracking and adhesion issues, followed by vacuum drying at 80 °C for 12 hours. The same procedure was repeated on the opposite side. The resulting double-coated electrode was calendared to optimize porosity and ensure uniform thickness, cut to 5.5 × 20 cm, and corresponded to ~4 g of active material.

The cylindrical half-cell was assembled as described in Section III.2.4.3 and used for experiments at both D2B and D20 (mounted cells shown in Figure III.10). ND acquisitions of several cylindrical cell components were performed to evaluate their contribution to the total ND patterns. On D2B, 2-hour measurements were conducted for the pristine $FeNb_{11}O_{29}$ powder, $FeNb_{11}O_{29}$-coated Cu foil, as well as the assembled cylindrical cell before and after filling electrolyte. On D20, 5-minute acquisitions were carried out for the same samples, and a strip of Celgard separator.

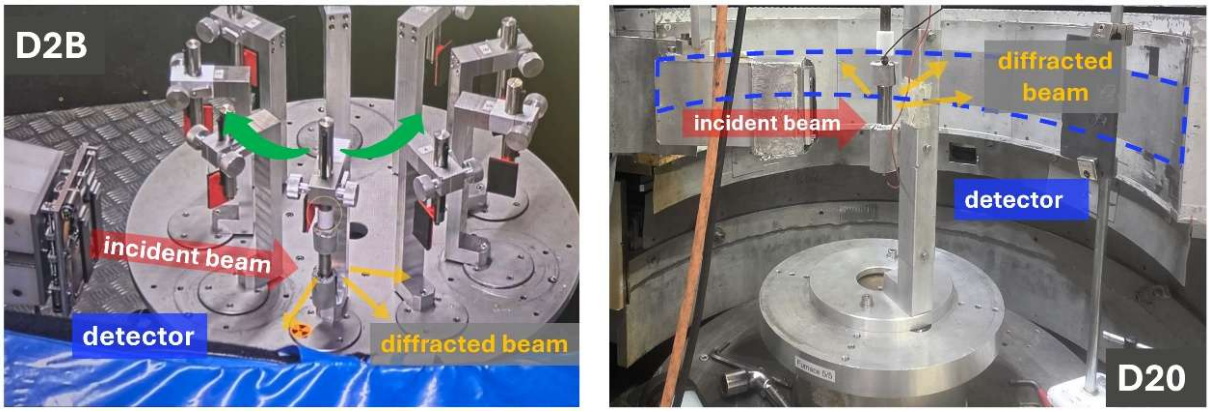

Figure III.10. Cylindrical cell mounted at D2B and D20 diffractometers at the ILL

At D2B, the first discharge followed a sequence of 2 h at C/12 (1 Li^+/h, 17.38 mA/g) and 6 h rest for ND data collection. This sequence was repeated five times to reach different $Li_xFeNb_{11}O_{29}$ compositions (x = 0, 2, 4, 6, 8, 10). To optimize beamtime, the sample stage was rotated to other samples during the 2 h discharge and returned for diffraction at the target compositions. After discharge, the cell was recharged off-beam to restore its initial state for subsequent experiments at D20.

At D20, ND patterns were collected every 5 minutes throughout the entire experiment, which consisted of three discharge-charge cycles at C/12, C/6 and C/2 rates. The first discharge process was conducted stepwise through 11 sequences, each comprising 1 h discharge at C/12 followed by 1 h rest for long ND acquisition of $Li_xFeNb_{11}O_{29}$ compositions (x =0–11). This discharge was followed by a C/12 charge step to restore the initial state. Two further cycles were then conducted at higher rates (C/6 and C/2), with each step of discharge or charge followed by a 30-minute constant-voltage hold to ensure complete reactions.

III.4.1.3. Refinement of ND patterns

For each set of ND data collected under the same configuration and instrument, the patterns exhibited consistent background features. Therefore, a point-by-point interpolated background function was used for each dataset and applied for background subtraction.

Rietveld refinements of the ND patterns were carried out using the FullProf Suite package [154]. For data obtained with the coin-type cell, only the $FeNb_{11}O_{29}$ active material phase was observed and thus considered in the refinement. By contrast, the patterns collected with the cylindrical cell contained three contributions: $FeNb_{11}O_{29}$ (refined by the Rietveld method) as well as the Cu current collector and Li counter electrode, both of which were refined using the Le Bail method (profile matching with fixed scale factors). The validity of Le Bail refinements was justified as the two additional phases (Cu and Li) have little overlap with the main phase.

Several challenges arose during refinement of $Li_xFeNb_{11}O_{29}$ and could not be fully resolved. Attempts to introduce lithium atoms into different sites among 12 possible crystallographic sites produced no significant improvement in the refinement quality of the lithiated compositions. Likewise, the use of Fourier difference maps to identify deficit nuclear densities—which may suggest lithium positions—was unsuccessful, as no clear regions of missing density were observed.

Considering these challenges and given the structural complexity of lithium sites in $Li_xFeNb_{11}O_{29}$, the Li amount of each lithiated composition is equally distributed over all 12 sites (equal Li site occupancies).. The refined parameters for $FeNb_{11}O_{29}$ included the lattice constants (a, b, c, β), scale factor, overall B factor. For Cu and Li phases, zero shift and cell parameters were refined for the first pattern in each series and subsequently fixed for all following refinements.

III.4.2. Comparison of electrochemical cycling in two *in situ* cells

Figure III.11 compares the galvanostatic cycling profiles of $FeNb_{11}O_{29}$/Li half-cells inside coin-type ILLBAT#1, cylindrical and lab-scale coin-cell configurations.

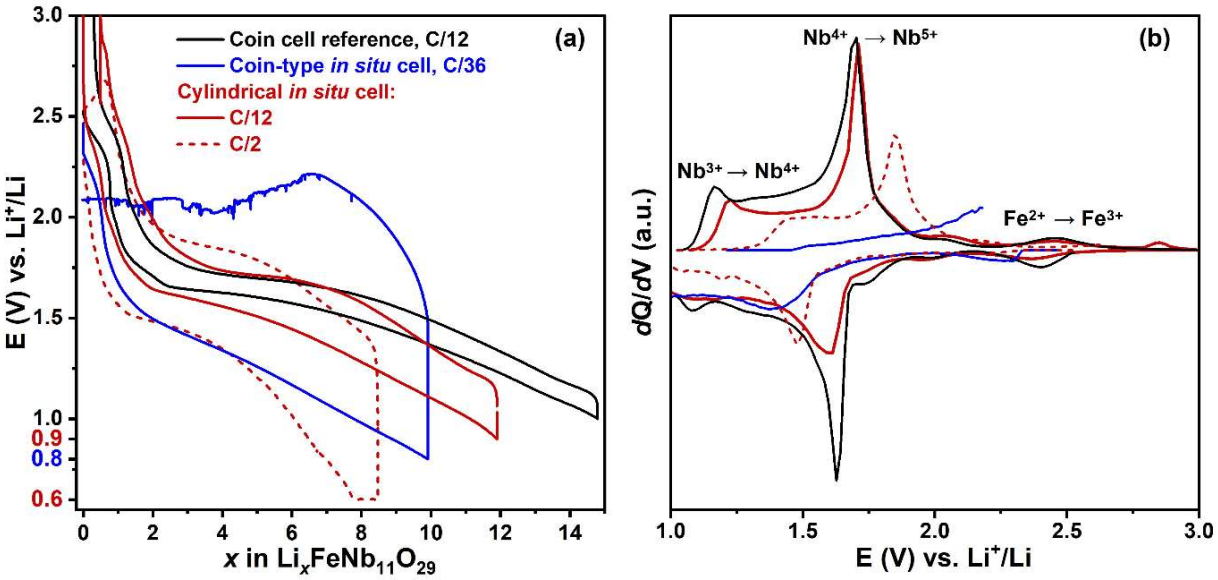

Figure III.11. Voltage profiles (a) and differential capacity curves (b) of $FeNb_{11}O_{29}$/Li half-cells in three different setups, showing stable performance up to C/2 of cylindrical cell, while ILLBAT#1 cell at C/36 suffered from strong polarization and unstable cycling.

Firstly, at the same current rate and comparable mass loading, the cylindrical and coin cells exhibit similar charge-discharge profiles with characteristic sloping features, consistent with *d*Q/*d*V peaks at ~2.4 V, 1.65 V, and 1.3 V, corresponding to $Fe^{3+/2+}$, $Nb^{5+/4+}$ and $Nb^{4+/3+}$ redox couples, respectively. The cylindrical cell enables reversible cycling and delivers a capacity corresponding to ~12 Li^+ per formula unit (f.u.), lower than that of the coin cell (~15 Li^+ per

f.u.). Its voltage profiles show higher polarisation and weaker dQ/dV peaks than the coin-cell reference, which could arise from local inhomogeneities at the rolled edges slight variations in lithium thickness, and an imperfect compaction of the outermost layers of the jelly-roll—effects that are difficult to eliminate completely by manual rolling. Despite these limitations, the cylindrical cell still exhibits modest polarisation (~200 mV) and low internal resistance (~1 Ω, Figure III.12). Increasing the rate to C/6 only led to a slight rise in polarisation and a minor capacity decrease, with approximatively ~10 Li^+ exchanged (Figure III.13). Even at C/2, despite more pronounced polarization, the cell still accommodated ~8 Li^+, highlighting its impressive ability to endure high current while obtaining decent specific capacity. This electrochemical stability was still maintained during prolonged cycling and during *operando* experiments (Figure III.13).

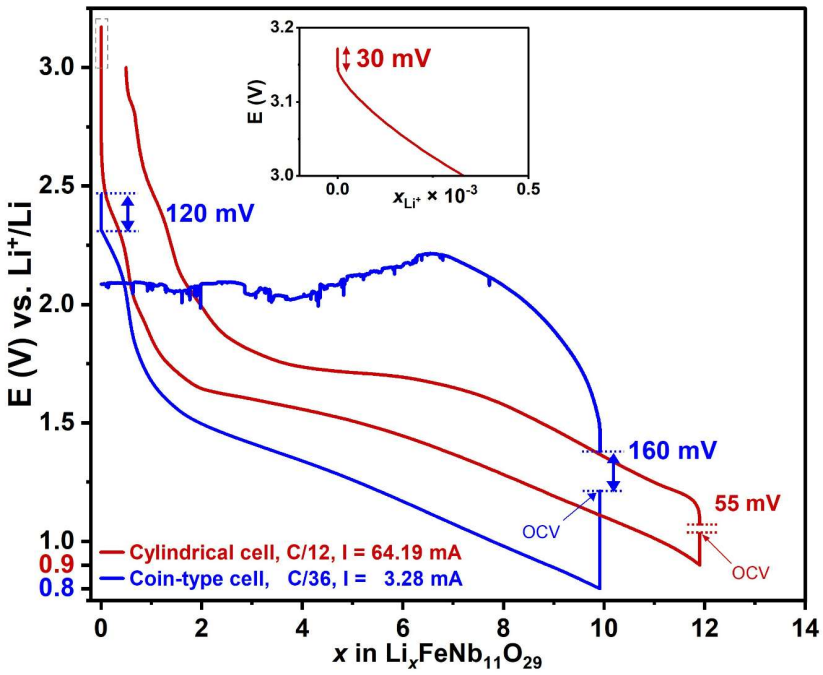

Figure III.12. Galvanostatic cycling curves of cylindrical and coin-type operando cells. The voltage step ΔE at the start of discharge and charge is used to estimate the internal resistance (R = ΔE/I). The cylindrical cell shows a much lower internal resistance (< 1 Ω) than the coin-type cell (~30–50 Ω).

By contrast, the coin-type cell exhibits markedly poorer behavior even at a much slower C/36 rate: lower capacity of ~10 Li^+, large internal resistance (≈ 30-50 Ω), and subsequent voltage instability. These features could be due to unstable contact, electrolyte decomposition and parasitic reactions in the thick self-standing electrode.

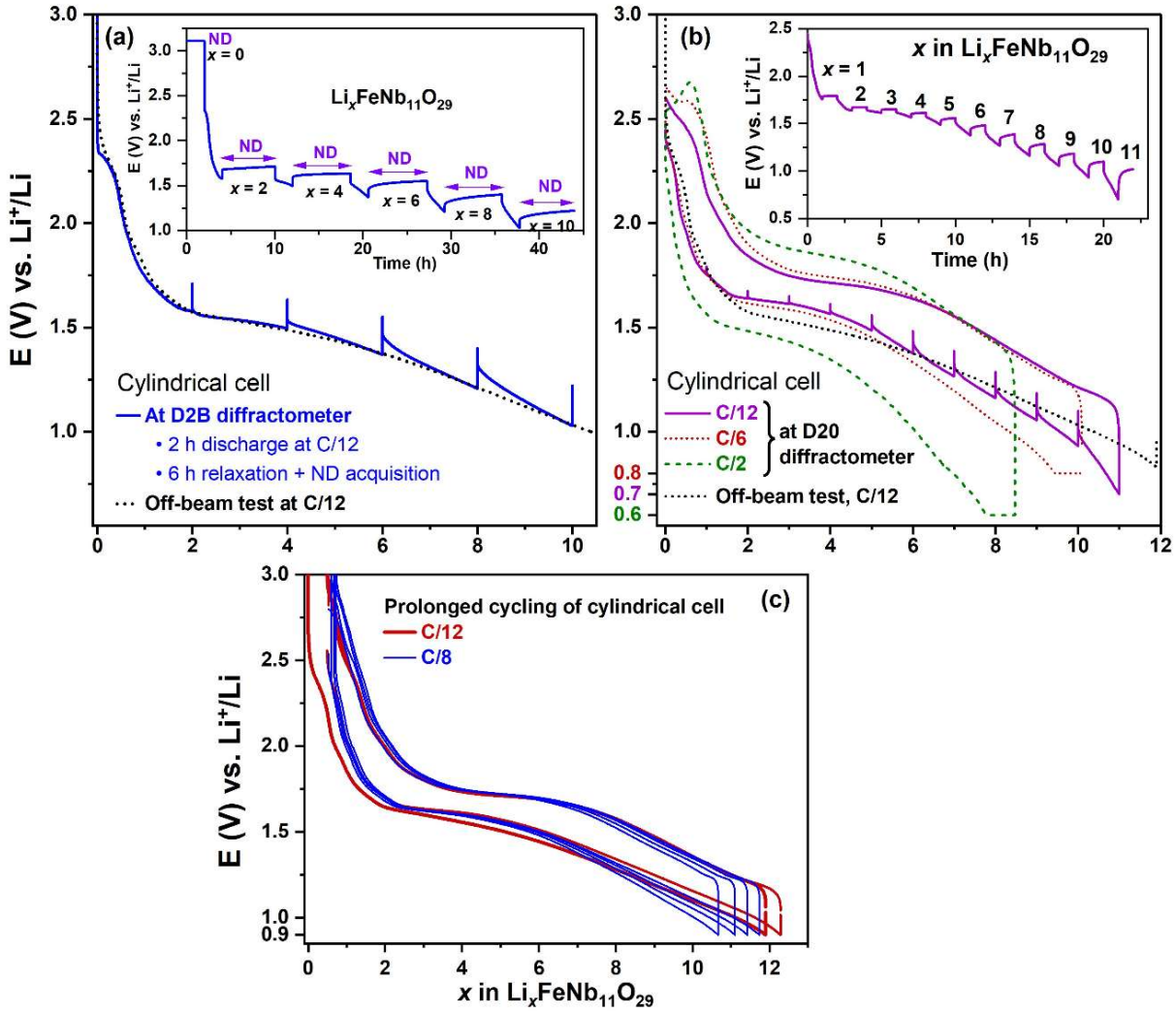

Figure III.13. Charge-discharge profiles of $FeNb_{11}O_{29}$/Li half-cell in cylindrical configuration during *in situ/operando* experiments at (a) D2B and (b) D20 diffractometers, and (c) prolonged cycling test.

III.4.3. Contribution of cell components to ND patterns in cylindrical cell

Figure III.14 presents ND patterns of individual components to compare their contribution to the overall pattern of the cylindrical cell. For $FeNb_{11}O_{29}$ electrodes coated on Cu foil, the Cu reflections dominate the diffractograms regardless of the mass loading. However, at a high loading of 20 mg_{FNO}/cm^2, $FeNb_{11}O_{29}$ signals become significantly strong, with well-defined peaks extending to high Q. This demonstrates the critical role of mass loading in enhancing the signal-to-noise ratio of the active phase. The electrode pattern at high loading also displays comparable $FeNb_{11}O_{29}$ phase intensity as that of the reference powder, both at D2B and D20, confirming the excellent data quality. Additionally, the large quantity of electrode material at this loading enabled high-quality data collection in only 5 minutes at D20.

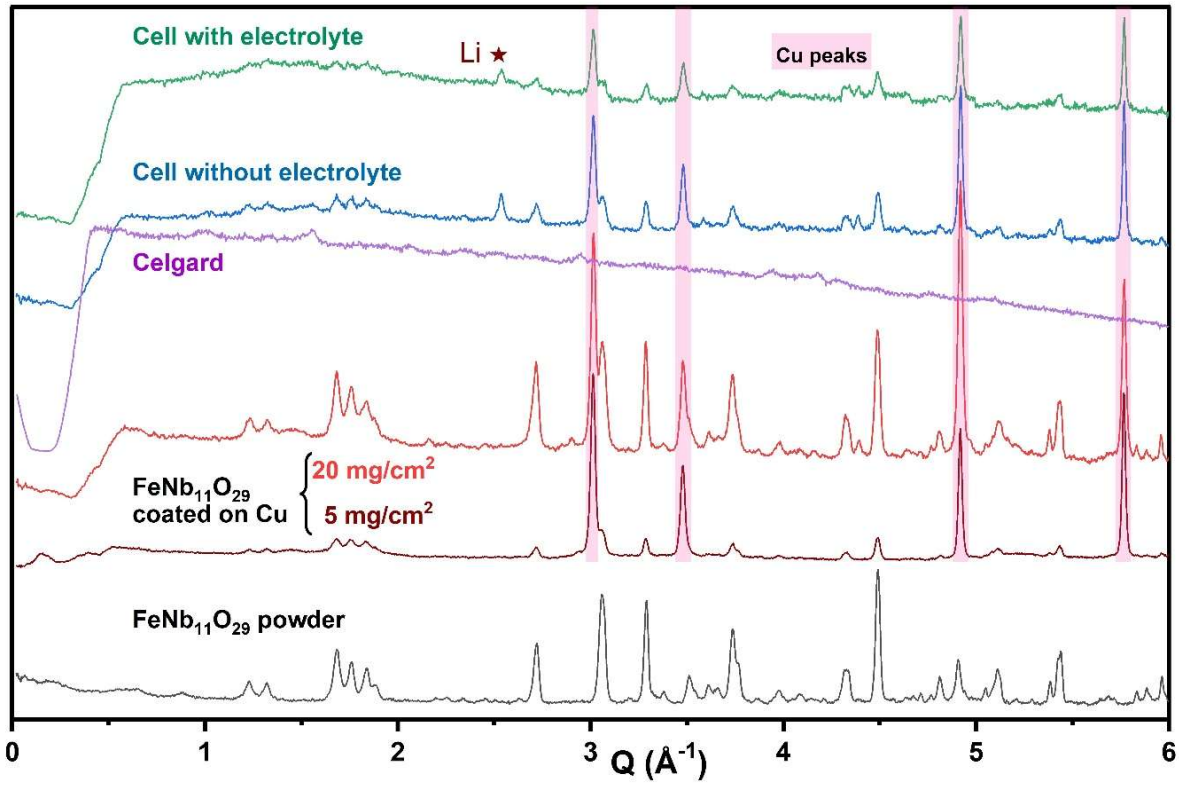

Figure III.14. Comparison of NPD patterns for $FeNb_{11}O_{29}$ powder, some components and the assembled cylindrical cell, obtained at D2B diffractometer in 2 hours (except Celgard, measured at D20 diffractometer in 5 minutes).

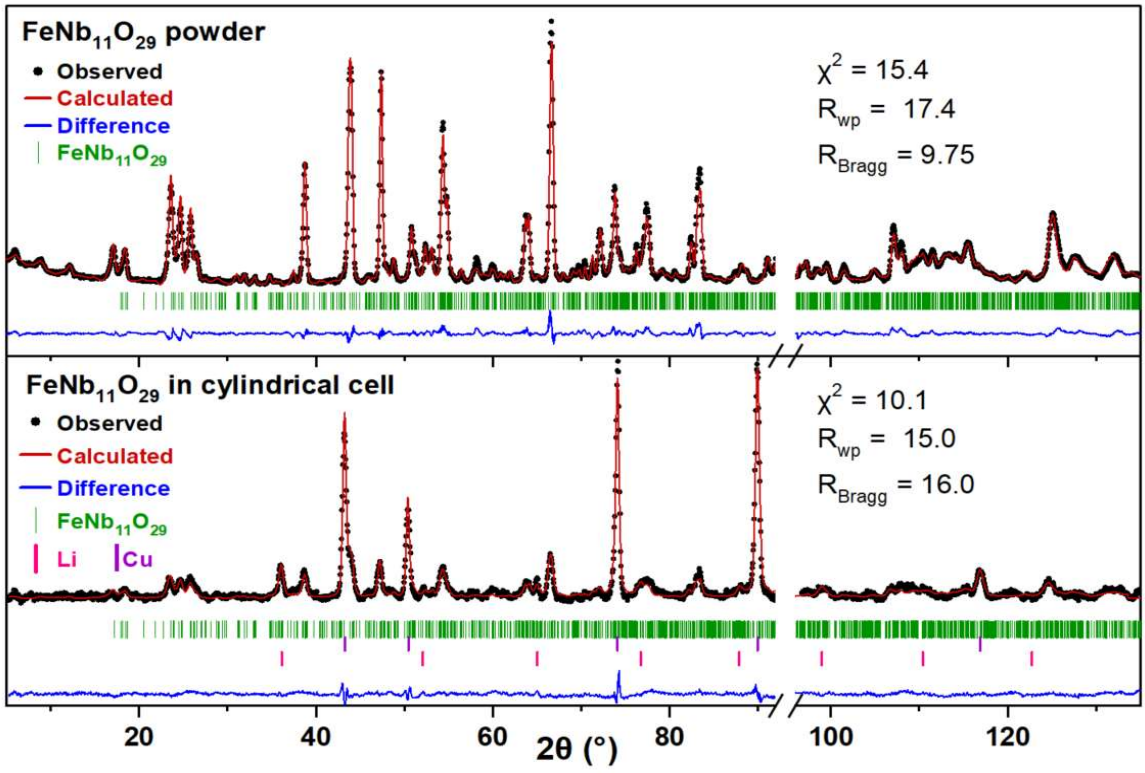

Figure III.15. Rietveld-refined ND patterns obtained at D2B of $FeNb_{11}O_{29}$ powder and cylindrical cell after background subtraction, fitted with $FeNb_{11}O_{29}$ (green), Cu (purple), and Li (pink).

The second component is Celgard separator, containing hydrogen, which significantly contributes to incoherent scattering and high background. However, when the full assembled stack (positive, negative, current collectors and separators) is assembled inside the cylindrical cell without electrolyte, a considerable drop in data quality is observed (blue), with diminished intensity and less resolved peaks. This likely arises from incoherent scattering by the cell components, especially Celgard separator, and strong absorption due to Li metal foil. After filling electrolyte, the signal-to-noise was slightly worsened, where the peaks become suppressed and less defined. However, after careful background subtraction, the data quality remains sufficiently good for Rietveld refinement as shown in Figure III.15 and Table III.2, by including three phases, $FeNb_{11}O_{29}$, Cu and Li.

These findings indicate that the conventional non-deuterated electrolyte is not the primary factor that decreases data quality; rather, the dominant contributions come from other cell components, notably the Celgard separator and the lithium foil. Importantly, a sufficiently high material mass—achieved by high areal loading on thin films—can compensate for these penalties and provide diffractograms of sufficient quality for structural analysis. Regarding perspectives, data quality could be further improved by minimizing the influence of cell components, for example, by adopting alternative separators with reduced background scattering or by using thinner Li foils.

Table III.2. Rietveld refinement results of ND patterns of $FeNb_{11}O_{29}$ phase in cylindrical cell

Neutron diffraction		**$FeNb_{11}O_{29}$**		***A*2/*m***	**Z = 2**	
	a (Å) 15.623(2)	*b* (Å) 3.8494(3)		*c* (Å) 20.694(2)	*β* 113.025(11)°	α = γ = 90°
Atom	Wyckoff position	Atomic coordinates *x*/*a*	*y*/*b*	*z*/*c*	Occ.	B_{iso} (Å^2)
Nb1/Fe1	4*i*	0.0942	0.0	0.0663	0.92/0.08	3.857
Nb2/Fe2	4*i*	0.0846	0.0	0.6912	0.92/0.08	3.718
Nb3/Fe3	4*i*	0.0945	0.0	0.8826	0.92/0.08	3.825
Nb4/Fe4	4*i*	0.3783	0.0	0.1517	0.92/0.08	3.185
Nb5/Fe5	4*i*	0.3725	0.0	0.7805	0.92/0.08	3.292
Nb6/Fe6	4*i*	0.3708	0.0	0.9568	0.92/0.08	3.142
O1	2*d*	0.5000	0.0	0.0000	0.5	6.622
O2	4*i*	0.0649	0.0	0.1665	1.0	4.458
O3	4*i*	0.0884	0.0	0.3667	1.0	4.849
O4	4*i*	0.0788	0.0	0.5873	1.0	4.624
O5	4*i*	0.0763	0.0	0.7773	1.0	6.014
O6	4*i*	0.0809	0.0	0.9855	1.0	6.209
O7	4*i*	0.2263	0.0	0.1075	1.0	5.653
O8	4*i*	0.2259	0.0	0.7267	1.0	5.755
O9	4*i*	0.2186	0.0	0.9169	1.0	4.593
O10	4*i*	0.3653	0.0	0.0516	1.0	4.065
O11	4*i*	0.3510	0.0	0.2479	1.0	6.513
O12	4*i*	0.3510	0.0	0.4514	1.0	5.176
O13	4*i*	0.3581	0.0	0.6641	1.0	4.191
O14	4*i*	0.3555	0.0	0.8610	1.0	5.110
O15	4*i*	0.5017	0.0	0.1901	1.0	4.414
R_{wp} = 12.3%, Bragg R-factor = 19.1%, RF-factor = 14.6%						

III.4.4. Comparison of ND patterns in cylindrical cell obtained at D2B and D20 diffractometer

The comparison between NPD patterns of the cylindrical cell at several $Li_xFeNb_{11}O_{29}$ compositions, obtained at two diffractometers, clarifies the instrumental characteristics (Figure III.16). For a given composition, both diffractometers recorded comparable peak positions and shapes, with closely similar cell parameters from Rietveld refinement. However, some differences between the two datasets could be observed. On the one hand, the patterns obtained at D2B instrument show slightly better separation between $FeNb_{11}O_{29}$ reflections and Cu peaks, e.g. near Q = 3 Å^{-1}. This may come from (i) the intrinsic higher resolution of D2B diffractometer or (ii) the phase relaxation and lithium homogenization within the electrode

during 6 h of rest, evidenced by the noticeable potential equilibration (Figure III.13), making the peaks closer to a thermodynamically stable state. On the other hand, D20 instrument with higher neutron flux enabled the collection of better signal-to-noise data in shorter time, although at the cost of slightly reduced peak resolution. These results confirmed that both instruments can deliver comparable structural information; and the choice between them mainly depends on either the reaction kinetics to be probed or thermodynamics equilibrium.

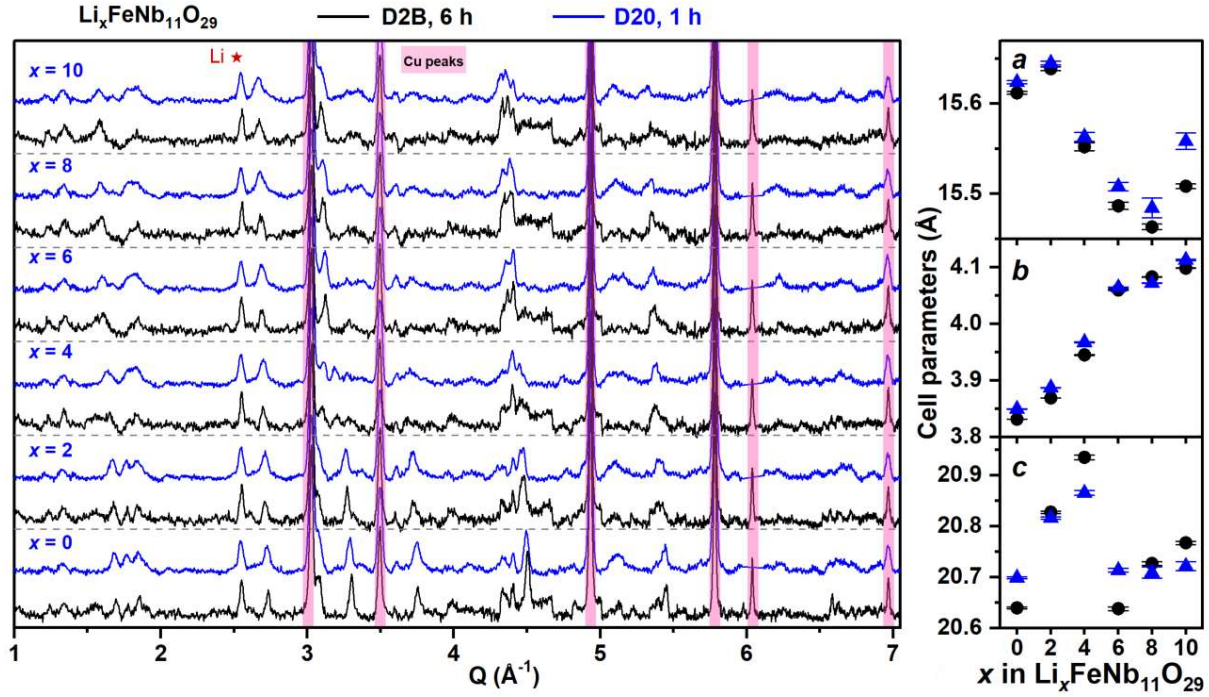

Figure III.16. ND patterns of $Li_xFeNb_{11}O_{29}$ collected on D2B (6 h, black) and D20 (1 h, blue), and the corresponding Rietveld-refined cell parameters. D2B provides higher resolution, especially near Q ≈ 3 Å^{-1} with better peak separation, while D20 offers better signal-to-noise.

III.4.5. *Operando* ND analysis in cylindrical cell at D20 at three current rates

Operando NPD of the cylindrical cell at D20 reveals the structural changes of $FeNb_{11}O_{29}$ at three current rates, together with the electrochemical profiles (Figure III.17). During the initial C/12 discharge, continuous and progressive peak shifts are observed for many reflections, such as (011), (206), (020) and (420), indicating gradual lattice evolution as lithiation proceeds from $x = 0$ to $x = 11$. During the subsequent charge, the Bragg reflections shift back reversibly, with nearly all lithium extracted, and the structure returns close to its initial state. At higher rates (C/6 and C/2), this smooth peak shift behavior is also seen, even though each five-minute acquisition corresponds to larger composition changes, making the patterns slightly less well-defined. Across three cycles, the absence of peak splitting or additional reflections is consistent with a single-phase, solid-solution mechanism [108,120]. Besides, this demonstrates the robust structural reversibility of $FeNb_{11}O_{29}$ at fast cycling, which was also previously reported

[108,120]. Overall, these results highlight the excellent capability of the cylindrical cell to support time-resolved measurements at high currents with good capacity retention.

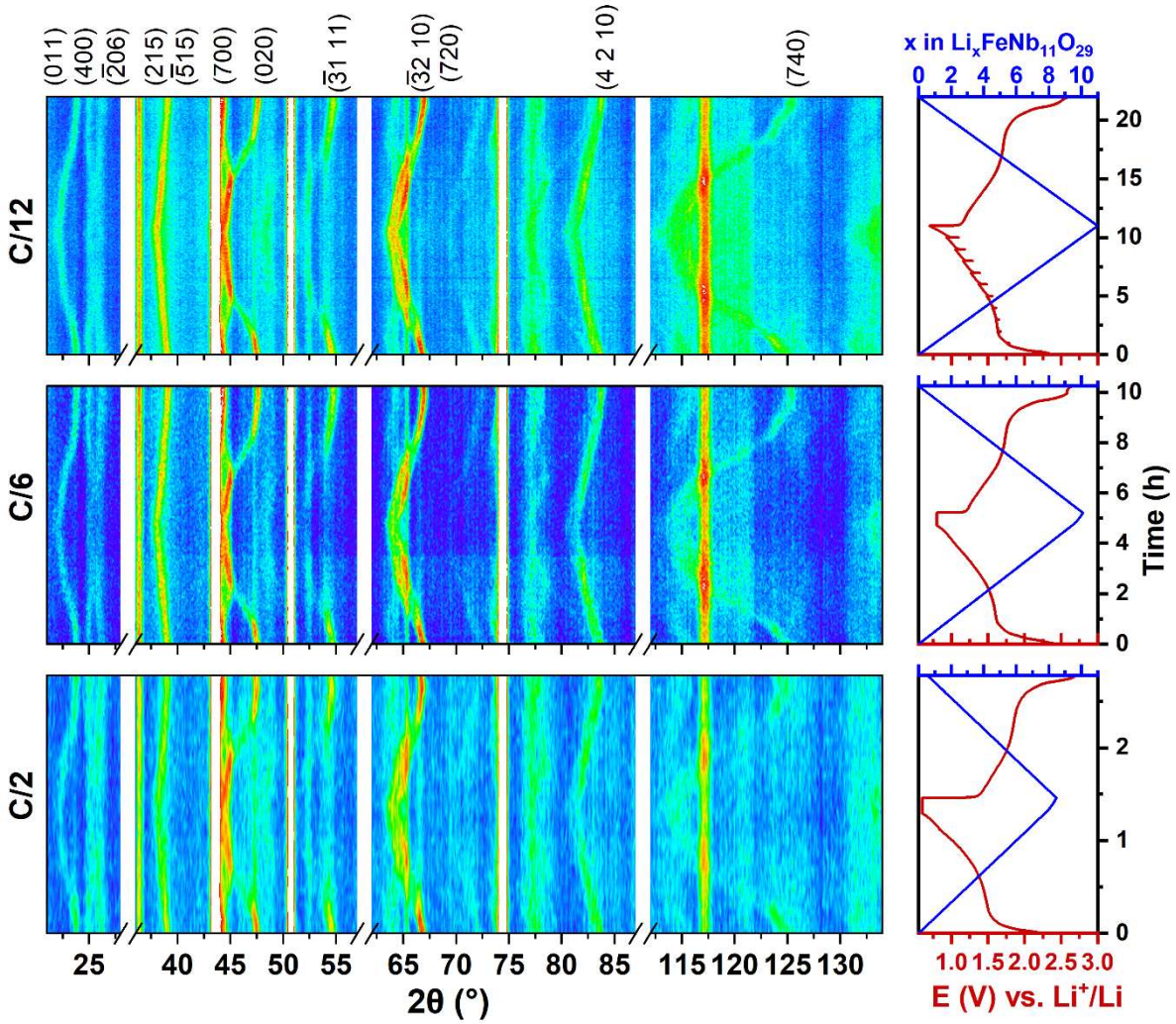

Figure III.17. *Operando* ND contour plots of $Li_xFeNb_{11}O_{29}$ collected at D20 during cycling at three current rates (C/12, C/6, and C/2), and the corresponding electrochemical profiles.

III.4.6. *Operando* ND of $FeNb_{11}O_{29}$ at D20: cylindrical and coin-type cells

Comparative analyses of *operando* NPD data obtained in cylindrical and coin-type cells help to clarify the effect of cell designs on electrochemistry and diffraction data. Note that the detectors were changed between the two experiments (same type, but newly installed). Overall, the NPD patterns of each $Li_xFeNb_{11}O_{29}$ composition collected in two cells exhibit comparable peak positions for most reflections, indicating similar structural transitions and the reliability of the cells (Figure III.18). However, differences could still be observed. For the cylindrical cell cycled at C/12, the contour plots exhibit clear, progressive peak shifts on discharge and a reversible evolution on charge, which are especially evident for the (011), (020), (420), (4 2 10), and (740) Bragg reflections (Figure III.17), similar to the gradual and reversible peak evolutions in Figure III.19.

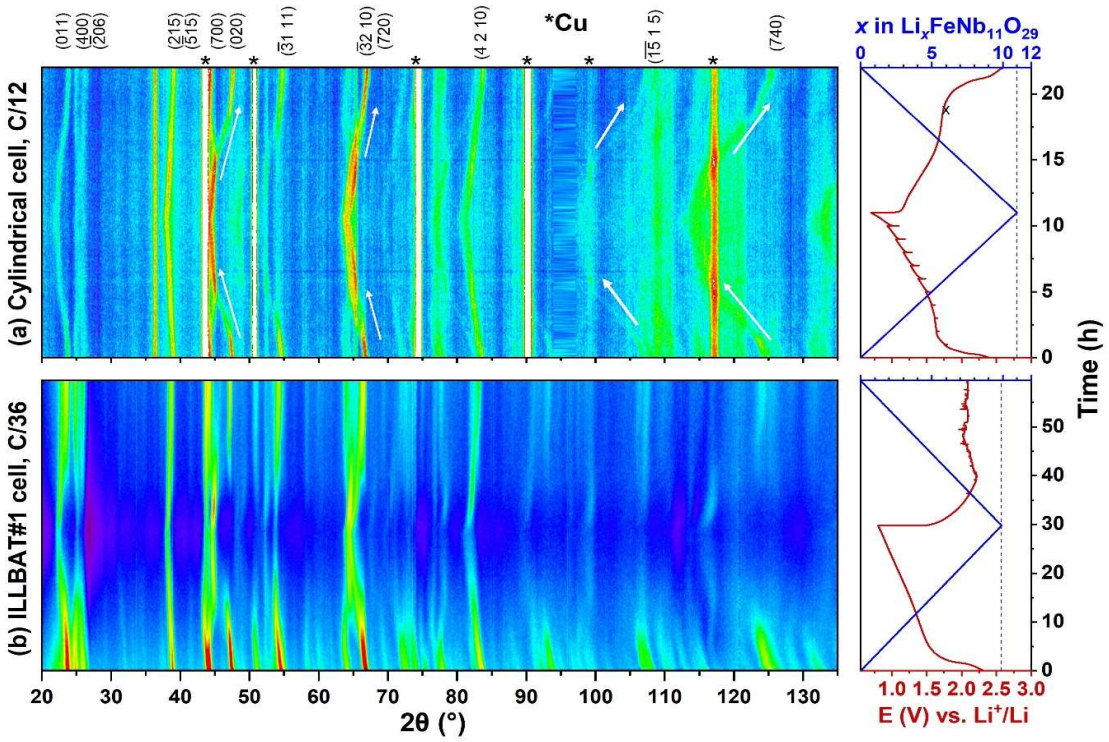

Figure III.18. *Operando* ND contour plots of $FeNb_{11}O_{29}$/Li half-cells at D20 using (a) a cylindrical cell (C/12) and (b) the ILLBAT#1 cell (C/36). Clear peak shifts are observed in the cylindrical cell, while the ILLBAT#1 cell shows weaker or discontinuous changes.

By contrast, analogous features are less evident for the coin-type cell cycled at C/36, both in the stacked patterns and in the contour plot (Figure III.18-19). Firstly, while the peaks still evolve progressively during discharge, this behaviour becomes weaker or discontinuous at the end of charge, e.g. (020) reflection showing almost no shift and only a gradual, incomplete recovery of intensity. Additionally, the peak shape and intensity of ($\bar{3}$ 0 10) and (700) reflections remain nearly unchanged at the end of charge, indicating that the lithiated phase cannot be fully delithiated. After cycling, all reflections exhibit a clear decrease in intensity accompanied by a broadening of their full width at half maximum (FWHM), which suggests the presence of several local lithiation states in the electrode. This could likely arise from the thick self-standing electrode, resulting in inhomogeneous electrochemical reactions and lithium gradient within the electrode volume. Such gradient in lithiation degree. simplified as Li-rich and Li-poor contribution (Figure III.19), could reasonably explain the observations above: subtle peak evolution, incomplete intensity recovery and broadened FWHM at the end of charge. This interpretation is further supported by the contour plots (Figure III.18), where the shifts of some high-angle Bragg reflections, e.g. ($\overline{15}$ 1 5) and (740), while can be unambiguously observed for cylindrical cell, are absent for coin-type cell. These results highlight the impact of electrode configuration on data quality, with the cylindrical cell providing more homogeneous electrochemical reactions and, consequently, clearer structural evolution.

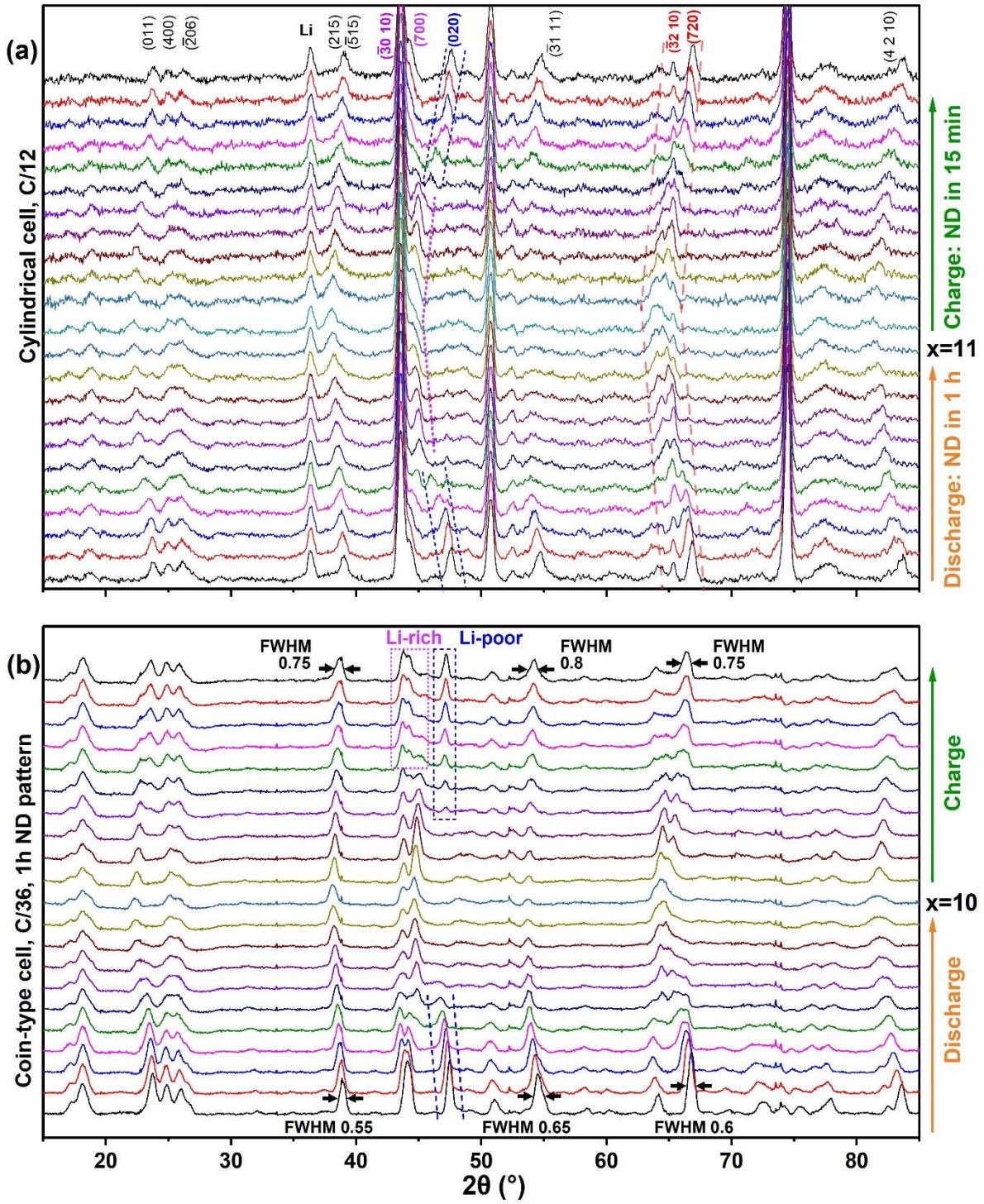

Figure III.19. Stacked ND patterns (15–85° 2θ) from *operando* experiments in (a) cylindrical and (b) ILLBAT#1 cells. The cylindrical cell shows gradual peak shifts and intensity recovery, whereas the ILLBAT#1 cell exhibits abrupt changes and reduced intensities after cycling.

III.4.7. *Operando* ND and SXRD studies of $FeNb_{11}O_{29}$: comparison of cell parameter evolution

Beside the qualitative evaluation, further quantitative analyses allow the comparison of $FeNb_{11}O_{29}$ cell parameters evolution during *operando* NPD experiments in different setups and reference data obtained from SXRD experiment in coin-type cells (Figure III.20). These values were refined by Rietveld method for cylindrical cell ND and SXRD data, while profile matching was used for ND data from ILLBAT#1 cell.

In the cylindrical configuration, the cell parameters evolve with a high degree of consistency across the three current rates (C/12, C/6, and C/2). Their values exhibit closely similar values with reliable standard uncertainties and follow identical trends, suggesting that the structural changes of $FeNb_{11}O_{29}$ during lithiation and delithiation are largely independent from kinetics and demonstrated the excellent ability of the cell to sustain electrochemical reversibility at high currents.

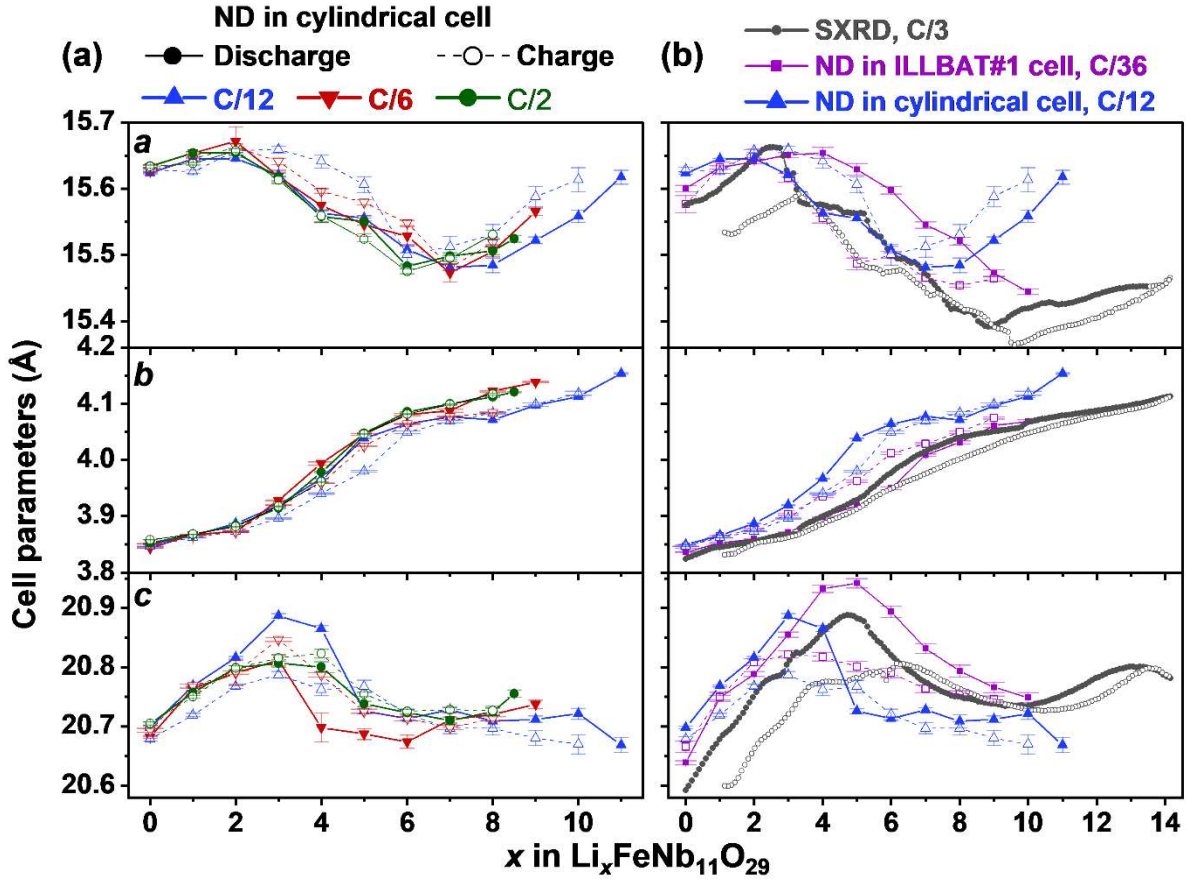

Figure III.20. Cell parameter evolution of $FeNb_{11}O_{29}$ obtained from *operando* ND experiments at D20 in (a) cylindrical at three current rates, (b) compared with results from ND in ILLBAT#1 cell and SXRD experiment. Error bars indicate the standard uncertainties of the refined parameters.

By contrast, comparison with the ILLBAT#1 coin-type cell and SXRD data reveals more noticeable discrepancies in parameter values, even though the overall trends are preserved. The standard uncertainties of the refined parameters, shown as error bars in Figure III.18, are comparable between ND data obtained in two cells, indicating similar reliability of the fits. The consistency in cell parameter evolution in three setups confirms the same underlying solid-solution mechanism, while their deviations highlight the influence of experimental conditions. Key differences include electrode formulation, cycling rate, and, most critically, mass loading and electrode thickness (~0.2 mm for the cylindrical cell versus ~1 mm for the ILLBAT#1 coin-type cell). Thicker electrodes are more likely to have inhomogeneous reactions across the electrode depth, which may introduce local stresses and lead to slight variations in the measured lattice parameters. Despite these discrepancies, the general agreement across the different setups highlights both the robust reversibility of the $FeNb_{11}O_{29}$ structure under varying conditions and the reliability of cylindrical cells for *operando* neutron diffraction studies.

III.4.8. Post-cycling analyses of $FeNb_{11}O_{29}$ in cylindrical cell

To evaluate the homogeneity of electrochemical reactions across different regions of the cylindrical cell, post-cycling ND and XRD measurements were carried out. Firstly, vertical ND scans were conducted on D20 using a 1 cm slit to probe distinct sections of the electrode. Despite the lower signal-to-noise ratios due to reduced probed volume, the characteristic $FeNb_{11}O_{29}$ reflections (marked with asterisks) remained clearly identifiable and appeared at the same 2θ positions across all vertical sections (A–E), as shown in Figure III.21.

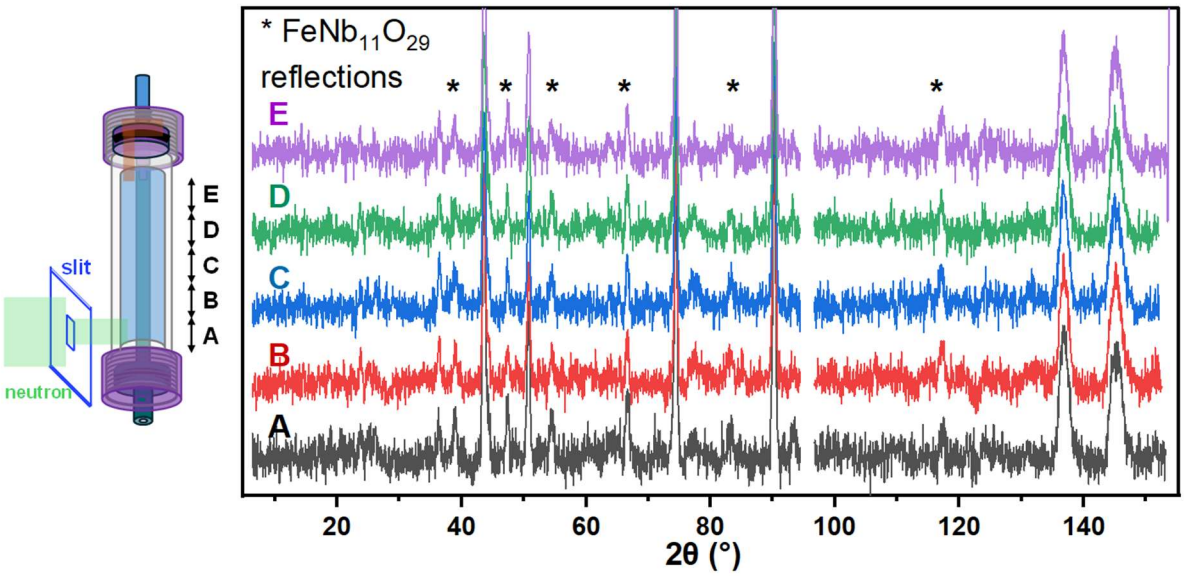

Figure III.21. Vertical ND scans on D20@ILL at different electrode positions (A–E) show consistent $FeNb_{11}O_{29}$ reflections (asterisks), confirming uniform electrochemical reactions throughout the cell.

Complementary post-cycling XRD was performed on electrode discs punched from different positions along the vertical and radial directions of the cylindrical cell (Figure III.22). The analysis reveals nearly identical peak positions and only minor fluctuations in the refined lattice parameters across all sampled regions.

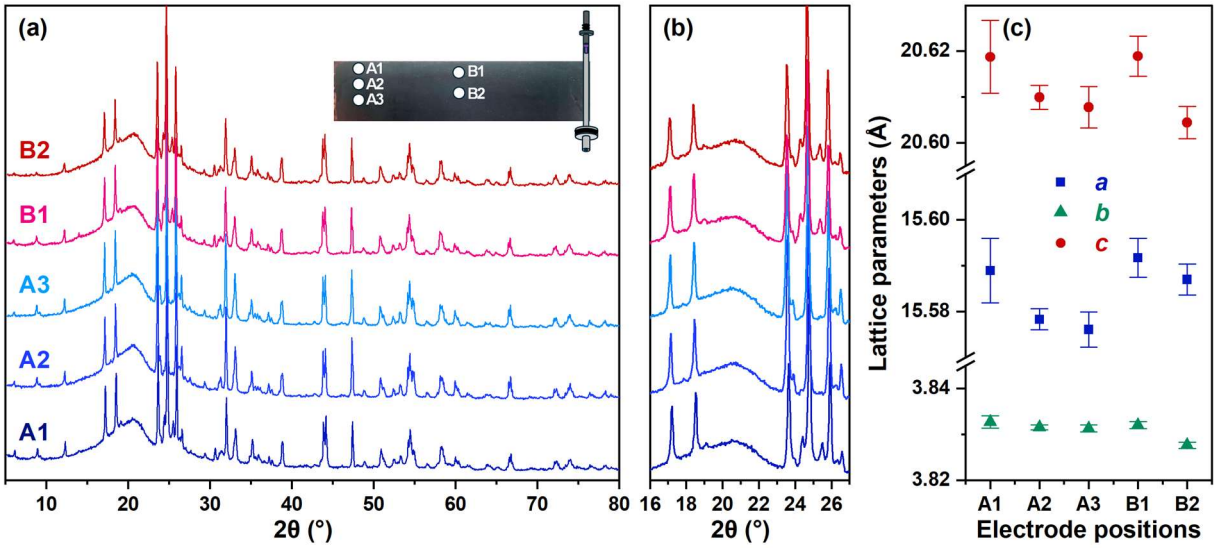

Figure III.22. Post-mortem laboratory XRD from different electrode positions shows nearly identical peak positions and minor lattice variations, confirming structural homogeneity.

Together, these results demonstrate that the $FeNb_{11}O_{29}$ electrode maintains structural homogeneity, with electrochemical reactions proceeding uniformly throughout the cell.

Table III.3. Refined lattice parameters of $FeNb_{11}O_{29}$ electrodes at different positions

Samples	**a (Å)**	**b (Å)**	**c (Å)**	**β (°)**	**χ^2**	**R_{wp}**
A1	15.589(2)	3.8627(5)	20.619(3)	113.030(11)	18.0	6.37
A2	15.5783(8)	3.8315(2)	20.6099(9)	112.9944(13)	7.49	6.13
A3	15.5761(13)	3.8313(3)	20.6078(15)	112.9978(6)	11.2	7.43
B1	15.5917(14)	3.8320(2)	20.6189(15)	113.053(6)	9.70	6.94
B2	15.5870(11)	3.8276(2)	20.6044(12)	113.061(5)	7.01	6.00

III.4.9. General discussions on two *in situ* cells and diffractometers

The findings of this work highlight the complementary characteristics of the two *in situ* cell configurations and diffractometers, each offering distinct advantages and limitations that make them suitable for different experimental purposes.

III.4.9.1. Coin-type ILLBAT#1 cell

The coin-type cell (ILLBAT#1) offers several practical benefits. It is highly user-friendly, as it can be easily assembled, disassembled, cleaned, and reused, which greatly facilitates experiments during beam time at neutron facilities. The entire fabrication process, including self-standing electrode preparation and cell assembly, can be completed from scratch in less than 30 minutes. This cell design is also particularly well suited when only a limited quantity of active material is available, since it requires only 200–300 mg of active material together with a small lithium foil.

To achieve sufficient data quality, however, the use of expensive deuterated electrolytes is essential, around 0.4 mL in this study. By employing hydrogen-free materials (e.g., deuterated electrolytes and glass-fiber separators) and separating the individual cell components, the contribution of inactive parts to the diffraction background is minimized. As a result, the Bragg reflections of the active material dominate, leading to a greatly enhanced signal-to-noise ratio and the acquisition of high-quality diffraction data.

Despite these advantages, several challenges remain. Only a relatively small amount of active material can be cycled reversibly in the cell, which inherently limits the counting statistics. In addition, thick self-standing electrodes tend to cause significant polarization and inhomogeneous electrochemical reactions. Consequently, the cycling performance of the cell is restricted to slow rates (C/24 in previous report [143], and C/36 in this study). Apart from the high cost of deuterated electrolyte, challenges may come from its reduced stability, especially at high voltage, which may not appear in initial cycle but becomes evident upon extended cycling.

III.4.9.2. Cylindrical cell

On the other hand, cylindrical cells can effectively address several of these challenges. First, larger amount of active material can be double coated onto the current collector as thin film, allowing for both homogeneous electrochemistry and sufficient counting statistics, making it possible to make shorter acquisitions of each pattern. Besides, thin electrodes enable faster cycling with lower and acceptable polarization. In this study, reliable structural evolution was observed at C/12 and C/6 and, for the first time to our knowledge, at the substantially higher rate of C/2.

The main drawback of this configuration is that all components of the cell are exposed to the neutron beam, contributing additional signals. This includes not only the metallic current collector for the two electrodes, which are unavoidable, but also lithium metal (in case of half-cell), the separator, and the electrolyte. The current collectors are highly crystalline and therefore give strong diffraction peaks, which may overlap with those of the active materials. Lithium metal gives weaker peaks, but it is a strong neutron absorber. The separator, often Celgard, is a dominant source of incoherent scattering because of its high hydrogen content, as demonstrated by the suppression of active-material peaks even before electrolyte filling. The electrolyte is another major source of background when it contains hydrogen, which contributes strongly to incoherent scattering. These absorption and incoherent scattering effects reduce the number of neutrons available for coherent scattering, leading to higher background and poorer statistics.

However, these drawbacks can be compensated by the large amount of active material, which has proved to give sufficient diffraction signals. Notably, this study demonstrates that acceptable data quality for structural refinements can still be achieved using conventional electrolytes, with background subtraction carefully done. Looking forward, further improvements regarding component signal mitigation could be achieved by selecting alternative separator materials (e.g., alumina or PET, as reported in [151], although they remain difficult to handle), using alternative current collector (V or $Ti_{2.08}Zr$), optimizing lithium foil thickness, and the use of partially deuterated electrolyte.

III.4.9.3. Neutron diffractometers at the ILL

Regarding the diffractometers, their complementary characteristics were also demonstrated in this work. D2B offers high resolution, enabling precise structural refinements, whereas D20 provides the high flux needed to capture fast kinetics in real-time *operando* measurements. In this study, *operando* ND was performed at D2B for the first time, producing patterns with slightly improved resolution compared to D20, while yielding consistent peak positions and cell parameters between both instruments. The major limitation of D2B is its relatively long acquisition time (6 h per pattern herein), which in our case was partly due to the low reactor power during the neutron beamtime. In practice, shorter acquisition times should be achievable by combining higher reactor flux with optimized cell components as discussed above, particularly through reducing hydrogen content (to which D2B is highly sensitive compared to D20) and minimizing absorption effects. Altogether, these results emphasize the complementary features of cell designs and diffractometers and pave the way towards the development of more accessible, cost-effective *in situ* or *operando* neutron diffraction experiments, bringing such measurements closer to routine use.

III.5. Conclusions and perspectives

In this study, we have benchmarked two sets of tools for *operando* neutron diffraction by comparing the cell configurations (coin-type ILLBAT#1 vs. cylindrical cells) and diffractometers (D2B vs. D20) at the ILL. The results highlight the complementary characteristics of each setup. The coin-type ILLBAT#1 cell offers ease of assembly, optimized material usage, and excellent signal-to-noise thanks to its hydrogen-free components, but its electrochemical performance is hindered by high resistance, strong polarization, and limited cycling capability mainly caused by the thick electrode. In contrast, cylindrical cells provide more realistic electrochemistry, larger sample amounts, and faster kinetics, enabling reliable *operando* studies, though at the cost of additional background contributions from cell components.

Similarly, the diffractometers serve different but complementary purposes: D2B delivers superior resolution for precise structural analysis, while D20 provides high flux for fast kinetics and real-time *operando* measurements. *Operando* experiments with cylindrical cells demonstrated continuous and reversible peak shifts during cycling, confirming a solid-solution lithiation mechanism in $FeNb_{11}O_{29}$, with homogeneous electrochemical reactions throughout the electrode even at high rates. Importantly, we showed that conventional electrolytes can still yield data of sufficient quality for structural refinements when paired with careful background subtraction.

Looking forward, these findings open perspectives for making *operando* neutron diffraction a more accessible and routine tool in battery research. Cylindrical cell represents a promising tool for balancing realistic electrochemistry with sufficiently good data quality, especially for investigating high-rate electrode materials by ND. The cell design could be further optimized by reducing parasitic scattering and absorption—for example, through the use of thinner lithium foils, alternative separators with reduced background, optimized current collector thickness, or partially deuterated electrolyte. On the instrumentation side, combined use of D2B and D20 can offer both high-resolution structural details and time-resolved insights, providing comprehensive information of electrochemical reactions.

Chapter IV

Evaluation of $FeNb_{11}O_{29}$ in full-cell configurations

IV.1. Prototyping of $FeNb_{11}O_{29}$ in 18650 full cells

IV.1.1. Current advances of Wadsley-Roth phases in Li-ion full cells

The practical viability of several Wadsley–Roth niobium-based oxides as high-performance negative electrode materials has been demonstrated in full-cell configurations using organic electrolytes and paired with various commercial cathodes. These studies reveal their promising performance, including safety, fast-charging capability, and long-term cyclability.

One of the most remarkable results comes from Takami and co-workers at Toshiba Corporation, who fabricated large-format $TiNb_2O_7$@C/$LiNi_{0.6}Co_{0.2}Mn_{0.2}O_2$ full cells with a capacity of 49 Ah [155]. These cells delivered an exceptional volumetric energy density of 350 $Wh \cdot L^{-1}$, higher than $Li_4Ti_5O_{12}$-based cells, with an ultralong cycle life—retaining 86% capacity after 7000 cycles at 1C. Furthermore, the cells performed excellently under fast-charging conditions, reaching 90% state of charge in 6 minutes at 10C, highlighting the ultrafast Li^+ transport and structural integrity of $TiNb_2O_7$ in large-scale tests.

Another direction is to take advantage of the high-voltage positive electrode $LiNi_{0.5}Mn_{1.5}O_4$ for higher energy density. Han and Goodenough investigated a $TiNb_2O_7$/$LiNi_{0.5}Mn_{1.5}O_4$ system, with a 3 V window and a longer cycle life than cells with a graphite negative electrode [69]. Their study provided insights on capacity balancing, where negative electrode-limited full cell exhibits a better performance than cathode-limited cells. This high-voltage spinel was also paired with $AlNb_{11}O_{29}$ in full cells, which exhibited a high operating voltage of ~3.05 V and a reversible capacity of 136 $mAh \cdot g^{-1}$, maintaining 93.2% capacity retention after 100 cycles at 1C [156].

In addition to their high-rate capability and long cycle life, full cells using $LiFePO_4$ also benefit from excellent thermal stability, contributing to enhanced safety under demanding conditions. For example, $Ti_2Nb_{10}O_{29}$@TiC-C/$LiFePO_4$ full cells exhibited remarkable kinetics and durability at high rates, retaining 125 $mAh \cdot g^{-1}$ at 10 C over 5000 cycles [157]. Besides, $Nb_{14}W_3O_{44}$/$LiFePO_4$ full cells were tested at 50 °C with impressive thermal resilience, delivering 100.5 $mAh \cdot g^{-1}$ after 1000 cycles at 10 C [158].

Overall, these examples highlight the versatility of Wadsley–Roth phases in full cells, which can be tailored for ultrafast charging, high energy density, or long cycle life applications with diverse commercial cathodes. Based on these advances, it is promising to valorize the electrochemical performance of $FeNb_{11}O_{29}$ in practical full-cell configurations. For this purpose, its integration into both 18650-format cylindrical cells and coin cells for degradation studies will be explored. The strengths and limitations of $FeNb_{11}O_{29}$ will be investigated and compared with state-of-the-art systems to assess its suitability for large-scale applications.

IV.1.2. Experimental

All experiments involving 18650 cylindrical cells were carried out at the Laboratoire de Réactivité et de Chimie des Solides (LRCS) in Amiens, in collaboration with François Rabuel and Mathieu Morcrette, during a one-week stay in February 2025.

IV.1.2.1. Large-scale synthesis and characterization

Large-scale solid-state synthesis of $FeNb_{11}O_{29}$ was carried out following similar protocols as described in chapter 2. Around 250 g of Nb_2O_5 (Thermo Fisher, 99.5%) and 13.65 g of Fe_2O_3 ($\geq$ 99 %, < 5 µm, Honeywell) were used as precursors. The powders were put inside a high-density polyethylene bottle (HDPE) with 12 stainless steel balls of 20 mm diameter and mixed by using a Turbula® 3D shaker mixer for 12 hours. The resulting powder was transferred to an alumina crucible, which was subjected to a 6-hour heat treatment at 1100 °C, with a ramping time of 3 hours. Compared with the small-scale synthesis, longer heating (6 hours) was used to ensure complete reaction throughout the larger volume of the sample. The obtained product was ground using the same Turbula® mixer for 4 hours to break the agglomeration and homogenize the powder.

Powder X-ray diffraction of the product was done using Bruker D8 diffractometer with Cu $K\alpha_1$ as the source of radiation. The pattern was collected within the 2theta range of 5 – 70°, with a step size of 0.033°. Scanning electron microscopy (SEM) and Energy Dispersive Spectroscopy (EDX) was carried out using Quanta 200F ESEM-FEG (FEI) microscope.

True density of three electrode components was measured by AccuPyc 1300 helium pycnometer (Micromeritics). True density only takes into account the volume of the particles, without considering the voids or space between them.

IV.1.2.2. Fabrication process of 18650-format cells

Figure IV.1 illustrates the fabrication process of 18650 cells, including slurry preparation, electrode coating and calendaring, winding, and final assembly with electrolyte filling

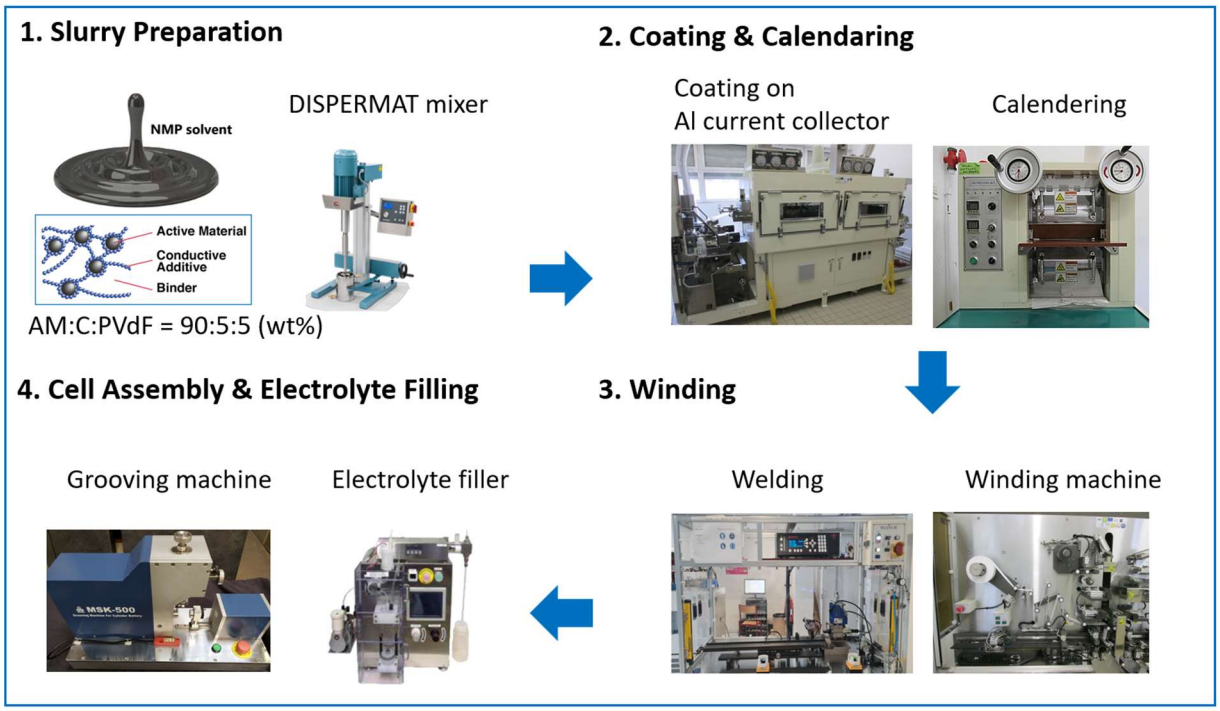

Figure IV.1. Fabrication process of 18650 cells involves slurry mixing, coating and calendaring, electrode winding, and final cell assembly with electrolyte filling

IV.1.2.2.a. Slurry preparation

Cell fabrication begins with slurry preparation, which requires homogeneous particle size of the active material for uniform coatings. A home-made sieving tool was used, consisting of a 100 µm mesh fixed to an HDPE bottle connected to a vacuum pump, with a beaker inside to collect the filtered material. Since $FeNb_{11}O_{29}$ is stable in water, a suspension of 200 g in ~200 mL deionized water was prepared, mixed, sieved through this setup, and dried for two days.

As in small-scale electrode casting, the slurry typically consists of active material, conductive carbon, and binder dispersed in solvent, then coated onto a metallic current collector foil (aluminium or copper, depending on the system). For $FeNb_{11}O_{29}$, which operates above 1.0 V vs. Li^+/Li, aluminum is preferred as a cheaper, lighter alternative to copper, while avoiding alloying with lithium. However, with aluminum, water-based slurries can induce corrosion, so NMP is preferred.

In a typical slurry preparation, 200 g of dry mass was used, composed of $FeNb_{11}O_{29}$, carbon black and PVdF in 90:5:5 weight ratio. A suitable amount of NMP is added to reach 50 – 55% dry mass. The dry mass percentage depends on the target mass loading, density, particle size and morphology of active material, casting blade gap, and solvent wetting properties. This mixture was then subjected to an efficient stirring, dispersing process inside the planetary Dispermat mixer (VMA-GETZMANN, model CV3-plus).

IV.1.2.2.b. Electrode coating and calendaring

The electrode coating step was carried out using a coater machine in the prototype platform of LRCS. This equipment enables the homogeneous deposition of slurries on both sides of the collector, and drying was done using two independent rollers with controlled airflow and controlled temperatures. At first, several trials of small coating were conducted with different gaps of doctor-blade to establish a calibration curve that relates the mass loading and the gap. From this calibration, a suitable gap for the target mass loading can be chosen.

The obtained electrodes are subjected to calendering, using a BPN-250 calendering machine (People and Technology Inc.). Calendering improves the adhesion of the electrode material to the current collector, which is essential for maintaining mechanical integrity during cycling. It also optimizes the balance between electronic conductivity and ionic transport within the electrode. Additionally, this process increases both the gravimetric and the volumetric energy density of the electrode, thereby enhancing the overall performance of the battery.

Positive electrodes of $LiNi_{0.6}Co_{0.2}Mn_{0.2}O_2$ (NMC622, denoted as NMC herein) were pre-fabricated by LRCS and paired with $FeNb_{11}O_{29}$ electrodes for full-cell assembly.

IV.1.2.2.c. Winding of jelly-roll cell

The electrodes are cut into strips of 5.6 cm in width and around 50 cm in length. The exact length of the positive and negative electrodes was adjusted to attain a target negative-to-positive (N/P) mass balance. Subsequently, a nickel-plated aluminum tab was welded onto one end of each electrode for the connection to the cylindrical can.

The next step involves winding the four layers—negative electrode, separator, positive electrode, and a second separator—into a tightly rolled cylindrical jelly-roll structure, using a semi-automatic winding machine. This equipment ensures precise alignment, consistent tension of the layers, while preventing short circuits. The jelly rolls were inserted into 18650-format casings. This format, 18 mm in diameter and 65 mm in length, was first introduced by Sony in 1991 and has become a widely adopted standard for lithium-ion cells.

For one three-electrode cell, a reference electrode made from a small $LiFePO_4$ strip coated on Al foil, wrapped in a Celgard separator for electronic insulation, was inserted into the jelly roll during the winding step. After cell assembly, a specific preconditioning step was applied: the $FeNb_{11}O_{29}$ and $LiFePO_4$ electrodes were precharged until around half of $LiFePO_4$ is delithiated, bringing the reference to its two-phase $LiFePO_4/FePO_4$ plateau at 3.45 V vs Li^+/Li.

IV.1.2.2.a. Cell closing and electrolyte filling

Afterwards, spot welding was carried out to electrically connect the electrode terminal tab to can's poles. This was followed by grooving, which creates a small inward indentation or "groove" near the top of the can, to lock the cap and gasket in place.

Subsequent processes were carried out inside the dry room, with a dew point of at least -40 °C, corresponding to very low relative humidity (RH). The cell was dried at 80 °C under vacuum for four days, then filled with commercial LP30 electrolyte. Finally, the cell was crimped to ensure airtight sealing, preventing electrolyte leakage and moisture intake.

IV.1.2.3. Electrochemical cycling

Two $FeNb_{11}O_{29}$/NMC full-cells were assembled and subjected to various electrochemical protocols below. Nominal capacity C is calculated based on the theoretical capacity of NMC positive capacity.

- Formation protocol: one initial cycle at C/20, followed by five cycles at C/5.
- Asymmetric rate tests

These tests compare the kinetics of Li^+ insertion and extraction by fixing either charge or discharge current while progressively increasing the other.

  - D-rate test: The charge current was fixed at C/5, while the discharge current was progressively increased every five cycles (D/5 → D/2 → 1D → 2D → 3D → D/5).
  - C-rate test: The discharge current was fixed at D/5, while the charge current was progressively increased every five cycles (C/5 → C/2 → 1C → 2C → 3C → C/5).
- Alternating slow/fast cycling

A repeated cycling sequence was used, consisting of one slow cycle (charge at C/5 and discharge at D/5) followed by ten fast cycles (1C/1D). This sequence was repeated 20 times.

- Constant power discharge test:

The cells were discharged at a fixed power (12 W), where the potentiostat continuously adjusts the current in response to the changing voltage to maintain constant power output ($P = E \times I$) until a voltage cutoff was reached. This approach allows the evaluation of energy delivery under different power loads, represented in a Ragone plot of energy density vs. power density.

For comparison, these tests were also performed on two $Li_4Ti_5O_{12}$/NMC full-cells, assembled from the same batch of NMC electrodes, and commercial $Li_4Ti_5O_{12}$ material (Targray).

IV.1.3. Results and discussion

IV.1.3.1. $FeNb_{11}O_{29}$ phase purity and elemental distribution

The XRD patterns of $FeNb_{11}O_{29}$ obtained from large-scale synthesis show high crystallinity, with characteristic peaks similar to those of small-scale samples, except for one unidentified impurity peak at around 31° (Figure IV.2a).

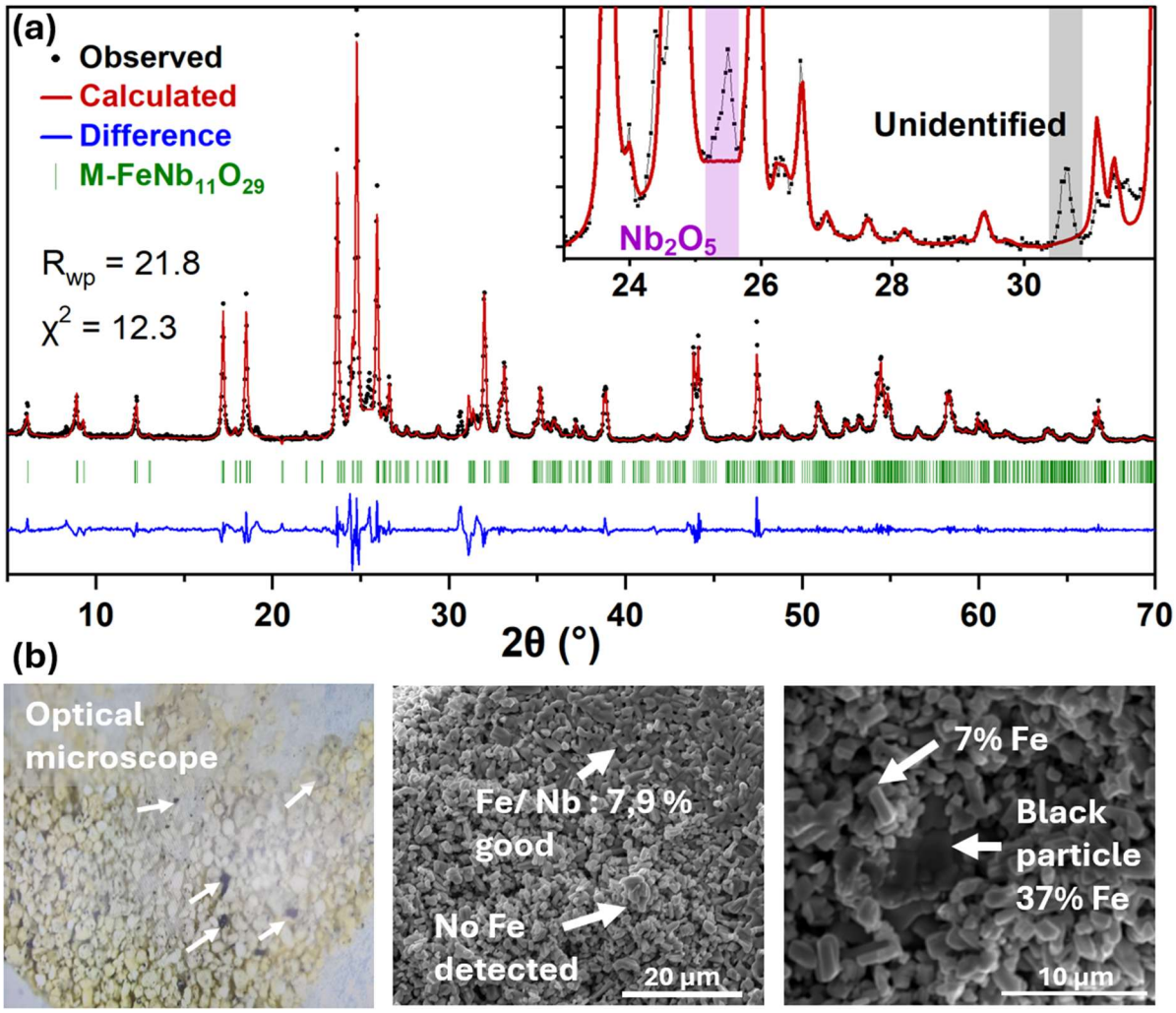

Figure IV.2. (a) Le Bail-refined XRD pattern of $FeNb_{11}O_{29}$ synthesized in a 250 g batch, with minor impurities (Nb_2O_5 and an unidentified phase). (b) Optical and SEM images showing inhomogeneous Fe distribution.

EDX analysis (Figure IV.2b) revealed inhomogeneous Fe distribution in large-scale $FeNb_{11}O_{29}$ powder. Some particles showed an Fe/Nb atomic ratio of 7.9%, close to the theoretical 9%, while others contained only trace Fe, likely due to insufficient mixing. Small black particles, observed by eyes and more visible under optical microscopy, showed up to 37 at.% Fe from EDX analysis, suggesting iron-based compounds from steel milling residues and/or unreacted Fe_2O_3 precursors. These impurities and uneven Fe distribution highlight the need for more effective precursor mixing to improve product purity.

IV.1.3.2. Electrode characteristics

Figure IV.3 shows how the electrode quality was improved via sieving of active materials, and the electrode properties are shown in Table IV.1. Prior to sieving, the inhomogeneous particle sizes of active material led to uneven slurry dispersion, resulting in non-uniform electrode thickness during coating. Such inhomogeneity significantly may affect subsequent cell fabrication steps, including (1) bent and wavy electrodes after calendaring due to uneven compaction, (2) misalignment during electrode winding, and (3) non-uniform current densities during electrochemical cycling, which can compromise cell performance.

To address these issues, a sieving step (<100 µm) of $FeNb_{11}O_{29}$ and $Li_4Ti_5O_{12}$ was introduced before electrode coating. The improvement was significant for $FeNb_{11}O_{29}$. Sieving $FeNb_{11}O_{29}$ powder in water led to considerably improved electrode coatings: smooth, defect-free, low porosity, and more uniform in thickness. This confirms that sieving enhances electrode uniformity and manufacturability, essential for reliable 18650 cell production.

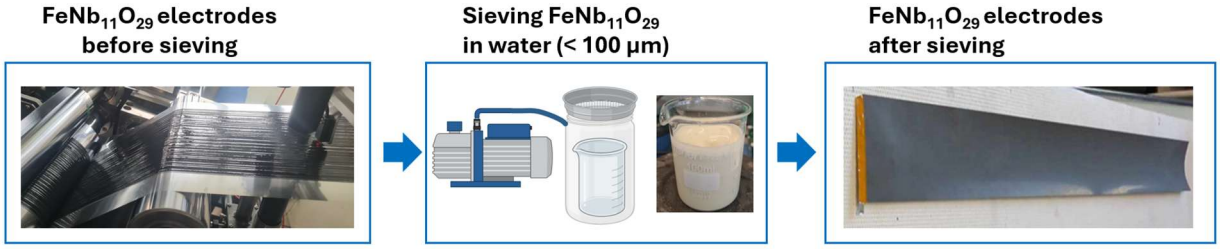

Figure IV.3. Improvement of electrode quality via material sieving: from inhomogeneous to uniform coating

Table IV.1. Electrode properties, including mass loading (per side), formulation, thickness, and porosity for $Li_4Ti_5O_{12}$, $FeNb_{11}O_{29}$, and NMC electrodes

	Active material (AM)	Mass loading/2 (mg cm^{-2})	Formulation (AM: C: PVdF)	Thickness (µm)	Porosity (%)
1	$Li_4Ti_5O_{12}$	~22	90:5:5	~280	~43.5%
2	$FeNb_{11}O_{29}$	~16	90:5:5	~150	~46.0%
3	NMC622	~20	92:4:4	~155	~35.0%

IV.1.3.3. Comparison of full-cell properties

Table IV.2 summarizes the cell-level characteristics of three full cells using $FeNb_{11}O_{29}$, $Li_4Ti_5O_{12}$, and graphite as negative electrode materials, each paired with an NMC positive electrode. All cells were assembled and tested at LRCS. Note that graphite/NMC cells, in particular, had been repeatedly tested and optimized at LRCS earlier to reach their best-performing state.

Table IV.2. Characteristics of full cells using $FeNb_{11}O_{29}$, $Li_4Ti_5O_{12}$, and graphite, paired with NMC cathodes

Parameters	$FeNb_{11}O_{29}$ /NMC	$Li_4Ti_5O_{12}$ /NMC	Graphite /NMC	Units
Specific capacity of negative electrode	240	175	420	mAh g^{-1}
Density of negative active material	4.5	3.4	2.2	g cm^{-3}
Cell-level discharge capacity (C/5)	1.8	1.2	1.7	Ah
Average Potential (discharge)	2.2	2.18	3.58	V
Specific energy (full cell)	94.3	66.5	152	Wh kg^{-1}

The discharge capacity of $FeNb_{11}O_{29}$/NMC cell after formation is comparable to that of graphite/NMC cell. While $FeNb_{11}O_{29}$ exhibits a lower specific capacity than graphite (240 vs. 420 mAh g^{-1}), its significantly higher density (4.5 vs. 2.2 g cm^{-3}) compensates this difference, contributing to higher mass loading of $FeNb_{11}O_{29}$ electrodes. In terms of specific energy at the cell level, $FeNb_{11}O_{29}$ (94.3 Wh kg^{-1}) lies between $Li_4Ti_5O_{12}$ (66.5 Wh kg^{-1}) and graphite (152 Wh kg^{-1}), offering a balanced compromise. Overall, $FeNb_{11}O_{29}$ presents a promising alternative as a negative electrode material by combining moderate specific capacity with high density, resulting in intermediate energy density between $Li_4Ti_5O_{12}$ and graphite.

IV.1.3.4. Alternating slow/fast cycling

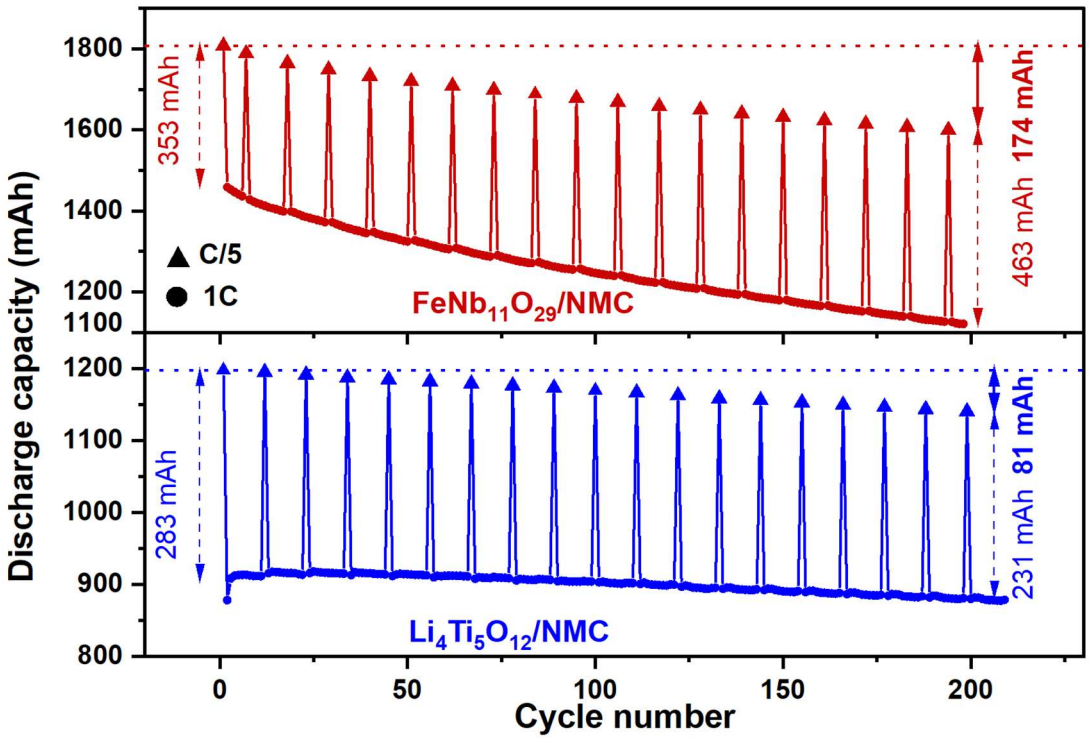

Figure IV.4. Discharge capacities of $FeNb_{11}O_{29}$/NMC and $Li_4Ti_5O_{12}$/NMC cells under alternating C/5 and 1C cycling over 200 cycles. Dashed arrows indicate capacity difference between C/5 and 1C before and after 200 cycles, while solid arrows show capacity fade at C/5.

Figure IV.4 compares the discharge capacities of $FeNb_{11}O_{29}$/NMC and $Li_4Ti_5O_{12}$/NMC cells under alternating C/5 and 1C cycling over 200 cycles. For $Li_4Ti_5O_{12}$, the difference in capacity between 1C and C/5 decreases after 200 cycles (from 283 to 231 mAh at C/5 and from 81 to 113 mAh at 1C), indicating reduced polarization. This behavior suggests that additional $Li_4Ti_5O_{12}$ becomes electrochemically accessible over time, possibly due to improved electrolyte penetration. However, the overall capacity still declines slightly.

In contrast, $FeNb_{11}O_{29}$ shows increased polarization over 200 cycles, as reflected in the growing capacity gap between 1C and C/5 rates (from 353 to 463 mAh). This indicates greater degradation, likely arising from lithium loss associated with SEI reformation, side reactions due to the presence of impurity phases.

IV.1.3.5. Asymmetric rate tests

Figures IV.5 and IV.6 compare the kinetic behavior of Li^+ insertion and extraction in $FeNb_{11}O_{29}$/NMC in comparison with $Li_4Ti_5O_{12}$/NMC full cells under varying current rates.

In Figure IV.5, asymmetric rate cycling tests reveal that $FeNb_{11}O_{29}$ exhibits slightly better capacity retention during Li^+ extraction (67.2% at 3D) than during Li^+ insertion (65.8% at 3C), suggesting that insertion is more kinetically limited. This is accompanied by more severe heating during insertion (up to 60 °C at 3C), indicating increased polarization and sluggish charge-transfer kinetics.

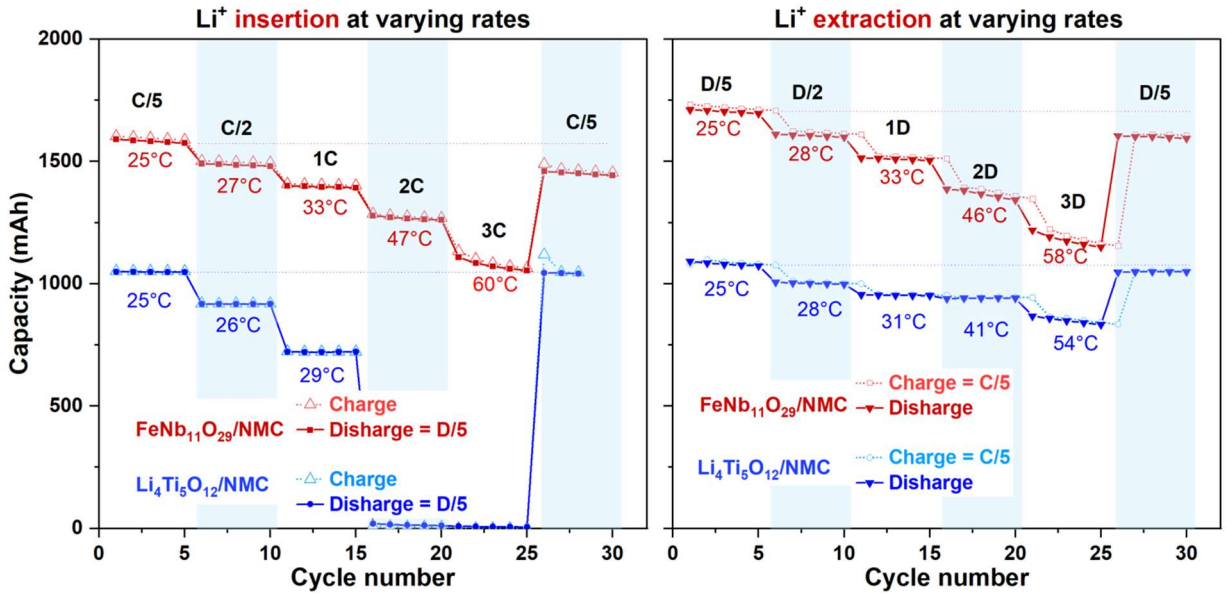

Figure IV.5. Asymmetric rate tests comparing Li^+ insertion (left) and extraction (right) kinetics in negative electrodes of $FeNb_{11}O_{29}$/NMC and $Li_4Ti_5O_{12}$/NMC full cells. $FeNb_{11}O_{29}$ shows greater capacity fading and temperature rise under increased rates.

In contrast, $Li_4Ti_5O_{12}$/NMC cells show significantly better rate performance, maintaining stable capacities and lower temperature rise even at higher rates, for extraction process. Regarding the lithium insertion process in $Li_4Ti_5O_{12}$ (cell charging), due to the cell's upper limit voltage of 2.7 V to avoid NMC degradation, the capacity drops sharply at high rates.

Figure IV.6 further supports asymmetric kinetic behavior of $FeNb_{11}O_{29}$. The differential capacity (dQ/dV) curves show that Li^+ insertion in $FeNb_{11}O_{29}$ (left panel) leads to pronounced peak shifts and broadening at higher C-rates, indicating stronger kinetic limitations compared to Li^+ extraction (right panel), where peak features are better preserved. These findings are consistent with trends observed in coin-cell configurations.

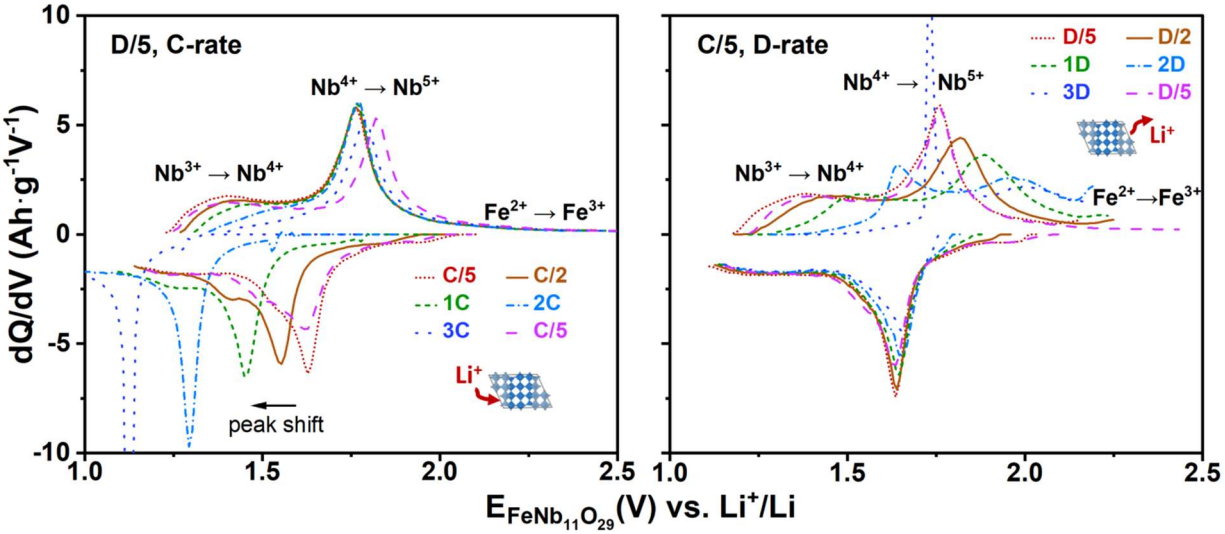

Figure IV.6. Differential capacity (dQ/dV) curves of $FeNb_{11}O_{29}$/NMC full cells during asymmetric rate tests, based on the $FeNb_{11}O_{29}$ electrode potential referenced to Li^+/Li. The left and right panels compare Li^+ insertion and extraction kinetics in $FeNb_{11}O_{29}$, respectively, under varying rates.

Overall, these results confirm that Li^+ insertion into $FeNb_{11}O_{29}$ is more kinetically hindered than extraction, and that $FeNb_{11}O_{29}$ exhibits higher polarization and thermal buildup compared to $Li_4Ti_5O_{12}$, particularly under high-rate conditions.

IV.1.3.6. Constant power test

Figure IV.7 presents a Ragone plot comparing the energy–power performance of $FeNb_{11}O_{29}$/NMC full cells with other common cell chemistries under constant power discharge.

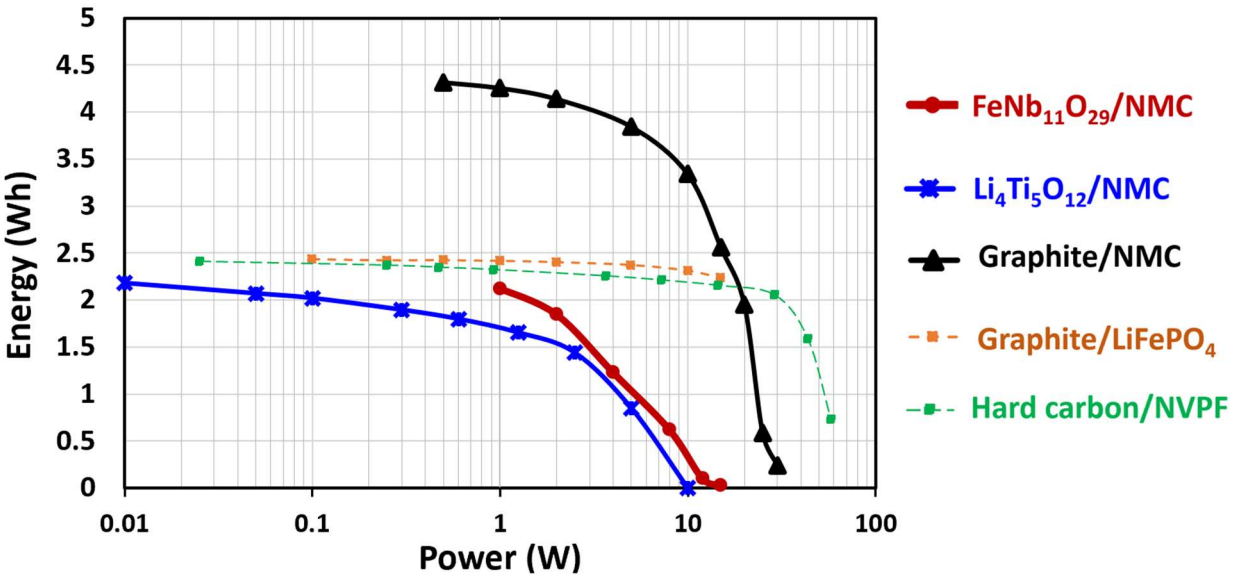

Figure IV.7. Ragone plot of $FeNb_{11}O_{29}$/NMC compared with other cells showing energy output as a function of power under constant power discharge.

$FeNb_{11}O_{29}$/NMC cells exhibit a balance between energy and power, with specific energy falling between that of $Li_4Ti_5O_{12}$/NMC and graphite/NMC cells across the entire power range. At low power, $FeNb_{11}O_{29}$/NMC delivers significantly higher energy than $Li_4Ti_5O_{12}$/NMC, due to its higher specific capacity. However, it does not reach the energy density of graphite-based cells, which dominate at both low and high power. At elevated power levels, the energy output of $FeNb_{11}O_{29}$/NMC decreases more steeply than hard carbon/NVPF and graphite/NMC. It should be noted that these results represent only the first trial of $FeNb_{11}O_{29}$/NMC cells, whose modest performance may arise from several factors, including residual impurities, the absence of microstructural optimization or carbon coating, and a insufficiently optimized electrode formulation. In contrast, the reference cells were assembled from commercial materials, and these systems have been extensively studied and optimized through repeated trials to achieve their best performance. Therefore, $FeNb_{11}O_{29}$-based cells hold strong promise for better performance upon further material and electrode optimization.

IV.1.4. Conclusions and perspectives

This study demonstrates the feasibility of scaling up $FeNb_{11}O_{29}$ synthesis and integrating it into 18650-format full cells. Large-scale solid-state synthesis produced highly crystalline material similar to small-batch synthesis, despite the presence of impurities and inhomogeneous Fe distribution, which emphasizes the necessity for better precursor mixing and contamination control. Material processing steps, particularly sieving, played a critical role in ensuring uniform slurry dispersion and homogeneous, high-quality electrode coatings. These criteria are essential for reliable cell fabrication and cell performance.

At the full-cell level, $FeNb_{11}O_{29}$/NMC cells exhibited competitive discharge capacity comparable to graphite/NMC systems, with intermediate energy density between $Li_4Ti_5O_{12}$ and graphite-based cells, as also represented in Ragone plot. This is because the high density of $FeNb_{11}O_{29}$ compensates for its lower intrinsic capacity, delivering promising gravimetric and volumetric energy density. Electrochemical cycling revealed both strengths and limitations: $FeNb_{11}O_{29}$-based cells delivered higher energy than $Li_4Ti_5O_{12}$-based cells at low power but showed higher polarization, more heating, and more pronounced degradation under long-term cycling. Kinetic asymmetry, especially sluggish Li^+ insertion, represents a key challenge. However, the presence of impurity and unoptimized electrode formulation in this first prototyping work may have led to the observed insufficient performance. Overall, these findings highlight the promise of $FeNb_{11}O_{29}$ as a next-generation negative electrode material while emphasizing the need for further optimization.

Future work could aim to optimize synthesis and processing to address the issues of impurity and elemental inhomogeneity. This may involve improving large-scale mixing and milling strategies, using alternative milling media, or exploring different synthesis routes. The electronic conductivity and electrochemical kinetics of $FeNb_{11}O_{29}$ active material can be enhanced through surface engineering or carbon coating. At the electrode level, performance could be improved by optimizing particle size via milling and sieving, fine-tuning slurry composition, coating and calendering parameters. Such approaches could help enhance coating quality, facilitate electronic and ionic transport, reduce polarization and limit the heat generation during cycling. Finally, long-term cycling studies with improved electrode formulations under various conditions, together with post-mortem analysis, would be crucial to clarify the stability limits and degradation mechanisms of $FeNb_{11}O_{29}$.

IV.2. Ageing tests of $FeNb_{11}O_{29}$/NMC coin cells

IV.2.1. Introduction

To better understand the insufficient performance observed in the previously discussed 18650-format $FeNb_{11}O_{29}$/NMC cells, further degradation studies were carried out using coin-cell configuration. This performance deterioration is a common challenge across all battery technologies. The nature and severity of these reactions depend not only on the battery's chemistry but also on its design and, most critically, its operating conditions, including temperature, cycling rate, and storage state-of-charge, voltage window and time.

The investigations of these degradation mechanisms have attracted considerable interests in recent years, particularly for Li-ion batteries, as they are increasingly used in electric vehicles and grid storage—applications where long cycle life is essential. It is now widely accepted that aging in Li-ion cells typically results from either (i) a loss of lithium inventory, caused by parasitic processes such as SEI layer formation, electrolyte degradation, and lithium plating, or (ii) a loss in active electrode material due to issues like particle cracking, delamination, or partial dissolution. At the negative electrode, degradation is mainly attributed to the instability of the Solid Electrolyte Interphase (SEI), particularly at elevated temperatures, and lithium plating, which becomes more prominent at lower temperatures. On the positive electrode, the decrease in performance is primarily originated from the dissolution of active materials during cycling or storage, as well as electrolyte oxidation—both of which are exacerbated by high temperatures and voltages.

In this study, given the high operating voltage of $FeNb_{11}O_{29}$, the extent and impact of SEI formation and growth remain unclear. Therefore, it is interesting to explore the dominant degradation mechanisms and the factors contributing to performance loss. For this purpose, two types of ageing tests were carried out in coin cells at two temperatures: (i) cycle-life aging, involving continuous cycling at different current rates to simulate repeated operation, and (ii) storage aging, in which cells were held at defined states of charge (SoC). While cycle-life aging provides insight into degradation during continuous operation, storage ageing offers a more realistic perspective as batteries typically spend most of their lifetime at open-circuit voltage (OCV).

IV.2.1. Experimental

IV.2.1.1. Electrode characteristics and cell assembling

Highly loaded $FeNb_{11}O_{29}$ electrodes (~20 mg cm^{-2}) were prepared following the procedures in chapter 3. The electrodes (1.27 cm diameter) were calendared using a hydraulic press at 2.5 T, yielding a porosity of ~42% based on mass and geometric measurements. Electrode porosity was calculated as: Porosity = $(1 - V_{theoretical}/V_{real}) \times 100\%$, where $V_{theoretical} = \Sigma_i (m_i/\rho_i)$ is the solid volume estimated from the mass and true density of each component (4.52 g cm^{-3} for $FeNb_{11}O_{29}$, 1.89 g cm^{-3} for carbon, and 1.79 g cm^{-3} for PVdF), and V_{real} = thickness × area is the macroscopic electrode volume after calendaring.

The positive electrodes are highly loaded $LiNi_{0.8}Mn_{0.1}Co_{0.1}O_2$ (NMC811) electrode (~22 mg cm^{-2}), provided by Laboratoire Electrochimie et Physicochimie des Matériaux et des Interfaces (LEPMI, Grenoble).

Coin cells were assembled in an Ar-filled glovebox using $FeNb_{11}O_{29}$ and NMC811 as negative and positive electrodes, separated by glass fiber separator (Whatman grade D) and filled with 1 M $LiPF_6$ in EC:DMC (3:7 vol.%) (Solvionic) as electrolyte. The negative-to-positive capacity ratio (N/P) was ~1.1.

IV.2.1.2. Electrochemical protocols

The assembled full cells first went through the formation stage, which includes 2 cycles at C/20. Two types of aging tests were conducted to evaluate battery longevity: cycle-life aging and storage aging. These tests were designed to assess the influence of the charged-discharge current rate, temperature, and state of charge (SoC) during storage on battery lifespan. All tests were carried out in approximately 60 days, as the battery's state of health (SoH) reached 80%. A summary of the testing conditions is provided in Tables IV.3. To ensure data reliability, each test was conducted on two separate cells.

Table IV.3. Testing conditions for cycle-life and storage aging of full cells at different temperatures, C-rates, and SoC levels. Two cells were tested for each condition; check-up intervals are listed below

		Cycle-life tests		**Storage tests**	
		C/10	C/5	50% SoC	100% SoC
Temperature	RT	× 2	× 2	× 2	× 2
	45 °C	× 2	× 2	× 2	× 2
Check-up every		25 cycles	50 cycles	15 days	

Cycle-life testing involved continuous charge-discharge cycles within a voltage window of 1.0 V - 3.2 V. These tests were carried out at two temperatures: room temperature (RT, around 25 °C) and 45 °C, and at two different C-rates: C/10 and C/5. Periodic interruptions were made during the cycling to perform check-up tests for tracking performance changes in the cells. These diagnostic tests were designed to minimize any contribution to further cell degradation.

For storage aging, cells were stored under different states of charge (SoC = 50% or 100%) and at RT or 45 °C under open-circuit voltage (OCV) conditions. Regular check-up tests were conducted every 15 days to monitor capacity loss.

Two types of check-up protocols were used: extended and short.

- The extended check-up was carried out at the beginning and end of the aging period. It consists of a rate capability test (C/20, C/10, C/5, C/2, 1C, 2C, and C/20) and 30-second charge/discharge pulse tests at 1C.
- The short check-up test was performed more frequently, every 25 cycles for C/10 cycling or every 50 cycles for C/5 cycling, or every 15 days for the storage tests. It included two standard cycles at a C/20 rate along with 1C pulse tests.

IV.2.2. Results and discussions

IV.2.2.1. Initial rate tests and resistance measurements

The initial rate performance of the full cells, as shown in Figure IV.8, clearly demonstrates that capacity retention is strongly influenced by both C-rate and temperature.

At room temperature (RT), the first-cycle Coulombic efficiency (CE) is ~90%, increasing to ~99.3% by the second cycle and remaining stable thereafter. In contrast, cells tested at 45 °C exhibit a slightly higher initial CE of ~91.5% but a lower second-cycle CE of ~98.5%, which then rises above 99% in subsequent cycles.

The galvanostatic charge-discharge (GCD) curves maintain a similar overall shape across increasing rates but exhibit increasingly shifted starting points at higher C-rates. These shifts are particularly pronounced in cells cycled at 45 °C, suggesting elevated internal resistance and polarization. These shifts shortened the electrochemical processes as the voltage limit is reached prematurely, leading to lower capacity.

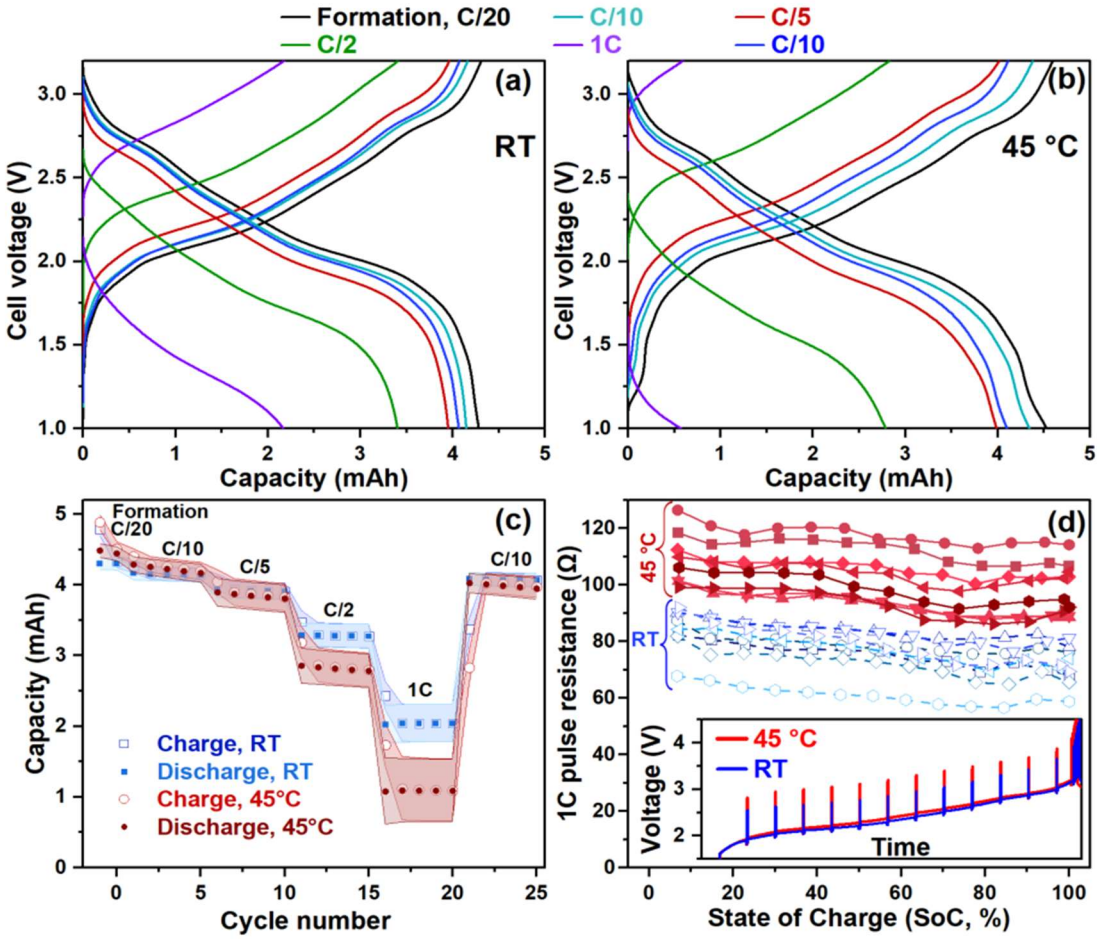

Figure IV.8. Rate performance of $FeNb_{11}O_{29}$/NMC full cells at RT and 45 °C. (a, b) GCD curves show increased polarization at higher C-rates, more pronounced at 45 °C. (c) Capacity drops sharply at 45 °C at C/2 and 1C. (d) 1C pulse resistance is higher at 45 °C, with greater voltage jumps (inset).

During the rate test, cells at both room temperature (RT) and 45 °C show similar capacity values at slow rate (C/20, C/10, C/5). From C/20 to C/10, 45 °C cells exhibit slightly higher capacities than those at RT, consistent with the higher initial CE values discussed previously (~91.5% vs. ~90%). This can be attributed to the reduced electrolyte viscosity and enhanced Li^+ diffusion in LP30—a behavior also observed in other Li/Na systems. Both groups of cells show a gradual capacity decrease with increasing current, as expected from kinetic limitations. At 45 °C, however, the drop is much stronger, especially at C/2 and 1C. For example, at 1C the capacity falls below 1.1 mAh for 45 °C cells, compared with ~2.0 mAh at RT. This suggests that high temperature accelerates interfacial degradation and limits Li^+ transport. When the current is reduced back to C/10, both groups of cells retained ~3.9 mAh, corresponding to ~11% capacity loss compared with the initial capacity of 4.4 mAh, likely due to SEI growth and other degradation processes.

These observations are supported by the pulse resistance measurements (30-second, 1C current pulses) shown in Figure IV.8d. The voltage-time profiles reveal significantly larger voltage jumps for the 45 °C cells, indicating greater instantaneous ohmic contribution. This is quantitatively confirmed in the resistance vs. SoC plot, where internal resistance values at 45 °C range from 100–120 Ω, compared to 60–80 Ω at RT. This elevated resistance at higher temperatures may be caused by SEI thickening, electrolyte decomposition, and worsened interfacial contact, all of which contribute to higher polarization and reduced usable capacity.

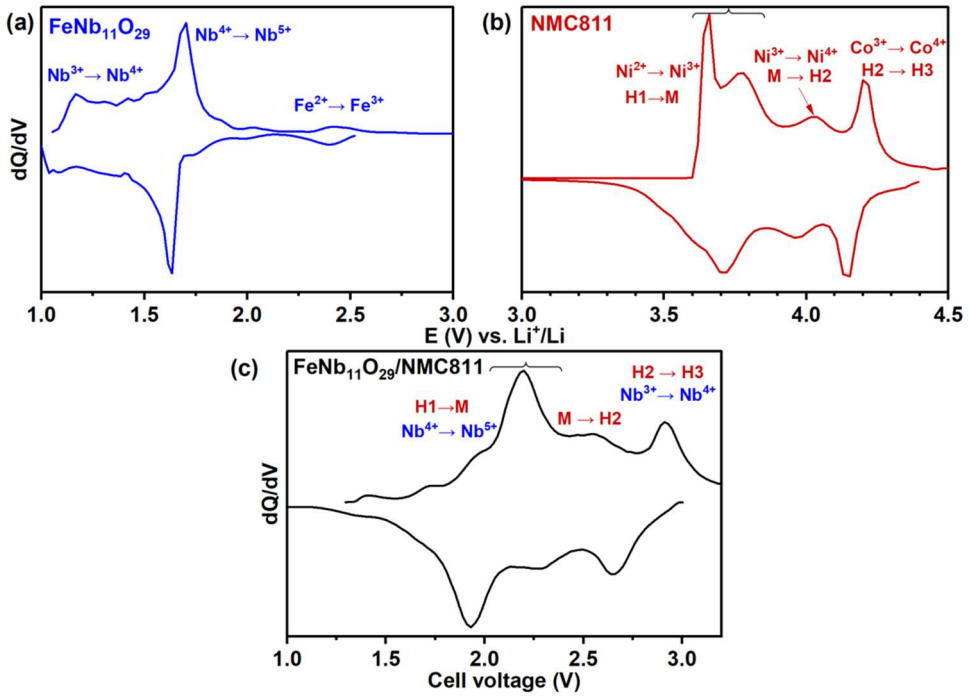

Figure IV.9. Differential capacity (dQ/dV) plots of (a) $FeNb_{11}O_{29}$ and (b) NMC811 half-cells, and (c) $FeNb_{11}O_{29}$/NMC811 full cell, showing characteristic redox features

To gain insights into the redox processes for further cell degradation evaluation, differential capacity (dQ/dV) analysis was performed on both half- and full-cells, as shown in Figure IV.9. For $FeNb_{11}O_{29}$, the redox activity was previously described, involving the Fe^{3+}/Fe^{2+} couple near 2.4 V, Nb^{5+}/Nb^{4+} around 1.6–1.7 V, and broad features below 1.5 V associated with Nb^{4+}/Nb^{3+}. Regarding NMC811 in half-cell, its delithiation proceeds via several structural transitions (H1 → M → H2 → H3), each corresponding to a transition metal redox process. The H1 (*R*-3*m*) to M (*C*2/*m*) transition corresponds to $Ni^{2+} \rightarrow Ni^{3+}$ oxidation, followed by $Ni^{3+} \rightarrow Ni^{4+}$ oxidation during M→H2 transition. At high voltage, the H2→H3 transformation, characterized by a collapsed c-axis and structural stress, is associated with $Co^{3+} \rightarrow Co^{4+}$ oxidation. In $FeNb_{11}O_{29}$/NMC full-cell, the dQ/dV profile shows characteristic peaks attributable to redox processes from both electrodes, as shown in Figure Figure IV.9c.

IV.2.2.2. Cycling-induced ageing under different rates and temperatures

Figure IV.10 shows the effect of prolonged cycling on capacity loss and internal resistance under two cycling rates (C/10 and C/5) and two temperatures (RT and 45 °C).

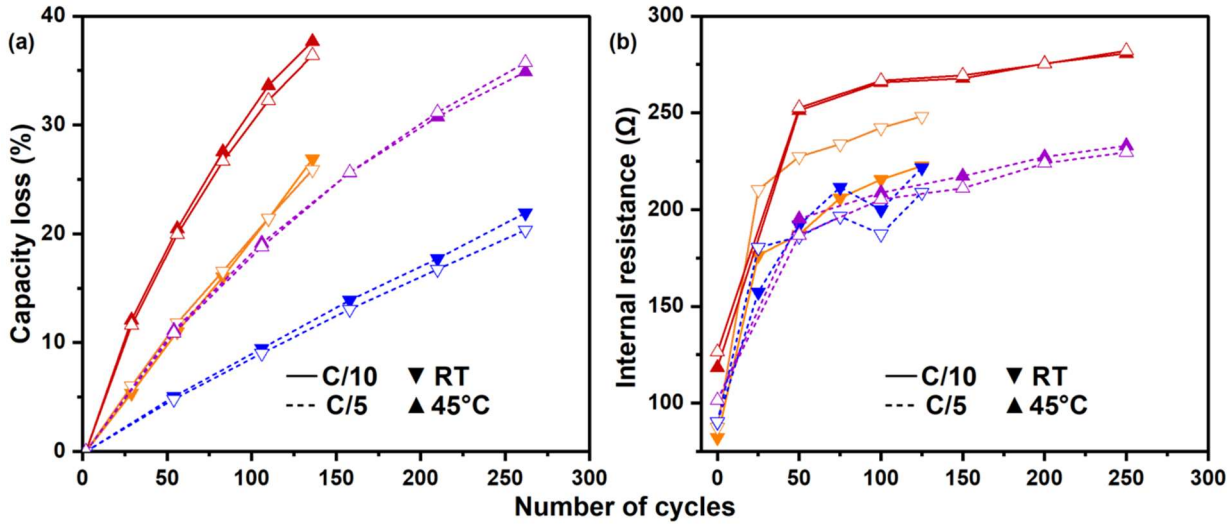

Figure IV.10. Capacity loss (a) and internal resistance (b) vs. cycle number for cells aged under different cycling conditions, with two cells per condition for repeatability.

Capacity decreases steadily under all cycling conditions, but to different extents. Cells cycled at 45 °C exhibit more pronounced degradation, consistent with the expected acceleration of side reactions at higher temperatures. Interestingly, slower cycling at C/10 leads to slightly greater capacity loss compared to C/5, despite the lower current. This can be explained by the longer time spent at high cell voltage, where the positive electrode is at high potential and the negative electrode is at low potential. Under these conditions, electrolyte degradation occurs through oxidation at the positive electrode and reduction at the negative electrode, promoting parasitic reactions and interfacial damage. Such behavior has also been reported in other aging

systems [159,160]. The combination of high temperature and slow cycling is especially detrimental: in the C/10–45 °C condition, capacity fading exceeds 35% after 125 cycles. While higher temperature initially improves performance in the first few cycles, it also accelerates electrolyte degradation in subsequent cycles, leading to faster capacity loss.

The evolution of internal resistance over cycling provides further insights, showing its dependence on both cycling rates and temperatures. While resistance increases in all cases, cells under slower cycling at C/10 exhibit larger resistance, similar to the results on capacity loss. Also, the effect of temperature is more significant at the slower rate: while cells at C/5 show comparable resistance growth at RT and 45 °C, those cycled at C/10 exhibit a much steeper rise at 45 °C, exceeding 250 Ω after only 50 cycles. Overall, these increases in resistance agree well with the observed capacity fade, indicating accelerated interfacial degradation under slow cycling at elevated temperatures. This is possibly due to more severe SEI thickening, electrolyte decomposition, or loss of electronic contact within the electrode under this condition.

The degradation trends are further supported by differential capacity (dQ/dV) analysis from periodic C/20 check-up tests (Figure IV.11).

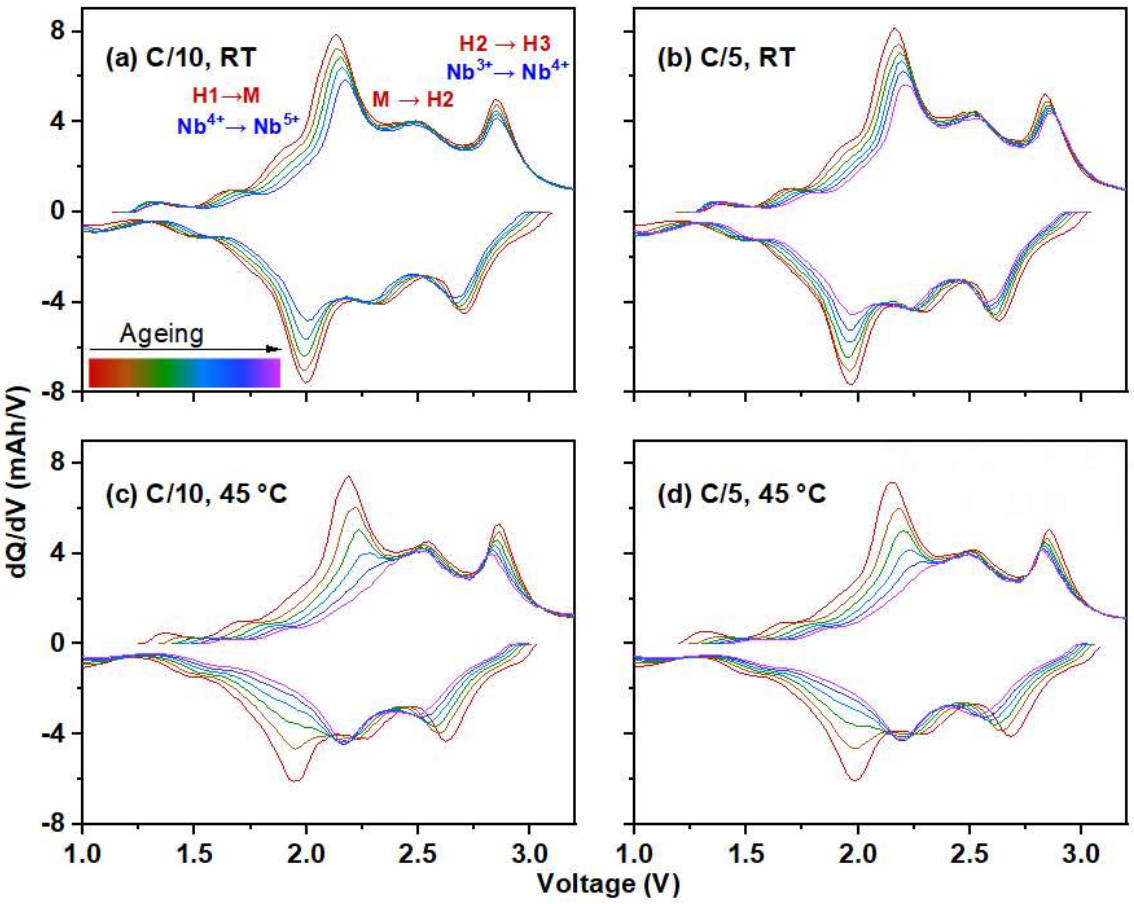

Figure IV.11. Evolution of differential capacity curves during C/20 check-up tests of full-cells aged under different cycling conditions.

At room temperature, both groups of cells cycled at C/10 and C/5 exhibit a gradual decline in peak intensity, particularly at lower voltages, while maintaining the overall peak shapes. This suggests partial loss of active material or increased polarization, yet the fundamental electrochemical processes remain largely intact. In contrast, cells cycled at 45 °C show significant changes: progressive disappearance of the first redox peak (typically associated with Nb^{5+}/Nb^{4+} and $Ni^{2+} \rightarrow Ni^{3+}$ reactions) and peak broadening of other features. This suggests irreversible loss of electrochemically active sites, lower crystallinity or elevated polarization. These results align well with the resistance and capacity loss data, reinforcing the evidence for interfacial degradation and structural deterioration induced by high temperatures.

IV.2.2.3. Storage-induced ageing under different states of charge and temperatures

The influence of temperature and state of charge (SoC) on cell degradation during the storage ageing test is represented in Figure IV.12, with corresponding dQ/dV curves during C/20 check-up tests shown in Figure IV.13.

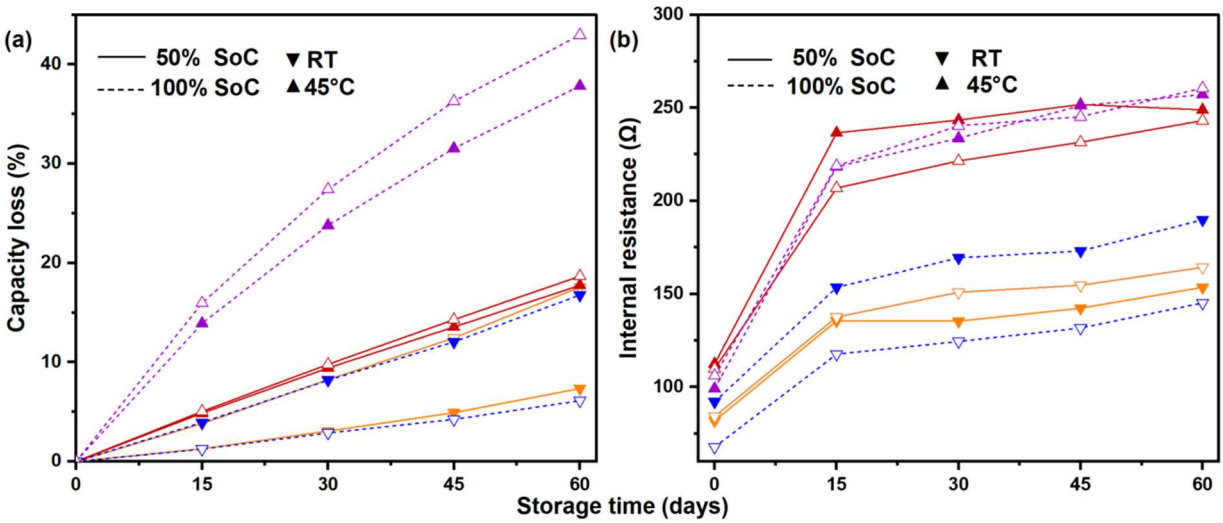

Figure IV.12. Capacity loss (a) and internal resistance (b) vs. cycle number for cells aged at different storage conditions. The most severe degradation occurred at high temperature and high SoC.

At RT, storage leads to similar degradation extent regardless of SoC (50% or 100%): small capacity loss (≈ 18% after 60 days), modest resistance increase to 140-170 Ω, and minimal change in dQ/dV profiles. This suggests little degradation under mild conditions.

However, storage at higher temperatures strongly accelerates cell ageing. For cells stored at 45 °C, resistance rises rapidly to 250 Ω regardless of SoC, indicating that resistance build-up during storage is primarily driven by temperature, likely due to more interfacial degradation and SEI growth. At 50% SoC, capacity loss remains moderate and dQ/dV peaks gradually decline in intensity, despite their positions and shapes being largely preserved, which suggests that degradation is dominated by interfacial resistance growth rather than structural breakdown.

Interestingly, temperature alone is not the dominant factor for capacity loss during storage ageing. In fact, ageing becomes most severe under the combined extreme conditions of 45 °C and 100% SoC, with capacity loss exceeding 40% and steep resistance rise after 60 days, while dQ/dV profiles show rapid suppression of the first redox peak along with broadening and shifting of the others. These results suggest substantial structural and electrochemical degradation, or electrolyte oxidation under the synergistic effect of high voltage and thermal stress.

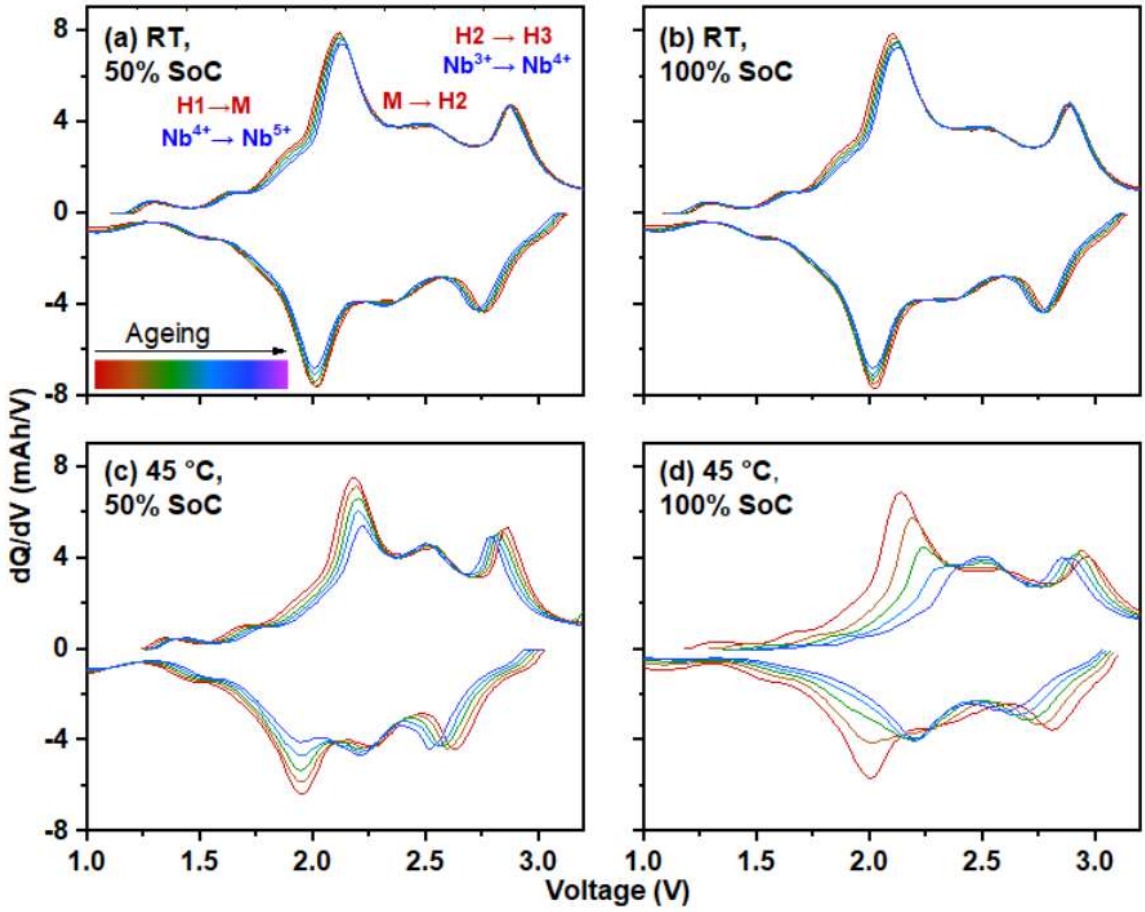

Figure IV.13. Evolution of differential capacity curves during C/20 check-up tests of full-cells aged under different storage conditions. High temperature and high SoC (d) exacerbate the ageing.

Overall, these results highlight the importance of storing Li-ion cells at moderate SoC and temperature to minimize both capacity loss and resistance rise. High SoC levels, especially when combined with elevated temperatures, accelerate not only capacity degradation but also the growth of internal resistance and loss of electrochemical features.

IV.2.2.4. Final rate test

Figure IV.14 presents the results of the extended check-up rate test, conducted after the cycling and storage aging protocols to evaluate the residual rate capability of each cell.

All aged cells exhibit substantial capacity loss compared to the pristine cell, indicating the cumulative effects of the whole aging process. The pristine cell can still retain about 50% of its

initial capacity when cycled at 1C at RT, indicating that Li^+ diffusion within the active material is still achievable at this stage. After cycling and storage ageing, however, the cells can no longer sustain operation at 1C, suggesting that SEI growth during the ageing process may impede Li^+ transport across the electrode–electrolyte interface. Between two temperatures, cells subjected to 45 °C consistently show poorer rate performance, regardless of cycling or storage ageing. This is especially apparent at higher rates.

In the cycling-aged cells, degradation is more severe at C/10, particularly at 45 °C. This agrees with earlier observations that prolonged cycling at low rate and high temperature promotes stronger aging, likely due to extended time at high SoC combined with thermal stress, which accelerates SEI growth and Li^+ inventory loss.

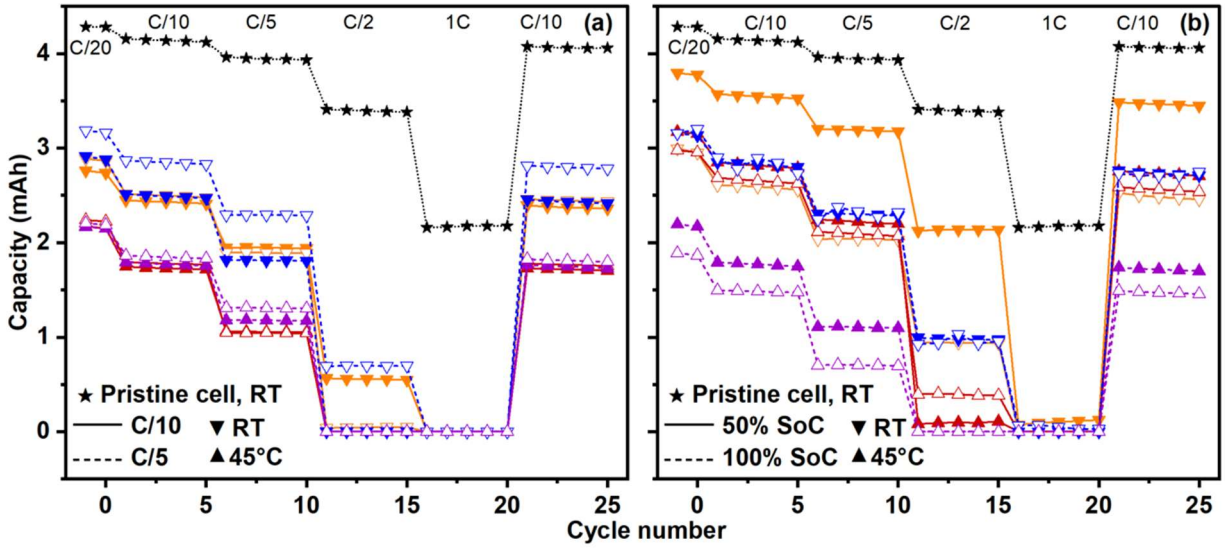

Figure IV.14. Extended rate check-up after cycling (a) and storage (b) ageing. Capacity loss is observed in all aged cells, with the worst performance at 45 °C and high SoC, especially at high rates.

Similarly, in the storage-aged cells, capacity is lowest for cells stored at 100% SoC and 45 °C, while the 50% SoC and RT condition yields better capacity. The contrast is particularly clear at high rates, suggesting that storage at high SoC and elevated temperature not only reduces capacity but also hinder Li^+ diffusion kinetics, likely due to irreversible interfacial damage and electrolyte decomposition.

In summary, the extended check-up test highlights that both temperature and SoC, during either cycling or storage, leave lasting impacts on rate capability, especially at higher currents where internal resistance becomes most significant.

IV.2.3. Conclusions and perspectives

This study systematically investigated the degradation of $FeNb_{11}O_{29}$/NMC full cells under different cycling and storage conditions using coin-cell configurations. The results highlight that capacity fading and resistance growth strongly depend on temperature, cycling protocol, and storage state-of-charge (SoC).

During cycling ageing, high temperature (45 °C) was the most critical factor on degradation. Cells cycled at C/10 at 45 °C showed the fastest capacity fade (>35% after 125 cycles) and steep resistance increase (>250 Ω after only 50 cycles). Interestingly, slower cycling induced stronger degradation than faster cycling, likely due to prolonged exposure to high voltage and high SoC, which promotes parasitic reactions and interfacial instability. Differential capacity (dQ/dV) analysis confirmed the progressive loss of redox activity under these harsh conditions.

During storage ageing, temperature also played a dominant role. At room temperature, capacity loss and resistance growth were modest (<20% capacity loss over 60 days), with little difference between 50% and 100% SoC. At 45 °C, however, resistance rose sharply to ~250 Ω, while the combination of high SoC (100%) and high temperature caused the most severe degradation (>40% capacity loss, rapid suppression of redox peaks), indicating structural and electrochemical deterioration, possibly driven by electrolyte oxidation and interfacial breakdown.

These findings highlight the importance of managing operating conditions for $FeNb_{11}O_{29}$-based cells. Maintaining moderate temperature and SoC, together with optimized cycling protocols that limit prolonged exposure to high voltages, is essential to mitigating performance loss. To gain further insights into the underlying degradation mechanism, post-mortem analyses such as XPS of interfacial layers and electrolyte decomposition studies will be necessary, which can shed light on processes like SEI thickening, transition-metal dissolution, or irreversible phase transformations.

IV.3. Chapter summary and perspectives

This chapter has demonstrated both opportunities and challenges concerning the practical implementation of $FeNb_{11}O_{29}$ as a negative electrode material, through prototyping in 18650-format full cells and systematic degradation studies in coin-cell configuration. The successful scale-up of synthesis and electrode processing confirms its feasibility for larger formats, while full-cell tests highlight its ability to deliver energy densities intermediate between graphite and $Li_4Ti_5O_{12}$. However, significant polarization and degradation indicate that its kinetic limitations and the presence of impurities must be addressed before it can compete with state-of-the-art negative electrode materials.

Ageing studies highlight the critical importance of operating conditions on $FeNb_{11}O_{29}$/NMC full-cell performance, including temperature, cycling rates, and state of charge (SoC) during storage. The results revealed that these full cells are particularly vulnerable under elevated temperature and high SoC or prolonged exposure to high voltage during cycling, where interfacial degradation and electrolyte instability strongly accelerate resistance growth and capacity loss.

Overall, $FeNb_{11}O_{29}$ can be considered a promising candidate for applications that require a balance between energy density and safety. It can potentially bridge the gap between fast but low-energy $Li_4Ti_5O_{12}$-based cells and high-energy but less stable graphite-based cells. To accomplish this objective, advances in large-scale synthesis, electrode engineering, and interfacial stabilization are needed. Besides optimization, future research should also clarify its degradation pathways through post-mortem studies, providing the necessary insights to valorize $FeNb_{11}O_{29}$ among next-generation negative electrodes for Li-ion batteries.

Chapter V

Wadsley-Roth $FeNb_{11}O_{29}$ as negative electrode material in solid-state batteries

V.1. Introduction

V.1.1. Challenges of other negative electrode material in SSBs

All-solid-state batteries (ASSBs) have attracted significant attention due to their enhanced safety, durability, and higher energy density [161]. The use of solid-state electrolytes (SSEs) in place of flammable liquid electrolytes plays a central role in ASSBs. This does not only reduce the risk of flammability but also facilitates the use of high-capacity electrode materials like alkali metals or silicon [161,162]. Additionally, SSEs can enable battery operation across a wider range of temperatures and current densities, making them suitable for a variety of applications. Various advanced negative electrode materials have been extensively studied for ASSBs, including lithium metal, graphite, Si-based, and zero-excess lithium (anode-free engineering). Each option presents distinct advantages and challenges, as summarized in Figure V.1.

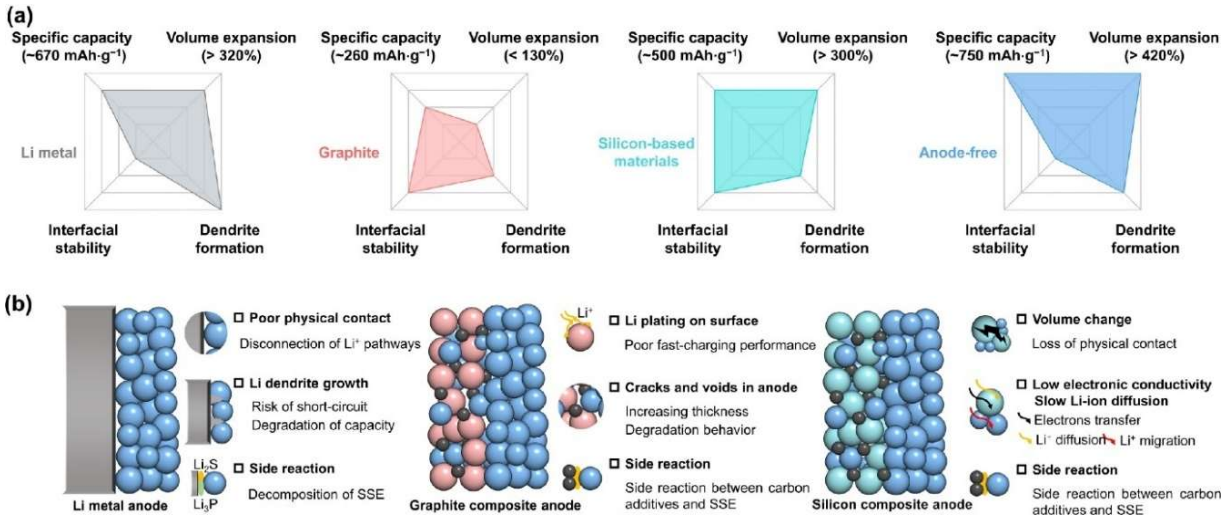

Figure V.1. **(a)** A comparison of specific capacity, volume expansion, dendrite formation, and interfacial stability among four types of advanced negative electrodes in SSBs. **(b)** Schematics of the different interfacial challenges observed in lithium metal, graphite composite, and silicon composite anodes. Adapted from [163].

V.1.1.1. Lithium metal electrodes

Lithium metal is regarded as the ideal negative electrode material for solid-state lithium batteries thanks to its low electrochemical potential and high specific capacity. However, it faces numerous challenges, including (electro-)chemical reactivity with SSEs, poor physical contact, poor Coulombic efficiency, and lithium dendrite growth [163,164].

A major issue lies at the Li/SSE interface, where the uneven surface of lithium metal results in insufficient contact with SSEs, leading to high interfacial impedance and inefficient Li^+ diffusion. This inadequate physical contact also causes non-uniform distribution of electrical potential during lithium plating and stripping processes, promoting uneven flow of ions and electrons across the interface and hence inhomogeneous lithium nucleation and growth.

Combined with the slow diffusion of Li^+ ions into the bulk of lithium metal, these factors contribute to the formation and propagation of lithium dendrites and internal short-circuit [163]. During lithium stripping, these interfacial instabilities are worsened due to void formation, driven by irregular ion flux and changes in morphology, especially under high current densities [165]. These voids are not fully refilled in subsequent Li plating steps, resulting in gap expansions, loss of connectivity and increased interfacial resistance [166].

Furthermore, the low redox potential and high reactivity of the lithium metal anode can promote unfavorable side reactions at the interface with SSEs. This interface often exhibits mixed ionic and electronic conduction properties, which accelerates continuous degradation and hinders the long-term performance of ASSBs [167,168]. To address these issues, various strategies have been proposed, such as alloying, constructing 3D current collectors [169] or mixed electron-ion conducting frameworks [170], creating modified interfacial layers between Li and SSEs [171]. However, these strategies, though effective in the short-term, do not guarantee long-term chemical and morphological stabilities throughout the repeating Li stripping and plating process. Therefore, it is vital to develop better interfacial engineering strategies or alternative negative electrode materials to address these challenges of lithium metal electrodes.

V.1.1.2. Graphite composite electrode

Graphite is regarded as a state-of-the-art and promising electrode material for ASSBs because of its excellent structural stability, light weight, and high electronic conductivity. However, several challenges exist, including its lower specific capacity, sluggish kinetics, and high chemical reactivity with SSEs at low operating potentials. The rate at which lithium ions are inserted into graphite is relatively slow, leading to limited rate capability during discharge. This sluggish kinetics, combined with low intercalation potential, can cause lithium plating on the graphite surface during fast discharging, increasing the risk of dendrite formation and short-circuiting [172,173]. Also, at low operating potentials, graphite can react with certain SSEs, leading to the formation of unstable interfaces. The significant polarization of graphite composite electrodes limits their fast-charging performance, particularly in electrodes with greater thickness or a high graphite volume fraction. This polarization, caused by ionic concentration gradients, can lead to reversible capacity degradation and even trigger lithium plating. Therefore, enhancing graphite composite structures and carefully optimizing the components, such as electronic conductors, ionic conductors, and binders, are essential for developing advanced graphite composites with optimal ionic−electronic networks [163,174].

V.1.1.3. Silicon composite electrode

Si-based materials is a promising candidate as next-generation electrodes for solid-state batteries due to their abundance, high theoretical capacity (3579 $mAh \cdot g^{-1}$), and low redox potential (around 0.35 V vs. Li^+/Li). These materials exhibit improved chemical stability and compatibility with SSEs, as the high lithiation potential of Si-based materials can mitigate the side reactions and reduce the risk of lithium plating compared to lithium metal electrode. However, Si-based electrodes face several challenges in practical applications, including drastic volume changes (up to 400%), significant stress generation and loss of physical contact, and low electronic conductivity [163,174,175]. This leads to poor irreversible coulombic efficiency and capacity fading during cycling. Recent studies have addressed some of these issues through materials engineering, including size and morphology control, alloying, and modification strategies, as well as by developing compatible fabrication and operational protocols, such as optimizing pressure and cut-off voltage [176].

V.1.2. Recent advances in high-voltage negative electrode materials for SSBs

In the search for high-rate and stable negative electrode materials for Li-SSBs, several high-voltage, zero-strain materials have emerged as promising candidates, including spinel $Li_4Ti_5O_{12}$ and block phases of the Wadsley-Roth niobium-based oxide family [177–185]. Their relatively high operating potential (~1.5–1.6 V vs. Li^+/Li) may enhance chemical compatibility with solid electrolytes, mitigate interfacial side reactions, and reduce the risk of lithium plating, though at the expense of energy density. In addition, their low volume change during lithiation/delithiation may help limit mechanical stress, suppress particle cracking, and preserve interfacial contact, which are key factors for long-term cycling stability [177–184]. These materials have been implemented in Li-SSBs using diverse improvement approaches. For example, downsizing strategy proved effective where pulverised $Li_4Ti_5O_{12}$ particles delivered excellent reversible capacity of ~90 $mAh \cdot g^{-1}$ at 3.8 $mA \cdot cm^{-2}$ and 25 °C [177]. Interface engineering further improved the performance: *in-situ* sulfide coating ($70Li_2S \cdot 30P_2S_5$) around $Li_4Ti_5O_{12}$ nanoparticles created intimate solid–solid contact, improving both rate capability and long-term cycling (110 $mAh \cdot g^{-1}$ at 1 C, 80 °C for 0.5 $mg \cdot cm^{-2}$ loading, retained after 300 cycles) [178]. Other efforts targeted at optimizing the electronic transport by incorporating carbon black and carbon nanotubes (CNTs) as complementary short- and long-range electron pathways, which demonstrated impressive performance of $Li_4Ti_5O_{12}$ [179] and $TiNb_2O_7$ electrodes [180]. More recently, interfacial stabilisation of $Nb_{1.6}Ti_{0.32}W_{0.08}O_{5-\delta}$ via *in-situ* $LiWS_2$ formation enabled durable cycling and high rate cycling, delivering 175 $mAh \cdot g^{-1}$ at 0.2 $A \cdot g^{-1}$ (1C) and 25 °C for 1.8 $mg \cdot cm^{-2}$ loading [181]. These advances highlight the prospects of high-voltage negative

electrode materials in Li-SSBs and motivates the investigation of other Wadsley-Roth block phases, many of which remained unexplored. Expanding this family could diversify available materials and reveal new candidates for solid-state applications.

V.1.3. Motivations and objectives for $FeNb_{11}O_{29}$ implementation in Li-SSBs

Within this family, $FeNb_{11}O_{29}$ is a promising candidate with favourable properties: a relatively high operating potential, robust structural stability, fast ion transport in liquid electrolyte systems [106–115,120], and low volume change during cycling [108,113,120]. These attributes make it an attractive alternative to conventional low-potential electrodes, particularly for high-power Li-SSB applications where interfacial and mechanical stability are critical. In this work, the feasibility of employing $FeNb_{11}O_{29}$ in Li-SSBs will be evaluated for the first time to explore both its opportunities and interfacial/transport limitations.

This chapter begins with an optimization of the electrode composite, focusing on tailoring the ratios and interactions between the active material, SSE, and conductive additive to achieve a well-connected ionic and electronic percolation network. Following this, the morphology, electronic conductivity, lithium diffusion characteristics of the composite are investigated to obtain insights into its transport behavior. Post-mortem analysis of cycled composite will be conducted to understand the interfacial chemical composition and morphology, with the aim of identifying the degradation mechanisms of the cells.

V.1.4. Choice of components for SSBs

V.1.4.1. In-Li alloy as counter electrode

In axially pressed solid-state battery set-up, it is complicated to insert a third electrode for monitoring the working electrode's potential. Therefore, the utilization of a counter electrode acting as the lithium source and reference electrode is desired. Counter electrodes should ideally meet several requirements for reliable electrochemical measurements: (1) provide large reservoir of accessible Li during cycling; (2) offer fast kinetics than the working electrodes, and (3) exhibit a flat and stable voltage profile across a wide range of charge transfer reactions [186].

Due to the numerous challenges associated with lithium metal electrodes, alternative counter electrodes are required for two-electrode measurements. Among these, lithium alloys present a promising option. Certain lithium intermetallic phases, for example Li alloys with Al, Ga, In, Sb, or Sn, exhibit higher Li^+-ion chemical diffusion coefficients compared with the slow lithium self-diffusion (*i.e.* slow diffusion of Li^+ ions into the bulk of lithium metal). This improved Li^+ diffusivity in the alloy facilitates their formation via solid-state diffusion at ambient temperature [187]. In addition to their favorable transport properties and facile synthesis, lithium alloys

exhibit enhanced thermodynamic stability towards many SSEs. In fact, their alloy formation potential typically lies just below the electrochemical stability window of certain SSEs (< 1 V vs. Li^+/Li), which makes them less likely to trigger reductive decomposition of SSEs compared to pure lithium metal. This facilitates the formation of a more stable electrode/solid electrolyte interface and enables improved long-term cycling performance. Moreover, lithium alloy could also minimize the risk of Li dendrite formation and short-circuit, thereby enhancing safety and reliable electrochemical testing results [187].

Among various lithium alloys, the lithium−indium (Li−In) system is commonly used in Li-SSB research. While the high cost of indium presents a barrier to large-scale applications, its high ductility offers significant advantages for assembling solid-state cells at the lab scale. Furthermore, the alloy provides a stable redox potential of approximately 0.62 V vs. Li^+/Li over a wide compositional range, providing a reliable reference voltage for electrochemical studies of other electrode materials and electrolytes [186,188]. Several processing methods can be used to fabricate Li−In counter electrodes, including manual mixing of the two metal powders, roll pressing, and uniaxially pressing of the foils. Different factors such as (i) Li:In molar ratio, (ii) foil thickness, (iii) foil stacking order, and the (iv) processing techniques can have a large impact on the electrochemical behavior and kinetics of the counter electrodes [186].

In this work, the following conditions are used: (i) Li:In molar ratio < 0.5; (ii) 100 µm thick In foil; (iii) Li-In-SSE stacking order (In in contact with the SSE); and (iv) uniaxially pressing fabrication. Firstly, a Li:In molar ratio below 0.5 is required for a flat, stable voltage plateau, as electrodes with < 50 at% Li form In and LiIn phases, yielding a well-defined equilibrium potential of ~0.62 V vs. Li^+/Li at room temperature (Figure V.2) [188]. Secondly, 100 µm thick In foils were chosen for *in situ* Li−In formation inside the solid-state cell, as thicker foils prevent Li from being accessible [186]. Thirdly, In foil is typically placed in direct contact with the SSEs to avoid decomposition reactions between SSEs and Li. Finally, uniaxially pressing of the two foils was employed and the cell was rested during 24 h to promote the complete formation of Li−In alloy before launching any electrochemical test.

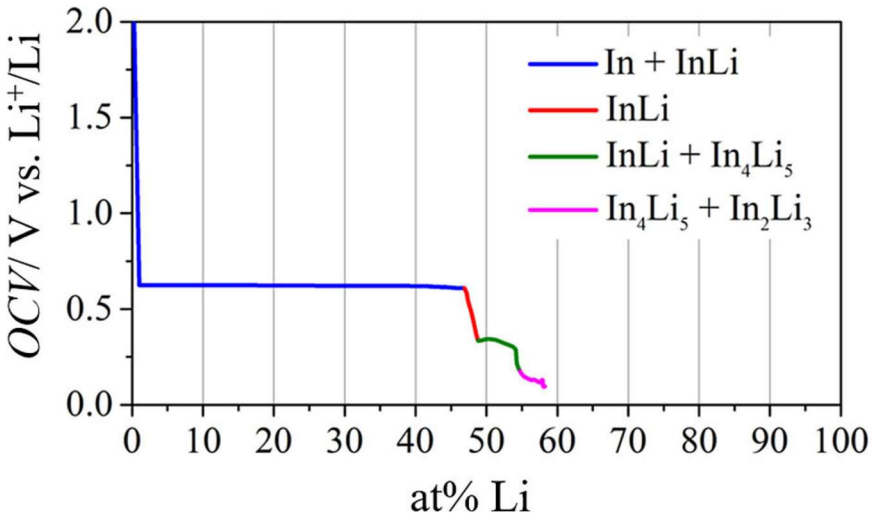

Figure V.2. Voltage profile showing alloying reactions between In and Li across different compositions. Below 50 at% Li, a flat plateau at ~0.62 V vs. Li^+/Li corresponds to the two-phase region of In and Li–In [188].

V.1.4.2. Argyrodite as solid-state electrolyte

The choice of SSEs is important as it determines the ionic transport and the electrochemical performance of the cell. Several stringent criteria are required for effective employment of solid electrolytes, including high ionic conductivity, negligible electronic conductivity, mechanical compatibility, wide electrochemical stability window, and good processibility [189,190]. Three main groups of inorganic SSEs have been extensively studied: oxides, sulfides and halides, with different properties (Figure V.3). While oxide SSEs exhibit excellent thermal, chemical, electrochemical stability and moderate ionic conductivity, their inherent rigidity and high Young's modulus present several challenges, including limited processibility, brittleness, poor interfacial contact and poor adaptation to volume changes during cycling [191]. Besides, the synthesis and densification of oxide SSEs often require high sintering temperature, which is energy-intensive and might induce undesirable interfacial reactions or large grain boundary resistance. Halide-based SSEs are well recognized as a promising candidate with high oxidation stability and high ionic conductivity, as well as mechanical flexibility offering ease of processing and cell assembling. However, several significant issues need to be addressed, including their moisture sensibility and poor reduction stability when in contact with alkali metal [192–194].

Meanwhile, sulfide-based SSEs are a commonly used conductor in the lab scale thanks to several benefits, including their high ionic conductivity, ease of synthesis, as well as mechanical deformability which facilitates cell fabrication, promotes contact and accommodates the expansion/contraction of electrode materials. However, several undesirable properties need to be acknowledged, such as their chemical instability in air and moisture leading to degradation, H_2S gas release, as well as their susceptibility to oxidation reactions with high-voltage cathode materials [195]. Conventional sulfide-based SSEs, such as Li_3PS_4, possess a very narrow

electrochemical stability window; nonetheless, a combination of sulfide with halide anion as in Li_6PS_5Cl (LPSCl) can increase significantly the electrochemical stability of the phase. In this study, Li_6PS_5Cl was used as the SSE in both the separator layer and electrode composite.

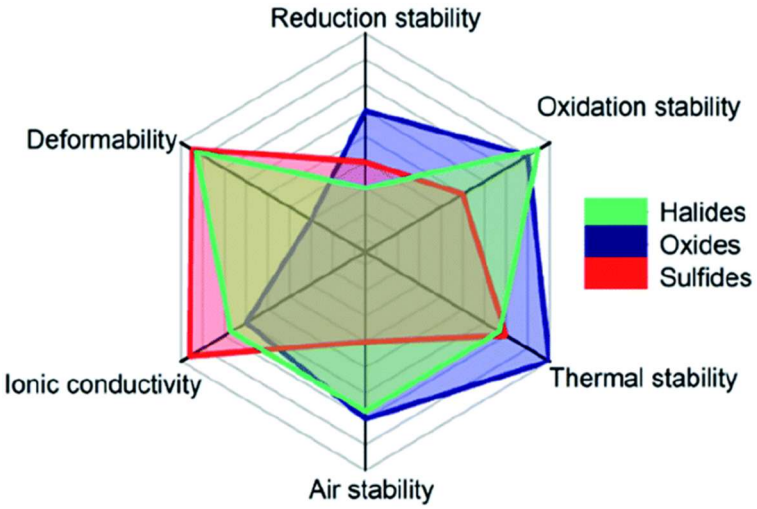

Figure V.3. Comparison of various properties among three inorganic SSEs. Adapted from [196].

V.2. Experimental

V.2.1. Preparation of electrode composites

Monoclinic $FeNb_{11}O_{29}$ was synthesized similar to chapter 2, by solid-state reaction at 1100 °C in 4 h from stoichiometric mixture of Fe_2O_3 (≥ 99 %, < 5 µm, Honeywell) and Nb_2O_5 (obtained by heating Nb powder (99.8 %, ~ 325 mesh, Alfa Aesar) at 900 °C for 24 h). Its phase purity was verified by X-ray diffraction.

Electrode composites were prepared by manually mixing $FeNb_{11}O_{29}$, solid-state electrolyte Li_6PS_5Cl (NEI Corporation, ionic conductivity of ~2.7 $mS \cdot cm^{-1}$), and vapor-grown carbon fiber (VGCF, Showa Denko VGCF-H) using a mortar and pestle inside an Ar-filled glovebox (O_2, H_2O < 0.1 ppm). Prior to mixing, $FeNb_{11}O_{29}$ and VGCF were dried overnight at 200 ºC in a Büchi oven under dynamic vacuum to remove residual moisture. To study the influence of electrode compositions on the ionic/electronic conductivity and cycling performance, the weight ratio of $FeNb_{11}O_{29}$ to Li_6PS_5Cl was fixed at 40:50, while the content of VGCF was systematically varied to have overall ($FeNb_{11}O_{29}$ + Li_6PS_5Cl):VGCF weight ratios of 90:3, 90:5, 90:10, 90:20, and 90:30. These composites are denoted as C03, C05, C10, C20, C030, and their compositions are summarized in Table V.1.

Table V.1. Compositions of composite electrodes with varying VGCF content

Composite	C03	C05	C10	C20	C30
$FeNb_{11}O_{29}$ (mg)			40		
Li_6PS_5Cl (mg)			50		
VGGCF (mg)	3	5	10	20	50

V.2.2. Half-cell configuration setup

All electrochemical measurements were conducted inside a PEEK-lined, airtight press cell equipped with stainless steel stamps (Φ = 7 mm) as current collectors.

The half-cell assembly process is schematically illustrated in Figure V.4.

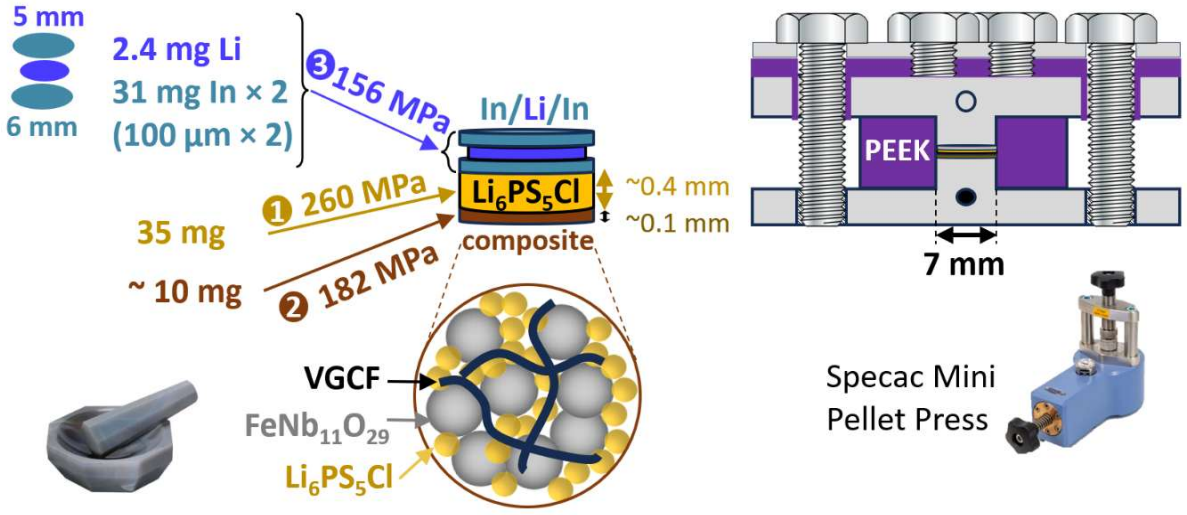

Figure V.4. Schematic illustration of the half-cell assembly processes. Steps ①–③ show the assembly sequence with corresponding uniaxial pressures. The cell stack includes the Li_6PS_5Cl separator, composite anode layer, and In/Li/In counter electrode.

Firstly, 35 mg of Li_6PS_5Cl was evenly spread in the cell and uniaxially pressed between two stamps/plungers under 1 T (260 MPa) for 3 minutes to form a uniform separator layer.

Secondly, ~10 mg of $FeNb_{11}O_{29}$ composite (active material loading ~10.9 mg·cm^{-2}) was then uniformly placed on one side of the separator. This amount is required to fully cover the area of cell interior (Φ = 7 mm). To allow fair comparison between different composite compositions, the active material loading was kept constant, while the total electrode mass was adjusted accordingly. All steps were performed carefully to ensure the homogeneous distribution and full coverage of the powders. The separator and the composite layer were densified with a uniaxial press at 0.7 T (182 MPa) for 3 minutes.

Thirdly, the counter electrode was prepared by stacking two indium discs (Φ = 6 mm, thickness = 0.127 mm, m ≈ 31.0 mg, Sigma-Aldrich 99.99%) and one lithium disc (Φ = 5 mm, m ≈ 2.5 mg) in In/Li/In configuration, which was then gently pressed onto the stamp. This stamp

is placed on the opposite side of the Li_6PS_5Cl separator, and the cell is subjected to final pressing step at 0.6 T (156 MPa) for 3 minutes. Before all tests, a resting duration of 24 h is necessary for Li−In alloy formation and pressure equilibration inside the cell. To ensure comparison, the practical parameters, such as applied pressure and material quantities, were maintained consistent for all experiments.

V.2.3. Benchmarking of the electrode composites

V.2.3.1. Rate capability tests

All galvanostatic cycling tests with potential limitations in this work were conducted in half-cells within a voltage window of 0.4–2.4 V vs. Li^+/Li−In, which equivalent to 1.0–3.0 V vs. Li^+/Li, similar to liquid electrolyte systems. The nominal capacity, 1 C, is defined as the exchange of 12 Li^+ ions per hour per $FeNb_{11}O_{29}$ formula unit, corresponding to a specific capacity of 209 $mAh \cdot g^{-1}$.

Concerning rate capability tests, current rates of 1, 2, 5, 10, 20, and 50 Li^+/h per formula unit were applied, followed by a return to 1 Li^+/h, with each rate held for 5 cycles. These conditions correspond to C-rates from C/12 to ~4.2 C, with equivalent gravimetric and areal current densities summarised in Table V.2.

Table V.2. Rate capability test expressed in terms of Li^+ exchanged per hour per formula unit, C-rate, gravimetric ($mA \cdot g^{-1}$) and areal ($mA \cdot cm^{-2}$) current densities.

Li^+/h	1	2	5	10	20	50
C-rate	C/12	C/6	0.4C	0.8C	1.7C	4.2C
$mA \cdot g^{-1}$	17.4	34.8	87	174	348	870
$mA \cdot cm^{-2}$	0.19	0.38	0.95	1.9	3.8	9.5

For comparison, a liquid electrolyte-based coin cell was assembled and tested under similar conditions. This cell used a conventional configuration of $FeNb_{11}O_{29}$: PVdF: Super P = 80:10:10 (wt.%) coated on Cu current collector, paired with Li metal as the counter/reference electrode and Whatman glass fiber separator soaked in 1M $LiPF_6$ in EC: DMC (3/7 by volume) as electrolyte. The active material loading is around 10 $mg \cdot cm^{-2}$, similar to that of solid-state cells. Rate capability measurements were then carried out following the same protocol.

V.2.3.2. Electronic and ionic conductivity measurements

Two symmetric cell configurations were used to determine the electronic and ionic conductivity of the electrode composite (Figure V.5), following reported methods [197,198], with some modifications to adapt to the cell dimensions in the laboratory.

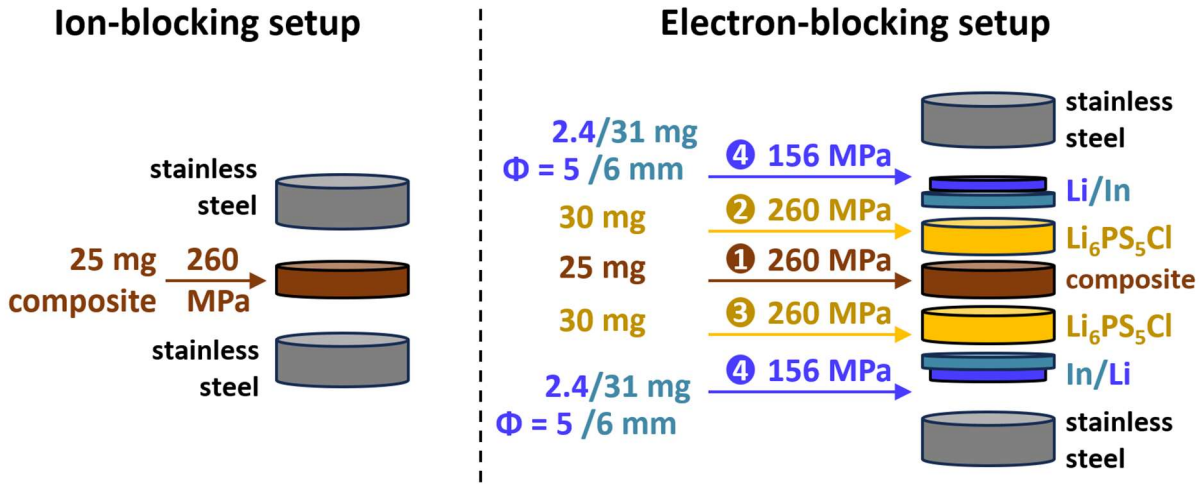

Figure V.5. Schematics of ion-blocking (left) and electron-blocking (right) setups for measuring electronic and ionic conductivity, respectively. Numbered steps indicate pressing sequence and applied pressures.

For ion-blocking setup (stainless steel | composite | stainless steel), 25 mg of composite was placed in the cell and uniaxially pressed under 1 T for 3 minutes. The two stainless steel plungers play the role as the ion-blocking electrodes, allowing only electronic transport to be measured. Electron-blocking setup was used to measure ionic conductivity, in which a sandwich stack of Li−In | Li_6PS_5Cl | composite | Li_6PS_5Cl | Li−In was assembled: 25 mg of composite was pressed, followed by the addition and densification of 30 mg Li_6PS_5Cl on each side, one at a time. Finally, indium and lithium discs were placed on both sides and pressed at 0.6 T. Before the conductivity test, a resting duration of 24 h was applied.

Direct current (DC) polarization with a stepwise voltage protocol was conducted using ion- or electron-blocking setups to determine the effective electronic and ionic conductivity of the composite. In each step, a constant voltage was applied, and the current response was recorded in 1 h until equilibrium. Voltage steps of 5 − 30 mV or 1 – 6 mV were selected to keep the current within the instrument's resolution range. Conductivity was then calculated using the equation $\sigma = L/(R \times S)$, where R is the steady-state resistance obtained from linear fitting of the stabilized current and the voltage step ($R = \Delta V/I$), L and S are the pellet thickness and area. For electron-blocking setup, assuming very low resistance of Li−In layers, the resistance of two Li_6PS_5Cl layers (calculated using $R = L/(\sigma \times S)$) is subtracted from the total resistance before the calculation of ionic conductivity for the composite.

V.2.4. Optimized composite characterization

The optimized composite is chosen for the following electrochemical tests.

V.2.4.1. Long-term cycling

Long-term galvanostatic cycling at the rate of C/6 (34.8 $mA \cdot g^{-1}$) was carried out for half-cells of the optimized composite for 50 cycles.

V.2.4.2. Asymmetric rate tests

Asymmetric rate tests were applied for half-cells containing optimised composite, in which either the charge or discharge current was fixed while the other was progressively increased. The purpose is to compare Li^+ insertion and extraction kinetics in $FeNb_{11}O_{29}$. In the D-rate test, the charge current was fixed at C/12, while the discharge current was varied stepwise every five cycles from D/12 to 4.2D, similar to the conventional rate protocol. Conversely, in the C-rate test, the discharge current was fixed at D/12 while the charge current was varied similarly.

V.2.4.3. Constant current - constant voltage (during discharge) (CC-CV)

A rate capability test was conducted but with slight modifications. A voltage hold was applied at the end of discharge to maximize lithium insertion into the active material. This constant-voltage step was maintained until the current dropped below C/40 (0.022 mA), or for a maximum of 5 hours, whichever limit was reached first.

V.2.4.4. Cyclic voltammetry

Cyclic voltammetry was performed on a solid-state half-cell using the optimized composite, and a liquid electrolyte-based coin cell to investigate its redox behavior and lithium-ion diffusion properties. Measurements were conducted within the same electrochemical window (1.0–3.0 V vs. Li^+/Li) at increasing scan rates of 0.10, 0.15, 0.20, 0.25, and 0.30 $mV \cdot s^{-1}$. The resulting voltammograms were analysed qualitatively based on the characteristic anodic and cathodic peaks and quantitatively using the Randles–Ševčík equation [199,200] to estimate Li^+ diffusion coefficients D ($cm^2 \cdot s^{-1}$), which relates the peak current to the square root of the scan rate:

$$i_p = (2.69 \times 10^5) n^{3/2} A C D^{1/2} v^{1/2}$$

- i_p is the peak current (A)
- The constant 2.69×10^5 has a unit of C mol^{-1} $V^{-1/2}$
- n is the number of electrons transferred; n = 1 for $Nb^{5+/4+}$ redox couple
- S is electrode surface area
- C is the concentration of redox species ($mol \cdot cm^{-3}$) in the electrode, calculated from the mass of active material and electrode volume (area × thickness)

V.2.5. Pre- and post-cycling analyses

The optimized composite was further examined using several *ex situ* techniques to investigate the changes in the morphology, composing phases and cell parameters, electronic states of the elements in the electrode composite before and after cycling. Three samples were analyzed. The first one is either pristine $FeNb_{11}O_{29}$ powder or pristine composite, as a reference. Second, the compacted sample, prepared by evenly distributing 10.0 mg of pristine composite into the cell and pressing it under 0.7 T. The cell was then disassembled, and the pellet was broken to recover the powder. The third sample was the composite after 50 cycles at C/6, which was recovered by disassembling the cell and scraping the cycled composite on the plunger.

V.2.5.1. X-ray diffraction

Two samples were analysed: (1) pristine and (2) cycled composite by X-ray diffraction (XRD). Measurements were acquired using a Panalytical X'pert Spinner diffractometer (equipped with Cu $K\alpha_{1,2}$ X-ray source) in Bragg-Brentano θ-θ geometry, within the angular range of 10-70° and with a step size of 0.033°. All the air-sensitive samples were protected using a Kapton® polyimide film covered on a silicon zero-background sample holder.

V.2.5.2. Scanning electron microscopy

Scanning electron microscopy (SEM) was performed using FEI Quanta 200 FEG. Energy-dispersive X-ray spectroscopy (EDS) was used alongside SEM to check the elemental distribution in the electrode. Three composite samples were investigated: (1) pristine composite, (2) compacted composite, and (3) the composite after 50 cycles. The sample preparation was carried out inside an Ar-filled glovebox, where the samples were deposited onto the carbon tape of the sample holder and then sealed in airtight vials and quickly transferred to the SEM chamber. This transfer process exposes the sample to air for less than 10 seconds.

V.2.5.3. X-ray photoelectron spectroscopy

X-ray photoelectron spectroscopy (XPS) was conducted on three samples: (1) pristine $FeNb_{11}O_{29}$ powder, (2) compacted and (3) cycled composites. XPS measurements were carried out with a THERMO Escalab 250Xi spectrometer at IPREM Institute in Pau, using focused monochromatic Al Kα radiation (hν = 1486.6 eV) with an X-ray spot size of 650 µm for longer axis ellipse. The spectrometer was calibrated with reference binding energies (BE) of clean samples: Cu (932.6 eV), Ag (368.2 eV) and Au (84.0 eV). The samples were never in contact with air nor moisture from their preparation to their analysis since the XPS spectrometer is directly connected to an Ar-filled glove box. The high-energy resolution spectra were recorded with constant pass energy of 20 eV. The charge neutralization was used for all the acquisitions.

The pressure in the analysis chamber was around 2×10^{-7} mbar during analyses. Short acquisition time spectra were recorded before each experiment to check that the samples were not subject to degradation during the X-ray irradiation. For the pristine material $FeNb_{11}O_{29}$, the binding energy scale was corrected using as reference the C 1s peak at 285.0 eV characteristic of the hydrocarbon species CH_2–CH_2. For the samples containing Li_6PS_5Cl, this correction was done with respect to the Cl 2p position at 199.0 eV. For data analysis, the spectra were mathematically fitted with Casa XPS software using a Shirley type background, and a combination of Gaussian and Lorentzian distributions for peaks fitting.

V.2.5.4. Electrochemical impedance spectroscopy (EIS)

EIS measurement was performed on a VSP impedance analyzer (Biologic), with an excitation voltage of 10 mV in the frequency range of 1 MHz - 100 mHz, and 10 points per decade were recorded. DRT analysis was performed with RelaxIS Online DRT (rhd instruments), using the radial-basis-function (RBF) discretization approach described by Ciucci and co-workers [201].

V.3. Results and discussions

V.3.1. Benchmarking of the electrode composites

V.3.1.1. Voltage profiles and differential capacity curves

Solid-state cells with $FeNb_{11}O_{29}$ composite electrodes with varying VGCF content, denoted as C*x*, were investigated using rate capability test to identify the optimized composition. For comparison, a coin cell using a liquid electrolyte and similar active material loading was tested under the same rate protocol. Their galvanostatic cycling performance was compared in Figure V.6, showing their voltage profiles and differential capacity (dQ/dV) curves at C/12 for the first two cycles. Both systems exhibit similar shapes of charge-discharge curves with characteristic sloping features, consistent with the comparable redox peaks at ~2.4 V, 1.65 V, and 1.3 V corresponding to $Fe^{3+/2+}$, $Nb^{5+/4+}$ and $Nb^{4+/3+}$ redox couples, respectively. These results confirm the successful implementation of $FeNb_{11}O_{29}$ in solid-state battery systems.

All composites exhibited a pronounced capacity drop from the first discharge to the first charge, reflected in their initial Coulombic efficiencies (iCEs). In every case, iCEs were below 90%, with the lowest values observed in the high-VGCF composites—81.1% for C30 and 85.8% for C20—while the others remained ~86%. In contrast, the liquid-electrolyte coin cell showed a much higher iCE of 96%. By the second cycle, the Coulombic efficiencies (CEs) of the solid-state cells improved to the range of 89–93%, whereas the coin cell achieved ~98%. The

considerably higher capacity observed in discharge suggests two possible scenarios: (1) a portion of the discharge current is consumed by side reactions, such as SSE decomposition or interfacial degradation, or (2) the charge process is unable to fully extract the lithium inserted during discharge. Both possibilities affect the long-term cycling stability and raise the question of chemical/electrochemical compatibility between $FeNb_{11}O_{29}$ and Li_6PS_5Cl.

Regarding capacity, a clear improvement was observed as the VGCF content decreased. In the second cycle at C/12, the charge capacities of C30, C20, C10, and C05 were ~145, 170, 195, and 212 mAh·g^{-1}, respectively. This superior performance of C05 is also evident in the dQ/dV plot, showing a stronger $Nb^{5+/4+}$ peak and, more prominently, a broader feature below 1.5 V. The reduced capacity at higher VGCF content may result from (i) surface functional groups on VGCF that promote irreversible reactions with Li_6PS_5Cl [40], and (ii) the poor densification of VGCF relative to $FeNb_{11}O_{29}$ or Li_6PS_5Cl, which may increase porosity in the composite pellets. On the other hand, lowering the VGCF content too far (C03) caused the discharge capacity to drop again (~185 mAh·g^{-1}), likely due to insufficient electronic conductivity.

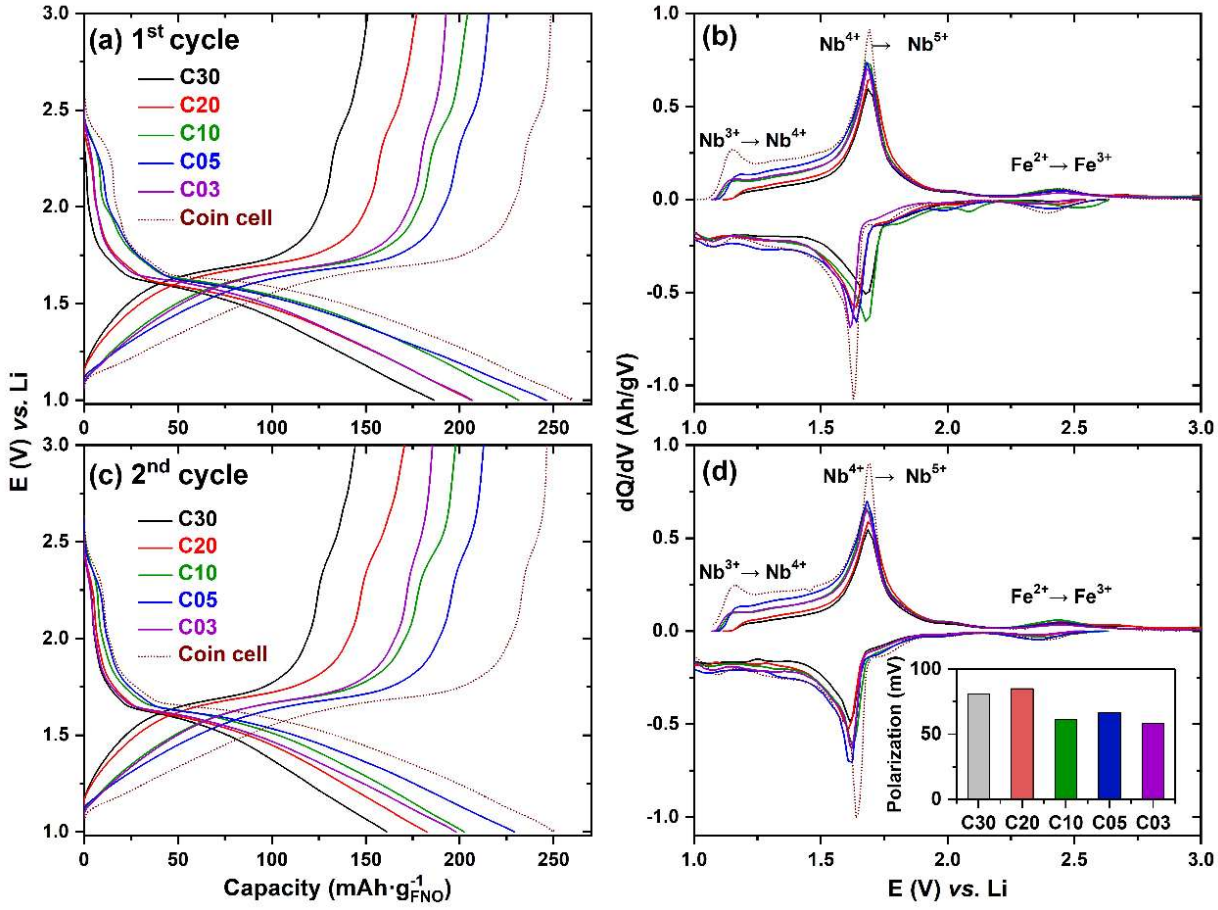

Figure V.6. Voltage profiles and differential capacity (dQ/dV) curves of five FNO composites and a liquid electrolyte-based coin cell, tested at C/12 current rate for the first cycle (a, b) and second cycle (c, d). The inset in (d) compares polarization values derived from peak separations in the dQ/dV curves. (1C = 2.28 mA·cm^{-2})

Cell polarisation can be quantitatively estimated from the voltage separation between the *d*Q/*d*V peaks during charge and discharge. In general, reducing the VGCF content in the composites leads to lower polarization. A similar trend is observed in the *d*Q/*d*V plots, though the peak separation does not follow a strictly monotonic pattern. However, composites with higher VGCF content, such as C30 and C20, exhibit larger polarization in the range of 80–100 mV, as shown in the inset bar chart of Figure V.6, while C10, C05 and C03 demonstrates a lower polarization (50–60 mV).

These trends in terms of capacity, coulombic efficiency and polarization indicate that the C05 composite is the best-performing composition, delivered the highest capacity, supported by the prominent low-voltage feature (< 1.5 V) associated with deeper Nb redox activity.

V.3.1.2. Rate capability tests

To further evaluate the performance of $FeNb_{11}O_{29}$ composites under practical cycling conditions, rate capability tests were conducted at increasing currents stepwise from C/12 to 4.2C, followed by a return to the initial rate (Figure V.7).

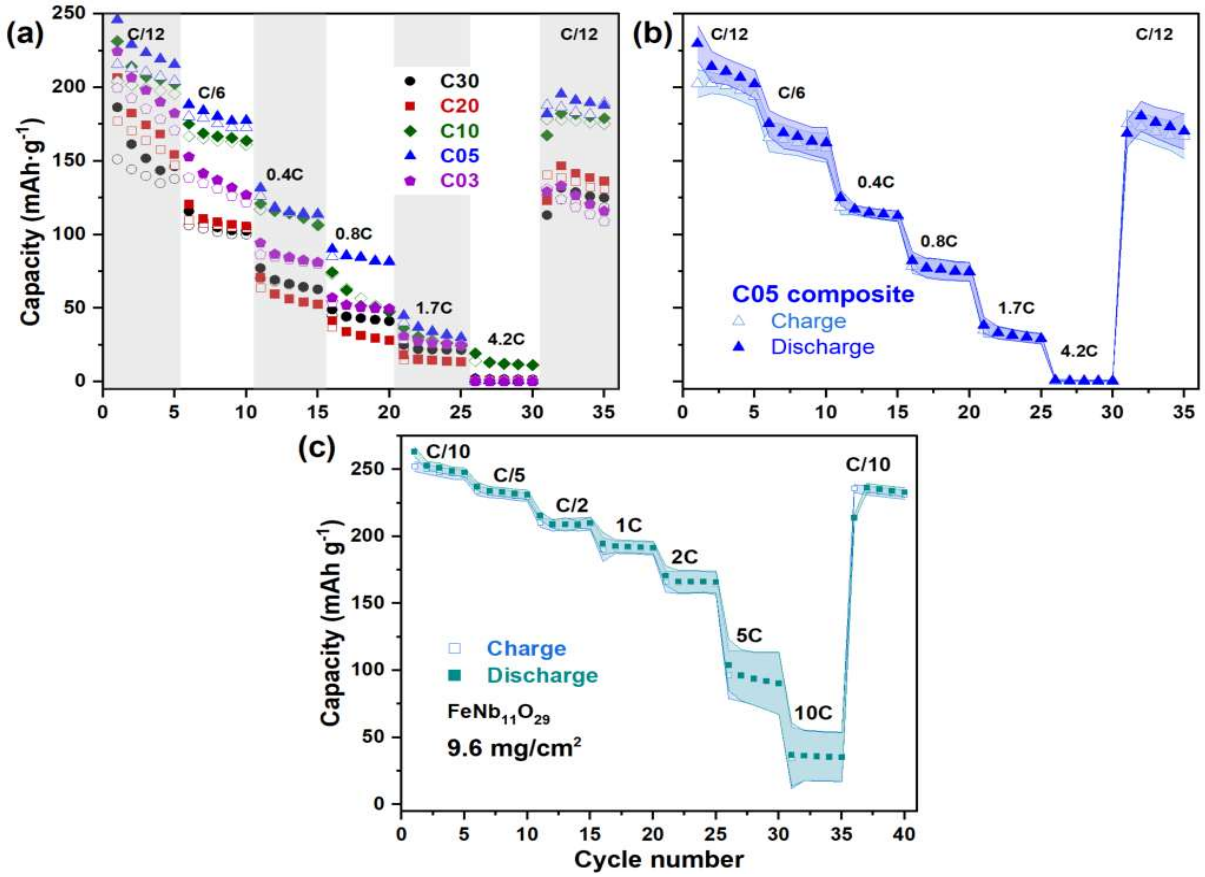

Figure V.7. Rate capability of (a) five composites in solid-state half-cells and reproducibility of (b) composite C05 and (c) $FeNb_{11}O_{29}$ in liquid electrolyte coin cells with comparable mass loading, averaged from four cells in each case. (1C = 2.28 mA·cm^{-2})

Across the entire current range, C05 composite consistently delivered the best performance, achieving > 220 mAh·g^{-1} at C/12 and retaining ~80 mAh·g^{-1}at 0.83C. Besides, reproducibility test on four C05-based cells (Figure V.7) showed highly consistent rate behaviour with small error margins, confirming the reliability of these tests. However, capacity retention remains limited, with a gradual decline observed, especially when cycled at higher current rates.

By contrast, high-VGCF composites (C30 and C20) exhibited substantially lower capacities and more severe capacity losses with increasing current, likely due to reduced contact between the composite components through the porous carbon network. The C10 composite demonstrated intermediate performance, whereas C03 performed reasonably well at low current rates but its capacity faded rapidly at higher rates, likely due to insufficient electronic conductivity. When the current rate was returned C/12, all composites showed partial capacity recovery, with C05 and C10 recovering most effectively.

Overall, the trends in capacity, CEs, polarization and rate capability suggest that the best performance was achieved for the $FeNb_{11}O_{29}$ composite with intermediate VGCF content. Specifically, C05 delivered the highest capacity and best rate performance, raising the question of how ion and electron transport affect the performance of solid-state cells.

V.3.1.3. Ionic and electronic conductivity tests of representative composites

To further investigate transport properties, the best-performing composite (C05) and the VGCF-richest one (C30) were examined using electron- and ion-blocking electrode setups with the DC polarization method (Figure V.8). The final equilibrium current at each voltage step was used to make the I–V plots, from which the resistance values were extracted via linear fitting and the effective values of σ_{ion} and σ_e were then calculated.

For C05, the electronic conductivity ($\sigma_e \approx 337$ mS·cm^{-1}) is about three orders of magnitude higher than its ionic value ($\sigma_{ion} \approx 0.110$ mS·cm^{-1}). Although modest, this ionic conductivity is sufficient to sustain Li^+ transport due to the well-dispersed $FeNb_{11}O_{29}$ and Li_6PS_5Cl particles observed in SEM (Figure V.15), consistent with its strong rate capability. In contrast, the C30 composite, with the largest VGCF fraction, exhibits an even higher electronic conductivity (~915 mS·cm^{-1}), nearly three times that of C05, reflecting the dominant carbon network for electronic conduction. However, its ionic conductivity (~0.099 mS·cm^{-1}) is slightly lower, suggesting that excessive carbon disrupts the Li_6PS_5Cl network and increases tortuosity for Li^+ migration. As a result, ionic transport becomes the bottleneck in C30, leading to higher overpotentials and poor rate behavior, whereas C05 achieves a more effective balance of ionic and electronic transport, enabling high capacity and robust rate performance. This optimized composite (C05) was therefore selected for further analysis.

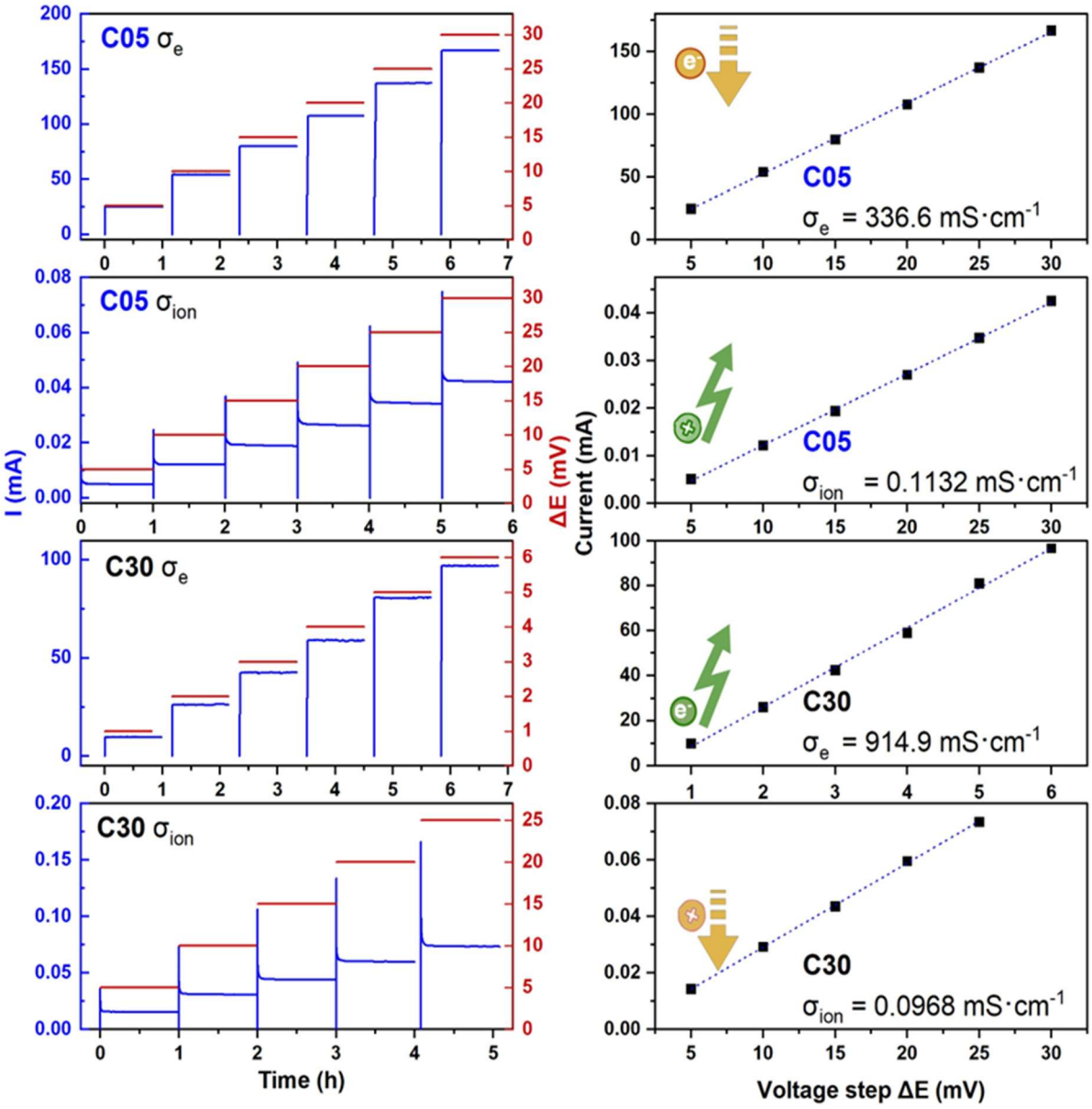

Figure V.8. DC polarization measurements for electronic and ionic conductivities of C05 and C30 composites. Left: Stepwise voltages (red) were applied, and current responses (blue) were recorded. Right: Current-voltage step plots were fitted linearly to extract resistance and calculate conductivity.

V.3.2. Comparison with other systems

V.3.2.1. $FeNb_{11}O_{29}$ in solid- and liquid-electrolyte cells

The performance of $FeNb_{11}O_{29}$ in solid- and liquid-electrolyte cells is compared based on rate capability test (Figure V.7) and Cyclic Voltammetry (Figure V.9).

At similar mass loadings, $FeNb_{11}O_{29}$ solid-state cells exhibit inferior rate capability (~30 $mAh \cdot g^{-1}$ at 1.7C) compared with liquid electrolyte coin-cells (~160 $mAh \cdot g^{-1}$ at 2C), as shown in Figure V.7.

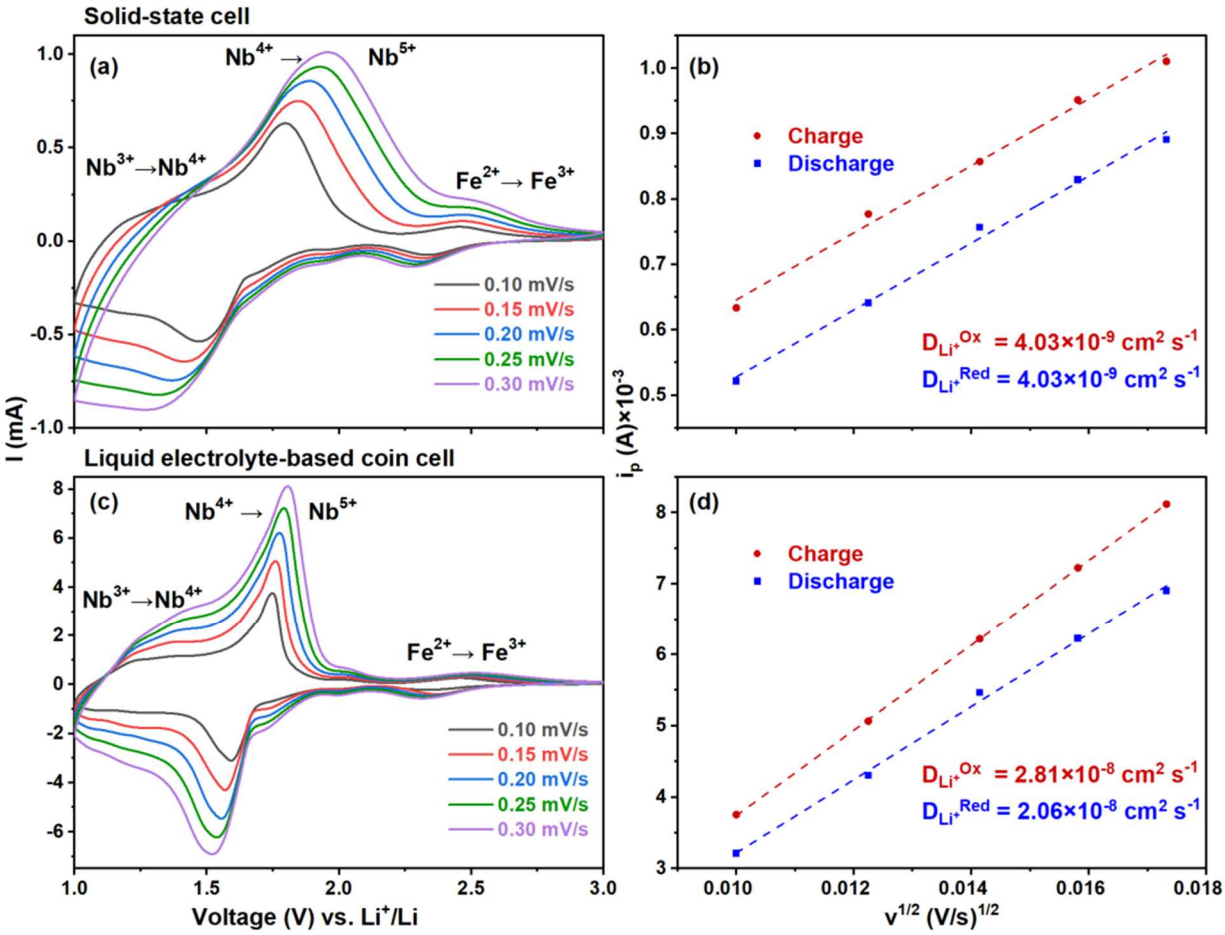

Figure V.9. Cyclic voltammetry of solid-state (top) and coin (bottom) cells at scan rates from 0.10 to 0.30 mV·s^{-1}. Left: CV curves. Right: Peak current vs. square root of scan rate, fitted using the Randles–Ševčík equation to estimate Li^+ diffusion coefficients.

This was also demonstrated by Cyclic Voltammetry, where analysis of $Nb^{5+/4+}$ redox peak gives apparent lithium-ion diffusivities of ~4 × 10^{-9} $cm^2 \cdot s^{-1}$ for solid-state cell, one order of magnitude lower than that in liquid electrolyte-based cell (~2 × 10^{-8} $cm^2 \cdot s^{-1}$) (Figure V.9). This reduced diffusivity and weaker rate performance could arise from limited ionic conductivity of the solid-state electrolyte compared with the liquid counterpart, as well as interfacial or microstructural limitations inherent to the solid-solid contacts. In solid-state cells, increasing the scan rate resulted in a pronounced increase of the peak separation (ΔE_p), which rose from 0.304 V at 0.1 mV·s^{-1} to 0.620 V at 0.3 mV·s^{-1}. This separation is significantly larger than that observed in coin cells of equivalent mass loading at identical scan rates (0.156 V at 0.1 mV·s^{-1} to 0.286 V at 0.3 mV·s^{-1}). These trends suggest a deviation from ideal reversible behavior, possibly due to kinetic limitations of electronic and ionic transport.

V.3.2.2. Performance of $FeNb_{11}O_{29}$ vs. other high-voltage materials in SSBs

$FeNb_{11}O_{29}$ shows strong promises when compared with other high-voltage negative electrode materials in Li-SSBs (Table V.3) [177–184]. Most reported cells typically used electrodes of low to moderate mass loadings (0.5–3 $mg \cdot cm^{-2}$), fabricated by various formulations and methods (slurry casting, uniaxial pressing, or pulsed laser deposition), often achieved higher capacities than $FeNb_{11}O_{29}$-based cells at comparable or higher current densities (see Table S3). However, the electrodes in this study were uniaxially pressed with a much high active material loading (~10 $mg \cdot cm^{-2}$) yet still delivered ~210 $mAh \cdot g^{-1}$ at C/12 and ~80 $mAh \cdot g^{-1}$ at 0.8C, which are competitive performance within the context of solid-state systems.

Table V.3. Electrochemical performance of some high-voltage negative electrode materials in half-cell SSBs

#	Electrode composition	Mass loading	Performance	Ref
1	$Li_4Ti_5O_{12}$:80Li_2S·20P_2O_5: acetylene black (27.3:63.6:9.1 wt.%) by uniaxial pressing	N/A	90 $mAh \cdot g^{-1}$ at 3.8 $mA \cdot cm^{-2}$, 25 °C	[177]
2	$Li_4Ti_5O_{12}$@LPS: LPS: VGCF: polybutadiene (PB) (5:4:1:0.5, weight) (LPS: 80Li_2S·20P_2O_5) Slurry-casted electrode	0.5 $mg \cdot cm^{-2}$	110 $mAh \cdot g^{-1}$ at 1C at 80 °C; sustained after 300 cycles	[178]
3	$Li_4Ti_5O_{12}$: PEO: carbon (75:10:15 wt.%) Slurry-casted electrode	3 $mg \cdot cm^{-2}$	150 $mAh \cdot g^{-1}$ at C/2 at 70 °C	[179]
4	$Li_4Ti_5O_{12}$ thin films by pulsed laser deposition	0.025 $mg \cdot cm^{-2}$	97 $mAh \cdot g^{-1}$ at C/7 at RT	[182]
5	NTWO: Li_6PS_5Cl: VGCF (6:3:1, weight) (NTWO: $Nb_{1.6}Ti_{0.32}W_{0.08}O_{5-\delta}$) By uniaxial pressing (Φ = 13 mm)	1.8 $mg \cdot cm^{-2}$	175 $mAh \cdot g^{-1}$ at 0.2 $A \cdot g^{-1}$ (1C) at 25 °C	[181]
6	$TiNb_2O_7$: PVdF: conductive SP-CNT (8:1:1 by weight) Slurry-casted electrode	N/A	241.3 $mAh \cdot g^{-1}$ at 1C at RT for Li|$Li_{1.3}Al_{0.3}Ti_{1.7}(PO_4)_3$ composite polymer|TNO-0.2	[180]
7	$FeNb_{11}O_{29}$: Li_6PS_5Cl: VGCF (40:50:5, weight), by uniaxial pressing (Φ = 7 mm)	10.9 $mg \cdot cm^{-2}$	~210 $mAh\ g^{-1}$ at C/12, RT (17.4 $mA \cdot g^{-1}$;0.19 $mA \cdot cm^{-2}$) ~80 $mAh\ g^{-1}$ at 0.83C, RT (174 $mA \cdot g^{-1}$; 1.9 $mA \cdot cm^{-2}$)	This work

V.3.3. Electrochemical characterizations of the optimized composite

From this point, the optimized composite C05 will be used for further characterizations.

V.3.3.1. Long-term cycling

Figure V.10 presents the long-term cycling performance of the optimized composite, averaged from 4 cells, at a moderate rate of C/6 over 50 cycles.

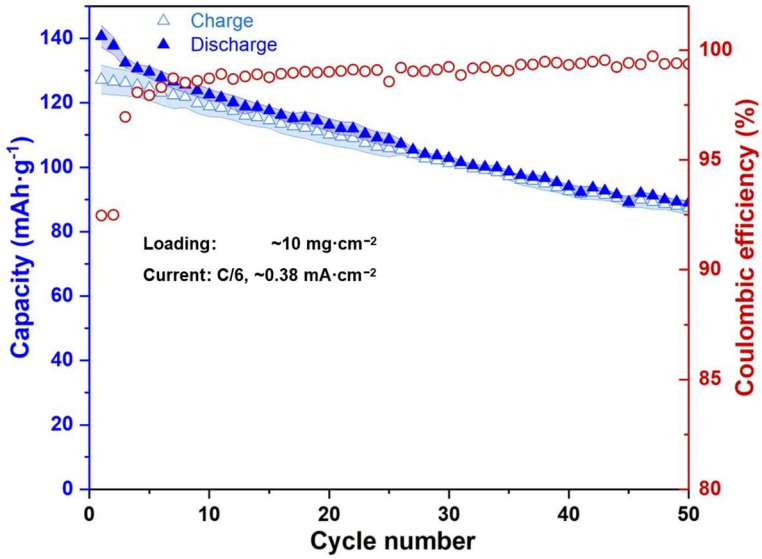

Figure V.10. Long-term cycling of the optimized composite at C/6, showing charge/discharge capacities, averaged from three cells (left axis) and coulombic efficiency (right axis) over 50 cycles

The cells deliver an initial charge capacity of ~127 mAh·g^{-1}, with an iCE of ~82%. From the 4th cycle, the CE remains consistently high (~98–99.8%), suggesting that the Li^+ ions can mostly participate in reversible intercalation after the first few cycles. A gradual capacity fade is observed over cycling: charge capacity remains above 100 mAh·g^{-1} for the first 30 cycles and declines to 87 mAh·g^{-1} after 50 cycles, equivalent to about 68% of the initial capacity. Despite its favourable transport characteristics, the composite still faces limitations in long-term stability, likely due to interfacial degradation, cumulative side reactions, or contact loss.

V.3.3.2. Asymmetric rate test

Asymmetric rate tests were conducted on half-cells containing the optimized composite to compare the kinetics of Li^+ insertion and extraction (Figure V.11).

At low currents (C/12 and C/6), both cases delivered similar capacities, indicating that lithium transport in $FeNb_{11}O_{29}$ is not kinetically limited under these conditions. However, from 0.4C onward, a clear asymmetry emerged: higher capacity was clearly observed for C-rate test in all cycles compared to the D-rate test. In the C-rate test, capacities remained relatively well retained, with ~50 mAh·g^{-1} (~20% of the initial value) still accessible at 1.7C. In contrast, the D-rate test showed rapid capacity fading beyond 0.4C, with nearly no capacity left at 1.7C.

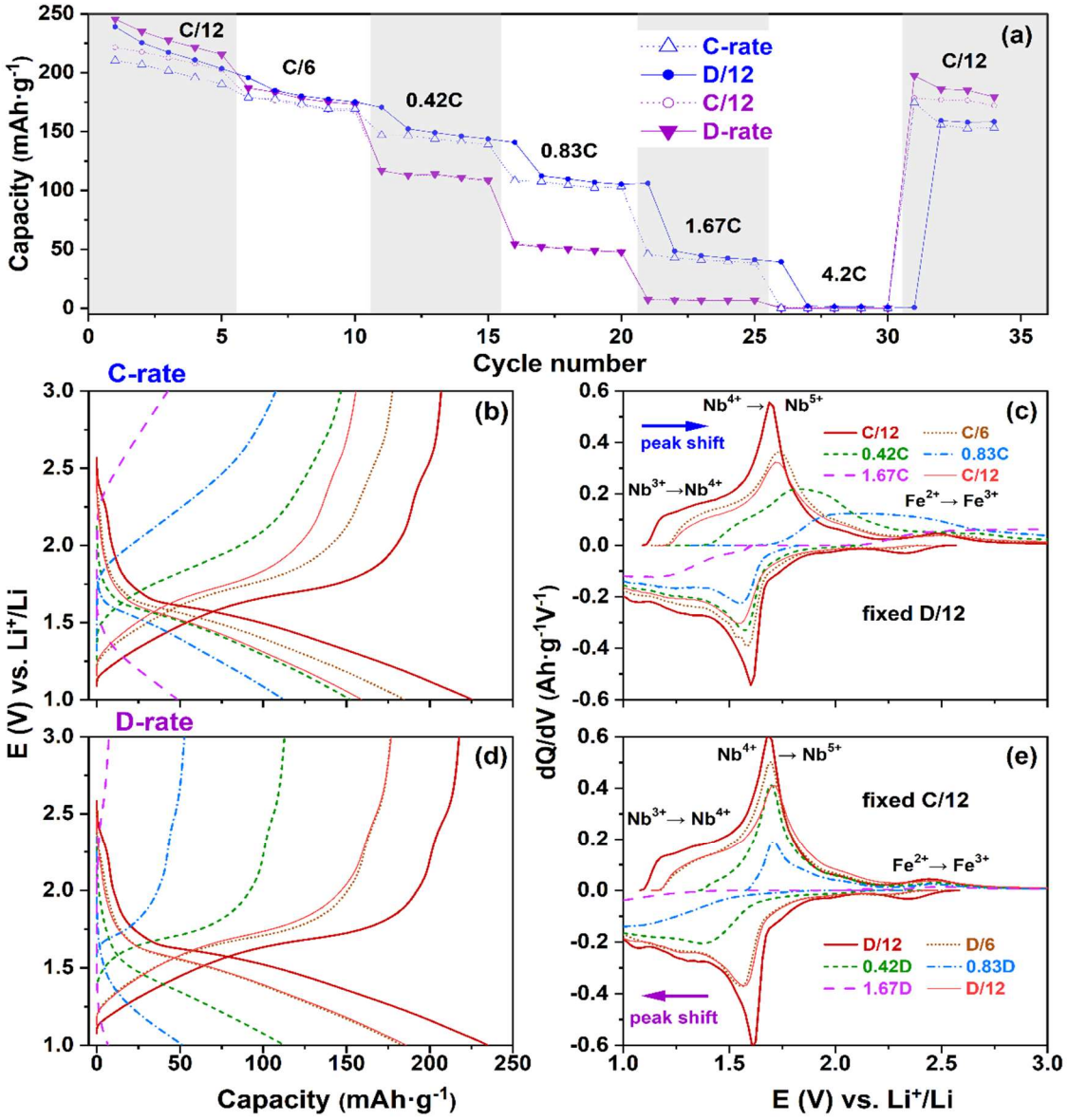

Figure V.11. Asymmetric rate tests of C05 composite: capacity retention (a); voltage profiles and differential capacity (dQ/dV) curves during C-rate (b-c) and D-rate tests (d-e).

This asymmetry kinetic behavior is further supported by the dQ/dV plots, where increasing current rates in both tests caused progressive broadening and suppression of the $Nb^{5+/4+}$ and $Nb^{4+/3+}$ peaks, along with gradual shifts in peak position. These changes were clearly more pronounced for the D-rate test: substantial peak broadening and strong peak shifts, reflecting higher overpotentials during discharge and sluggish Li^+ insertion under fast rates. This behavior indicates that Li^+ insertion (discharge) is more kinetically limited than Li^+ extraction (charge) in the composite, highlighting an intrinsic asymmetry in Li^+ transport kinetic. Such behavior was also observed in $FeNb_{11}O_{29}$-based liquid electrolyte cells (Figure V.12) and has also been reported for graphite electrodes [202].

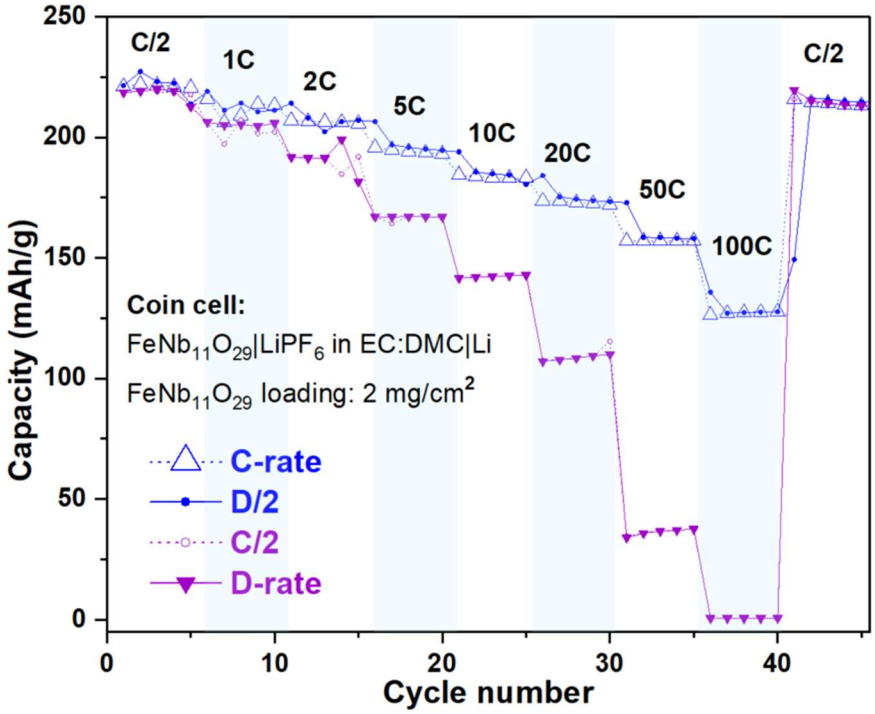

Figure V.12. Asymmetric rate test of $FeNb_{11}O_{29}$ in liquid electrolyte coin cell, showing limited Li^+ insertion kinetics, similar to observations in solid-sate cells

V.3.3.3. Constant current – constant voltage (CC–CV) cycling

Constant current–constant voltage (CC–CV) rate cycling was applied to mitigate the kinetic limitations of lithium insertion into $FeNb_{11}O_{29}$ (Figure V.13).

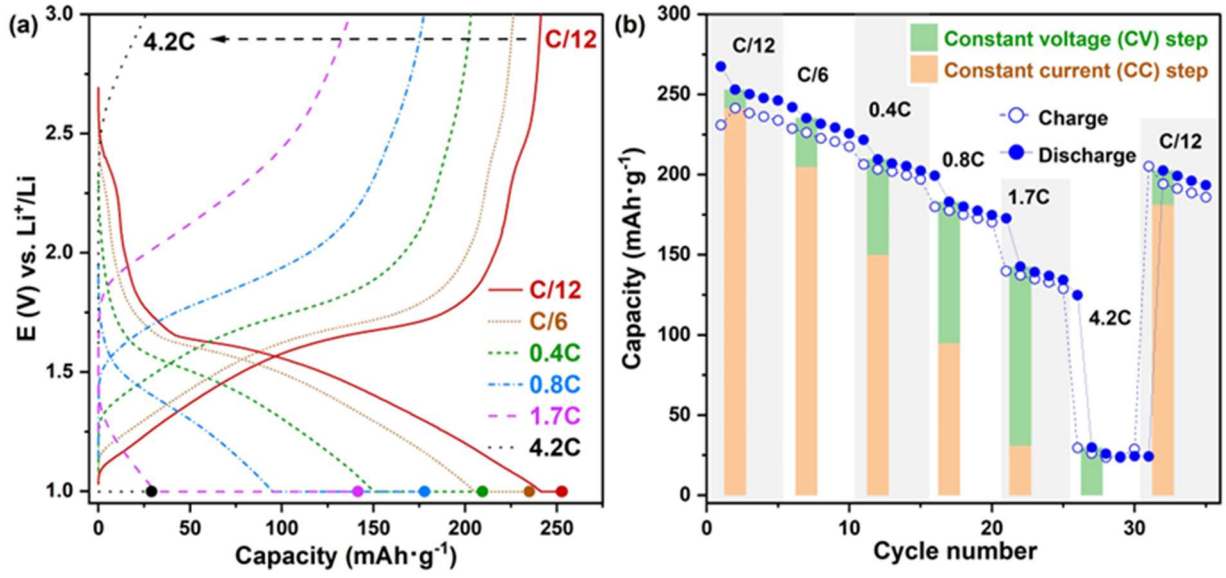

Figure V.13. Charge–discharge voltage profiles of the C05 composite at varying current rates (1–50 Li^+/h) with a constant-voltage hold applied at the end of discharge (left). Corresponding cycling performance showing capacity contributions from constant-current (orange) and constant-voltage (green) steps (right).

A constant-voltage (CV) hold was introduced at the end of each discharge to ensure complete lithiation. Since lithium insertion into $FeNb_{11}O_{29}$ is kinetically limited, a constant-voltage (CV) hold was applied at the end of each discharge during the rate test to ensure its complete lithiation. At low rates (C/12–0.42C), most of the capacity originated from the constant-current (CC) step, approaching values obtained in liquid-electrolyte coin cells. Beyond 0.83C, however, the CC contribution dropped sharply, and at 4.2C it became negligible, reflecting insufficient time for complete lithiation under high currents. At the highest rate (4.2C), the discharge profile becomes steep, with minimal capacity delivered during the CC step.

The application of a CV step effectively relieves kinetic limitations and promotes deeper lithium insertion. As the current rate increases and the CC step becomes less effective, the CV step accounts for a progressively larger contribution to the total capacity. This trend is evident in Figure V.13b, where the green bars representing the CV contribution become dominant at 1.67C and 4.2C. Importantly, capacity fully recovers when the current returns to C/12, confirming that the CV step enables reversible lithiation rather than driving parasitic reactions. Overall, these findings demonstrate that the intrinsic kinetic barrier to lithium insertion at high current rates can be partially mitigated by incorporating a CV hold, thereby improving capacity utilization and achieving more complete lithiation.

V.3.4. Pre- and post-cycling analyses

To investigate the evolution of the electrode during operation, pre- and post-cycling analyses were carried out to examine changes in phase composition, morphology, and the electronic states of the elements in the optimized composite.

V.3.4.1. X-ray diffraction

Ex situ XRD measurements were performed on the pristine and cycled composite. Le Bail refinements of their XRD patterns (Figure V.14) reveal more pronounced changes in the cell parameters of $FeNb_{11}O_{29}$, compared to little changes in those of Li_6PS_5Cl. Specifically, $FeNb_{11}O_{29}$ shows slight but consistent expansion along the *a*, *b*, and *c* axes after cycling (Table V.4), suggesting that a small amount of lithium remains trapped within the host framework at the end of charge. In contrast, the lattice parameter of Li_6PS_5Cl remains nearly unchanged, indicating the structural stability of the bulk electrolyte during cycling. However, its interaction and chemical stability with other components of composite electrode, i.e. $FeNb_{11}O_{29}$ and VGCF, need to be investigated with surface-sensitive techniques.

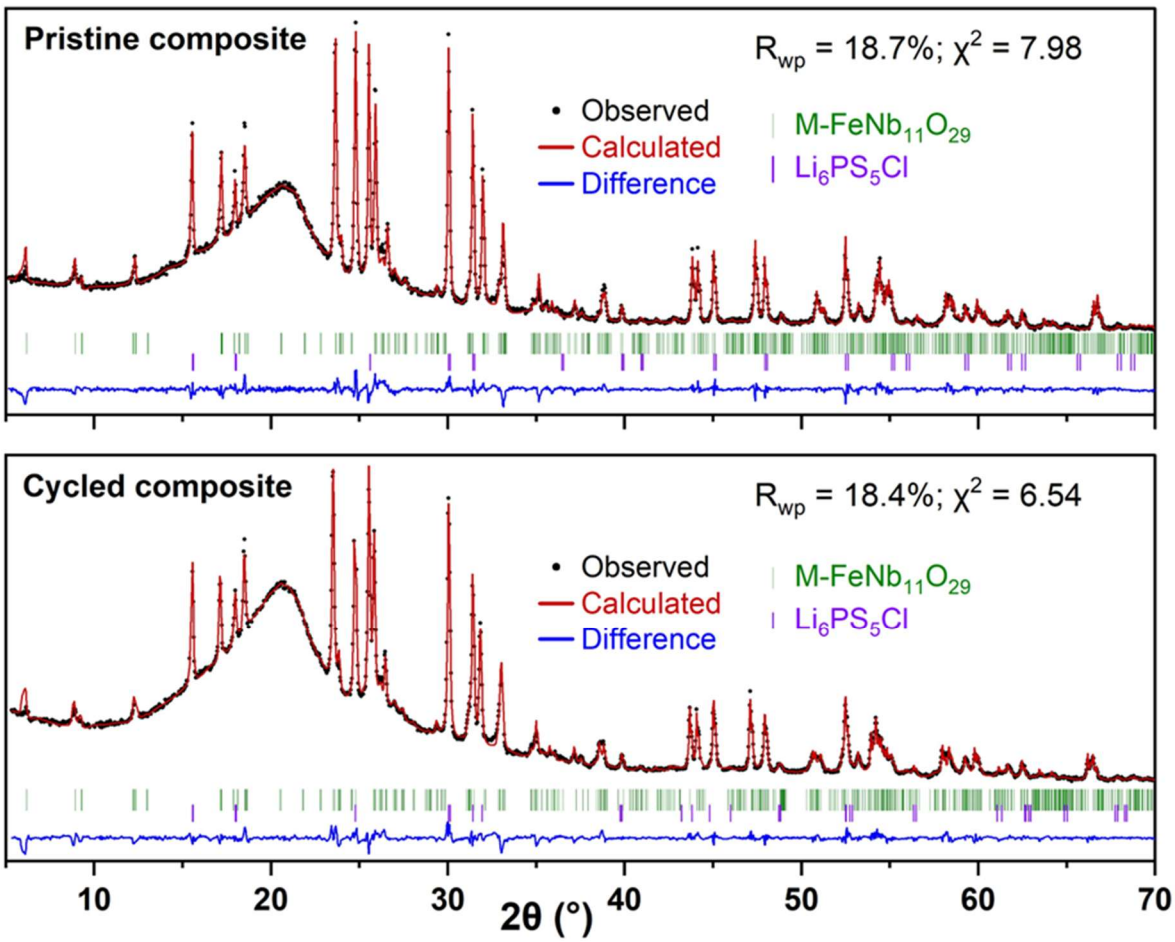

Figure V.14. Le Bail refinement results of pristine (top) and cycled (bottom) composite.

Table V.4. Le Bail-refined lattice parameters of $FeNb_{11}O_{29}$ and Li_6PS_5Cl in pristine and cycled samples

Phase	Lattice parameter	Pristine	Cycled sample
$FeNb_{11}O_{29}$	*a* (Å)	15.5893(10)	15.5942(10)
	b (Å)	3.8333(2)	3.8546(2)
	c (Å)	20.6312(11)	20.6997(11)
	β (°)	113.031(5)	112.908(4)
Li_6PS_5Cl	*a* (Å)	9.8524(4)	9.8537(5)

V.3.4.2. Scanning Electron Microscopy

SEM and EDX were used to examine the microstructure of pristine, compacted, and cycled composites (Figure V.15). The top and middle rows show secondary electron (SE) images at high and low magnifications, revealing surface morphology and texture, while the bottom row shows backscatter electron (BSE) images that highlight heavier elements Nb/Fe in $FeNb_{11}O_{29}$.

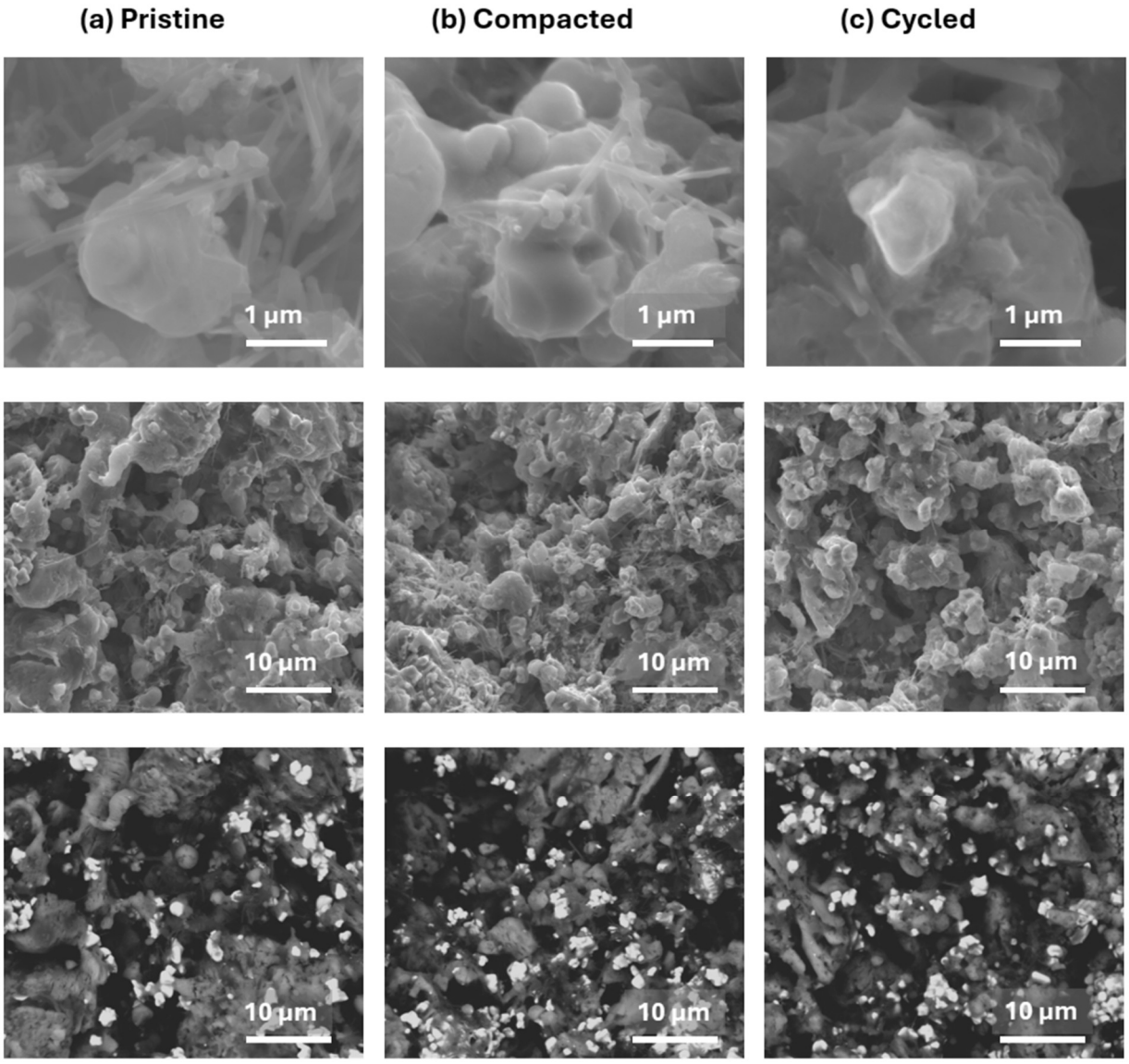

Figure V.15. SEM images of pristine, compacted and cycled composites at different scales: secondary electron images (top and middle), and backscattered electron images (bottom).

At high magnification, the fibrous VGCF structure is visible, with fibers ~0.1 µm in diameter and several micrometers in length, in close contact with $FeNb_{11}O_{29}$ and Li_6PS_5Cl particles. Medium-magnification SE images reveal similar surface texture in three samples, with VGCF fibers uniformly distributed. In BSE images, bright regions attributed to $FeNb_{11}O_{29}$ are evenly dispersed without significant agglomeration or phase segregation, indicating uniform mixing of three composite components. $FeNb_{11}O_{29}$ morphology and particle size remain unchanged after cycling.

These SEM images are further supported by EDS mapping (Figure V.16), also showing homogeneous elemental distribution, suggesting that all three samples exhibit a uniform phase dispersion and interconnected network, supporting efficient ionic and electronic transport. However, possible interfacial ageing during cycling may occur but is not evident in SEM.

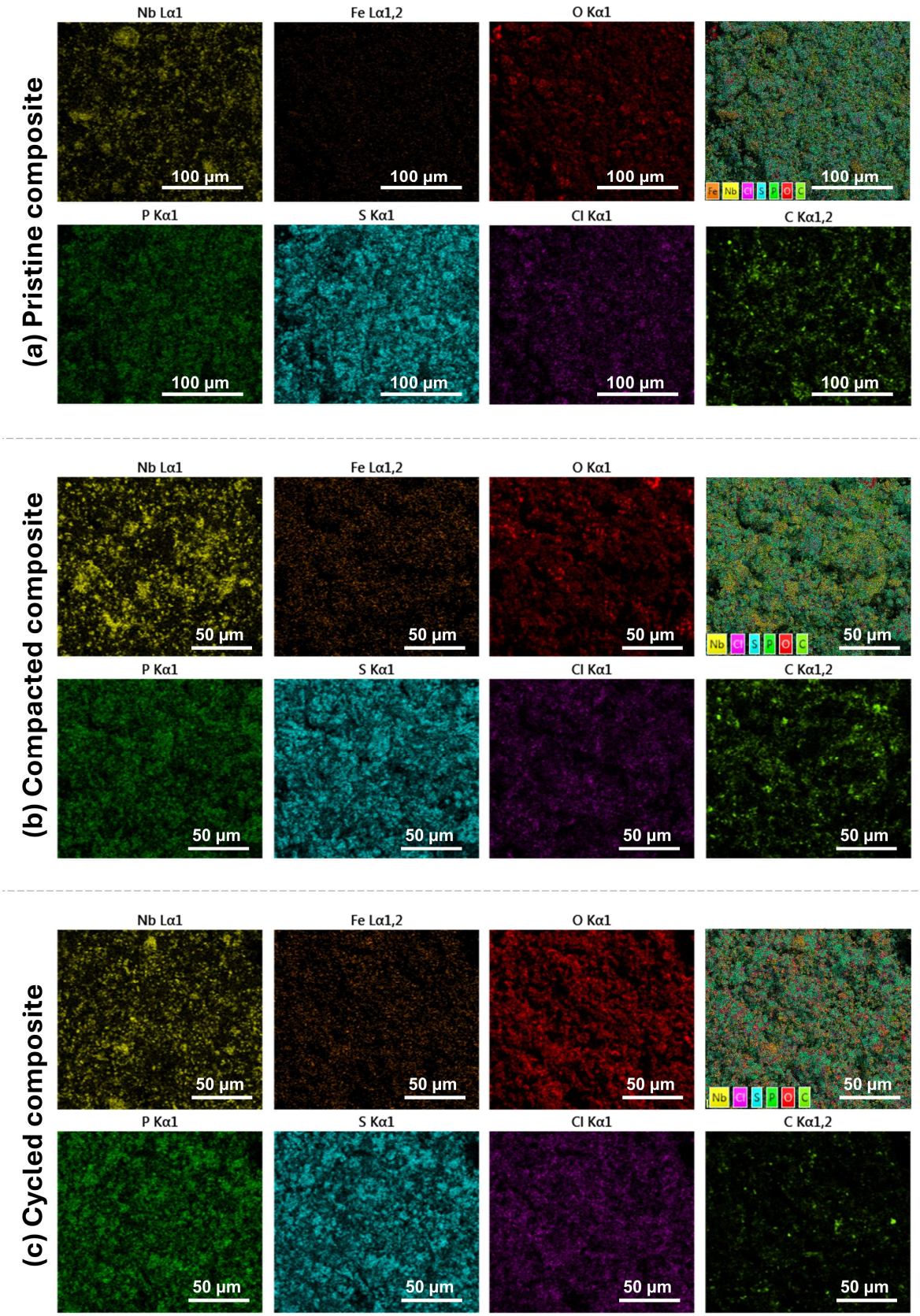

Figure V.16. Energy Dispersive Spectroscopy (EDS) mapping of the optimized composite at three states: (a) pristine, (b) compacted and (c) cycled, showing homogeneous elemental distribution

V.3.4.3. X-ray photoelectron spectroscopy

To probe changes in electronic and chemical states at the interface, X-ray photoelectron spectroscopy (XPS) was performed on three samples: pristine $FeNb_{11}O_{29}$ powder, compacted and cycled composites (Figure V.17, Table V.5).

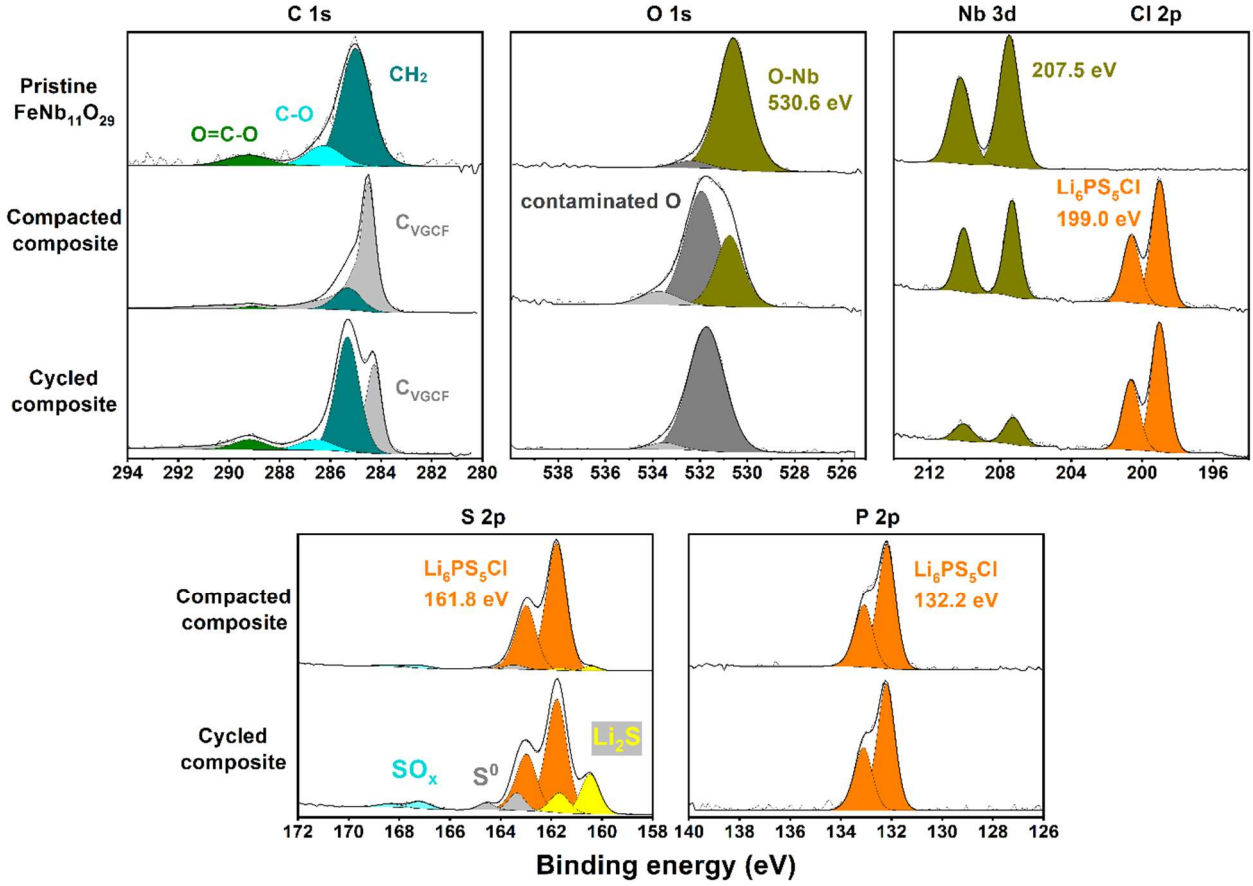

Figure V.17. XPS peak deconvolution of C 1s, O 1s, Nb 3d, Cl 2p, S 2p, and P 2p regions showing binding energies and chemical states in pristine $FeNb_{11}O_{29}$, compacted C, and cycled C05 composites.

Table V.5. Surface atomic percentage and elemental ratios of prisitine Li_6PS_5Cl, $FeNb_{11}O_{29}$, and C05 composites (compacted, aged) obtained from XPS

	$FeNb_{11}O_{29}$			Li_6PS_5Cl				S-containing decomposition products			$O_{contaminant}$	Elemental ratio of Li_6PS_5Cl			
	Nb	Fe	O	Li	P	S	Cl	Li_2S	S^0	SO_x		S/P	S/Cl	Li/S	P/Cl
$FeNb_{11}O_{29}$	24.5	0.8	46.5								5.1				
Compacted composite	0.7		3.1	20.5	3.3	12.5	3.3	0.4	0.4	0.4	5	3.8	3.8	1.6	1.0
Cycled composite	0.2			35	2.4	11.7	3.1	3.8	1.3	0.8	12.7	4.9	3.8	3.0	0.8

For pristine $FeNb_{11}O_{29}$, the peaks confirm Nb^{5+} in an oxide environment. Notably, iron is barely detectable on its surface, possibly due to its low stoichiometric amount. Nb 3d peak positions remain unchanged in compacted and cycled composites, suggesting little chemical degradation of $FeNb_{11}O_{29}$ during cycling.

Notable changes were observed in the XPS spectra of three samples:

- C 1s: CH_2, CO, and CO_2 contaminants were detected in all samples. VGCF signals appear in two composites, with lower intensity in the cycled sample.
- O 1s, Nb 3d: In the compacted sample, O–Nb and Nb 3d signals slightly decrease in intensity, indicating partial surface coverage of $FeNb_{11}O_{29}$ particles by other components. After extended cycling, the O–Nb peak disappears and Nb 3d intensities become considerable low, suggesting the formation of a new surface layered.
- S 2p, P 2p, Cl 2p: These Li_6PS_5Cl-related peak positions remain unchanged across all samples. Elemental ratios in the compacted sample match those of the pristine state, confirming negligible changes during processing. In contrast, the cycled sample shows reduced P/Cl and increased Li/S and S/P ratios, along with new peaks assigned to sulfur oxide species (SO_x), S^0 and Li_2S, as previously reported [203].

These findings suggest the formation of a chemically modified surface layer, likely a solid–electrolyte interphase (SEI), characterized by a clear presence of sulfur oxides, S and Li_2S. On the negative electrode, Li_6PS_5Cl has been reported to undergo decomposition into Li_2S, LiCl and Li_3P [181,203]. These products, especially Li_2S, with poor ionic and electronic conductivities, has been shown to significantly increase interfacial resistance at the negative electrode material/Li_6PS_5Cl contact [167].

V.3.4.4. Electrochemical impedance spectroscopy (EIS)

Electrochemical impedance spectroscopy (EIS) was used to follow the evolution of interfacial and charge transfer resistance in the solid-state half-cells at different stages: (A) pristine, (B) after the rate test, and (C) after 50 cycles at C/6. Figure V.18 presents the Nyquist plots together with the distribution of relaxation times (DRT) analysis, which decomposes the impedance spectra into characteristic frequencies: each peak corresponds to a distinct process, and its area reflects the associated impedance.

Given many components and interfaces in the cells, multiple processes could be included in the spectra, such as bulk and grain-boundary ionic resistance, charge transfer across the interfaces in $FeNb_{11}O_{29}$ composite electrode, interfacial resistances at $FeNb_{11}O_{29}$/Li_6PS_5Cl and Li-In/Li_6PS_5Cl contacts. However, due to the complexity of the system and the significant

overlap in the relaxation times of the interfacial processes (Figure V.18b), a complete deconvolution of these contributions is not possible. Therefore, the data will be analyzed in terms of impedance magnitude and characteristic frequency at the semicircle maximum (f_{peak}), which defines the characteristic relaxation time of the process, $\tau = 1/(2\pi f_{peak})$.

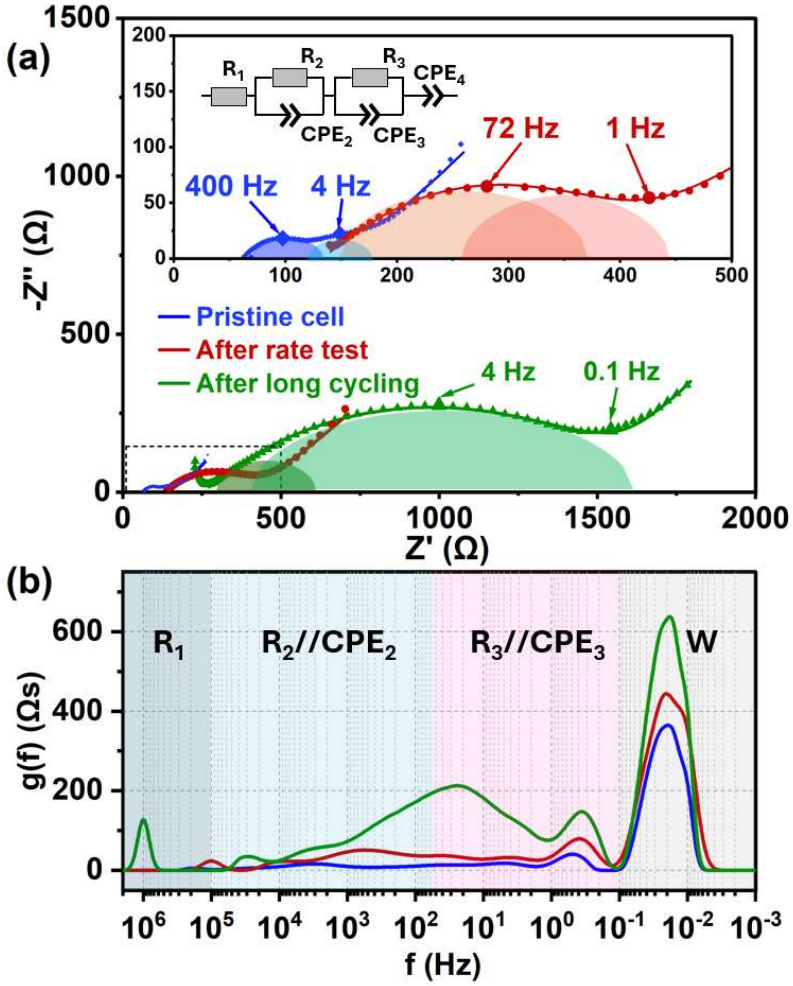

Figure V.18. Electrochemical impedance spectroscopy (EIS) of solid-state half-cells: pristine (blue), after rate test (red), and after long cycling (green). (a) Nyquist plots with equivalent circuit (inset). Characteristic frequencies are highlighted. (b) Distribution of relaxation times (DRT) analysis, resolving the impedance into frequency-dependent processes. The spectra reveal progressive increases in ohmic, interfacial & charge-transfer resistance, and a shift of the dominant relaxation toward lower frequencies upon cycling.

In this work, Nyquist plots exhibit two overlapping depressed semicircles, each modelled by a resistor (R) in parallel with a constant-phase element (CPE). These spectra can be fitted using the equivalent circuit in Figure V.18, which could be assigned to (i) resistance of the bulk SSE (R_1), (ii) interfacial resistance and non-ideal capacitance (R_2//CPE_2), (iii) a charge-transfer resistance in parallel with the electrode double-layer capacitance (R_3//CPE_3), and (iv) diffusion inside SSE particles (CPE_4) [179,204]. The CPE is characterized by its α parameter ($0 < \alpha \leq 1$), which quantifies the deviation from the ideal capacitive behavior (when $\alpha = 1$), due to electrode inhomogeneity.

At high frequencies, the x-axis intercept of these spectra, which represents total Ohmic resistance (R_1), shifts progressively to higher Z' value during cycling, reflecting a gradual increase in bulk ionic resistance. The initial spectrum (A) consists of two depressed semicircles, with f_{peak} values of around 400 Hz and 5 Hz, corresponding to a fast interfacial resistance and slow charge-transfer resistance process, respectively. In the DRT analysis, this slow process manifests as small peaks near 1 Hz in all three cases, with their peak areas increasing during cycling. As cycling progresses, the semicircles grow significantly in size, with Z' rising from ~250 Ω (spectrum A) to above 700 Ω (B) and finally extending beyond 1500 Ω (C). This agrees with the substantial increase in the fitted resistance values shown in Table V.6**.** Notably, the peak frequency shifts from 400 Hz (A) to 72 Hz (B) and finally to 4 Hz (C), indicating a progressive transition toward a slower process with longer relaxation time. This trend is further supported by pronounced features that emerge after extended cycling in the mid- and especially low-frequency region of the DRT plot. Such behavior is clear evidence of increasing relaxation time, which is likely due to the formation of the SEI. Furthermore, EIS semicircles observed in the cell after cycling are greatly compressed and the α value of the CPE deviates significantly from the ideal value of 1. These observations indicate that several semicircles, as in a transmission line model, would be required to fit the interfacial resistance. In this case, the transmission line model is thus simplified by using a CPE to represent an average sum of all the interfacial resistances. The existence of several semicircles indicates that the system is inhomogeneous after cycling as the SEI formation does not occur uniformly in all particles.

Table V.6. Impedance fitting results: R_1 (ohmic resistance), R_2 and R_3 (interfacial/charge-transfer processes) with corresponding α_{CPE} parameter and characteristic frequency (f) for each parallel R//CPE element.

	R_1	R_2 / α_{CPE2} / f_2	R_3 / α_{CPE3} / f_3
Pristine	63(1) Ω	42(1) Ω / 0.74(1) / 728 Hz	109(1) Ω / 0.43(1) / 1.5 Hz
After rate test	128(2) Ω	228(9) Ω / 0.26(2) / 113 Hz	204(2) Ω / 0.55(1) / 45 Hz
After prolonged cycling	180(1) Ω	279(2) Ω / 0.19(5) / 144 Hz	1180(14) Ω / 0.49(1) / 4.7 Hz

Overall, the gradual increase of ohmic resistance (R_1) and the growing dominance of the slow process indicate increased Li_6PS_5Cl ionic resistance and a substantial interfacial layer build-up. This SEI layer, rich in Li_2S, S^0, and SO_x species as confirmed by XPS, becomes thickened during cycling and impedes Li^+ transport across the $FeNb_{11}O_{29}/Li_6PS_5Cl$ interface, thereby accelerating impedance growth and hindering charge-transfer kinetics.

V.4. Conclusions and perspectives

This study systematically investigates the electrochemical performance and interfacial behavior of $FeNb_{11}O_{29}$-based electrodes in Li-ASSBs. Different electrode compositions were prepared to identify the optimum balance between the electroactive material and VCGF additive to ensure the best performance of $FeNb_{11}O_{29}$ in SSBs. Among the various formulations tested, the C05 composite—with an intermediate VGCF content—exhibited the best performance, delivering the highest reversible capacity, lowest polarization, and superior rate capability. This optimal behavior stems from a favorable balance between electronic conductivity and ionic percolation, as evidenced by conductivity measurements and electrochemical analysis.

Cyclic voltammetry and asymmetric rate protocols revealed kinetic limitations of $FeNb_{11}O_{29}$ in SSBs, particularly during lithium insertion at high rates, which could be partially mitigated by a constant-voltage step during discharge. This strategy could enhance lithium intercalation and improve capacity under fast cycling conditions.

Pre- and post-cycling characterizations further showed structural stability of the active material and SSE in the bulk, but there was chemical degradation at their interface. XRD revealed slight lattice expansion of $FeNb_{11}O_{29}$ upon cycling, indicating partial lithium retention, while the solid electrolyte Li_6PS_5Cl maintained its structural stability. SEM images confirmed morphological integrity in aged composite, with no significant change of microstructure among the samples. XPS analysis demonstrated the formation of an interfacial layer, rich in S, Li_2S and SO_x^{n-}, during cycling.

Overall, this work highlights the critical importance of microstructural optimization in composite electrodes for solid-state batteries. Excessive VGCF, despite its better electronic conductivity, may impede ionic transport or disrupt effective contact between the electrode and the solid electrolyte, leading to increased overpotentials and lower performance. Achieving a balanced electron–ion transport network is key to minimizing polarization, maximizing capacity, and maintaining long-term cycling stability. These discussions on VGCF content, interfacial reactions, and transport limitations provide valuable insights for the design of electrode composite architectures in solid-state batteries.

Future works could focus on further optimization of active material/SSE ratio to achieve higher mass loading while still maintaining a well-connected ionic conduction network. Also, the chemical/electrochemical degradation at the interface needs more investigation. Finally, $FeNb_{11}O_{29}$-based negative electrode composite can be tested in full cell configurations, for example, with high-voltage material such as NMC.

General conclusion

This PhD work investigated the Wadsley–Roth phase $FeNb_{11}O_{29}$ as a promising negative electrode material for Li-ion and solid-state batteries. The study addressed four main objectives: the influence of synthesis methods on microstructure and electrochemical behavior, the benchmarking of *operando* neutron diffraction tools, the evaluation of full-cell performance and ageing, and the implementation of $FeNb_{11}O_{29}$ in solid-state systems.

Firstly, the effect of synthesis route and particle size on electrochemical behavior was investigated. Microwave-assisted solid-state synthesis was demonstrated as a rapid and efficient method to prepare $FeNb_{11}O_{29}$ polymorphs, suppressing particle growth and enhancing Li^+ diffusion. The resulting monoclinic submicrometric powders delivered excellent performance, with 179 mAh g^{-1} and 90% capacity retention after 500 cycles at 2 A g^{-1}. Comparisons with furnace-heated powders confirmed the advantages of smaller particle size, while also highlighting the intrinsic fast kinetics of Wadsley–Roth phases, as even micrometric particles retained remarkable high-rate performance. These results establish particle-size control and microwave heating as effective approaches for enhancing performance of $FeNb_{11}O_{29}$ as well as other battery materials.

Secondly, via *operando* neutron diffraction experiments on the $FeNb_{11}O_{29}$ model material, we have systematically benchmarked different cell designs and diffractometers at the Institut Laue-Langevin (ILL). The coin-type ILLBAT#1 cell, while easy to assemble and capable of delivering high-quality data, suffered from strong polarization, limited cycling rate, and a reliance on deuterated electrolytes. In contrast, cylindrical cells enabled faster cycling and provided sufficiently good diffraction quality even with conventional electrolytes, making them better suited for routine studies, and particularly for investigating high-rate electrode materials. Moreover, the high-resolution D2B diffractometer was successfully employed for *operando* studies for the first time, opening perspectives for more widespread and accessible neutron diffraction in battery research.

Thirdly, the practical implementation of $FeNb_{11}O_{29}$ in full cells was explored through prototyping in 18650-format cells and systematic ageing studies in coin cells. The successful scale-up of synthesis and electrode processing confirms its feasibility for larger formats, while full-cell tests highlight its ability to deliver energy densities intermediate between graphite and $Li_4Ti_5O_{12}$. Ageing studies demonstrated the strong influence of operating conditions: elevated temperature, slow cycling, and high state of charge significantly accelerated capacity fading and resistance growth, which is linked to interfacial degradation and electrolyte instability. These findings highlight both the potential and the current limitations of $FeNb_{11}O_{29}$ in practical full

cells, as well as emphasizing the need for electrode optimization, interfacial stabilization, and post-mortem analyses to clarify degradation mechanisms.

Finally, $FeNb_{11}O_{29}$ was investigated as a negative electrode in Li solid-state batteries, with a focus on electrode composition and interfacial behavior. Among the tested formulations, an intermediate VGCF content achieved the best balance between electronic and ionic transport, delivering the highest reversible capacity, lowest polarization, and best rate capability. While the active material and the solid electrolyte (Li_6PS_5Cl) showed bulk stability, interfacial degradation occurred during cycling, with sulfur-rich compounds forming at the interface. These results highlight the critical importance of composite electrode optimization and interface engineering, as well as the need for future studies in full-cell configurations.

Overall, this thesis presents $FeNb_{11}O_{29}$ as well as other Wadsley-Roth phases as promising negative electrode materials that could bridge the gap between high-energy graphite and safe but low-energy $Li_4Ti_5O_{12}$. Its favourable structural stability, good rate capability even for micrometric particles, and compatibility with both liquid and solid-state systems are clear strengths. However, kinetic limitations, polarization, and interfacial degradation remain critical challenges. Beyond the findings specific to this material, this work contributes methodological advances in microwave-assisted synthesis, *operando* neutron diffraction benchmarking and prototyping insights, offering valuable perspectives for the development of Wadsley-Roth phases and other electrode materials in next-generation battery technologies.

References

[1] A. Manthiram, An Outlook on Lithium Ion Battery Technology, ACS Cent. Sci. 3 (2017) 1063–1069. https://doi.org/10.1021/acscentsci.7b00288.

[2] A. Manthiram, A reflection on lithium-ion battery cathode chemistry, Nat Commun 11 (2020) 1550. https://doi.org/10.1038/s41467-020-15355-0.

[3] R. Marom, S.F. Amalraj, N. Leifer, D. Jacob, D. Aurbach, A review of advanced and practical lithium battery materials, J. Mater. Chem. 21 (2011) 9938. https://doi.org/10.1039/c0jm04225k.

[4] J.B. Dunn, L. Gaines, J.C. Kelly, C. James, K.G. Gallagher, The significance of Li-ion batteries in electric vehicle life-cycle energy and emissions and recycling's role in its reduction, Energy Environ. Sci. 8 (2015) 158–168. https://doi.org/10.1039/C4EE03029J.

[5] N. Nitta, F. Wu, J.T. Lee, G. Yushin, Li-ion battery materials: present and future, Materials Today 18 (2015) 252–264. https://doi.org/10.1016/j.mattod.2014.10.040.

[6] L. Croguennec, M.R. Palacin, Recent Achievements on Inorganic Electrode Materials for Lithium-Ion Batteries, J. Am. Chem. Soc. 137 (2015) 3140–3156. https://doi.org/10.1021/ja507828x.

[7] D. Deng, Li-ion batteries: basics, progress, and challenges, Energy Science & Engineering 3 (2015) 385–418. https://doi.org/10.1002/ese3.95.

[8] M.S. Whittingham, Lithium Batteries and Cathode Materials, Chem. Rev. 104 (2004) 4271–4302. https://doi.org/10.1021/cr020731c.

[9] J.-M. Tarascon, M. Armand, Issues and challenges facing rechargeable lithium batteries, Nature 414 (2001) 359–367. https://doi.org/10.1038/35104644.

[10] J.B. Goodenough, Y. Kim, Challenges for Rechargeable Li Batteries, Chem. Mater. 22 (2010) 587–603. https://doi.org/10.1021/cm901452z.

[11] A. Manthiram, Materials Challenges and Opportunities of Lithium Ion Batteries, J. Phys. Chem. Lett. 2 (2011) 176–184. https://doi.org/10.1021/jz1015422.

[12] J.B. Goodenough, K.-S. Park, The Li-Ion Rechargeable Battery: A Perspective, J. Am. Chem. Soc. 135 (2013) 1167–1176. https://doi.org/10.1021/ja3091438.

[13] M. Armand, Building better batteries, 451 (2008).

[14] G.E. Blomgren, The Development and Future of Lithium Ion Batteries, J. Electrochem. Soc. 164 (2017) A5019–A5025. https://doi.org/10.1149/2.0251701jes.

[15] J.W. Choi, D. Aurbach, Promise and reality of post-lithium-ion batteries with high energy densities, Nat Rev Mater 1 (2016) 16013. https://doi.org/10.1038/natrevmats.2016.13.

[16] T. Kim, W. Song, D.-Y. Son, L.K. Ono, Y. Qi, Lithium-ion batteries: outlook on present, future, and hybridized technologies, J. Mater. Chem. A 7 (2019) 2942–2964. https://doi.org/10.1039/C8TA10513H.

[17] D. Larcher, J.-M. Tarascon, Towards greener and more sustainable batteries for electrical energy storage, Nature Chem 7 (2015) 19–29. https://doi.org/10.1038/nchem.2085.

[18] P. Molaiyan, S. Bhattacharyya, G.S. Dos Reis, R. Sliz, A. Paolella, U. Lassi, Towards greener batteries: sustainable components and materials for next-generation batteries, Green Chem. 26 (2024) 7508–7531. https://doi.org/10.1039/D3GC05027K.

[19] F. Wu, J. Maier, Y. Yu, Guidelines and trends for next-generation rechargeable lithium and lithium-ion batteries, Chem. Soc. Rev. 49 (2020) 1569–1614. https://doi.org/10.1039/C7CS00863E.

[20] B. Xu, D. Qian, Z. Wang, Y.S. Meng, Recent progress in cathode materials research for advanced lithium ion batteries, Materials Science and Engineering: R: Reports 73 (2012) 51–65. https://doi.org/10.1016/j.mser.2012.05.003.

[21] G. Zubi, R. Dufo-López, M. Carvalho, G. Pasaoglu, The lithium-ion battery: State of the art and future perspectives, Renewable and Sustainable Energy Reviews 89 (2018) 292–308. https://doi.org/10.1016/j.rser.2018.03.002.

[22] A. Tomaszewska, Z. Chu, X. Feng, S. O'Kane, X. Liu, J. Chen, C. Ji, E. Endler, R. Li, L. Liu, Y. Li, S. Zheng, S. Vetterlein, M. Gao, J. Du, M. Parkes, M. Ouyang, M. Marinescu, G. Offer, B. Wu, Lithium-ion battery fast charging: A review, eTransportation 1 (2019) 100011. https://doi.org/10.1016/j.etran.2019.100011.

[23] J.Y. Ko, F.A. Benavente, H. Ekström, G. Lindbergh, Modeling Capacity and Power Fade of Cylindrical NCA-Si Graphite Battery Cell in Electric Vehicles, Meet. Abstr. MA2020-02 (2020) 1612. https://doi.org/10.1149/MA2020-02211612mtgabs.

[24] Tesla Model 3 charging time, range, and cost | EVBox, (n.d.). https://evbox.com/en/electric-cars/tesla/tesla-model-3 (accessed June 16, 2025).

[25] S. Ahmed, I. Bloom, A.N. Jansen, T. Tanim, E.J. Dufek, A. Pesaran, A. Burnham, R.B. Carlson, F. Dias, K. Hardy, M. Keyser, C. Kreuzer, A. Markel, A. Meintz, C. Michelbacher, M. Mohanpurkar, P.A. Nelson, D.C. Robertson, D. Scoffield, M. Shirk, T. Stephens, R. Vijayagopal, J. Zhang, Enabling fast charging – A battery technology gap assessment, Journal of Power Sources 367 (2017) 250–262. https://doi.org/10.1016/j.jpowsour.2017.06.055.

[26] M. Weiss, R. Ruess, J. Kasnatscheew, Y. Levartovsky, N.R. Levy, P. Minnmann, L. Stolz, T. Waldmann, M. Wohlfahrt-Mehrens, D. Aurbach, M. Winter, Y. Ein-Eli, J. Janek, Fast Charging of Lithium-Ion Batteries: A Review of Materials Aspects, Advanced Energy Materials 11 (2021) 2101126. https://doi.org/10.1002/aenm.202101126.

[27] J. He, J. Meng, Y. Huang, Challenges and recent progress in fast-charging lithium-ion battery materials, Journal of Power Sources 570 (2023) 232965. https://doi.org/10.1016/j.jpowsour.2023.232965.

[28] M. Li, M. Feng, D. Luo, Z. Chen, Fast Charging Li-Ion Batteries for a New Era of Electric Vehicles, Cell Reports Physical Science 1 (2020) 100212. https://doi.org/10.1016/j.xcrp.2020.100212.

[29] M. Yuan, H. Liu, F. Ran, Fast-charging cathode materials for lithium & sodium ion batteries, Materials Today 63 (2023) 360–379. https://doi.org/10.1016/j.mattod.2023.02.007.

[30] M.T. F. Rodrigues, S.-B. Son, A.M. Colclasure, I.A. Shkrob, S.E. Trask, I.D. Bloom, D.P. Abraham, How Fast Can a Li-Ion Battery Be Charged? Determination of Limiting Fast Charging Conditions, ACS Appl. Energy Mater. 4 (2021) 1063–1068. https://doi.org/10.1021/acsaem.0c03114.

[31] T.R. Jow, M.B. Marx, J.L. Allen, Distinguishing Li+ Charge Transfer Kinetics at NCA/Electrolyte and Graphite/Electrolyte Interfaces, and NCA/Electrolyte and LFP/Electrolyte Interfaces in Li-Ion Cells, J. Electrochem. Soc. 159 (2012) A604. https://doi.org/10.1149/2.079205jes.

[32] K. Xu, A. von Cresce, U. Lee, Differentiating Contributions to "Ion Transfer" Barrier from Interphasial Resistance and Li+ Desolvation at Electrolyte/Graphite Interface, Langmuir 26 (2010) 11538–11543. https://doi.org/10.1021/la1009994.

[33] C. Song, S.H. Han, H. Moon, N.-S. Choi, Unlocking fast-charging capabilities of lithium-ion batteries through liquid electrolyte engineering, EcoMat 6 (2024) e12476. https://doi.org/10.1002/eom2.12476.

[34] I.V. Thorat, D.E. Stephenson, N.A. Zacharias, K. Zaghib, J.N. Harb, D.R. Wheeler, Quantifying tortuosity in porous Li-ion battery materials, Journal of Power Sources 188 (2009) 592–600. https://doi.org/10.1016/j.jpowsour.2008.12.032.

[35] C.R. Birkl, M.R. Roberts, E. McTurk, P.G. Bruce, D.A. Howey, Degradation diagnostics for lithium ion cells, Journal of Power Sources 341 (2017) 373–386. https://doi.org/10.1016/j.jpowsour.2016.12.011.

[36] K. Brandt, Historical development of secondary lithium batteries, Solid State Ionics 69 (1994) 173–183. https://doi.org/10.1016/0167-2738(94)90408-1.

[37] A. Yoshino, K. Sanechika, T. Nakajima, Secondary battery, US4668595A, 1987. https://patents.google.com/patent/US4668595A/en (accessed September 23, 2025).

[38] S.S. Zhang, The effect of the charging protocol on the cycle life of a Li-ion battery, Journal of Power Sources 161 (2006) 1385–1391. https://doi.org/10.1016/j.jpowsour.2006.06.040.

[39] J.C. Burns, D.A. Stevens, J.R. Dahn, In-Situ Detection of Lithium Plating Using High Precision Coulometry, J. Electrochem. Soc. 162 (2015) A959. https://doi.org/10.1149/2.0621506jes.

[40] J. Cannarella, C.B. Arnold, The Effects of Defects on Localized Plating in Lithium-Ion Batteries, J. Electrochem. Soc. 162 (2015) A1365. https://doi.org/10.1149/2.1051507jes.

[41] S. Tippmann, D. Walper, L. Balboa, B. Spier, W.G. Bessler, Low-temperature charging of lithium-ion cells part I: Electrochemical modeling and experimental investigation of degradation behavior, Journal of Power Sources 252 (2014) 305–316. https://doi.org/10.1016/j.jpowsour.2013.12.022.

[42] M. Petzl, M. Kasper, M.A. Danzer, Lithium plating in a commercial lithium-ion battery – A low-temperature aging study, Journal of Power Sources 275 (2015) 799–807. https://doi.org/10.1016/j.jpowsour.2014.11.065.

[43] S.S. Zhang, K. Xu, T.R. Jow, Study of the charging process of a LiCoO2-based Li-ion battery, Journal of Power Sources 160 (2006) 1349–1354. https://doi.org/10.1016/j.jpowsour.2006.02.087.

[44] K.G. Gallagher, S.E. Trask, C. Bauer, T. Woehrle, S.F. Lux, M. Tschech, P. Lamp, B.J. Polzin, S. Ha, B. Long, Q. Wu, W. Lu, D.W. Dees, A.N. Jansen, Optimizing Areal Capacities through Understanding the Limitations of Lithium-Ion Electrodes, J. Electrochem. Soc. 163 (2016) A138–A149. https://doi.org/10.1149/2.0321602jes.

[45] T. Waldmann, B.-I. Hogg, M. Kasper, S. Grolleau, C.G. Couceiro, K. Trad, B.P. Matadi, M. Wohlfahrt-Mehrens, Interplay of Operational Parameters on Lithium Deposition in Lithium-Ion Cells: Systematic Measurements with Reconstructed 3-Electrode Pouch Full Cells, J. Electrochem. Soc. 163 (2016) A1232. https://doi.org/10.1149/2.0591607jes.

[46] Z. Chen, Y. Qin, Y. Ren, W. Lu, C. Orendorff, E.P. Roth, K. Amine, Multi-scale study of thermal stability of lithiated graphite, Energy Environ. Sci. 4 (2011) 4023–4030. https://doi.org/10.1039/C1EE01786A.

[47] J. Asenbauer, T. Eisenmann, M. Kuenzel, A. Kazzazi, Z. Chen, D. Bresser, The success story of graphite as a lithium-ion anode material – fundamentals, remaining challenges, and recent developments including silicon (oxide) composites, Sustainable Energy Fuels 4 (2020) 5387–5416. https://doi.org/10.1039/D0SE00175A.

[48] H. Zhang, Y. Yang, D. Ren, L. Wang, X. He, Graphite as anode materials: Fundamental mechanism, recent progress and advances, Energy Storage Materials 36 (2021) 147–170. https://doi.org/10.1016/j.ensm.2020.12.027.

[49] L.F. Li, B. Xie, H.S. Lee, H. Li, X.Q. Yang, J. McBreen, X.J. Huang, Studies on the enhancement of solid electrolyte interphase formation on graphitized anodes in LiX-

carbonate based electrolytes using Lewis acid additives for lithium-ion batteries, Journal of Power Sources 189 (2009) 539–542. https://doi.org/10.1016/j.jpowsour.2008.10.063.

[50] C. Wang, S. Wang, L. Tang, Y.-B. He, L. Gan, J. Li, H. Du, B. Li, Z. Lin, F. Kang, A robust strategy for crafting monodisperse Li4Ti5O12 nanospheres as superior rate anode for lithium ion batteries, Nano Energy 21 (2016) 133–144. https://doi.org/10.1016/j.nanoen.2016.01.005.

[51] H. Zhang, W. Lin, L. Kang, Y. Zhang, Y. Zhou, S. Jiang, Highly safe lithium vanadium oxide anode for fast-charging dendrite-free lithium-ion batteries, Nanotechnology Reviews 13 (2024). https://doi.org/10.1515/ntrev-2023-0179.

[52] T. Nemeth, P. Schröer, M. Kuipers, D.U. Sauer, Lithium titanate oxide battery cells for high-power automotive applications – Electro-thermal properties, aging behavior and cost considerations, Journal of Energy Storage 31 (2020) 101656. https://doi.org/10.1016/j.est.2020.101656.

[53] K. Ariyoshi, R. Yamato, T. Ohzuku, Zero-strain insertion mechanism of Li[Li1/3Ti5/3]O4 for advanced lithium-ion (shuttlecock) batteries, Electrochimica Acta 51 (2005) 1125–1129. https://doi.org/10.1016/j.electacta.2005.05.053.

[54] J. Wolfenstine, U. Lee, J.L. Allen, Electrical conductivity and rate-capability of Li4Ti5O12 as a function of heat-treatment atmosphere, Journal of Power Sources 154 (2006) 287–289. https://doi.org/10.1016/j.jpowsour.2005.12.044.

[55] B. Gadermaier, K. Hogrefe, P. Heitjans, H.M.R. Wilkening, Broadband impedance spectroscopy of Li4Ti5O12: from nearly constant loss effects to long-range ion dynamics, Zeitschrift Für Anorganische Und Allgemeine Chemie 647 (2021) 2167–2171. https://doi.org/10.1002/zaac.202100143.

[56] C. Kim, N.S. Norberg, C.T. Alexander, R. Kostecki, J. Cabana, Mechanism of Phase Propagation During Lithiation in Carbon-Free Li4Ti5O12 Battery Electrodes, Advanced Functional Materials 23 (2013) 1214–1222. https://doi.org/10.1002/adfm.201201684.

[57] Y.-B. He, B. Li, M. Liu, C. Zhang, W. Lv, C. Yang, J. Li, H. Du, B. Zhang, Q.-H. Yang, J.-K. Kim, F. Kang, Gassing in Li4Ti5O12-based batteries and its remedy, Sci Rep 2 (2012) 913. https://doi.org/10.1038/srep00913.

[58] R.S. Roth, A.D. Wadsley, Mixed oxides of titanium and niobium: the crystal structure of TiNb24O62 (TiO2.12Nb2O5), Acta Cryst 18 (1965) 724–730. https://doi.org/10.1107/S0365110X65001664.

[59] R.S. Roth, A.D. Wadsley, Multiple phase formation in the binary system Nb2O5–WO3. I. Preparation and identification of phases, Acta Cryst 19 (1965) 26–32. https://doi.org/10.1107/S0365110X65002712.

[60] R.S. Roth, A.D. Wadsley, Multiple phase formation in the binary system Nb2O5–WO3. II. The structure of the monoclinic phases WNb12O33 and W5Nb16O55, Acta Cryst 19 (1965) 32–38. https://doi.org/10.1107/S0365110X65002724.

[61] R.S. Roth, A.D. Wadsley, Multiple phase formation in the binary system Nb2O5–WO3. III. The structures of the tetragonal phases W3Nb14O44 and W8Nb18O69, Acta Cryst 19 (1965) 38–42. https://doi.org/10.1107/S0365110X65002736.

[62] R.S. Roth, A.D. Wadsley, Multiple phase formation in the binary system Nb2O5–WO4. IV. The block principle, Acta Cryst 19 (1965) 42–47. https://doi.org/10.1107/S0365110X65002748.

[63] A. Magnéli, Structures of the ReO3-type with recurrent dislocations of atoms: `homologous series' of molybdenum and tungsten oxides, Acta Cryst 6 (1953) 495–500. https://doi.org/10.1107/S0365110X53001381.

[64] R.J. Cava, D.W. Murphy, E.A. Rietman, S.M. Zahurak, H. Barz, Lithium insertion, electrical conductivity, and chemical substitution in various crystallographic shear structures, Solid State Ionics 9–10 (1983) 407–411. https://doi.org/10.1016/0167-2738(83)90267-9.

[65] R.J. Cava, D.W. Murphy, S.M. Zahurak, Secondary Lithium Cells Employing Vanadium Tungsten Oxide Positive Electrodes, J. Electrochem. Soc. 130 (1983) 243. https://doi.org/10.1149/1.2119672.

[66] R.J. Cava, D.W. Murphy, S.M. Zahurak, Lithium Insertion in Wadsley-Roth Phases Based on Niobium Oxide, J. Electrochem. Soc. 130 (1983) 2345. https://doi.org/10.1149/1.2119583.

[67] N. Kumagai, Y. Koishikawa, S. Komaba, N. Koshiba, Thermodynamics and Kinetics of Lithium Intercalation into Nb2 O 5 Electrodes for a 2 V Rechargeable Lithium Battery, J. Electrochem. Soc. 146 (1999) 3203. https://doi.org/10.1149/1.1392455.

[68] J.-T. Han, Y.-H. Huang, J.B. Goodenough, New Anode Framework for Rechargeable Lithium Batteries, Chem. Mater. 23 (2011) 2027–2029. https://doi.org/10.1021/cm200441h.

[69] J.-T. Han, J.B. Goodenough, 3-V Full Cell Performance of Anode Framework TiNb2O7/Spinel LiNi0.5Mn1.5O4, Chem. Mater. 23 (2011) 3404–3407. https://doi.org/10.1021/cm201515g.

[70] B. Guo, X. Yu, X.-G. Sun, M. Chi, Z.-A. Qiao, J. Liu, Y.-S. Hu, X.-Q. Yang, J.B. Goodenough, S. Dai, A long-life lithium-ion battery with a highly porous $TiNb_2O_7$ anode for large-scale electrical energy storage, Energy Environ. Sci. 7 (2014) 2220–2226. https://doi.org/10.1039/C4EE00508B.

[71] K.J. Griffith, I.D. Seymour, M.A. Hope, M.M. Butala, L.K. Lamontagne, M.B. Preefer, C.P. Koçer, G. Henkelman, A.J. Morris, M.J. Cliffe, S.E. Dutton, C.P. Grey, Ionic and Electronic Conduction in TiNb2O7, J. Am. Chem. Soc. 141 (2019) 16706–16725. https://doi.org/10.1021/jacs.9b06669.

[72] J.W. Kim, V. Augustyn, B. Dunn, The Effect of Crystallinity on the Rapid Pseudocapacitive Response of Nb2O5, Advanced Energy Materials 2 (2012) 141–148. https://doi.org/10.1002/aenm.201100494.

[73] M. Catti, M.R. Ghaani, On the lithiation reaction of niobium oxide: structural and electronic properties of $Li_{1.714}$ Nb_2 O_5, Phys. Chem. Chem. Phys. 16 (2014) 1385–1392. https://doi.org/10.1039/C3CP54215G.

[74] V. Augustyn, J. Come, M.A. Lowe, J.W. Kim, P.-L. Taberna, S.H. Tolbert, H.D. Abruña, P. Simon, B. Dunn, High-rate electrochemical energy storage through Li+ intercalation pseudocapacitance, Nature Mater 12 (2013) 518–522. https://doi.org/10.1038/nmat3601.

[75] X. Wu, J. Miao, W. Han, Y.-S. Hu, D. Chen, J.-S. Lee, J. Kim, L. Chen, Investigation on Ti2Nb10O29 anode material for lithium-ion batteries, Electrochemistry Communications 25 (2012) 39–42. https://doi.org/10.1016/j.elecom.2012.09.015.

[76] D. Saritha, V. Pralong, U.V. Varadaraju, B. Raveau, Electrochemical Li insertion studies on WNb12O33—A shear ReO3 type structure, Journal of Solid State Chemistry 183 (2010) 988–993. https://doi.org/10.1016/j.jssc.2010.03.003.

[77] K.J. Griffith, A.C. Forse, J.M. Griffin, C.P. Grey, High-Rate Intercalation without Nanostructuring in Metastable Nb2O5 Bronze Phases, J. Am. Chem. Soc. 138 (2016) 8888–8899. https://doi.org/10.1021/jacs.6b04345.

[78] K.J. Griffith, A. Senyshyn, C.P. Grey, Structural Stability from Crystallographic Shear in TiO2–Nb2O5 Phases: Cation Ordering and Lithiation Behavior of TiNb24O62, Inorg. Chem. 56 (2017) 4002–4010. https://doi.org/10.1021/acs.inorgchem.6b03154.

[79] K.J. Griffith, K.M. Wiaderek, G. Cibin, L.E. Marbella, C.P. Grey, Niobium tungsten oxides for high-rate lithium-ion energy storage, Nature 559 (2018) 556–563. https://doi.org/10.1038/s41586-018-0347-0.

[80] S. Patoux, M. Dolle, G. Rousse, C. Masquelier, A Reversible Lithium Intercalation Process in an ReO_3-Type Structure PNb_9O_{25}, Journal of The Electrochemical Society 149 (2002) A391–A400. https://doi.org/10.1149/1.1455647.

[81] M. Wang, Z. Yao, Q. Li, Y. Hu, X. Yin, A. Chen, X. Lu, J. Zhang, Y. Zhao, Fast and extensive intercalation chemistry in Wadsley-Roth phase based high-capacity electrodes, Journal of Energy Chemistry 69 (2022) 601–611. https://doi.org/10.1016/j.jechem.2022.02.014.

[82] M.B. Preefer, M. Saber, Q. Wei, N.H. Bashian, J.D. Bocarsly, W. Zhang, G. Lee, J. Milam-Guerrero, E.S. Howard, R.C. Vincent, B.C. Melot, A. Van der Ven, R. Seshadri, B.S. Dunn, Multielectron Redox and Insulator-to-Metal Transition upon Lithium Insertion in the Fast-Charging, Wadsley-Roth Phase PNb_9O_{25}, Chem. Mater. 32 (2020) 4553–4563. https://doi.org/10.1021/acs.chemmater.0c00560.

[83] Battery Streak CBMM Mobility Tech Day, (n.d.). https://assets.niobium.tech/-/media/niobiumtech/documentos/2019-formula-e---berlin/nt_battery-streak-charge-lightning-fast.pdf (accessed July 4, 2025).

[84] Titanium Niobium Oxide (TNO) Anode Powder for Lithium-ion Batteries | NEI Corporation, (n.d.). https://www.neicorporation.com/products/batteries/cathode-anode-powders/lithium-ion/titanium-niobium-oxide/ (accessed July 10, 2025).

[85] Toshiba Starts Sample Shipments of "SCiB^{TM}Nb", its Innovative Rechargeable Lithium-ion Battery with Niobium Titanium Oxide Anode | News | Toshiba, (n.d.). https://www.global.toshiba/ww/news/corporate/2025/06/news-20250604-01.html (accessed July 10, 2025).

[86] Toshiba, Sojitz and CBMM Unveil an Ultra-Fast Charging Electric Bus Prototype Powered by Next-Generation Lithium-ion Batteries with Niobium Titanium Oxide Anodes | News | Toshiba, (n.d.). https://www.global.toshiba/ww/news/corporate/2024/06/news-20240620-01.html (accessed June 3, 2025).

[87] World's Leading Niobium Anode Battery Materials Supplier, Echion Technologies (n.d.). https://www.echiontech.com (accessed June 3, 2025).

[88] High-Power, Fast-Charging Battery Technology | Nyobolt, (n.d.). https://nyobolt.com/ (accessed July 10, 2025).

[89] Abundance in Earth's Crust for all the elements in the Periodic Table, (n.d.). https://periodictable.com/Properties/A/CrustAbundance.an.html (accessed June 24, 2025).

[90] F. Albarède, ed., The properties of elements, in: Geochemistry: An Introduction, 2nd ed., Cambridge University Press, Cambridge, 2009: pp. 5–24. https://doi.org/10.1017/CBO9780511807435.005.

[91] Z. Hu, S. Gao, Upper crustal abundances of trace elements: A revision and update, Chemical Geology 253 (2008) 205–221. https://doi.org/10.1016/j.chemgeo.2008.05.010.

[92] File:Elemental abundances.svg - Wikipedia, (2003). https://commons.wikimedia.org/wiki/File:Elemental_abundances.svg (accessed June 24, 2025).

[93] H. Pan, Y.-S. Hu, L. Chen, Room-temperature stationary sodium-ion batteries for large-scale electric energy storage, Energy Environ. Sci. 6 (2013) 2338. https://doi.org/10.1039/c3ee40847g.

[94] K.J. Schulz, N.M. Piatak, J.F. Papp, Niobium and tantalum, U.S. Geological Survey, 2017. https://doi.org/10.3133/pp1802M.

[95] Niobium | NioCorp Developments Ltd., (n.d.). https://www.niocorp.com/niobium/ (accessed June 3, 2025).

[96] CBMM Driving the Future of Advanced Materials, SFA (Oxford) (n.d.). https://www.sfa-oxford.com/market-news-and-insights/niobium-swing-producer-cbmm-driving-the-future-of-advanced-materials/ (accessed July 4, 2025).

[97] R.J. Cava, A. Santoro, D.W. Murphy, S.M. Zahurak, R.S. Roth, The structures of the lithium inserted metal oxides Li0.2ReO3 and Li0.36WO3, Journal of Solid State Chemistry 50 (1983) 121–128. https://doi.org/10.1016/0022-4596(83)90239-6.

[98] R.J. Cava, A. Santoro, D.W. Murphy, S. Zahurak, R.S. Roth, Structural aspects of lithium insertion in oxides: LixReO3 and Li2FeV3O8, Solid State Ionics 5 (1981) 323–326. https://doi.org/10.1016/0167-2738(81)90258-7.

[99] C.P. Koçer, K.J. Griffith, C.P. Grey, A.J. Morris, Cation Disorder and Lithium Insertion Mechanism of Wadsley–Roth Crystallographic Shear Phases from First Principles, J. Am. Chem. Soc. 141 (2019) 15121–15134. https://doi.org/10.1021/jacs.9b06316.

[100] Y. Yang, J. Zhao, Wadsley–Roth Crystallographic Shear Structure Niobium-Based Oxides: Promising Anode Materials for High-Safety Lithium-Ion Batteries, Advanced Science 8 (2021) 2004855. https://doi.org/10.1002/advs.202004855.

[101] M. Kunz, I.D. Brown, Out-of-Center Distortions around Octahedrally Coordinated *d*0 Transition Metals, Journal of Solid State Chemistry 115 (1995) 395–406. https://doi.org/10.1006/jssc.1995.1150.

[102] P. Jing, M. Liu, H.-P. Ho, Y. Ma, W. Hua, H. Li, N. Guo, Y. Ding, W. Zhang, H. Chen, B. Zhao, J. Wang, M. Liu, Tailoring the Wadsley–Roth crystallographic shear structures for high-power lithium-ion batteries, Energy Environ. Sci. 17 (2024) 6571–6581. https://doi.org/10.1039/D4EE02293A.

[103] Q. Deng, Y. Fu, C. Zhu, Y. Yu, Niobium-Based Oxides Toward Advanced Electrochemical Energy Storage: Recent Advances and Challenges, Small 15 (2019) 1804884. https://doi.org/10.1002/smll.201804884.

[104] H. Brunner, R. Gruehn, W. Mertin, Contributions to the Study of Inorganic Non-Stoichiometric Compounds, V. Preparation and Electron Optical Investigation of FeNb11O29, FeNb29O74 and TiNb14O37, Zeitschrift Für Naturforschung B 31 (1976) 549–553. https://doi.org/10.1515/znb-1976-0504.

[105] P. Tabero, Synthesis and properties of $FeNb_{11}O_{29}$, Ceram. Silik. 49 (2005) 126–131.

[106] I. Pinus, M. Catti, R. Ruffo, M.M. Salamone, C.M. Mari, Neutron Diffraction and Electrochemical Study of $FeNb_{11}O_{29}$/ $Li_{11}FeNb_{11}O_{29}$ for Lithium Battery Anode Applications, Chem. Mater. 26 (2014) 2203–2209. https://doi.org/10.1021/cm500442j.

[107] M. Bini, FeNb11O29 and related niobate anodes for fast-charging lithium-ion batteries: a review, J Solid State Electrochem (2024). https://doi.org/10.1007/s10008-024-05847-0.

[108] Y. Yang, H. Zhu, F. Yang, F. Yang, D. Chen, Z. Wen, D. Wu, M. Ye, Y. Zhang, J. Zhao, Q. Liu, X. Lu, M. Gu, C.C. Li, W. He, Ten Thousand-Cycle Ultrafast Energy Storage of Wadsley–Roth Phase Fe–Nb Oxides with a Desolvation Promoting Interfacial Layer, Nano Lett. 21 (2021) 9675–9683. https://doi.org/10.1021/acs.nanolett.1c03478.

[109] D. Spada, M. Aramini, M. Fittipaldi, A. Cini, M. Fracchia, P. Ghigna, A. Girella, C. Milanese, M. Bini, Spectroscopic Techniques and DFT Calculations to Highlight the Effect of Fe^{3+} on the Properties of $FeNb_{11}O_{29}$, Anode Material for Lithium-Ion Batteries, J. Phys. Chem. C 126 (2022) 4698–4709. https://doi.org/10.1021/acs.jpcc.1c10573.

[110] M. Bini, I. Quinzeni, D. Spada, The Doping of $FeNb_{11}O_{29}$ as a Way to Improve Its Electrochemical Performances, ChemistrySelect 4 (2019) 5656–5661. https://doi.org/10.1002/slct.201901182.

[111] D. Spada, I. Quinzeni, M. Bini, Orthorhombic and monoclinic modifications of $FeNb_{11}O_{29}$, as promising anode materials for lithium batteries: Relationships between pseudocapacitive behaviour and structure, Electrochimica Acta 296 (2019) 938–944. https://doi.org/10.1016/j.electacta.2018.11.047.

[112] D. Spada, B. Albini, P. Galinetto, D. Versaci, C. Francia, S. Bodoardo, G. Bais, M. Bini, $FeNb_{11}O_{29}$, anode material for high-power lithium-ion batteries: Pseudocapacitance and symmetrisation unravelled with advanced electrochemical and in situ/operando techniques, Electrochimica Acta 393 (2021) 139077. https://doi.org/10.1016/j.electacta.2021.139077.

[113] R. Zheng, S. Qian, X. Cheng, H. Yu, N. Peng, T. Liu, J. Zhang, M. Xia, H. Zhu, J. Shu, $FeNb_{11}O_{29}$ nanotubes: Superior electrochemical energy storage performance and operating mechanism, Nano Energy 58 (2019) 399–409. https://doi.org/10.1016/j.nanoen.2019.01.065.

[114] D. Spada, M.C. Mozzati, B. Albini, P. Galinetto, I. Quinzeni, D. Capsoni, M. Bini, Deepening the shear structure $FeNb_{11}O_{29}$: influence of polymorphism and doping on structural, spectroscopic and magnetic properties, Dalton Trans. 47 (2018) 15816–15826. https://doi.org/10.1039/C8DT02896F.

[115] X. Lou, C. Lin, Q. Luo, J. Zhao, B. Wang, J. Li, Q. Shao, X. Guo, N. Wang, Z. Guo, Crystal Structure Modification Enhanced $FeNb_{11}O_{29}$ Anodes for Lithium-Ion Batteries, ChemElectroChem 4 (2017) 3171–3180. https://doi.org/10.1002/celc.201700816.

[116] H. Fu, Y. Lian, Y. Bai, Z. Wang, Y. Hu, J. Zhao, H. Zhang, Porous biscuit-like nanoplate FeNb11O29−x@C for lithium-ion storage and oxygen evolution, Nanoscale 14 (2022) 17428–17437. https://doi.org/10.1039/D2NR05020J.

[117] Z. Lv, H. Zhu, W. Meng, L. Wei, Y. Yang, Y. Zhang, M. Ye, C.C. Li, Cation mixing in Wadsley-Roth phase anode of lithium-ion battery improves cycling stability and fast Li^+ storage, Applied Physics Reviews 8 (2021) 031404. https://doi.org/10.1063/5.0054030.

[118] J. Huang, Q. Chen, S. Chen, L. Luo, J. Li, C. Lin, Y. Chen, Al3+-doped FeNb11O29 anode materials with enhanced lithium-storage performance, Adv Compos Hybrid Mater 4 (2021) 733–742. https://doi.org/10.1007/s42114-021-00291-4.

[119] P. Galinetto, D. Spada, M.C. Mozzati, B. Albini, M. Bini, Effects of reaction atmosphere on physico-chemical properties of V-doped FeNb11O29, Optical Materials null (2019) null. https://doi.org/10.1016/J.OPTMAT.2019.04.035.

[120] D. Le Thanh, A. Guiet, E. Suard, R. Berthelot, Downsizing FeNb11O29 anode material through ultrafast solid-state microwave-assisted synthesis for enhanced electrochemical performance, Journal of Solid State Chemistry 330 (2024) 124444. https://doi.org/10.1016/j.jssc.2023.124444.

[121] V. Augustyn, P. Simon, B. Dunn, Pseudocapacitive oxide materials for high-rate electrochemical energy storage, Energy Environ. Sci. 7 (2014) 1597. https://doi.org/10.1039/c3ee44164d.

[122] J. Wang, J. Polleux, J. Lim, B. Dunn, Pseudocapacitive Contributions to Electrochemical Energy Storage in TiO2 (Anatase) Nanoparticles, J. Phys. Chem. C 111 (2007) 14925–14931. https://doi.org/10.1021/jp074464w.

[123] M. Catti, I. Pinus, K. Knight, Lithium insertion properties of Li TiNb2O7 investigated by neutron diffraction and first-principles modelling, Journal of Solid State Chemistry 229 (2015) 19–25. https://doi.org/10.1016/j.jssc.2015.05.011.

[124] X. Lou, Z. Xu, Z. Luo, C. Lin, C. Yang, H. Zhao, P. Zheng, J. Li, N. Wang, Y. Chen, H. Wu, Exploration of Cr0.2Fe0.8Nb11O29 as an advanced anode material for lithium-ion batteries of electric vehicles, Electrochimica Acta 245 (2017) 482–488. https://doi.org/10.1016/J.ELECTACTA.2017.05.168.

[125] E.E. Levin, J.H. Grebenkemper, T.M. Pollock, R. Seshadri, Protocols for High Temperature Assisted-Microwave Preparation of Inorganic Compounds, Chem. Mater. 31 (2019) 7151–7159. https://doi.org/10.1021/acs.chemmater.9b02594.

[126] F. Murgia, P. Antitomaso, L. Stievano, L. Monconduit, R. Berthelot, Express and low-cost microwave synthesis of the ternary Chevrel phase $Cu_2Mo_6S_8$ for application in rechargeable magnesium batteries, Journal of Solid State Chemistry 242 (2016) 151–154. https://doi.org/10.1016/j.jssc.2016.07.022.

[127] K.K. Gupta, K. Li, S. Balaji, P.S. Kumar, C. Lu, Microwave-assisted synthesis and electrochemical characterization of $TiNb_2O_7$ microspheres as anode materials for lithium-ion batteries, J Am Ceram Soc. (2023) jace.19000. https://doi.org/10.1111/jace.19000.

[128] V.C. Wu, H.A. Evans, R. Giovine, M.B. Preefer, J. Ong, E. Yoshida, P. Cabelguen, R.J. Clément, Rapid and Energy-Efficient Synthesis of Disordered Rocksalt Cathodes, Advanced Energy Materials 13 (2023) 2203860. https://doi.org/10.1002/aenm.202203860.

[129] P. Aswathy, S. Suriyakumar, S.A. Kumar, M.S. Oliyantakath Hassan, V. Vijayan, M.M. Shaijumon, Microwave-Assisted Synthesis of Sulfide Solid Electrolytes for All-Solid-State Sodium Batteries, ACS Appl. Energy Mater. 5 (2022) 12592–12601. https://doi.org/10.1021/acsaem.2c02224.

[130] A.R. Reach, A. Zohar, M.A. Wright, T. Li, R. Seshadri, Rapid Microwave Preparation of AlNb11O29 and Ti2Nb10O29 Wadsley–Roth Lithium–Ion Anode Compounds from Parent Oxides, ACS Appl. Energy Mater. 8 (2025) 7714–7721. https://doi.org/10.1021/acsaem.5c01005.

[131] J. Hu, B.M. Reddy, Advances in Microwave-assisted Heterogeneous Catalysis, Royal Society of Chemistry, 2023.

[132] J.B. Leriche, S. Hamelet, J. Shu, M. Morcrette, C. Masquelier, G. Ouvrard, M. Zerrouki, P. Soudan, S. Belin, E. Elkaïm, F. Baudelet, An Electrochemical Cell for Operando Study of Lithium Batteries Using Synchrotron Radiation, J. Electrochem. Soc. 157 (2010) A606. https://doi.org/10.1149/1.3355977.

[133] J. Kim, S. Park, S. Hwang, W.-S. Yoon, Principles and Applications of Galvanostatic Intermittent Titration Technique for Lithium-ion Batteries, J. Electrochem. Sci. Technol 13 (2022) 19–31. https://doi.org/10.33961/jecst.2021.00836.

[134] Neutron scattering lengths and cross sections, (n.d.). https://www.ncnr.nist.gov/resources/n-lengths/ (accessed March 28, 2025).

[135] A.J. Dianoux, Institut Laue-Langevin, eds., Neutron data booklet, 2. ed, Old City, Philadelphia, PA, 2003.

[136] Ö. Bergstöm, A.M. Andersson, K. Edström, T. Gustafsson, A neutron diffraction cell for studying lithium-insertion processes in electrode materials, J Appl Crystallogr 31 (1998) 823–825. https://doi.org/10.1107/S002188989800538X.

[137] H. Berg, H. Rundlöv, J.O. Thomas, The $LiMn_2O_4$ to λ-MnO2 phase transition studied by in situ neutron diffraction, Solid State Ionics 144 (2001) 65–69. https://doi.org/10.1016/S0167-2738(01)00894-3.

[138] V. Godbole, M. Hess, C. Villevieille, H. Kaiser, J.-F. Colin, P. Novak, Circular in situ neutron powder diffraction cell for study of reaction mechanism in electrode materials for Li-ion batteries, RSC Advances 3 (2013) 757–763. https://doi.org/10.1039/C2RA21526H.

[139] F. Rosciano, M. Holzapfel, W. Scheifele, P. Novák, A novel electrochemical cell for *in situ* neutron diffraction studies of electrode materials for lithium-ion batteries, J Appl Crystallogr 41 (2008) 690–694. https://doi.org/10.1107/S0021889808018025.

[140] J.-F. Colin, V. Godbole, P. Novák, *In situ* neutron diffraction study of Li insertion in $Li_4Ti_5O_{12}$, Electrochemistry Communications 12 (2010) 804–807. https://doi.org/10.1016/j.elecom.2010.03.038.

[141] W.K. Pang, V.K. Peterson, A custom battery for operando neutron powder diffraction studies of electrode structure, J Appl Cryst 48 (2015) 280–290. https://doi.org/10.1107/S1600576715000679.

[142] A.V. Dobromyslov, N.I. Taluts, Structure studies of quenched and tempered Zr-Ti alloys, Fiz. Met. Metalloved.; (USSR) 63:1 (1987). https://www.osti.gov/etdeweb/biblio/5683306 (accessed June 27, 2025).

[143] M. Bianchini, J.B. Leriche, J.-L. Laborier, L. Gendrin, E. Suard, L. Croguennec, C. Masquelier, A New Null Matrix Electrochemical Cell for Rietveld Refinements of In-Situ or Operando Neutron Powder Diffraction Data, J. Electrochem. Soc. 160 (2013) A2176–A2183. https://doi.org/10.1149/2.076311jes.

[144] N. Sharma, G. Du, A.J. Studer, Z. Guo, V.K. Peterson, In-situ neutron diffraction study of the MoS_2 anode using a custom-built Li-ion battery, Solid State Ionics 199–200 (2011) 37–43. https://doi.org/10.1016/j.ssi.2011.07.015.

[145] N. Sharma, M.V. Reddy, G. Du, S. Adams, B.V.R. Chowdari, Z. Guo, V.K. Peterson, Time-Dependent in-Situ Neutron Diffraction Investigation of a $Li(Co_{0.16}\ Mn_{1.84}\ )O_4$ Cathode, J. Phys. Chem. C 115 (2011) 21473–21480. https://doi.org/10.1021/jp2026237.

[146] W.R. Brant, S. Schmid, G. Du, H.E.A. Brand, W.K. Pang, V.K. Peterson, Z. Guo, N. Sharma, In Situ Neutron Powder Diffraction Using Custom-made Lithium-ion Batteries, JoVE (2014) 52284. https://doi.org/10.3791/52284.

[147] G. Du, N. Sharma, V.K. Peterson, J.A. Kimpton, D. Jia, Z. Guo, Br-Doped $Li_4Ti_5O_{12}$ and Composite TiO_2 Anodes for Li-ion Batteries: Synchrotron X-Ray and in situ Neutron Diffraction Studies, Adv Funct Materials 21 (2011) 3990–3997. https://doi.org/10.1002/adfm.201100846.

[148] M. Roberts, J.J. Biendicho, S. Hull, P. Beran, T. Gustafsson, G. Svensson, K. Edström, Design of a new lithium ion battery test cell for in-situ neutron diffraction measurements, Journal of Power Sources 226 (2013) 249–255. https://doi.org/10.1016/j.jpowsour.2012.10.085.

[149] W.R. Brant, M. Roberts, T. Gustafsson, J.J. Biendicho, S. Hull, H. Ehrenberg, K. Edström, S. Schmid, A large format in operando wound cell for analysing the structural dynamics of lithium insertion materials, Journal of Power Sources 336 (2016) 279–285. https://doi.org/10.1016/j.jpowsour.2016.10.071.

[150] L. Boulet-Roblin, P. Borel, D. Sheptyakov, C. Tessier, P. Novák, C. Villevieille, Operando Neutron Powder Diffraction Using Cylindrical Cell Design: The Case of $LiNi_{0.5}Mn_{1.5}O_4$ vs Graphite, J. Phys. Chem. C 120 (2016) 17268–17273. https://doi.org/10.1021/acs.jpcc.6b05777.

[151] L. Boulet-Roblin, D. Sheptyakov, P. Borel, C. Tessier, P. Novák, C. Villevieille, Crystal structure evolution via operando neutron diffraction during long-term cycling of a customized 5 V full Li-ion cylindrical cell $LiNi_{0.5}Mn_{1.5}O_4$ vs. graphite, J. Mater. Chem. A 5 (2017) 25574–25582. https://doi.org/10.1039/C7TA07917F.

[152] L. Vitoux, M. Reichardt, S. Sallard, P. Novák, D. Sheptyakov, C. Villevieille, A Cylindrical Cell for Operando Neutron Diffraction of Li-Ion Battery Electrode Materials, Frontiers in Energy Research 6 (2018). https://www.frontiersin.org/articles/10.3389/fenrg.2018.00076 (accessed May 8, 2023).

[153] K. Choudhary, I.O. Santos Mendoza, A. Nadeina, D. Becker, T. Lombard, V. Seznec, J.-N. Chotard, Operando X-ray diffraction in transmission geometry « at home » from tape

casted electrodes to all-solid-state battery, Journal of Power Sources 553 (2023) 232270. https://doi.org/10.1016/j.jpowsour.2022.232270.

[154] J. Rodriguez-Carvajal, Recent developments of the program FULLPROF, commission on powder diffraction, IUCr Newsl. 26 (2001).

[155] N. Takami, K. Ise, Y. Harada, T. Iwasaki, T. Kishi, K. Hoshina, High-energy, fast-charging, long-life lithium-ion batteries using TiNb2O7 anodes for automotive applications, Journal of Power Sources 396 (2018) 429–436. https://doi.org/10.1016/j.jpowsour.2018.06.059.

[156] X. Lou, R. Li, X. Zhu, L. Luo, Y. Chen, C. Lin, H. Li, X.S. Zhao, New Anode Material for Lithium-Ion Batteries: Aluminum Niobate ($AlNb_{11}O_{29}$), ACS Appl. Mater. Interfaces 11 (2019) 6089–6096. https://doi.org/10.1021/acsami.8b20246.

[157] Z. Yao, X. Xia, Y. Zhang, D. Xie, C. Ai, S. Lin, Y. Wang, S. Deng, S. Shen, X. Wang, Y. Yu, J. Tu, Superior high-rate lithium-ion storage on Ti2Nb10O29 arrays via synergistic TiC/C skeleton and N-doped carbon shell, Nano Energy 54 (2018) 304–312. https://doi.org/10.1016/j.nanoen.2018.10.024.

[158] Y. Yang, H. Zhu, J. Xiao, H. Geng, Y. Zhang, J. Zhao, G. Li, X.-L. Wang, C.C. Li, Q. Liu, Achieving Ultrahigh-Rate and High-Safety Li+ Storage Based on Interconnected Tunnel Structure in Micro-Size Niobium Tungsten Oxides, Advanced Materials 32 (2020) 1905295. https://doi.org/10.1002/adma.201905295.

[159] M.R. Palacín, Understanding ageing in Li-ion batteries: a chemical issue, Chem. Soc. Rev. 47 (2018) 4924–4933. https://doi.org/10.1039/C7CS00889A.

[160] L.H.B. Nguyen, P.S. Camacho, J. Fondard, D. Carlier, L. Croguennec, M.R. Palacin, A. Ponrouch, C. Courrèges, R. Dedryvère, K. Trad, C. Jordy, S. Genies, Y. Reynier, L. Simonin, First 18650-format Na-ion cells aging investigation: A degradation mechanism study, Journal of Power Sources 529 (2022) 231253. https://doi.org/10.1016/j.jpowsour.2022.231253.

[161] C. Li, Z. Wang, Z. He, Y. Li, J. Mao, K. Dai, C. Yan, J. Zheng, An advance review of solid-state battery: Challenges, progress and prospects, Sustainable Materials and Technologies 29 (2021) e00297. https://doi.org/10.1016/j.susmat.2021.e00297.

[162] C. Arbizzani, G. Gabrielli, M. Mastragostino, Thermal stability and flammability of electrolytes for lithium-ion batteries, Journal of Power Sources 196 (2011) 4801–4805. https://doi.org/10.1016/j.jpowsour.2011.01.068.

[163] Y. Zheng, Y. Shen, J. Guo, J. Li, J. Wang, D. Ning, Y. Liu, Y. Huang, Y. Tang, Y. Deng, H. Yan, H. Shao, Recent advances in solid-state lithium batteries based on anode engineering, Nano Research Energy 3 (2024). https://doi.org/10.26599/NRE.2024.9120118.

[164] F. Han, A.S. Westover, J. Yue, X. Fan, F. Wang, M. Chi, D.N. Leonard, N.J. Dudney, H. Wang, C. Wang, High electronic conductivity as the origin of lithium dendrite formation within solid electrolytes, Nat Energy 4 (2019) 187–196. https://doi.org/10.1038/s41560-018-0312-z.

[165] K. Yoon, S. Lee, K. Oh, K. Kang, Challenges and Strategies towards Practically Feasible Solid-State Lithium Metal Batteries, Advanced Materials 34 (2022) 2104666. https://doi.org/10.1002/adma.202104666.

[166] J. Feng, Z. Gao, L. Sheng, Z. Hao, F.R. Wang, Progress and perspective of interface design in garnet electrolyte-based all-solid-state batteries, Carbon Energy 3 (2021) 385–409. https://doi.org/10.1002/cey2.100.

[167] S. Wenzel, S.J. Sedlmaier, C. Dietrich, W.G. Zeier, J. Janek, Interfacial reactivity and interphase growth of argyrodite solid electrolytes at lithium metal electrodes, Solid State Ionics 318 (2018) 102–112. https://doi.org/10.1016/j.ssi.2017.07.005.

[168] Y. Zhou, C. Doerrer, J. Kasemchainan, P.G. Bruce, M. Pasta, L.J. Hardwick, Observation of Interfacial Degradation of Li6PS5Cl against Lithium Metal and LiCoO2 via In Situ Electrochemical Raman Microscopy, Batteries & Supercaps 3 (2020) 647–652. https://doi.org/10.1002/batt.201900218.

[169] H. Liu, E. Wang, Q. Zhang, Y. Ren, X. Guo, L. Wang, G. Li, H. Yu, Unique 3D nanoporous/macroporous structure Cu current collector for dendrite-free lithium deposition, Energy Storage Materials 17 (2019) 253–259. https://doi.org/10.1016/j.ensm.2018.07.010.

[170] J. Wang, X. Yan, Z. Zhang, R. Guo, H. Ying, G. Han, W.-Q. Han, Rational Design of an Electron/Ion Dual-Conductive Cathode Framework for High-Performance All-Solid-State Lithium Batteries, ACS Appl. Mater. Interfaces 12 (2020) 41323–41332. https://doi.org/10.1021/acsami.0c10463.

[171] Z. Tong, S.-B. Wang, Y.-K. Liao, S.-F. Hu, R.-S. Liu, Interface Between Solid-State Electrolytes and Li-Metal Anodes: Issues, Materials, and Processing Routes, ACS Appl. Mater. Interfaces 12 (2020) 47181–47196. https://doi.org/10.1021/acsami.0c13591.

[172] L. Höltschi, F. Jud, C. Borca, T. Huthwelker, C. Villevieille, V. Pelé, C. Jordy, M. El Kazzi, P. Novák, Study of Graphite Cycling in Sulfide Solid Electrolytes, J. Electrochem. Soc. 167 (2020) 110558. https://doi.org/10.1149/1945-7111/aba36f.

[173] L. Höltschi, C.N. Borca, T. Huthwelker, F. Marone, C.M. Schlepütz, V. Pelé, C. Jordy, C. Villevieille, M.E. Kazzi, P. Novák, Performance-limiting factors of graphite in sulfide-based all-solid-state lithium-ion batteries, Electrochimica Acta 389 (2021) 138735. https://doi.org/10.1016/j.electacta.2021.138735.

[174] C. Liu, J. Sun, P. Zheng, L. Jiang, H. Liu, J. Chai, Q. Liu, Z. Liu, Y. Zheng, X. Rui, Recent advances of non-lithium metal anode materials for solid-state lithium-ion batteries, J. Mater. Chem. A 10 (2022) 16761–16778. https://doi.org/10.1039/D2TA03905B.

[175] R. Miyazaki, High-Capacity Anode Materials for All-Solid-State Lithium Batteries, Front. Energy Res. 8 (2020). https://doi.org/10.3389/fenrg.2020.00171.

[176] D. Cao, T. Ji, A. Singh, S. Bak, Y. Du, X. Xiao, H. Xu, J. Zhu, H. Zhu, Unveiling the Mechanical and Electrochemical Evolution of Nanosilicon Composite Anodes in Sulfide-Based All-Solid-State Batteries, Advanced Energy Materials 13 (2023) 2203969. https://doi.org/10.1002/aenm.202203969.

[177] H. Kitaura, A. Hayashi, K. Tadanaga, M. Tatsumisago, High-rate performance of all-solid-state lithium secondary batteries using Li4Ti5O12 electrode, Journal of Power Sources 189 (2009) 145–148. https://doi.org/10.1016/j.jpowsour.2008.10.005.

[178] Y. Cao, Q. Li, S. Lou, Y. Ma, C. Du, Y. Gao, G. Yin, Enhanced electrochemical performance of Li4Ti5O12 through in-situ coating 70Li2S-30P2S5 solid electrolyte for all-solid-state lithium batteries, Journal of Alloys and Compounds 752 (2018) 8–13. https://doi.org/10.1016/j.jallcom.2018.04.149.

[179] A. Orue Mendizabal, N. Gomez, F. Aguesse, P. López-Aranguren, Designing Spinel Li4Ti5O12 Electrode as Anode Material for Poly(ethylene)oxide-Based Solid-State Batteries, Materials 14 (2021) 1213. https://doi.org/10.3390/ma14051213.

[180] L.-Q. Cheng, X. Xie, K. Chen, Y. He, H. Xu, R. Liu, M. Feng, Enhancing the electrochemical properties of $TiNb_2O_7$ anodes with SP-CNT binary conductive agents for both liquid and solid state lithium ion batteries, RSC Adv. 14 (2024) 15722–15729. https://doi.org/10.1039/D4RA02216E.

[181] C. Kim, G. Nam, Y. Ahn, X. Hu, M. Liu, Nb1.60Ti0.32W0.08O5−δ as negative electrode active material for durable and fast-charging all-solid-state Li-ion batteries, Nat Commun 15 (2024) 8832. https://doi.org/10.1038/s41467-024-52767-8.

[182] R. Pfenninger, S. Afyon, I. Garbayo, M. Struzik, J.L.M. Rupp, Lithium Titanate Anode Thin Films for Li-Ion Solid State Battery Based on Garnets, Advanced Functional Materials 28 (2018) 1800879. https://doi.org/10.1002/adfm.201800879.

[183] L.-Q. Cheng, J. Pan, K. Chen, X. Hao, X. Xie, X. Dong, Z. Wang, R. Liu, M. Feng, Synergistic effects of charge redistribution and morphology regulation in Mo-doped TiNb2O7 anodes for solid-state battery applications, J Mater Sci 60 (2025) 3014–3025. https://doi.org/10.1007/s10853-025-10637-8.

[184] Y. Wu, D. Liu, D. Qu, J. Li, Z. Xie, X. Zhang, H. Chen, H. Tang, Porous oxygen-deficient TiNb2O7 spheres wrapped by MXene as high-rate and durable anodes for liquid and all-solid-state lithium-ion batteries, Chemical Engineering Journal 438 (2022) 135328. https://doi.org/10.1016/j.cej.2022.135328.

[185] B.-S. Zhao, L. Wang, S. Liu, G.-R. Li, X.-P. Gao, High-Efficiency Hybrid Sulfur Cathode Based on Electroactive Niobium Tungsten Oxide and Conductive Carbon Nanotubes for All-Solid-State Lithium–Sulfur Batteries, ACS Appl. Mater. Interfaces 14 (2022) 1212–1221. https://doi.org/10.1021/acsami.1c21573.

[186] G. Whang, J. Huang, P.N. Le Pham, M.A. Kraft, W.G. Zeier, Not All Lithium–Indium Counter Electrodes Are Made Equal: Probing the Inhomogeneities and Kinetics of Uniaxially Pressed Li–In Counter Electrodes in All Solid-State Batteries, ACS Electrochem. 1 (2025) 249–262. https://doi.org/10.1021/acselectrochem.4c00060.

[187] W.J. Jeong, C. Wang, S.G. Yoon, Y. Liu, T. Chen, M.T. McDowell, Electrochemical behavior of elemental alloy anodes in solid-state batteries, ACS Energy Lett. 9 (2024) 2554–2563. https://doi.org/10.1021/acsenergylett.4c00915.

[188] A.L. Santhosha, L. Medenbach, J.R. Buchheim, P. Adelhelm, The Indium−Lithium Electrode in Solid-State Lithium-Ion Batteries: Phase Formation, Redox Potentials, and Interface Stability, Batteries & Supercaps 2 (2019) 524–529. https://doi.org/10.1002/batt.201800149.

[189] T. Famprikis, P. Canepa, J.A. Dawson, M.S. Islam, C. Masquelier, Fundamentals of inorganic solid-state electrolytes for batteries, Nat. Mater. 18 (2019) 1278–1291. https://doi.org/10.1038/s41563-019-0431-3.

[190] F. Zheng, M. Kotobuki, S. Song, M.O. Lai, L. Lu, Review on solid electrolytes for all-solid-state lithium-ion batteries, Journal of Power Sources 389 (2018) 198–213. https://doi.org/10.1016/j.jpowsour.2018.04.022.

[191] K.J. Kim, M. Balaish, M. Wadaguchi, L. Kong, J.L.M. Rupp, Solid-State Li–Metal Batteries: Challenges and Horizons of Oxide and Sulfide Solid Electrolytes and Their Interfaces, Advanced Energy Materials 11 (2021) 2002689. https://doi.org/10.1002/aenm.202002689.

[192] H. Kwak, S. Wang, J. Park, Y. Liu, K.T. Kim, Y. Choi, Y. Mo, Y.S. Jung, Emerging Halide Superionic Conductors for All-Solid-State Batteries: Design, Synthesis, and Practical Applications, ACS Energy Lett. 7 (2022) 1776–1805. https://doi.org/10.1021/acsenergylett.2c00438.

[193] L. Huang, L. Zhang, J. Bi, T. Liu, Y. Zhang, C. Liu, J. Cui, Y. Su, B. Wu, F. Wu, An Insight into Halide Solid-State Electrolytes: Progress and Modification Strategies, Energy Material Advances 5 (2024) 0092. https://doi.org/10.34133/energymatadv.0092.

[194] X. Nie, J. Hu, C. Li, Halide-based solid electrolytes: The history, progress, and challenges, Interdisciplinary Materials 2 (2023) 365–389. https://doi.org/10.1002/idm2.12090.

[195] K.H. Park, Q. Bai, D.H. Kim, D.Y. Oh, Y. Zhu, Y. Mo, Y.S. Jung, Design Strategies, Practical Considerations, and New Solution Processes of Sulfide Solid Electrolytes for All-

Solid-State Batteries, Advanced Energy Materials 8 (2018) 1800035. https://doi.org/10.1002/aenm.201800035.

[196] W. Ji, D. Zheng, X. Zhang, T. Ding, D. Qu, A kinetically stable anode interface for Li_3YCl_6-based all-solid-state lithium batteries, J. Mater. Chem. A 9 (2021) 15012–15018. https://doi.org/10.1039/d1ta03042f.

[197] P. Minnmann, L. Quillman, S. Burkhardt, F.H. Richter, J. Janek, Editors' Choice—Quantifying the Impact of Charge Transport Bottlenecks in Composite Cathodes of All-Solid-State Batteries, J. Electrochem. Soc. 168 (2021) 040537. https://doi.org/10.1149/1945-7111/abf8d7.

[198] Y. Rudel, M. Rana, J. Ruhl, C. Rosenbach, J. Müller, P. Michalowski, A. Kwade, W.G. Zeier, Investigating the Influence of the Effective Ionic Transport on the Electrochemical Performance of Si/C-Argyrodite Solid-State Composites, Batteries & Supercaps 6 (2023) e202300211. https://doi.org/10.1002/batt.202300211.

[199] A. Ševčík, Oscillographic polarography with periodical triangular voltage, Collect. Czech. Chem. Commun. 13 (1948) 349–377. https://doi.org/10.1135/cccc19480349.

[200] J.E.B. Randles, A cathode ray polarograph. Part II.—The current-voltage curves, Trans. Faraday Soc. 44 (1948) 327–338. https://doi.org/10.1039/TF9484400327.

[201] T.H. Wan, M. Saccoccio, C. Chen, F. Ciucci, Influence of the Discretization Methods on the Distribution of Relaxation Times Deconvolution: Implementing Radial Basis Functions with DRTtools, Electrochimica Acta 184 (2015) 483–499. https://doi.org/10.1016/j.electacta.2015.09.097.

[202] D. Guerard, A. Herold, Intercalation of lithium into graphite and other carbons, Carbon 13 (1975) 337–345. https://doi.org/10.1016/0008-6223(75)90040-8.

[203] T.K. Schwietert, V.A. Arszelewska, C. Wang, C. Yu, A. Vasileiadis, N.J.J. de Klerk, J. Hageman, T. Hupfer, I. Kerkamm, Y. Xu, E. van der Maas, E.M. Kelder, S. Ganapathy, M. Wagemaker, Clarifying the relationship between redox activity and electrochemical stability in solid electrolytes, Nat. Mater. 19 (2020) 428–435. https://doi.org/10.1038/s41563-019-0576-0.

[204] P. Vadhva, J. Hu, M.J. Johnson, R. Stocker, M. Braglia, D.J.L. Brett, A.J.E. Rettie, Electrochemical Impedance Spectroscopy for All-Solid-State Batteries: Theory, Methods and Future Outlook, ChemElectroChem 8 (2021) 1930–1947. https://doi.org/10.1002/celc.202100108.

Abstract

Conventional Li-ion battery negative electrode materials have inherent trade-offs: graphite delivers high capacity but raises safety concerns, whereas $Li_4Ti_5O_{12}$ provides excellent safety and rate performance but lower energy density. These limitations motivate the search for high-rate alternatives such as Wadsley–Roth phases, which combine structural stability, fast ion transport, and a favourable operating potential. This thesis aims to valorise $FeNb_{11}O_{29}$ composition in four directions. Firstly, microwave-assisted synthesis was shown to suppress particle growth and enhance Li^+ diffusion, yielding submicrometric powders with excellent cycling stability. While particle downsizing improved transport, the intrinsic fast kinetics of Wadsley–Roth phases were also confirmed in micrometric powders. Secondly, *operando* neutron diffraction was employed to track the structural evolution of $FeNb_{11}O_{29}$ and benchmark experimental setups at the ILL. While coin-type cells provided high-quality diffraction data but poor electrochemistry, cylindrical cells enabled faster cycling with sufficient data quality using conventional electrolytes. For the first time, the high-resolution D2B diffractometer was successfully applied to operando studies, opening the door to more routine neutron use in battery research. Thirdly, the practical feasibility of $FeNb_{11}O_{29}$ was assessed through 18650-format prototypes and ageing studies in coin cells. The material delivered intermediate energy densities between graphite and $Li_4Ti_5O_{12}$, but degradation was strongly accelerated by high temperature, slow cycling, and high state of charge. Finally, in solid-state batteries, electrode composition was found to be essential: an intermediate carbon content provided a balanced ionic and electronic transport, minimizing polarization and maximizing capacity. Although the active material and electrolyte showed bulk stability, sulfur-rich interfacial species formed during cycling, highlight the need for composite optimization and interface engineering.

Keywords: Li-ion batteries, Wadsley-Roth oxides, microwave synthesis, *operando* analysis, neutron diffraction, prototyping

Résumé

Les matériaux d'électrode négative Li-ion conventionnels présentent des compromis : le graphite offre une grande capacité mais pose des enjeux de sécurité, tandis que le $Li_4Ti_5O_{12}$ est sûr et rapide au prix d'une densité énergétique plus faible. D'où l'intérêt pour des phases de Wadsley–Roth, stables, à transport ionique rapide et à potentiel favorable. Cette thèse valorise $FeNb_{11}O_{29}$ selon quatre axes. (i) La synthèse assistée par micro-ondes limite la croissance des particules et améliore la diffusion du Li^+, donnant des poudres submicroniques stables en cyclage, tout en confirmant la cinétique rapide intrinsèque des phases Wadsley–Roth dans les poudres micrométriques. (ii) La diffraction neutronique *operando* a permis de suivre l'évolution structurale et de tester différents montages à l'ILL : les piles bouton fournissent d'excellentes données mais une électrochimie limitée, tandis que les cellules cylindriques offrent un compromis qualité/dynamique. Le diffractomètre haute résolution D2B a été utilisé pour la première fois en *operando*. (iii) La faisabilité pratique a été validée par des prototypes au format 18650 et des études de vieillissement : la densité énergétique se situe entre le graphite et le $Li_4Ti_5O_{12}$, mais la dégradation s'accélère à haute température, faible vitesse de charge/décharge et fort état de charge. (iv) En batteries tout solide, une teneur intermédiaire en carbone optimise les transports ionique et électronique, réduisant la polarisation. Malgré la stabilité en volume des matériaux, des espèces interfaciales soufrées apparaissent, montrant l'importance de l'ingénierie des interfaces.

Mots-clés : Batteries Li-ion, oxydes de Wadsley–Roth, synthèse micro-ondes, analyse *operando*, diffraction neutronique, prototypage